AD-A253 450

OXIDATION PROTECTION SYSTEMS FOR
CARBON-CARBON COMPOSITES
FORMED BY CHEMICAL VAPOR DEPOSITION
AND PLASMA ASSISTED CHEMICAL VAPOR
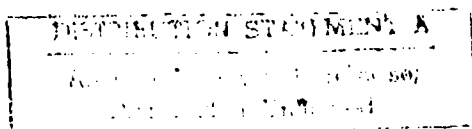### DEPOSITION TECHNIQUES

Written By:

Yongyi Shi
Jean L. Stojak
Jun He

Principal Investigators:

Jarlen Don
Maurice A. Wright*

Department of Mechanical Engineering and Energy Processes
*Materials Technology Center
Southern Illinois University at Carbondale
Carbondale, IL   62901

92-19910

92 7 23 058

	REPORT DATE	REPORT TYPE AND DATES COVERED
	22 April 92	Final 1 March 88-28 Feb 91

TITLE AND SUBTITLE
OXIDATION PROTECTION SYSTEMS FOR CARBON-CARBON COMPOSITE FORMED BY CHEMICAL VAPOR AND DEPOSITION AND PLASMA ASSISTED CHEMICAL VAPOR DEPOSITION TECHNIQUES

5. FUNDING NUMBERS
G
AFOSR-88-0130

AUTHOR(S)

Y. Shi, J. Stojak, J. He

J. Don and M.A. Wright (compilers)

7. PERFORMING ORGANIZATION NAME(S) AND ADDRESS(ES)

SOUTHERN ILLINOIS UNIVERSITY AT CARBONDALE
CARBONDALE, ILLINOIS 62901

8. PERFORMING ORGANIZATION REPORT NUMBER

AFOSR-3

9. SPONSORING / MONITORING AGENCY NAME(S) AND ADDRESS(ES)

AIR FORCE OFFICE OF SCIENTIFIC RESEARCH
BOLLING AIR FORCE BASE
WASHINGTON, DC 20332-6448

10. SPONSORING / MONITORING AGENCY REPORT NUMBER

11. SUPPLEMENTARY NOTES

12a. DISTRIBUTION / AVAILABILITY STATEMENT

UNCLASSIFIED/UNLIMITED

12b. DISTRIBUTION CODE

UNCLASSIFIED

13. ABSTRACT (Maximum 200 words)

A final report written in three sections. 1) "CVI Densification of Carbon-Carbon Composites" deals with the densification of porous preforms of carbonized carbon-resin mixtures using various methane and hydrogen gas mixtures. The experimental conditions include temperatures between 1000°C and 1200°C and total pressures between 5 and 15 torr. The resulting solid was characterized using optical and electron microscopy. 2) "Oxidation Protection of Carbon-Carbon Composites Using Pack Cementation" deals with formation of oxidation protective films formed from combinations of boron carbide, silicon carbide and zirconium carbide. Films were processed using a reactive process called pack cementation. The effects of initial powder composition and temperature were correlated with microstructure and oxidation resistance. 3) In "The Formation of Oxidation Protective Coatings on Carbon-Carbon Composites Using a Chemical Vapor Deposition (CVD) Technique" four types of CVD coatings were investigated: SiC, ZrB_2, ZrB_2/SiC multilayer and graded SrC/ZrC. Coatings were produced as a function of temperature, pressure and gas flow rates. The resulting coatings were then characterized in terms of microstructure and oxidation resistance.

14. SUBJECT TERMS
OXIDATION RESISTANCE, CHEMICAL VAPOR DEPOSITION, CARBON-CARBON

15. NUMBER OF PAGES
399

16. PRICE CODE

17. SECURITY CLASSIFICATION OF REPORT	18. SECURITY CLASSIFICATION OF THIS PAGE	19. SECURITY CLASSIFICATION OF ABSTRACT	20. LIMITATION OF ABSTRACT
UNCLASSIFIED	UNCLASSIFIED	UNCLASSIFIED	UL

OXIDATION PROTECTION SYSTEMS FOR CARBON-CARBON COMPOSITES
FORMED BY CHEMICAL VAPOR DEPOSITION AND
PLASMA ASSISTED CHEMICAL VAPOR DEPOSITION TECHNIQUES

Written By:

Yongyi Shi
Jean L. Stojak
Jun He

Principal Investigators:

Jarlen Don
Maurice Wright*

Department of Mechanical Engineering and Energy Processes
*Materials Technology Center
Southern Illinois University ar Carbondale
Carbondale, IL 62901

DTIC QUALITY INSPECTED 1

Accession For

NTIS GRA&I	☑	
DTIC TAB	☐	
Unannounced	☐	
Justification		

By

Distribution/

Availability Codes

Dist	Avail and/or Special
A-1	

FOREWORD

This three-year research program was the culmination of efforts by several people. Dr. Jarlen Don, Department of Mechanical Engineering and Energy Processes, outlined the original research plan. Dr. Maurice Wright, Director of the Materials Technology Center, contributed to the technical discussions. Dr. Don guided the research program in his role as technical director. He supervised the practical work and advised research assistants as they performed daily activities.

The practical work for this project was performed by three graduate research assistants in the Department of Mechanical Engineering and Energy Processes as research for their master degree theses. All worked under Dr. Don's direction. Mr. Yongyi Shi was responsible for the CVI densification work. Ms. Jean Stojak completed the study on oxidation protection using pack cementation. Ms. Jun He performed the study on protective coatings using the chemical vapor deposition technique.

The thesis prepared by each of these outstanding students comprises a section of this final report.

OXIDATION PROTECTION SYSTEMS FOR CARBON-CARBON COMPOSITES FORMED BY CHEMICAL VAPOR DEPOSITION AND PLASMA ASSISTED CHEMICAL VAPOR DEPOSITION TECHNIQUES

Section 1:

CVI Densification of Carbon-Carbon Composites

By

Yongyi Shi

A thesis submitted in partial fulfillment of
the requirements for the degree of
Master of Science

ACKNOWLEDGEMENTS

ABSTRACT

Chemical vapor infiltration (CVI) of 2-D carbon-carbon composite preforms was investigated. The process of CVI for densification of porous preforms consists of gaseous reactant diffusion and decomposition followed by solid product formation in the porous body. The competition between the diffusion of the reactant species into the preform and the chemical reactions on the pore surfaces is the key to understand this process.

The CVI experiments were conducted using a CVI system equipped with a TGA weight gain measurement unit interfaced with a computer for data-acquisition and parameter control. Methane and hydrogen gas mixture was used as a precursor gas. The experimental temperatures varied from 1000 °C to 1200 °C, and the pressures varied between 5 and 15 torr. Direct density measurement, *mineral spirits measurement*, density profile measurement, as well as optical and electron microscopy, were performed to characterize the densified specimens. The weight gain and CVI rate curves were analyzed together with other characterization results.

The results of CVI, in terms of densification uniformity, were greatly influenced by experimental parameters. The chemical reaction was a strong function of temperature, with an activation energy between 124 to 152 kcal/mole. Increasing the temperature caused the reactant gases to deplete upon progressing into the pores, which resulted in a concentration gradient between the surface and the center of the preform being densified. Bottle-neck pores or surface crust will form which hinders further infiltration. The specimens processed at high temperatures typically have a large density gradient and

low overall density.

Increasing pressure promoted infiltration as opposed to near-surface pore closure. The preform geometry influenced the reactant gas transport. Decreasing pore size as infiltration proceeded may change a originally reaction controlled process into a diffusion limited process. The combined effect of decrease in total available surface area and the pore sizes was found to be responsible for the decrease of CVI rate at low processing temperatures.

A model incorporating *overlap* concept was found to fit well with experimental weight gain curves.

TABLE OF CONTENTS

Section

LIST OF TABLES

LIST OF FIGURES

CHAPTER 1

INTRODUCTION

Carbon fiber reinforced carbon matrix composite materials, or otherwise known as carbon-carbon (C-C) composites, possess many of the desirable high-temperature properties of conventional carbon and graphite materials[1-3]. These properties include high strength, high modulus, and low creep at temperatures as high as 2800 °C, high thermal shock resistance due to high thermal conductivity and low coefficient of thermal expansion. In addition, special characteristics of carbon-carbon composites are high specific strength, high fracture toughness, and pseudoplasticity[4]. Due to these unique features of carbon-carbon composites, they are used mainly in flight-related applications such as jet engine afterburner nozzles, nose cones, and high performance aircraft brakes[1,5]. Recently, carbon-carbon composite heating elements for high temperature vacuum and inert atmosphere furnaces have become commercially available. Now, carbon-carbon composites have become the most highly developed fiber reinforced composite materials.

Carbon-carbon composites are fabricated by impregnating a carbon precursor into a preform of carbon fibers, followed by the pyrolysis of the precursor to form matrix carbon, as shown in the schematic diagram in Figure 1-1[1]. The precursors can be either liquid organic materials such as resin or pitch, or gaseous hydrocarbons such as methane, propylene, etc. The liquid precursors have to be pyrolyzed at about 1000 °C after impregnation, this process is called carbonization. This pyrolysis process drives the volatile elements out of the matrix to form solid carbon. During this process,

porosity and cracks form due to the release of the volatile species and the thermal expansion coefficient mismatch between the fiber and the matrix materials. Multiple impregnation-carbonization cycles are used in industry to densify the composites[1]. An alternative method which can also be employed to form the matrix carbon is the in-situ pyrolysis of a hydrocarbon gas to deposit pyrolytic carbon on the walls of open porosity. This process is known as chemical vapor infiltration, or CVI. The carbon thus converted from the gas phase is referred to as "pyrolytic carbon", or "CVD carbon"[7]. An obvious advantage of this process is the potential to achieve full densification.

A major problem associated with CVI processing is the tendency of preferred deposition of pyrolytic carbon near the surface of the substrate[6,7]. Since the driving force of transporting the hydrocarbon gas molecules into and the gaseous by-product out of the open porosity is mainly diffusion, a concentration gradient normally exists between the center and the surface of the substrate being densified[6]. In order to achieve uniform densification throughout the composites, the overall reaction rate should be controlled in the chemical reaction limited regime, so that there will always be sufficient supply of reaction gases inside the preform[7]. Kinetic studies show that this can be achieved in two ways: (1) to lower the chemical reaction rate, or (2) to enhance the mass transfer step.

Enhancing the mass transfer step normally requires a complicated processing apparatus, whereas reducing the chemical reaction rate is a relatively easy task, it can be achieved by reducing the processing temperature since chemical reaction rate is much more sensitive to temperature than diffusion[1,7]. Theoretically, the ideal condition for

uniform deposition of pyrolytic carbon throughout the composite body will be given at infinitely small rates[7]. This can be realized by selecting a processing temperature as low as possible. But low processing temperature, and the resulting low reaction rate, will also require long processing time in order to achieve a desired density. From an economical point of view, this is a very severe situation. In carbon and composite industry, this is considered as the major drawback of the CVI process[1].

Over the years, several CVI techniques have been developed aimed at obtaining uniform densification in a shorter time[6,7], but the more traditional isothermal-isobaric CVI technique is almost exclusively used in industrial production[1][5]. The apparent advantages of this process includes its relatively simple reactor system, and the readiness to be applied to a large number of composite parts in one batch, which can be different sizes and shapes, including very irregular shapes of varying thickness. But the isothermal technique is also the one that suffers most from the common drawbacks of CVI processing such as non-uniform densification through the composite thickness, long processing time, and the interruptions of the process sometimes needed for surface crust removal in order to expose more open porosity for further infiltration[6]. Better utilization of this processing technique depends on an understanding of the basic kinetic steps involved, and the influence of processing parameters on these steps.

There has been increasing amount of effort dedicated to the development of the CVI process due to its increasing role in the processing of fiber-reinforced composites. This has resulted in the development of various new techniques as well as greater interests in basic mechanistic and kinetic study of process[6, 8-14]. Systematic experimental study

of the CVI densification process toward the understanding of the relationship of processing parameters and the infiltration rate, as well as microstructure of the infiltrated composites, is definitely in need. Therefore, this study was conducted focusing on the better understanding of the these aspects in CVI densification of carbon-carbon composites using an in-house CVI reactor equipped with a TGA microbalance.

The specific objectives of this thesis investigation are:

(1) To study the effects of processing parameters, especially temperature and pressure, on the isothermal CVI processing of carbon-carbon composite through the densification of 2-D carbon-carbon specimens, incorporating on-line TGA measurement;

(2) To characterize the microstructure of the CVI densified carbon-carbon composite using optical and electron microscopy, as well as density profile measurements, and correlate the results with densification conditions;

(3) To model the infiltration processing based on the kinetics of gas-solid heterogeneous reactions and experiment results;

(4) To provide guidelines for optimizing the isothermal CVI technique in terms of achieving uniform densification in a reduced processing time.
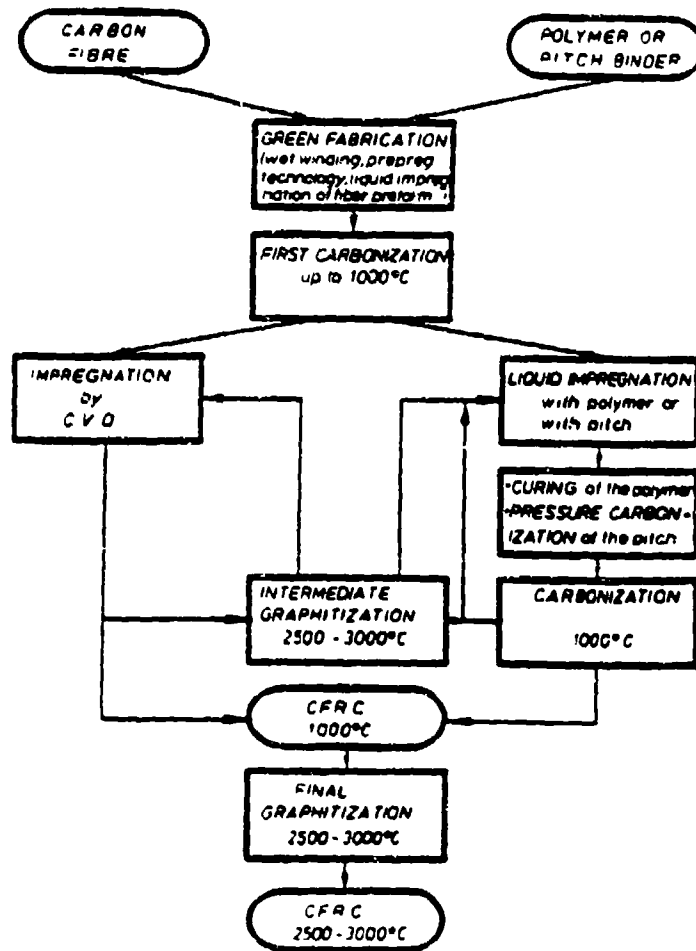
Figure 1-1. Production Scheme of Carbon-Carbon Composites

CHAPTER 2

LITERATURE REVIEW

2.1. Chemical Vapor Infiltration

Chemical vapor infiltration (CVI) is a densification process used to form the matrix of a composite by depositing specific materials from a gaseous phase in the open porosity or between the fibers or particles of a preform heated in a reaction atmosphere[6]. It has proven to be an attractive process for fabricating fiber- or particulate-reinforced composites [6, 15-18]. During a CVI cycle, a preform consisting of either woven fabric or a porous fiber-reinforced construction is heated in a furnace; precursor gases flowing through the furnace diffuse into the open pores, and deposit on the walls of these pores, thus becoming part of the matrix in the composite. As this process proceeds, the sizes of the pores gradually decrease until they are filled with the solid deposit.

The CVI process has gained special attention in fabricating continuous fiber-reinforced ceramic and carbon composites for several reasons[6]: (1) it is a relatively low temperature and low stress process, therefore minimizes damage to the reinforcing materials in the preform; (2) it can be used to further densify preforms fabricated by other methods, due to the better permeability of gases into porous solids; (3) the CVI process can be used when fabricating composites of irregular shapes and can be viewed as a near net shape process; (4) the purity and microstructure of a CVI matrix are superior to those normally obtained with other fabrication methods; (5) in processing ceramic matrix composites, a precoat can be applied to the reinforcing constituents (e.g., fibers) prior to the matrix introduction in order to tailor the fiber-matrix bonding.

Another potential application of this technique, which will be especially beneficial to carbon-carbon composites, is to incorporate oxidation inhibitors into the CVI matrices[19]. A better inhibition effect is expected than that of the particulate forms of inhibitors currently used, due to the better dispersion of the oxidation protective compounds obtained using CVI.

The CVI process can be considered as a special form of chemical vapor deposition (CVD). In both CVI and CVD, the solid deposits come from thermally activated chemical reactions between gaseous reactants. However, in the CVI process, deposition on the internal surfaces in the open pores is desired; whereas in the CVD process, deposition on the exterior surface of the substrate becomes the primary goal. The reactions involved in CVD and CVI can be of several types[6]: thermal decomposition, reduction, or displacement. The following are three examples of these three types, respectively:

$$CH_4(g) \Rightarrow C(s) + 2H_2(g)$$

$$TiCl_4(g) + 2BCl_3(g) + 5H_2(g) \Rightarrow TiB_2(s) + 10HCl(g)$$

$$SiCl_4(g) + CH_4(g) \Rightarrow SiC(s) + 4HCl(g)$$
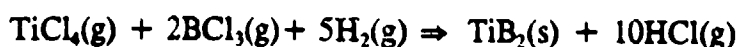
The differences between CVD and CVI mainly come from kinetic considerations. This distinction results in the difference in selecting processing parameters, which includes the reactant gas composition and the ratio of dilution, the processing temperature, and the total pressure.

The following steps are normally used to describe heterogeneous reactions in general, as illustrated in Figure 2-1[20]:

8

1. Forced flow of reactant gases into the system;

2. Diffusion and bulk flow of reactant gases through the gaseous concentration boundary layer to the substrate surface;

3. Adsorption of gases onto the substrate surface;

4. Chemical reactions of the adsorbed species;

5. Desorption of gaseous reaction products from the substrate;

6. Diffusion and bulk flow of product gases through the boundary layer to the bulk gas;

7. Forced exit of gases from the system.

The slowest of these steps controls the rate of the overall process.

In CVI processing, in addition to the above reactions occurring on the bulk surface, the following steps which are parallel to steps 2 through 5 above will occur:

i. Transport of reactant gas molecules into the open porosity;

ii. Adsorption of gas molecules onto the porosity wall;

iii. Chemical reactions of the adsorbed species;

iv. Desorption of product gas molecules from the walls of the open-pores;

v. Transport of gaseous reaction products out of the open porosity;

In the absence of a pressure gradient across the preform being densified, the transport steps depend on the diffusion of gas molecules in the pores. Kinetically, whether or not a uniform densification can be achieved depends on the competition between chemical reaction kinetics and the diffusion of gaseous species in the pores.

A major challenge associated with the CVI process is to achieve uniform deposition

of the matrix material throughout the thickness of a composite piece. Therefore mass transfer of the gaseous reactants must be sufficiently high in the preform to keep a relative constant concentration of reactant molecules throughout. This means that chemical reaction on the bulk as well as inner surfaces should control the overall reaction rate. Kinetic studies show that the temperature dependence of the chemical reaction is many times higher than that of the diffusion[1], as shown in the Arrhenius plot in Figure 2-2[7]. Therefore low processing temperatures will promote infiltration rather than preferential near-surface deposition, which hinders the infiltration of the porosity. But low temperature, and the consequential low reaction rate, also results in long processing times of up to several days or even weeks[6,7]. Another parameter affecting the infiltration is pressure. According to gas kinematics, diffusion is faster at low pressures[1]. Also, chemical reaction rates typically decrease with a reduction in reactant concentration or pressure. Many investigators thus concluded that low pressure will enhance uniform infiltration as opposed to promoting near-surface coating of the preform.

Based on the above analyses, virtually all the processing parameter changes which favor uniform infiltration also, unfortunately, reduce the overall rate of matrix deposition, which leads to long processing times. Several different CVI techniques other than the conventional isothermal-isobaric CVI processing have been developed in an attempt to solve this problem[6, 15,16,18, 21, 22].

CVI processes can be classified into four basic types, based on whether the preform is uniformly heated and how the gaseous reactants contact the preform, as illustrated in Figure 2-3[6]:

(1) *Isothermal-isobaric CVI*, in which the preform is uniformly heated and the gaseous reactants flow through the reactor, resulting in a solid deposit in the open pores. The tendency of preferential near surface coating exists due to two reasons: (a) the concentration of gaseous reactants decreases upon progressing into the preform, and (b) the concentration of gaseous reaction products, which tend to retard deposition, increase within the preform. In industrial practice, this process has two major disadvantages. First, it may have to be interrupted several times to allow removal of the outer crust by mechanical means. Secondly, it requires long processing times. Despite the above mentioned drawbacks, isothermal CVI is the type that is most commonly used in large scale industrial production. The apparent advantages of this process include its relatively simple reactor system and its capacity to densify composite preforms of complex shape.

(2) *Thermal gradient CVI*, in which a temperature gradient is maintained through the thickness of the preform thus deposition occurs at a moving boundary. The thermal gradient may be established by heating only a portion of the preform (e.g., one face of a disc). The gas supply flows over the cold surface, and the part of the preform away from the heating source is cooler due to the self-insulation provided by the porous preform. The deposition rate at the hot surface is much higher than that at the cold surface. As the infiltration proceeds, a density gradient is established between the hot and the cold surfaces, with higher density at the hot end. Higher density results in increased thermal conductivity. This change in thermal conductivity causes more of the preform to be heated to a temperature high enough to obtain significant deposition rate increase. Therefore the densification proceeds gradually from the hot surface towards

the cold surface. This technique can significantly increase the infiltration uniformity and make surface crust removal unnecessary. One disadvantage of this process is the possible existence of microstructure and property gradient between the hot and cold surfaces.

(3) *Forced-flow CVI* (sometimes being referred to as *pressure-differential CVI*), in which the gaseous reactants are forced to flow through the uniformly heated preform. This induces a pressure drop across the thickness to enhance the mass transfer. This type of process is more suitable for preforms with high initial gas permeability, such as a fibrous layout without previous matrix introduction. An impermeable region will form due to a higher deposition rate in the upstream portion because of higher reactant concentration. This will terminate the process prematurely and a density gradient through the composite thickness is almost inevitable.

(4) *Pulsed flow CVI*, in which the reactor chamber is cycled between reaction atmosphere and vacuum while the substrate is uniformly heated. It is sometimes considered to be a special form of the isothermal process. In-depth deposition is expected because of the frequent removal of the gaseous reaction products, which tend to slow down the diffusion of reactants to the inner surface by evacuation. This technique may also induce a temperature gradient between the center and the surface of the preform caused by constant introduction of cold reactant gases.

In addition to the above-mentioned basic types of CVI, a combination of these techniques is also sometimes employed to further enhance the infiltration and reduce the processing time, such as the *thermal gradient-forced flow CVI* process, shown as type 5

in Figure 2-3. It takes advantage of both the thermal-gradient and forced-flow techniques. Greater reduction in infiltration time and greater composite uniformity have been reportedly achieved by using this technique[6,14,15].

In fabricating composite materials by CVI processing, the preforms may consist of continuous or chopped fibers, whiskers, particles, or their combination. They may be in the form of a piece of felt, stacked multiple layers of cloth, filament windings of uni- or multi-directional tubes or cones, as well as 3-D woven skeletons. Fiber loadings of up to 70% can be achieved for cloth lay-up preforms, but 45-50% is more typical[6].

2.2. CVD/CVI of Carbon and Carbon-Carbon Composites

The first reported application of a CVI process to densify a porous solid was the infiltration of a graphite substrate with pyrolytic carbon by Bickerdike et al in 1962 [23]. They increased the modulus and doubled the flexural and compressive strength of the graphite. CVI was also the initial method utilized in the production of carbon-carbon composites prior to the liquid impregnation technique.

The carbon CVI process is conceptually very simple, although from a fundamental physical and chemical standpoint, it is very complex.

Among the literature available on pyrolytic carbon formation and CVI densification, Kotlensky reviewed the deposition of pyrolytic carbon in porous solids, this is also considered to be a thorough review of the CVI processing technique[7]. The mechanism, structure, and properties of pyrolytic carbon deposited in fibrous carbon substrate as well as porous carbon and graphite substrate were reviewed in the article. Recent publications

on this subject still focus more or less on the understanding of the above aspects; in addition, kinetic study and modeling work have attracted increasing interest and research efforts[24-30].

The equipment required for chemical vapor infiltration with pyrolytic carbon normally consists of a reaction chamber, a flow system for metering and controlling the amount and ratio of reaction gas mixtures, a porous substrate which is to be densified, a graphite tube furnace or some means to heat the porous substrate, and a throttle valve couple with a vacuum pump for maintaining the desired pressure in the chamber[7].

The precursor gases used in producing pyrolytic carbon are typically low molecular weight hydrocarbon gas~s such as acetylene, methane, propane, propylene, etc[7]. Sometimes a dilution gas such as hydrogen, nitrogen, or argon are mixed with the hydrocarbon gas precursors prior to their introduction into the reaction chamber. Binary mixtures of hydrocarbon gases have also been used reportedly[24].

Numerous CVI techniques have been employed in the CVI of carbon-carbon composites in laboratory scale experiments. These include isothermal, pulse, pressure-gradient, thermal gradient, dc-plasma enhanced CVD and their combinations[7,31]. Among them, the isothermal-isobaric CVI technique is the one used in the large scale industrial production of carbon-carbon composite components. The thermal-gradient CVI has been applied to the fabrication of 3-D carbon-carbon missile nose cones[2].

Although several theories were proposed to describe the mechanism of pyrolytic carbon formation, a thorough understanding of the problem still requires more research effort and the application of advanced analytical instrumentation. All the existing

theories attempt to show the path along which carbon atoms in a low molecular weight hydrocarbon aggregate during pyrolysis to form large planar molecules containing hundreds or even thousands of carbon atoms in a hexagonal array. The process, which starts with small hydrocarbon molecules and ends up with large carbon particles, must involve growth or condensation as well as dehydrogenation. The various theories differ mainly in predicting the sequences involved in aggregation[7,24,33]. Of the six possible mechanisms summarized by Kotlensty[7], only three are directly related to the CVD/CVI carbon formation technology currently being employed, namely: acetylene theory, hydrocarbon-polymerization theory, and the surface decomposition theory.

Numerous investigators have detected high-molecular-weight hydrocarbons during the pyrolysis of simple carbon-bearing precursor gases, which supports the hydrocarbon-polymerization theory. In a recent report, Lucas and Marchand[34] utilized gas chromatography and mass spectrometry techniques to measure the residual gas mixtures from the CVD carbon reactor during the pyrolysis of methane in the temperature range of 1030-1092 °C, and the pressure range of 150-400 torr. They detected light hydrocarbons such as acetylene, ethylene, and benzene; as well as heavier hydrocarbons composed of mainly polyaromatic hydrocarbon compounds which were further classified into six nonsubstituted molecules: naphtalene, anthracene, phenanthrene, acenaphtylene, pyrene, and flouranthene. Based on the above discovery, they proposed a possible four-step route of pyrolytic carbon formation: (1) methane decomposition into free radicals which react to form the so-called "C_2" molecules, particularly acetylene; (2) acetylene condensation into benzene; (3) benzene transformation into poly aromatic compounds of

increasing molecule weight; followed by (4) pyrolytic carbon formation. This study is by far the most thorough one concerning the hydrocarbon-polymerization mechanism.

The surface decomposition theory addressed the idea that certain active species (radicals) are formed from the carbon bearing gas, and as they come in contact with the deposition surface, carbon is deposited. This theory is also supported by extensive experimental evidence. Tesner[24], in his study of pyrolysis kinetics, obtained pyrolytic carbon on different substrates using various hydrocarbon gaseous precursors. He used a high flow rate technique to ensure a low degree of decomposition of the hydrocarbon precursor, and therefore concluded that the pyrolytic carbon formed did not come from the intermediate pyrolysis products, but instead formed directly from the precursor gas molecules which were directly introduced into the reactor. Hoffman et. al.[25] studied the pyrolysis of propylene over a graphitized carbon black substrate in the temperature range 600-800 °C. They found the carbon active surface area was catalytic for the pyrolysis of hydrocarbons, and therefore attributed the increased deposition rate to the self-catalytic process which enhances the rate of hydrocarbon cracking into elemental carbon.

Although the mechanism of carbon deposition is still not well understood, the kinetics of the process have been widely studied. Early reports[7] showed that the average activation energy for carbon formation from methane was 103 kcal/mole, with the gas-phase reaction being a first-order one in a wide temperature range. Eisenberg and Bliss[7] studied the pyrolysis of methane in a flow reactor and found this process to be first-order at temperatures above 1200 °C; the reaction was reported to be

autocatalytic and not a first order in the temperature range between 1100-1200 °C. Hoffman et. al.[25] studied the pyrolysis of propylene over carbon substrates with different active surface area and obtained the activation energy of about 57 kcal/mole; whereas in Marinkovic et. al.'s[27,35] CVI study using propylene as precursor gas, the activation energy was found to be about 48 kcal/mole.

Kinetic studies conducted by Tesner[24] showed that the initial rate of pyrolytic carbon formation depends on the substrate nature. As the substrate was being covered with a pyrolytic carbon layer the formation rate would increase or decrease, but a stationary rate would be reached when the substrate was covered with a certain thickness of pyrolytic carbon. The thickness of this transition layer depended on the substrate and the precursor, as well as the temperature. With all other conditions being equal, the higher the processing temperature, the thicker the transition layer would be, but the shorter the time of its formation. Another conclusion from his study and from some other researchers was that the pyrolytic carbon formation rate is first-order with respect to the hydrocarbon partial pressure, as demonstrated in Figure 2-4 and Table 2-1. For methane, the first-order relation held over the pressure range from 270 Pa to 1.5 MPa (2 to 11265 torr). Carefully comparing the activation energy values given in Table 2-1 with the same values obtained by other researchers, remarkable variations are easily seen.

Hydrogen inhibition is found to be responsible for the apparent deviation from the first-order relationship[24]. The inhibition effect is stronger under vacuum than at atmosphere pressure.

2.3. Modelling of the CVI Process

As stated in the previous sections, chemical vapor infiltration is a multi-step heterogeneous process. The theoretical analysis of the CVI densification of a porous preform requires the consideration of the diffusion and the reaction of gases in porous substrates occurring simultaneously with the deposition of a solid product. The solid deposit affects the preform porosity, which influences the transport of the gaseous reactants into the preform and thus the distribution of the resulting CVI matrix. The process will cease on two occasions: (1) the complete filling of the open pores, or (2) the formation of a surface crust on the exterior of the preform which converts the open porosity into closed porosity.

The successful modeling study of the CVI process requires the knowledge of the major kinetic steps and their dependence on processing parameters, such as temperature, pressure, and reactant concentration. The competition between the transport of gaseous reactants to the deposition sites in the open pores and the chemical reaction which forms the solid deposits is the key point in understanding the CVI process. Which mechanism becomes the rate-limiting step under the applied processing condition will determine the uniformity of the densification.

The rate constant k of the chemical reactions involved in the CVI processing of carbon varies with temperature according to the Arrhenius-type relationship[7]:

$$k = k_0 \exp(-\frac{E_a}{RT})$$

(2.1)

where: k_0 = pre-exponential factor

E_a = activation energy (kcal/mole)

R = gas constant (1.97 cal/mole °K)

T = reaction temperature (°K)

For diffusion in a porous preform, Fick's law for the transport steps can be expressed as[36]:

$$J = -D \frac{dc}{Dz} \qquad (2.2)$$

where: J = flux in the cross section of the preform(mole/s m^2)

D_{eff} = the effective diffusivity (m^2/s)

c = concentration of reactant gas (mole/m^3)

z = distance in the preform thickness direction (m)

For large pore diameters, the diffusivity is the ordinary molecular gas diffusivity D_m, which varies with temperature as $T^{1.5-1.8}$ and with total pressure as P^{-1}. When the pore sizes are so small that their dimensions are comparable or smaller than the mean-free-path of the gas molecules, gas-gas collisions are no longer dominant. Instead, gas-wall collisions are important and the mode of diffusional transport is altered. The Knudsen diffusivity D_k takes the place of D in equation 2-2. The criteria distinguishing molecular and Knudsen diffusions are[9]:

$$\frac{mfp}{d} \geq 10 \quad (\textit{Kudsen diffusion})$$
(2.3)

$$0.01 \leq \frac{mfp}{d} \leq 10 \quad (\textit{transition region diffusion})$$
(2.4)

$$0.01 \geq \frac{mfp}{d} \quad (\textit{molecular diffusion})$$
(2.5)

In the transition region where both molecular diffusion and Knudsen diffusion contribute to the transport process, the effective diffusivity can be expressed by the following relations:[36]

$$\frac{1}{D_{eff}} = \frac{1}{D_m} + \frac{1}{D_K}$$
(2.6)

Early modeling work[23] of the CVI process was usually conducted by assuming a first order chemical reaction and a pseudo-steady state condition within the porous substrate, as shown in Figure 2-5[11]. Under these conditions, the mass balance equation(s) can be obtained in the form of:

$$D\frac{d^2 C_z}{dz^2} - kC_z S = 0$$
(2.7)

with boundary conditions

$$C_z = C_0 \ (at \ z = \pm L) \tag{2.8}$$

$$\frac{dC_z}{dz} = 0 \ (at \ z = 0) \tag{2.9}$$

Here z is the coordinate in the direction of the specimen thickness, C_z the concentration of the gaseous reactants along the z-axis, k the first-order reaction rate constant, S the surface area for deposition per unit volume, and 2L the thickness of the specimen. The solution for C_z can thus be obtained:

$$\frac{C_Z}{C_0} = \frac{\cosh(\Phi z)}{\cosh(\Phi \frac{L}{2})} \tag{2.10}$$

where Φ is the Thiele modulus which satisfies the relation:

$$\Phi^2 = \frac{kS}{D_{eff}} \tag{2.11}$$

The key parameter in this solution that determines uniformity of deposition is the Thiele modulus[37,38]. It is a general parameter which takes into account both reaction kinetics (k) and transport step (D_{eff}). Small values of the Thiele modulus ($\Phi < 1$) lead to uniform deposition along the specimen thickness. This model was first applied to the analysis of CVI processing of porous carbon by Bickerdike et al[23].

A similar approach was also used on the CVI densification of fibrous preforms by assuming long cylindrical pore structures[9,38,39]. The results of this kind of analyses provide a guideline for selecting the CVI processing parameters. It shows that the favorable CVI conditions (small Φ value) are realized by obtaining a low reaction rate

(small k value) and fast transportation of the reaction species (large D_{eff} value). Since this type of model does not incorporate the geometric changes of the preform during the densification, it is difficult to match the modelling result with the composite density change during the CVI process. Also due to the limitations of the experimental capabilities, most researchers do not measure the dynamic weight change during their CVI experiments; instead, only the final weight gain after the CVI run is measured, therefore the results of the modeling work is to some extent difficult to verify.

Currier[8] developed a model applying the *overlap* concept, also known as the Avrami theorem, to deposition on the long-continuous fibrous yarns, as shown in Figure 2-6. Neglecting growth along the fiber length, the change in the volume enclosed by the actual overlapping system, V (per unit volume of space), is related to the change in the enclosed volume of the corresponding nonoverlapping volume determined by

$$\frac{dV}{dV_0} = 1 - V \qquad (2.12)$$

where V_0 is defined as the total volume occupied by the nonoverlapping cylinders and the (1-V) term represents the fractional void volume within the yarn strand. This relationship satisfies the physical requirements of the system, or represented mathematically, along with the initial and boundary conditions:

$$\frac{dV}{dt} = \frac{dV_0}{dt} \quad (when \ V=0) \qquad (2.13)$$

$$\frac{dV}{dt} = 0 \quad (when \ V=1) \qquad (2.14)$$

$$\frac{dV_0}{dt} \ is \ finite \ when \ V=1 \qquad (2.15)$$

and

$$V-V_{0i} \ as \ V_0-V_{0i} \quad (no \ overlap \ initially) \qquad (2.16)$$

Here V_{0i} represents the initial volume occupied by the uncoated fibers. The solution to the above equations is

$$V=1-(1-V_{0i})\exp[-(V_0-V_{0i})] \qquad (2.17)$$

By introducing chemical kinetics and imposing different limiting cases (pure chemical-kinetics-control and pseudo-steady-state approximation), this model gives a solution which demonstrates the change of the total available surface area and the solid volume evolution during CVI processing. This relationship can be further related to the CVI rate change during densification. The trend of CVI rate change predicted by this relationship is in agreement with the experimentally obtained rate curve[40,41].

Table 2-1. EQUATIONS FOR THE FIRST-ORDER RATE
CONSTANTS OF PYROLYTIC CARBON
FORMATION ($g \ cm^{-2} \ s^{-1} \ Pa^{-1}$)

| Hydrocarbon	Temperature limits (°C)	Equation
Methane	650-1500	$8.0 \times 10^{-3} \ exp(-272,000/RT)$
Ethylene	500-700	$7.6 \times 10^{-7} \ exp(-155,000/RT)$
Propylene	550-650	$4.0 \times 10^{-7} \ exp(-151,000/RT)$
Butadiene	475-600	$7.5 \times 10^{-7} \ exp(-142,000/RT)$
Benzene	750-870	$3.0 \times 10^{-3} \ exp(-230,000/RT)$
Toluene	650-850	$9.9 \times 10^{-2} \ exp(-243,000/RT)$
Xylene	600-750	$15.5 \times 10^{-2} \ exp(-239,000/RT)$
Naphthalene	750-850	$6.6 \times 10^{-3} \ exp(-222,000/RT)$
Anthracene	730-900	$19.4 \times 10^{-3} \ exp(-218,000/RT)$
Acetylene	550-1100	$17.1 \times 10^{-7} \ exp(-138,000/RT)$
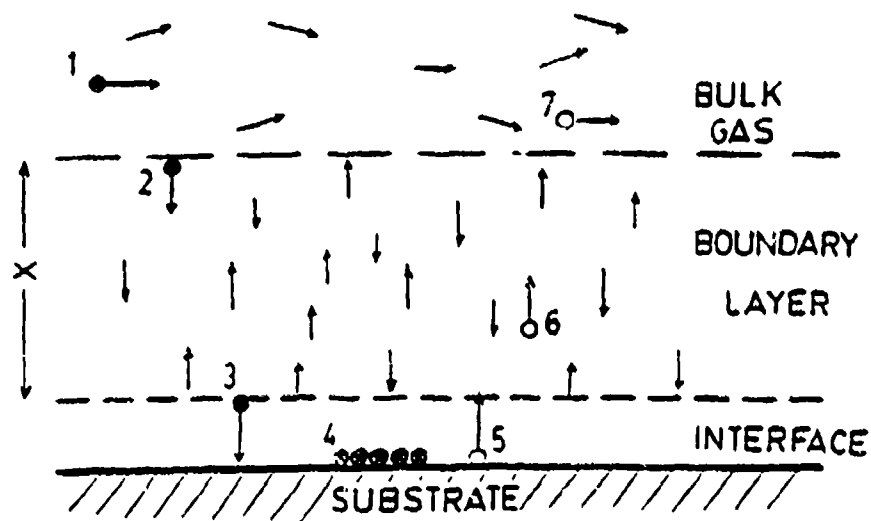
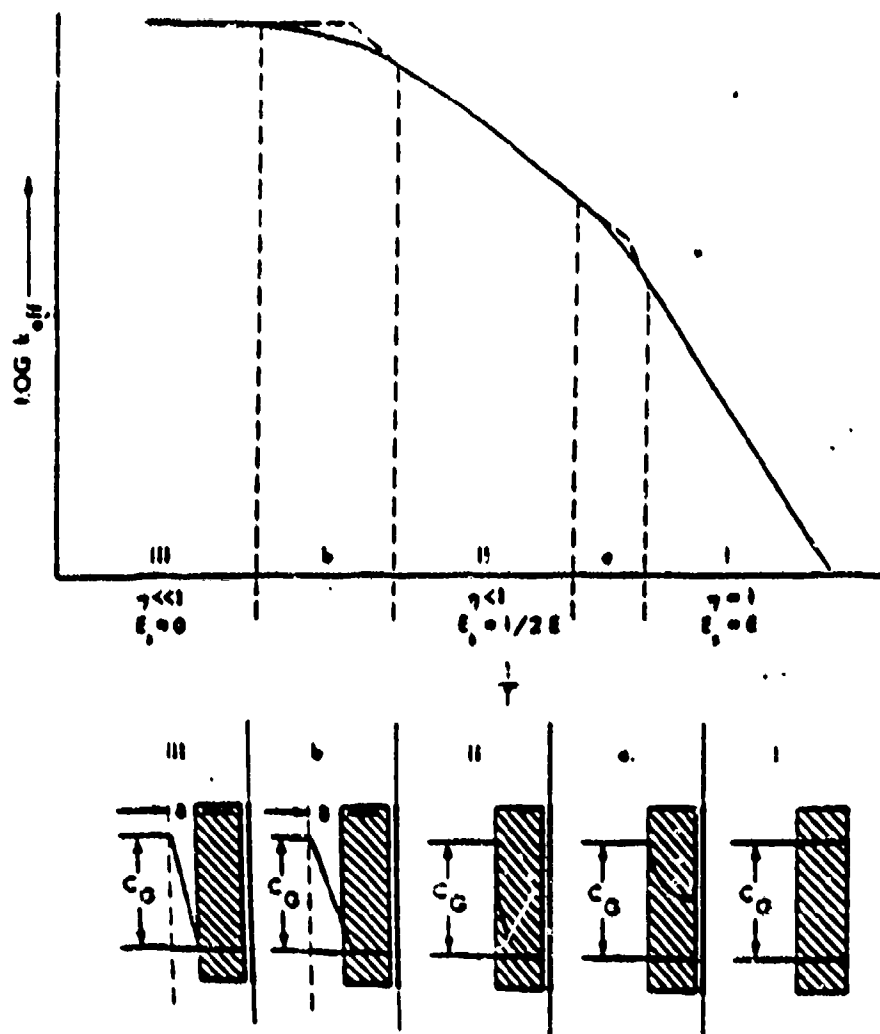Figure 2-1. The Seven Mechanistic Steps to Describe
Heterogeneous Reactions

Figure 2-2. Schematic Arrhenius Plot for Reactions of Gases
with Porous Solids as Applied to Infiltration

      I. The Rate of Conversion is Determined Only
        by the Rate of Chemical Reaction
     II. The Diffusion Through the Pores of the Solids
       Influences the Rate of Conversion
    III. The Conversion Rate is Determined by the
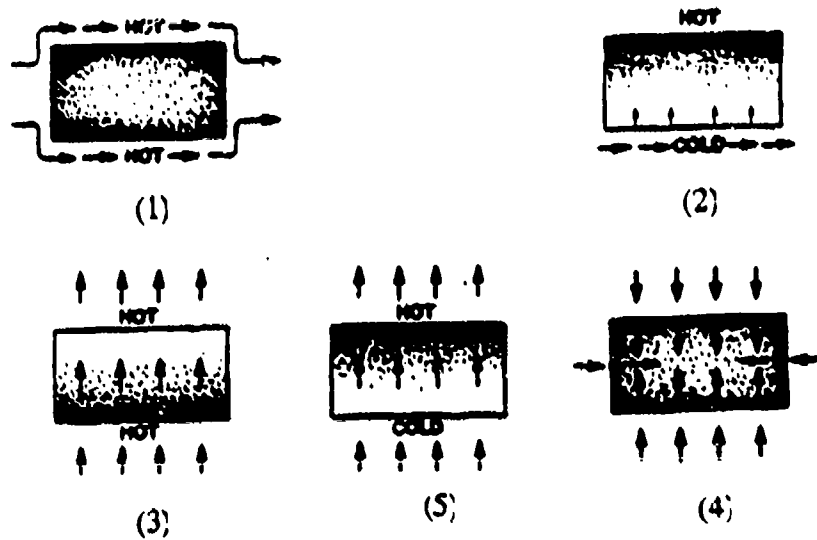   Diffusion Through A Boundary Gas Layer
a,b: Transition Zones

Figure 2-3. Basic Types of CVI Techniques
(1) Isothermal-Isobaric
(2) Thermal Gradient
(3) Isothermal-Forced Flow
(4) Pulsed Flow
(5) Thermal Gradient-Forced Flow

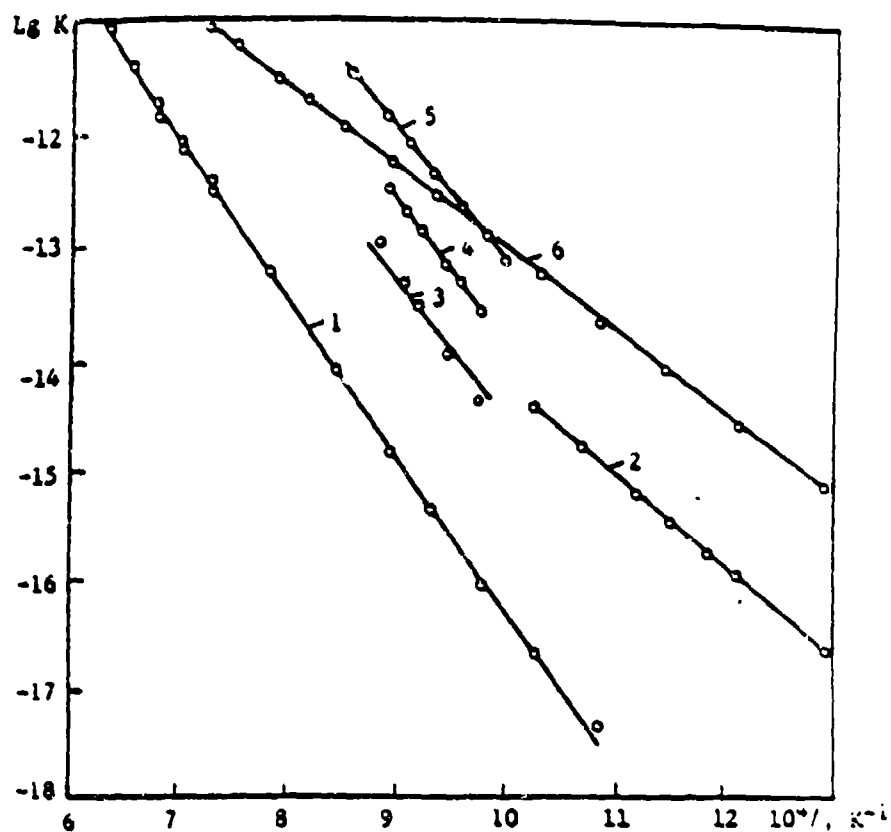**Figure 2-4.** Logarithms of rate constants of PyC formation from individual hydrocarbons (g cm^{-2} s^{-1} Pa^{-1}): 1, methane; 2, ethylene; 3, benzene; 4, naphtalene; 5, anthracene; 6, acetylene.
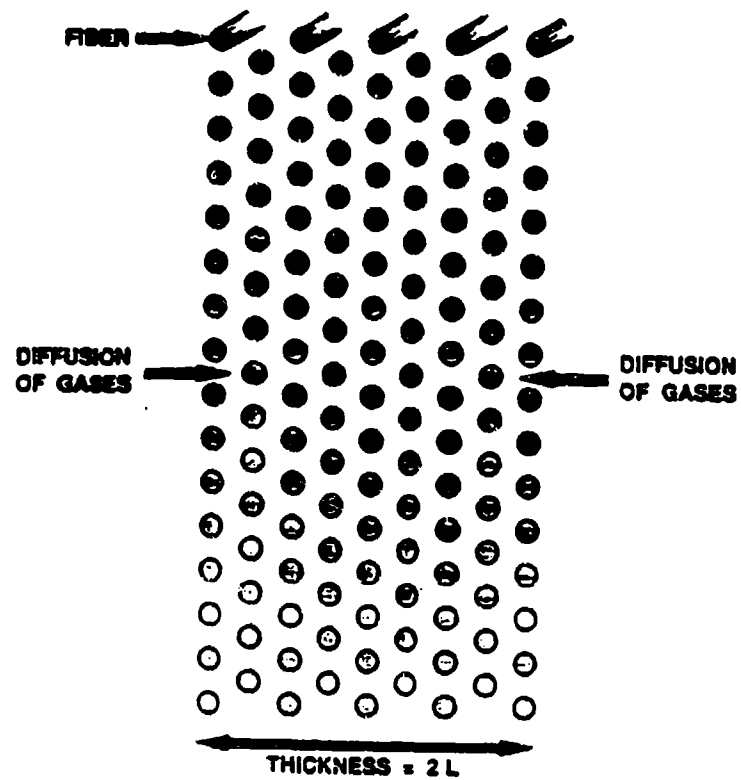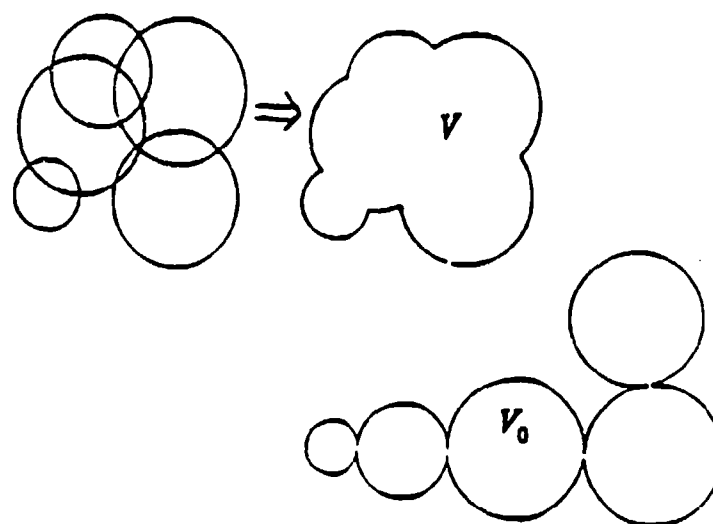
Figure 2-5. 2-D Depiction of a Fibrous Preform

Figure 2-6. Graphic Description of the Overlap Concept
The Figure Illustrates How The Growth
Centers Shown in (a) Gives Rise to The
Real Volume Coressponding to (b) and The
Extended Volume Shown in (c)

V: The True Volume Occupied by the Overlap System
V_0: The Extended Volume Represent the Nonoverlap System

CHAPTER 3

EXPERIMENTAL PROCEDURES

3.1   The Preform

2-D carbon-carbon composites were used as preforms for the CVI densification process in this study. The preform was provided as one panel 3/16" in thickness by BP Chemical Hitco Corporation. It was later machined to the dimension of 2" X 2" squares. The preform consisted of 18 layers (so called plies in the composite industry) of 8 harness woven of polyacrylnitrile (PAN) fibers. The twelve plies near the composite surface were positioned with alternating 0, 90, 0, 90, and 0, 90 degree orientations. The other six plies in the center of the composite were in a 45, -45, 45, -45, and 45, -45 degree manner.

The preform was impregnated with a phenolic resin as matrix binder material. The process history of the as-received preform was: (1) cloth layup; (2) resin impregnation: (3) autoclave molding; (4) carbonization.

The apparent bulk density of the as-received carbon-carbon preform measured 1.415 g/cm^3.

3.2   Preform High Temperature Heat Treatment

The machined preforms were heat treated to 2500 °C at 1 atm. in argon (Ar) atmosphere for two hours. The furnace used for this purpose was a Centorr high temperature furnace equipped with graphite heating elements with maximum temperature capability of 2700 °C. The temperature was monitored by an optical pyrometer which

had been calibrated against a Molybdenum sheathed Tungsten-5% Rhenium vs. Tungsten-26% Rhenium thermocouple to 1900 °C under vacuum. The procedure of the high temperature treatment which was used is described as follows:

(1) Pump down the chamber to less than 100 millitorr and then purge with Ar to atmospheric pressure, repeat this evacuation procedure for two more times to ensure the full release of oxygen and moisture from the furnace;

(2) heat up the furnace by gradually increasing the power, keep Ar flowing through the furnace with a very small flow rate;

(3) when the specimen temperature reaches 2500 °C, maintain the temperature for two hours;

(4) shut down the furnace power and wait until the furnace cool down to room temperature, remove the specimens from the furnace and put them into a desiccator connected to wall-vacuum for storage.

3.3 CVI system

The schematic diagram of the CVI apparatus used in this study is shown in Figure 3-1. The whole system consists of seven subsystems which perform different functions: (1) the gas feeding system, (2) the chemical reaction chamber, (3) the temperature control unit, (4) the gas exhaust and pressure control system, (5) the thermogravimetric analysis (TGA) weight measurement system, (6) the exhaust-gas analysis system, and (7) the computer control system.

3.3.1. The Gas Feeding System

Methane (CH₄) was used as a precursor gas to form solid carbon in the CVI experiments. Technical grade tank methane (98% purity) was exclusively used in this study. Hydrogen (H₂) was used as a diluent gas to prevent homogeneous gas-phase nucleation. Argon was used to purge the reaction chamber prior to the introduction of the methane/hydrogen gas mixture. Four MKS flow meters/regulators (200, 5000, 2000, and 500 sccm maximum flow rates on channels #1, #2, #3, and #4 respectively) and a MKS four channel multi-gas controller (MKS 147B) were used to control the gas flow rate. The MKS-147 received set-points from and sent measured flow rate values to the computer.

Methane, hydrogen, and argon were assigned to channels #2, #3, and #4 respectively. Channel #1 was installed for further development but not used in this study.

3.3.2. The Chemical Reaction Chamber

The essential part of the experimental apparatus was the inductively heated reactor. It had a carbon susceptor with 6 inches inner-diameter and an effective hot-zone of about 6 inches in length. A CE-2000 dual station radio frequency (RF) generator (The Taylor. Winfield Corporation) with a water-cooled induction coil was used to heat the susceptor.

The reaction temperature was measured by K-type (Chromel-Alumel junction) thermocouples with Inconel 600 alloy sheath. An alumina tube was used to further

protect the thermocouples. A stainless steel bell jar served as a reaction atmosphere envelope, which measured about 3 feet in height and 3 feet in diameter.

3.3.3. The Temperature Control Unit

The thermocouple output was sent to a temperature controller (Omege CN2010). The controller sent analog signals to the computer and a control current to the RF generator to control the output power of the generator and maintain the reaction temperature.

3.3.4. The Exhaust-gas and Pressure Control System

A rotary pump (Sargent-Welch 1397) was used to pump the reaction chamber down to low-vacuum. A pressure gauge (MKS 107A) measured the pressure in the reaction chamber and sent signals to a pressure controller (MKS 116A). The pressure controller also received set-points from the computer and controlled the openness of the throttling release valve (MKS 248). These formed a complete loop which was capable of controlling the reaction pressure at the desired value.

3.3.5. The TGA Weight Measurement System

The specimen weight changes during the CVI experiments were measured using a TGA unit. The force transducer (± 10 grams full range, 0.5 mg sensitivity) was coupled with a balance mechanism, which ensured the specimen weight during a CVI run to be within the measurement range of the transducer. The specimen was hung to the TGA

unit using a metal wire. The transducer sent analog signals to the computer which saved these data into a disk file for further analysis.

3.3.6. The Exhaust-Gas Analysis System

This unit was installed to monitor the gaseous reaction products and residuals in terms of nature as well as quantity. The core component was a quadrupole mass spectrometer (Hidden Analytical model HAL). The high vacuum required by the component was obtained using a turbo-molecular pump backed up by a rotary pump. The system can detect more than seventy gas mixtures from single atom gas to high molecular weight polyaromatic gases.

3.3.7. The Computer Control System

All the control and data-acquisition units mentioned above were interfaced with a computer. The control program sent out set-point values to the control units and recorded all data into a disk file. The gas flow rate, pressure, and specimen weight curves were displayed on the monitor screen during the CVI experiments to provide man-machine interactions.

3.4 CVI Experimental Procedure

The following operation steps are normally followed during the CVI experiment:

(1) Switch on the computer, the flow and pressure controllers, and the temperature controller. Check the conditions of each unit and the amount of gases in the tanks.

(2) Blow the specimen surface with compressed air. Measure the dimensions of the specimen using a digital caliper, and measure the weight of the specimen using a electronic balance (1 mg sensitivity in 0 to 40 grams range).

(3) Load the specimen into the reactor hot-zone with a wire holder. Care should be taken to position the specimen at the center of the hot zone. Cover the carbon susceptor assembly with the alumina plate. Install the thermocouple into the alumina tube positioned on the plate. Cover the stainless steel reaction chamber.

(4) Adjust the balance mechanism to ensure the TGA unit operates in the proper range. Calibrate the TGA unit with standard balance weights (5 and 10 grams) to ensure correct measurement.

(5) Turn the cooling water on. Close the manual gas release valve.

(6) Warm up the induction generator for at least 10 minutes before heating.

(7) Access the CVDI control program. The following steps are conducted in this program.

(8) Turn on the pump. Pump the system to pressures to below 1 torr. This drives out the moisture trapped in the reaction chamber and the gas line.

(9) Set the pressure to the designated experimental pressure and start purging argon until the pressure reached that value.

(10) Manually increase the power output from the temperature controller. This precaution will prevent the overloading of the induction generator.

(11) When the temperature is within 50 °C from the designated temperature, turn the temperature controller to "AUTO" mode.

(12) During the heating process, set the experimental parameters such as flow rate, and pressure.

(13) When the designated temperature is reached, switch to "operational mode" from the program. This step turns on all the reaction gas channels and starts the TGA weight change recording.

(14) When the specimen weight change rate is smaller than a predetermined value, stop the experiment as described below.

(15) Manually switch the temperature controller power output to zero. Pump down the reaction chamber to below 300 millitorr. Close the chamber by turning a manual release valve. Keep the cooling water running until the chamber cooled down to room temperature.

(16) Introduce air into the chamber. Remove the specimen from the TGA unit.

(17) Measure the final weight of the specimen. Keep it in a vacuum desiccator until it is needed for other analyses.

3.5 Characterization of CVI Densified Specimens

3.5.1. Density Profile Measurement

The density profile measurement was performed to evaluate the densification uniformity throughout the specimen thickness. Under different CVI conditions, the densification uniformity was expected to be different. The procedure used is described as following:

(1) Cut a square piece of about 1" X 1" in dimension from the densified specimen using

a low speed cut-off saw (Buehler) with a diamond tip saw blade.

(2) Blow the carbon particles from the specimen surface with compressed air.

(3) Measure the weight of the specimen using a electronic balance, measure the dimensions with a digital micrometer.

(4) Glue the specimen on a piece of PlexiGlass holder about 1.1" X 1.1" X 1/2" in dimension.

(5) Wait until the glue sets. Measure the weight and the thickness of the specimen/holder piece.

(6) Grind about 200 micrometers (μm) from the exposed surface of the specimen using a grinder equipped with diamond wheel (this step was conducted by the Fine Machine Shop).

(7) Measure the thickness and weight of the remaining specimen/holder piece.

(8) Repeat steps (6) and (7) until the specimen is exhausted.

3.5.2. The Mineral Spirit Measurement

This technique was provided by Aircraft Braking Systems Corporation[42]. Slight modification was applied to suit the needs of this study. It was used to measure the density and open porosity of composite specimens. The technique used mineral spirits to determine the percentage of total volume which was accessible to mineral spirits. It was a nondestructive measurement which maintained the integrity of the specimens for other characterization. A bridge attachment was designed to apply this technique using a electronic plate balance.

In order to ensure accurate measurement, the density of the mineral spirits was calibrated each time when the measurement was preformed. A 10 gram brass standard balance weight was used for this purpose. Its volume was also measured by Archimedes' principle using water as a liquid medium. Weigh the balance-weight both in air and immersed in mineral spirits. Calculate the density of the mineral spirits density using the following equations:

$$Density\ M.S. = \frac{10\ g\ -\ Brass\ Wt.\ (Immersed)}{Brass\ Volume\ (Calc.)} \qquad (3.1)$$

The following describes the detailed procedure of this technique:

(1) Clean specimens in an ultrasonic cleaner using isopropyl alcohol for 15 minutes.

(2) Dry specimen in oven for 2 hours at 150 to 160 °C.

(3) Cool specimens to handling temperature. Place them in a vacuum chamber. Evacuate for 1 hour at 27 torr or higher vacuum.

(4) Place each specimen in a separate beaker or petri dish. Pour a sufficient amount of mineral spirits into each disk to cover the specimen.

(5) Place all beakers with specimens immersed in mineral spirits into a vacuum chamber. Evacuate until specimens show no evolution of bubbles.

(6) Release the vacuum and allow at least one hour for the specimens immersed in mineral spirits at atmosphere pressure.

(7) Remove each saturated specimen from its beaker and quickly place it into a wire holder and then immerse it into a deep petri dish containing the same mineral spirits.

(8) Weigh the immersed specimen. Subtract the weight of the wire holder immersed to

the same depth.

(9) Remove the specimen, in its holder, from the liquid and quickly blot it with a tissue to remove surface film on the specimen surface.

(10) Attach the blotted specimen in the holder to the balance and record the weight every 15 seconds while evaporation occurs. Six such weights should be plotted and extrapolated to time zero (the estimated time at which blotting took place). This weight, minus the holder weight, equals the absorbed weight in air.

(11) Repeat steps (2) and (3) on the measured specimen.

(12) Remove the specimen from the vacuum chamber and measure the weight immediately. This is the final dry weight.

(13) The weight displaced by the material which is incapable of being penetrated by the mineral spirits is calculated as:

$$Wt \ (Displaced \ M.S.) = Final \ Dry \ Wt. - Immersed \ Wt. \qquad (3.2)$$

(14) Specimen impervious volume is calculated as:

$$Impervious \ Volume = \frac{Wt. \ (Displaced \ M.S.)}{Density \ M.S.} \qquad (3.3)$$

(15) Impervious density is calculated by:

$$Impervious \ Density = \frac{Final \ Dry \ Wt.}{Impervious \ Volume} \qquad (3.4)$$

(16) The Weight displaced by specimen volume as defined by the meniscus of liquid in the external pores after blotting is calculated as:

(17) Specimen bulk volume is defined by:

$$Wt.(Dis.\ M.S.\ Extro.) = Wt.\ (air\ blotted\ specimen) - Immersed\ Wt. \qquad (3.5)$$

$$Volume\ (Bulk) = \frac{Wt.\ (Dis.\ M.S.\ Extro.)}{Density\ M.S.} \qquad (3.6)$$

(18) The Specimen bulk density is calculated by:

$$Bulk\ Density = \frac{Final\ Dry\ Weight}{Bulk\ Volume} \qquad (3.7)$$

(19) The percentage open porosity is:

$$\%\ Open\ Porosity = 100 \times \frac{Bulk\ Volume - Impervious\ Volume}{Bulk\ Volume} \qquad (3.8)$$

3.5.3. Optical Microscopy

Optical microscopy was employed to observe the distribution of different constituents in the composites, the thickness of the CVI layer in different part of the densified specimen, and the optical anisotropy.

The cross-sectional specimen was cut using a low speed cut-off saw to approximately 25 mm X 10 mm X 1 mm in dimension with a diamond wafering blade. The cut-off section was then mounted in epoxy resin, ground with silicon carbide abrasive papers following the 240, 320, 400, 600 grit sequence, polished using 6 μm and 1 μm diamond paste on Buehler Vibrational and Mini-Met polisher, respectively, and finally finished to 0.05 μm with alumina slurry.

A Nikon Microphot reflective optical microscope equipped with a polarizer was used in this study. Optical micrographs were taken on 35 mm (Kodak) films and developed

using RC printing papers (Kodak and Oriental).

3.5.4. Scanning Electron Microscopy (SEM)

SEM was employed mainly to detect the distribution of CVI carbon in the composite

matrix. The above mentioned procedure for preparing optical microscopy specimens was

also employed in the preparation of SEM specimens. Since secondary electron detection

in SEM could only distinguish morphological differences on the specimen surface, a

plasma chemistry reactor (March: Solid State Plasmod) was used to etch the mounted

specimen surface in atomic oxygen. This step developed the features necessary to be

detected by the SEM, since different constituents in the densified specimen: namely,

PAN-fiber, carbonized-resin-matrix, and CVI carbon; each had a different etching rate

under atomic oxygen.

The following describes the procedure which was used in the plasma etching process:

(1) Load the epoxy resin mounted specimens into the plasma reaction chamber using a

watch glass.

(2) Turn on the vacuum pump and AC power.

(3) Turn on the vacuum switch and close the inner chamber door. Wait approximately

two minutes for pump down.

(4) Tune the reactor in the tuning mode using the knobs and switches on the reactor to

obtain minimum reflected power reading on a meter. This step may need to be repeated

several times.

(5) Switch to the normal operational mode and adjust the power level; the purple plasma

should be seen through the window. Operate for 10 to 40 minutes and shut down the reactor.

(6) Remove the specimen and observe it under an optical microscope for the etching effect. Repeat step (5) if necessary.

The atomic oxygen etched specimen was then sputter-coated by a thin (200 to 300 Å) platinum layer to ensure the conductivity required by the SEM operation. SEM observation was conducted on a Hitachi S-570 scanning electron microscope. Polaroid PN-55 films were used to record the SEM images.

3.5.5. Transmission Electron Microscopy(TEM)

TEM study is conducted to obtain the detailed information on the interfaces of fiber/CVI-carbon and resin-matrix/CVI-carbon, as well as the crystalline isotropy/anisotropy of the different constituents.

TEM specimens have to be less than 2000 Å in thickness in order for electron beams to penetrate through. A special thinning technique, atomic milling, is employed to prepare the specimen. This technique assures minimum disturbance of the microstructure and internal defects, and therefore provides reliable microstructural characterization. The procedure is described as following:

(1) Cut a slice of approximately 500 μm in thickness using a Buehler Isomet low speed saw with diamond blade.

(2) Mount the thin slice onto a polishing holder with a thin wax layer. Grind the exposed surface with 600 grit silicon carbide abrasive paper until the slice is about 200

μm in thickness. Polish the surface on 0.05 μm alumina polishing wheel.

(3) Remove the slice from the polishing holder. Mount it polished-face down on an aluminum base plate with wax. Position the slice under a low speed precision coring drill (VCR Group model V7110) and core-drill a 3 mm diameter disk from the slice.

(4) Mount the slice on a dimpler sample holder with wax. Dimple it on a mechanical dimpler (VCR model D500) through four stages using 15, 3, 1, and finally 0.5 μm diamond slurry to an approximate thickness of 0 to 20 μm.

(5) Dissolve the holding wax by soaking the holder in acetone. Rinse the removed slice with methanol alcohol.

(6) Position the specimen on the atom miller (VCR Group Maxmill model 306B/TM170) sample holder. Load the holder into the milling chamber. Mill the specimen with argon atom beams at temperature of -70 to -80 °C (using liquid nitrogen as a coolant). A beam current of 1 mA and an initial incident beam angle of 20 to 30° should be employed until perforation.

(7) Lower the atom bombardment angle to 8 to 15°. Mill for another 8 hours and carefully remove the specimen from the milling chamber.

TEM studies were conducted using a Hitachi H500-H TEM. Bright-field and dark-field imaging, as well as selected area diffraction (SAD) were employed in this study.
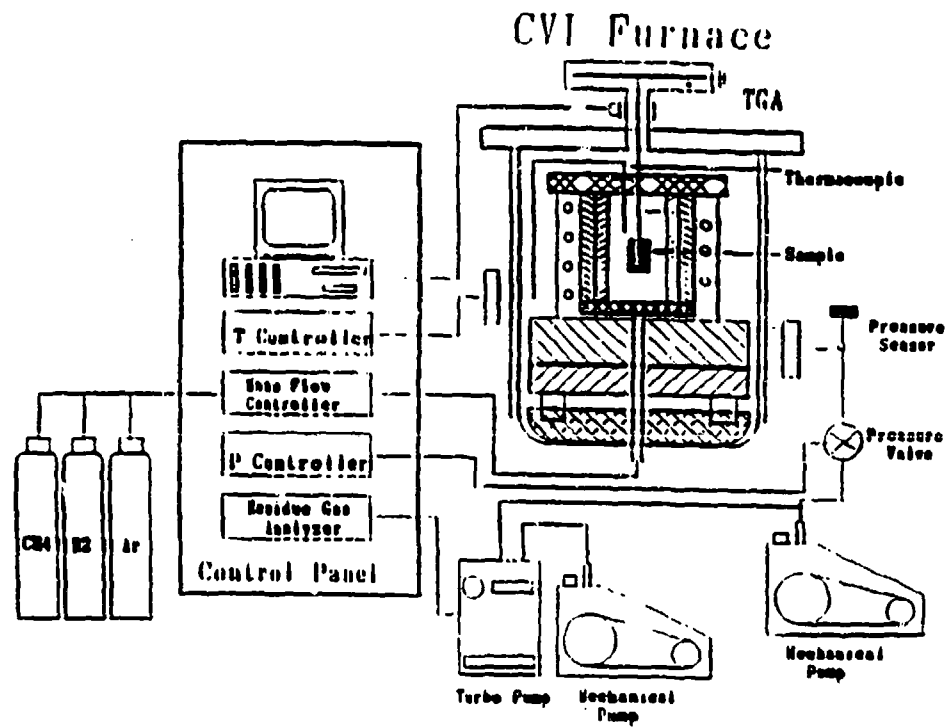
Figure 3-1. Schematic Diagram of CVI Apparatus

CHAPTER 4

RESULTS

Porosity is inevitable, due to the method of manufacturing carbon-carbon composites[7]. The carbonization process causes the emission of volatile species in the form of hydrogen and some hydrocarbon gases from the organic resin. This subsequently causes the resin to shrink in volume. The density of the as-received resin-matrix-bonded PAN-fiber-reinforced composite sample measured 1.415 g/cm³ using direct weight and volume measurement, and measured 1.433 g/cm³ using the *mineral spirits method*. The *mineral spirits method* also suggested a 25.6% open porosity. When this porosity portion is fully densified, the composite density should reach 1.95 g/cm³, assuming the density of pyrolytic carbon to be 2.1 g/cm³.

In this study, the experimental apparatus set-up, as well as the precursor gases and the experimental conditions, were thus designed and selected with the needs of industry in mind.

Hydrogen diluted methane was used in this study as a precursor gas to form pyrolytic carbon by the following general reaction:

$$CH_4(g) \rightarrow C(s) + 2H_2(g)$$
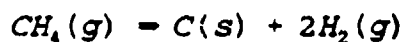
The main consideration in choosing methane as a precursor gas over other light hydrocarbon gases is the economics involved with large scale industrial production. As the main composition in natural gas, methane is an abundant resource and is relatively inexpensive.

The methane-to-hydrogen ($CH_4:H_2$) ratio was maintained at 4 to 1 through all the

CVI experiments in this study. It reflected a carbon-to-hydrogen (C:H) ratio of 1 to 4.5 This ratio was chosen based on some preliminary thermodynamic and experimental studies on the system.

Table 4-1 summarizes the experimental conditions employed in this study, as well as the corresponding final weight gain, bulk density, and porosity of the densified specimens. The bulk density values measured by the *mineral spirits* technique were slightly higher than the values obtained by directly measuring the specimen weight and bulk volume. This was attributed to the surface roughness due to its woven nature, which resulted in the directly measured specimen volume to be greater than the one obtained by the mineral spirits method.

The results of the dynamic TGA weight measurement and those from the characterization worked performed on the densified specimens are presented in this chapter.

4.1. The TGA Weight Gain Curves

After each CVI experiment, the weight gain data recorded during the runs were analyzed and plotted using computer graphics tools. Since the data were normally recorded every 20 seconds during the experiments, reduction of the data was conducted by averaging the original data on a 30 data points basis. Another piece of information which became immediately available was the CVI rate curve during the densification process. Figures 4-1 to 4-4 present three of this type of plots obtained under different experimental conditions. The initial weight gain was relatively slow, followed by a near-

linear weight increase, then the curves gradually lost their linearity and started to bend over, finally reaching a point beyond which no obvious weight gain could be obtained. The associated CVI rate curves show an initial increase, followed by a maximum value, and then a gradual decrease toward a minimum. It can be easily seen that the rate change of the low temperature (HT-D: 1050 °C, 15 torr) CVI run is less obvious than those of the higher temperature ones.

Figure 4-5 is a specimen weight gain plot showing the percentage weight gain and the density increase vs. processing time for the CVI runs conducted under conditions shown in Table 4-1. Figure 4-6 is the associated CVI rate curves. By comparing these curves, we can see that the turning point of the bend-over, in terms of processing time and composite density, varies markedly under different processing conditions. Higher processing temperature results in a higher initial CVI rate and early bend-over, and correspondingly a lower final bulk density. Comparatively, the influence of pressure on the CVI densification is not as strong as temperature. Weight gain curves under different pressures but the at same temperature have similar initial linear rate, but lower pressure leads to an earlier bend-over of the weight gain curve.

4.2. Density Profile Measurements

Figures 4-7 to 4-11 are density profile plots showing the densification uniformity along the specimen thickness on five specimens with different processing histories. The low temperature (Figure 4-7) specimen has relatively uniform density throughout its thickness and a high overall density. The specimens processed at higher temperatures

have lower overall density and a non-uniform density distribution from surface to center. The degree of nonuniformity becomes greater as temperature increases. Lower processing pressure seemingly has an effect similar to higher temperature in this respect as revealed in Figures 4-10 and 4-11.

The odd density values measured at the skin layers (left-most and right-most bars in each profile) results from two reasons: (1) the roughness of specimen surface due to the woven texture of carbon cloth, and (2) the penetration of the glue used to bond the specimen with the Plexiglass holder. It should not be viewed as an actual characteristic of the densified composite. The profiles of the low density portions in Figure 4-10 suffer from irregular variations. This may be due to the grinding damage on the less dense portion of the specimen due to their inferior structural integrity as compared to better CVI-densified specimens.

4.3. Microscopic Characterization

4.3.1. Transmission Electron Microscopy Study

TEM investigation of the densified composite shows that the CVI carbon is mainly distributed in the relatively large pores (cracks) between resin matrix and the adjacent fibers (Figure 4-12). These pores are believed to originate from the shrinkage of matrix resin away from the fibers during carbonization and the successive high temperature heat treatment, and/or from the release of volatile species and the thermal expansion coefficient mismatch between these two constituents. Figure 4-13 provides a more detailed image showing an interbundular area between four fibers. The microcracks

observed in the resin-converted matrix, and the matrix platelets separated by them, are parallel to the fiber surface contour, and seemingly follow a flow type morphology. This kind of alignment originates from the prepreg lay-up and auto-clave processing. The CVI carbon has deposited evenly on accessible surfaces of both fibers and resin-converted matrix. The thickness of the CVI layer on surfaces of both types of the preform constituents appears to be identical. It is interesting to notice the absence of CVI carbon in the microcracks in the resin-converted matrix. One possible reason is that these microcracks are noncontinuous along the fiber axis direction, so that they are not open pores like the cracks between the fiber and matrix. It is also possible that the sizes of these microcracks are too small to allow effective gas diffusion to occur during CVI processing.

TEM micrographs taken from the interfacial regions in the same specimen are shown in Figures 4-14, 4-15, and 4-16. It is revealed that CVI carbon bonds well with both the resin-converted matrix and the PAN fibers. It is also obvious that these pores can be filled quite effectively by applying the CVI technique. The dark field image (Figure 4-15) taken from the fiber/CVI interface reveals a smooth transition region between these two constituents. The crystallites in the CVI region appear to be slightly elongated, whereas the crystallites in the fiber region are basically equaxial. The crystallite sizes in the outer layer of the fiber are found to be larger than those in the core. The selected area diffraction (SAD) pattern of CVI carbon shows very weak anisotropy, as revealed by the weak (002) preferred orientation, whereas the SAD pattern of fiber taken with the incident beam parallel to the fiber axis reveals an isotropic

nature (Figure 4-13). The dot pattern of an SAD taken from the resin-converted matrix portion (Figure 4-16) indicates the crystallites of the resin-converted matrix are highly oriented. The platelet morphology is similar to that of the high temperature heat-treated pitch-converted matrix as discussed by C. Ju et. al.[43].

4.3.2. Scanning Electron Microscopy Study

SEM micrographs of the atomic-oxygen-etched specimens were taken to compare the microstructure of specimens densified under different conditions. Due to the different etching rates of the three major constituents (fiber, carbonized resin, and CVI matrix) under atomic oxygen attack, their distribution could be exposed. The skin-core feature, which is characteristic of PAN fiber, was also clearly revealed, as shown in both Figures 4-17 and 4-18.

Micrographs shown here were taken from transverse sections of two specimens with different processing histories. The extent of surface closure was much more severe in the 1100°C/41 hours (HT-B) specimen compared to the 1050°C/120 hours (HT-E) specimen (both at 15 torr pressure) (Figure 4-17). More CVI carbon was found in the center of the 1050°C/120 hours specimen, but there was virtually no CVI carbon found in the 1100°C specimen at locations comparable to those of the 1050°C specimen(Figure 4-18).

4.3.3. Polarized Reflective Light Microscopy Study

Polarized optical microscopy observation showed that the CVI carbon layer thickness

was relatively uniform at a specific distance from the specimen surface. No obvious deposit thickness variation was distinguishable when observed at a equal distance from either side of the two surfaces.

Under appropriate CVI conditions, identical CVI layer thickness was observed throughout the composite thickness, indicating uniform densification. As shown in Figure 4-19, the filling of the micropores in between individual fibers was quite effective, while this technique failed to fill the relative large pores.

Uniform densification was obtained in specimens processed under low temperature and moderate pressure. This is clearly revealed in Figure 4-20 on a specimen densified under 1050 °C, 15 torr. The CVI layer thickness at the surface was identical to that in the center of the specimen. High processing temperature results in nonuniform densification or even severe surface crust formation, as seen in Figures 4-21 and 4-22 taken from 1100 °C/15 torr and 1200 °C/15 torr specimens, respectively. The extent of surface blocking increased as temperature increased. This is in agreement with the density profile measurement results and SEM observations. In some instances, even the large cracks in resin-converted matrix at the specimen surface, which were obviously formed during the cooling down stage of the carbonization process, were also sealed, as shown in Figure 4-23. This is similar to the overcoat found in CVD processed specimens.

The overall isotropic/anisotropic features of the three major constituents under optical microscope are in agreement with the TEM study. It would be much easier to reveal this characteristic using color prints, on which purple represents *isotropic* structure as

opposed to the *anisotropic* structure as revealed by the bright blue and yellow under ideal polarization.

Table 4-1. PARAMETERS AND RESULTS OF C-C CVI EXPERIMENTS

Experiment I.D.	Temperature (C)	Pressure (torr)	Proc. Time (hour)	Weight Gain (%)	Final Density (g/cc) direct/M.S.	Porosity (%) M.S.	Surface Deposit Thickness (um)
Preform	N/A	N/A	N/A	N/A	1.415/1.433	25.6	N/A
HT-A	1200	15	19	9	1.54/1.57	16.3	5
HT-B	1100	15	41	11.8	1.58/1.63	10.7	3
HT-C	1100	5	29	7.8	1.53/1.57	16.5	2
HT-D	1050	15	120	16.5	1.65/1.68	6	1.5
HT-E	1050	5	72	11.5	1.58/1.62	11	1
HT-F	1000	15	25	0.6	1.42/N.A.	N/A	N/A
HT-G	1000	5	35	0.6	1.42/N.A.	N/A	N/A

N/A or N.A.: Not Avalaible at the time of writing
M.S.: Mineral Spirit Method

CVI Weight Gain and Rate Curve
HT-D: 1050 C, 15 torr, 120 hr
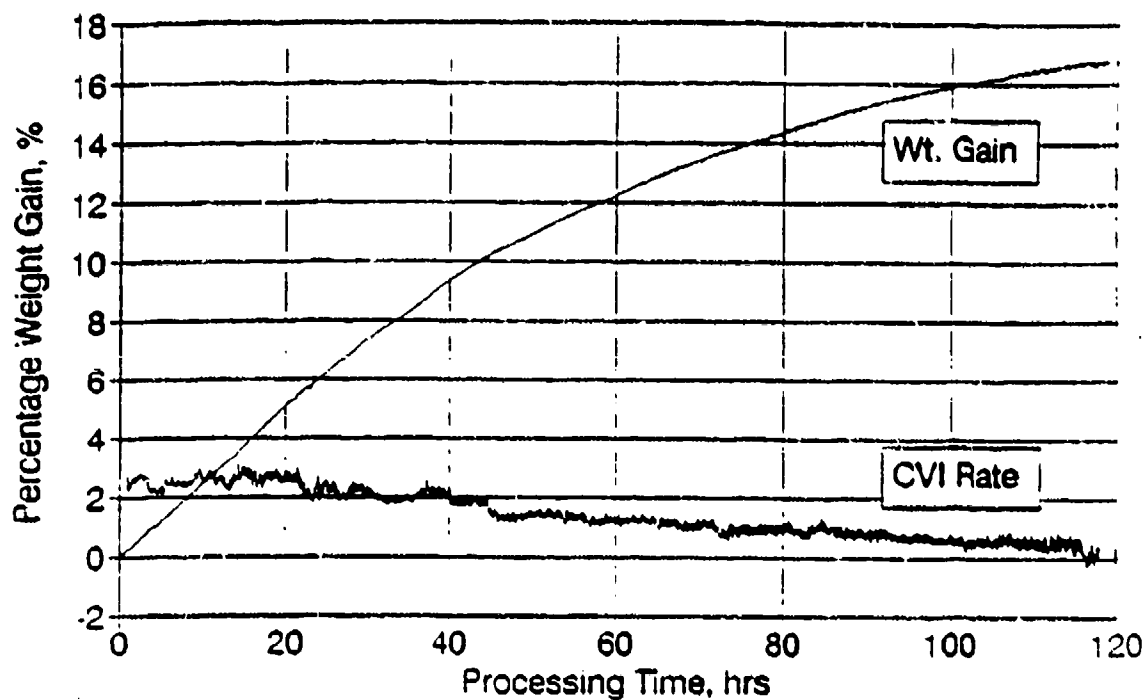
Figure 4-1. CVI Weight Gain and Rate Curves
for the 1050°C/15 torr Run

CVI Weight Gain and Rate
HT-B: 1100 C, 15 torr, 41 hrs
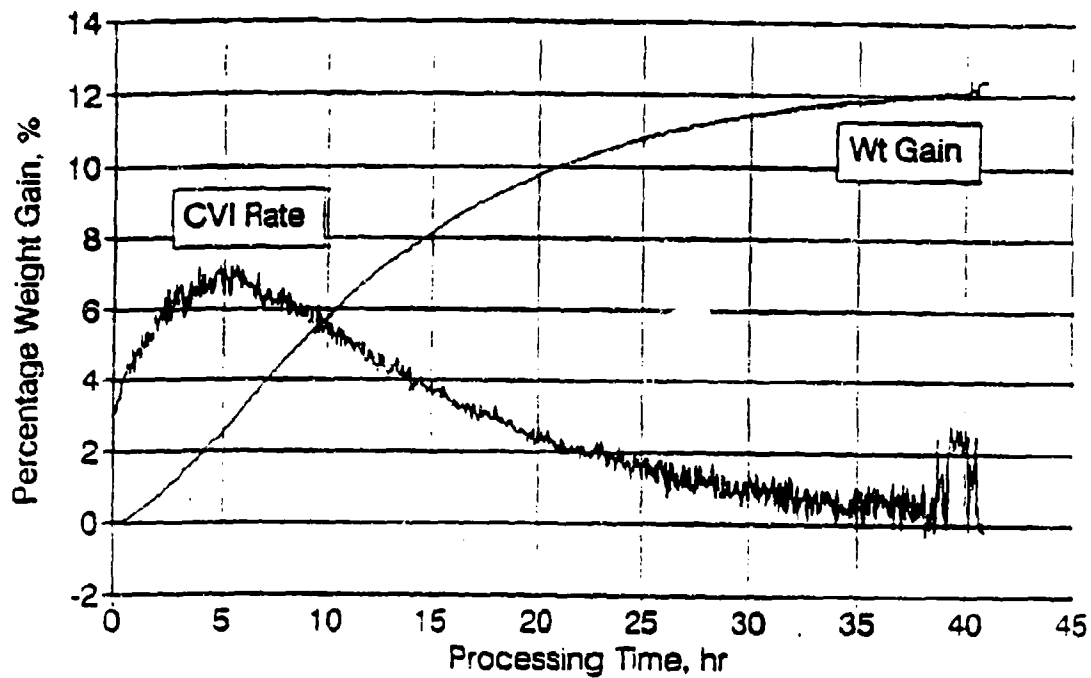
Figure 4-2. CVI Weight Gain and Rate Curves
for the 1100°C/15 torr Run

CVI Weight Gain and Rate
HT-A: 1200 C, 15 torr, 19 hrs
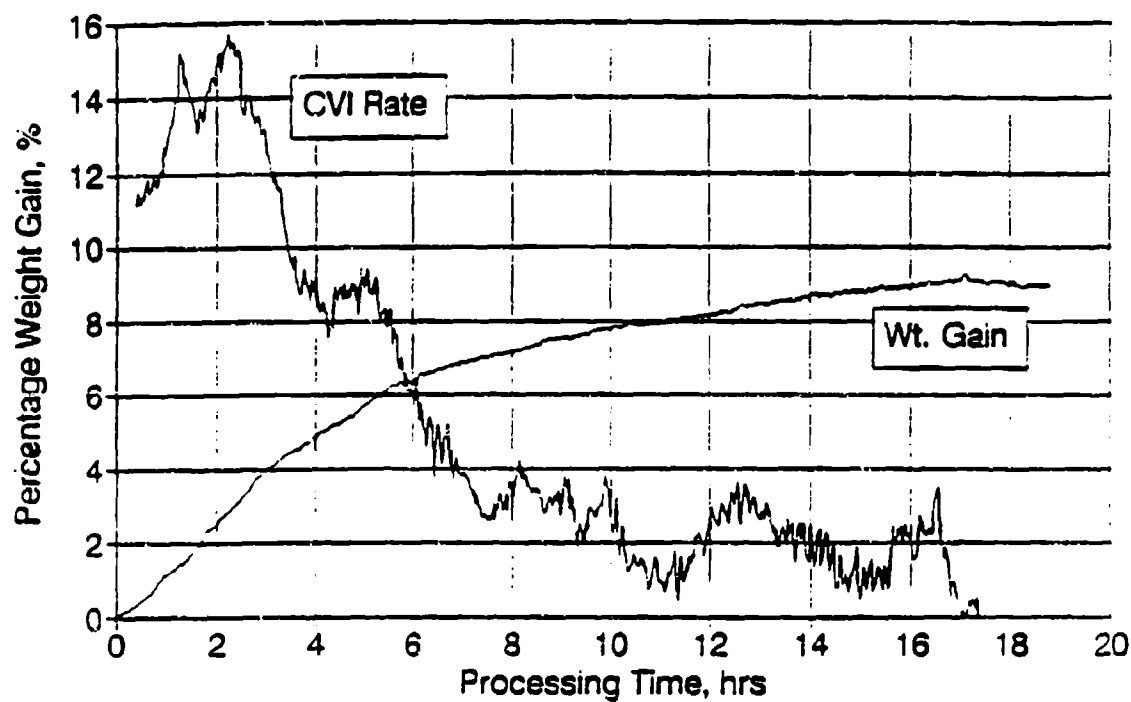
Figure 4-3. CVI Weight Gain and Rate Curves
for the 1200°C/15 torr Run

CVI Weight Gain and Rate Curve
HT-C: 1100 C, 5 torr, 29 hr
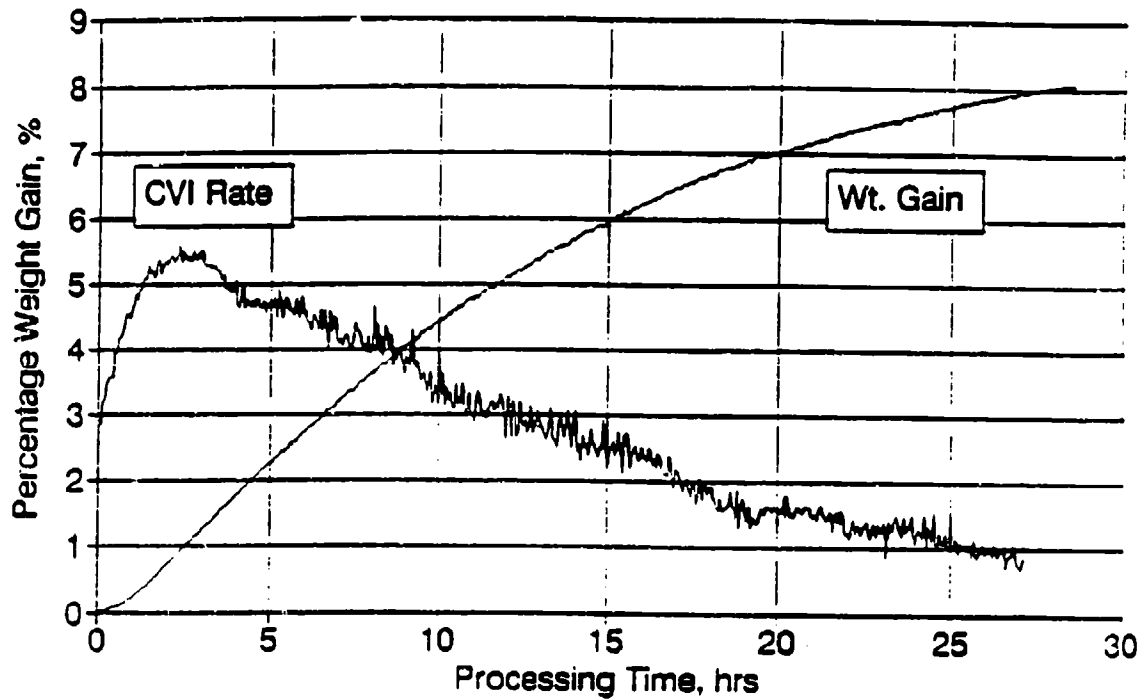
Figure 4-4. CVI Weight Gain and Rate Curves
for the 1100°C/5 torr Run
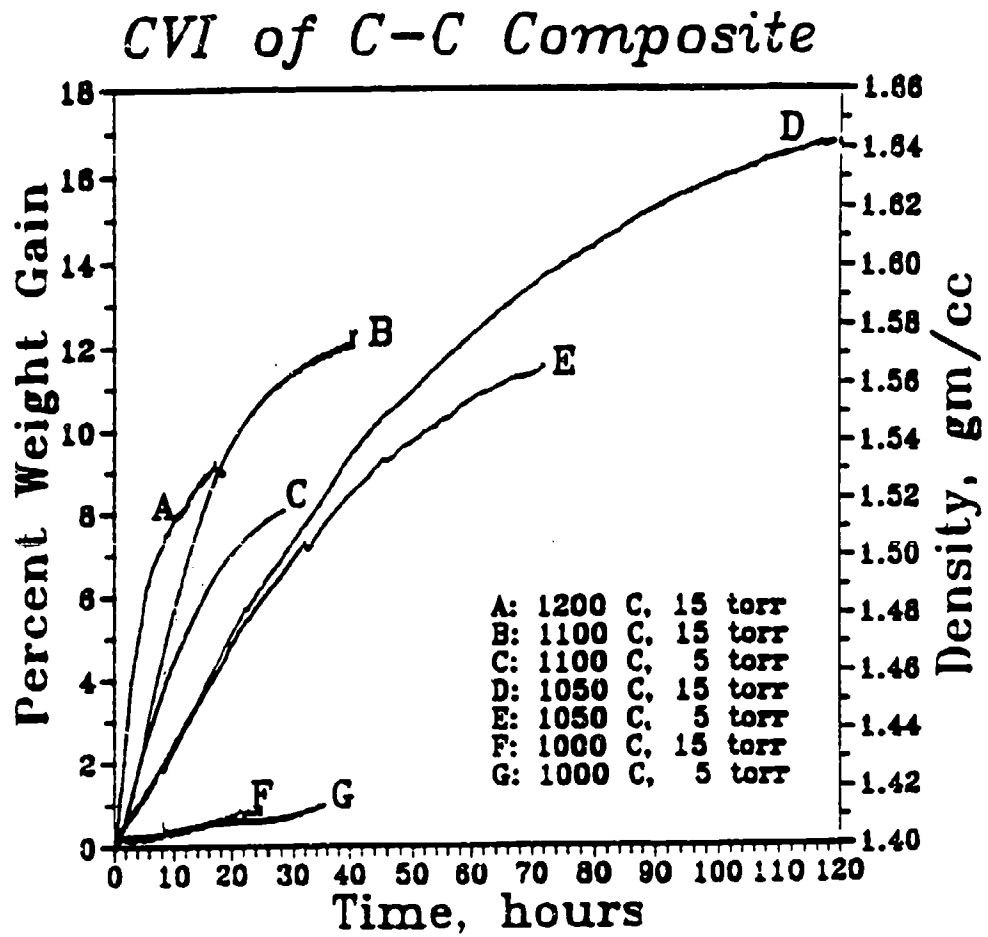
Figure 4-5. Comparison of CVI Weight Gain Curves
under Different Experiment Conditions

CVI RATES

A:	1200 C,	15	torr
B:	1100 C,	15	torr
C:	1100 C,	5	torr
D:	1050 C,	15	torr
E:	1050 C,	5	torr
F:	1000 C,	15	torr
G:	1000 C,	5	torr
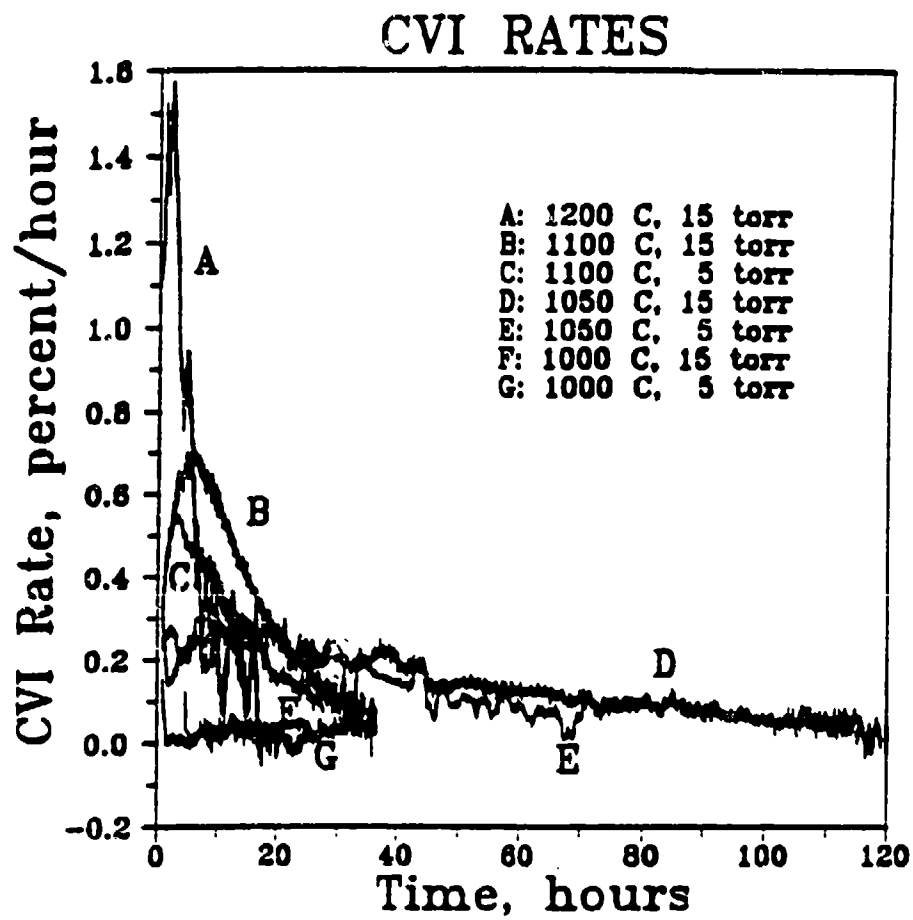
Figure 4-6. Comparison of CVI Rate Curves under
Different Experiment Conditions

Density Profile Measurement
HT-D: 1050 C. 15 torr. 120 hrs
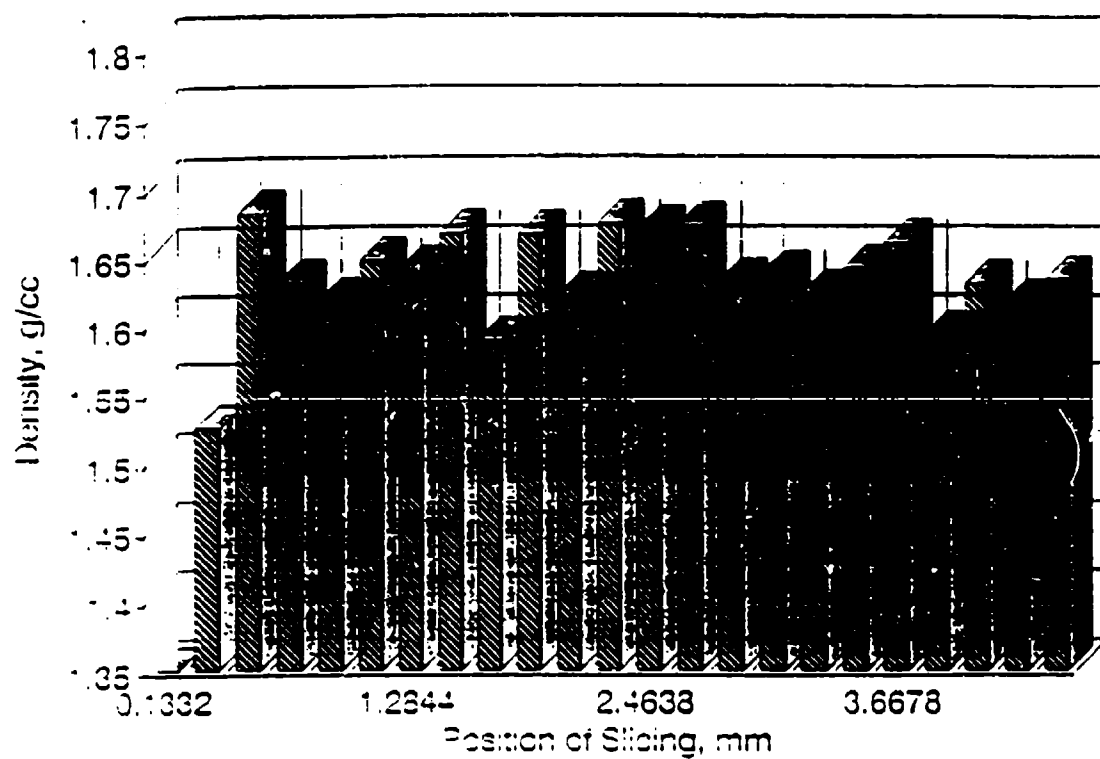
Figure 4-7. Density Profile of the 1050°C/15 torr
Processed Specimen

Density Profile Measurement
HT-B: 1100 C, 15 torr, 41 hrs
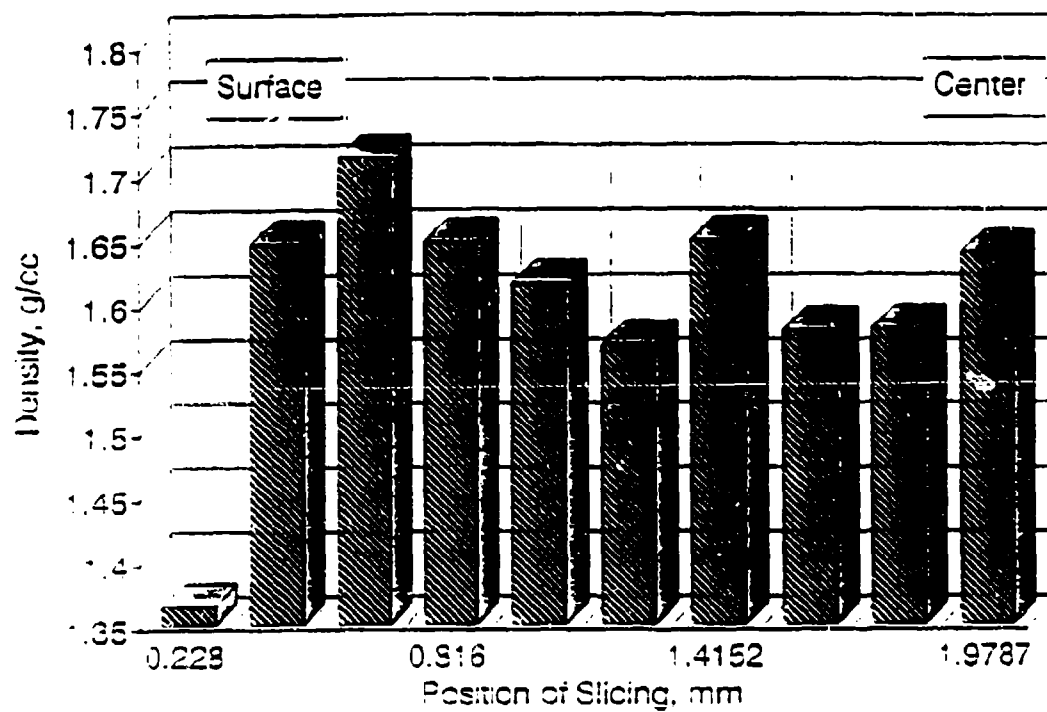
Figure 4-8. Density Profile of the 1100°C/15 torr
Processed Specimen

Density Profile Measurement
HT-A: 1200 C. 15 torr, 19 hrs
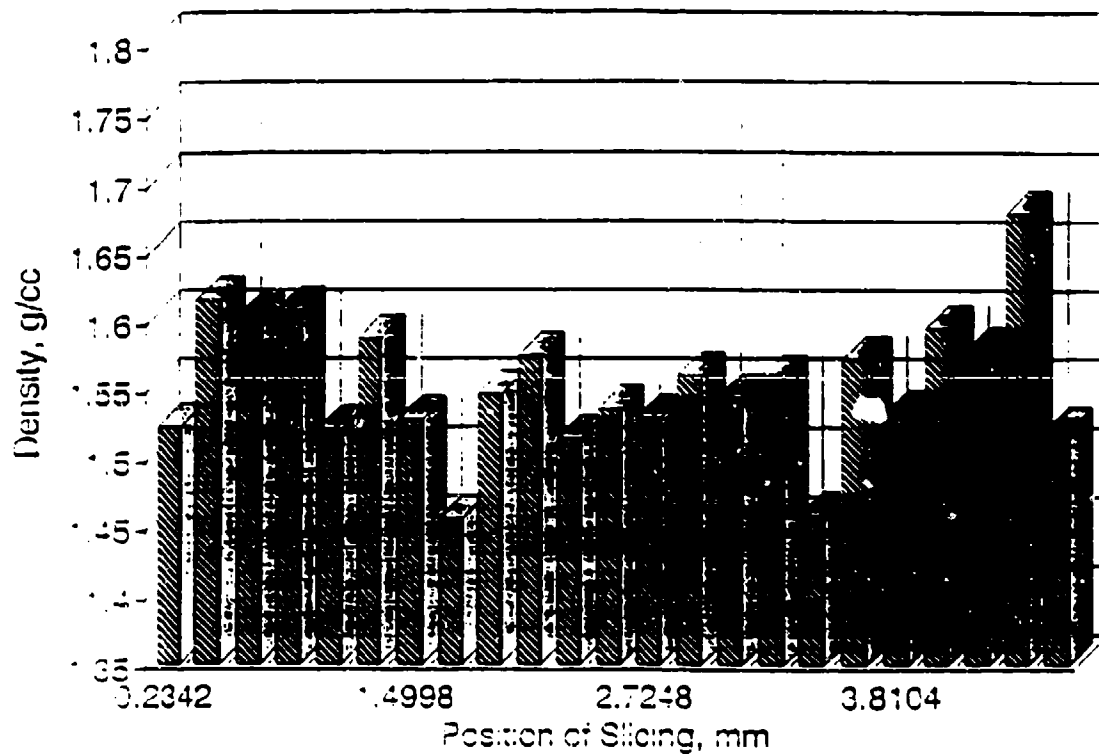
Figure 4-9. Density Profile of the 1200°C/15 torr
Processed Specimen

Density Profile Measurement
HT-E: 1050 C. 5 torr, 72 hr
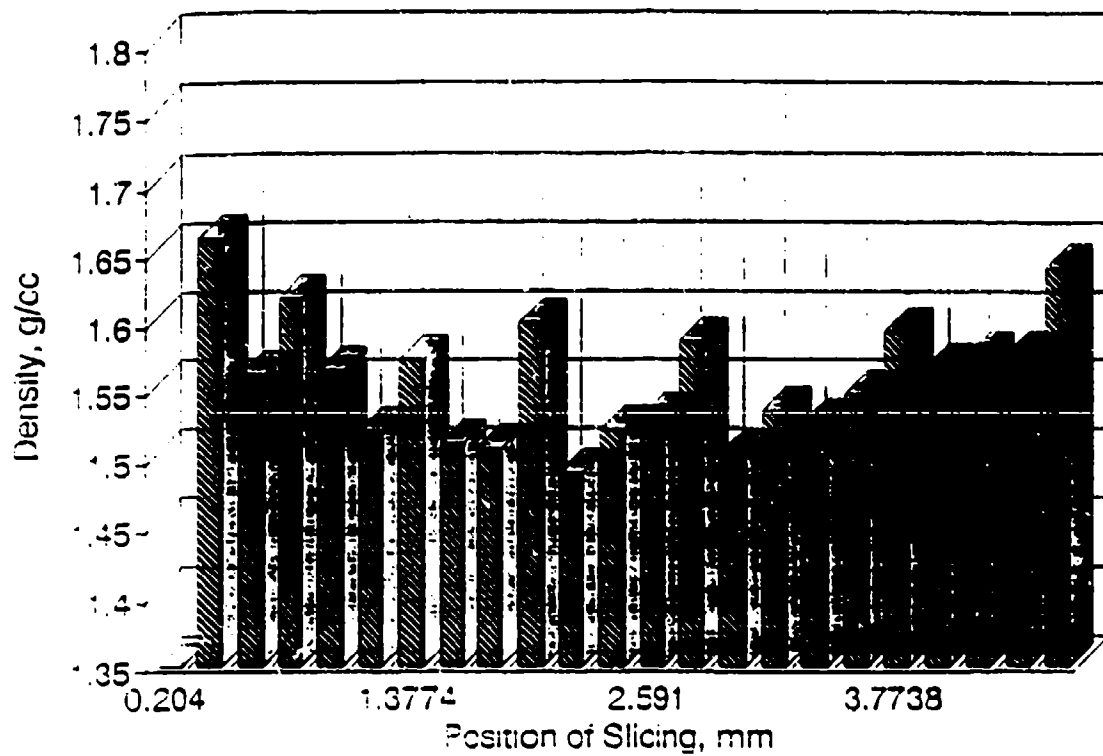
Figure 4-10. Density Profile of the 1050°C/5 torr
Processed Specimen

Density Profile Measurement
HT-C: 1100 C. 5 torr, 29 hrs
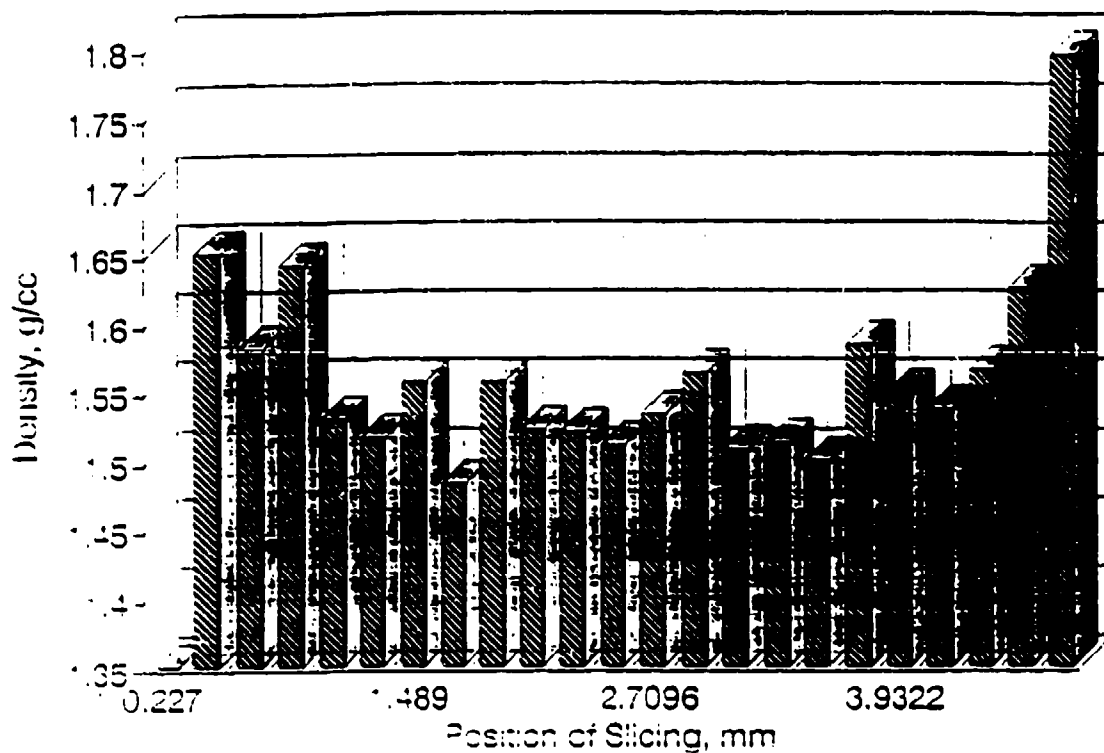
Figure --11. Density Profile of the 1100°C/5 torr
Processed Specimen

Figure 4-12. TEM Micrograph Showing Morphology
of A Densified Specimen
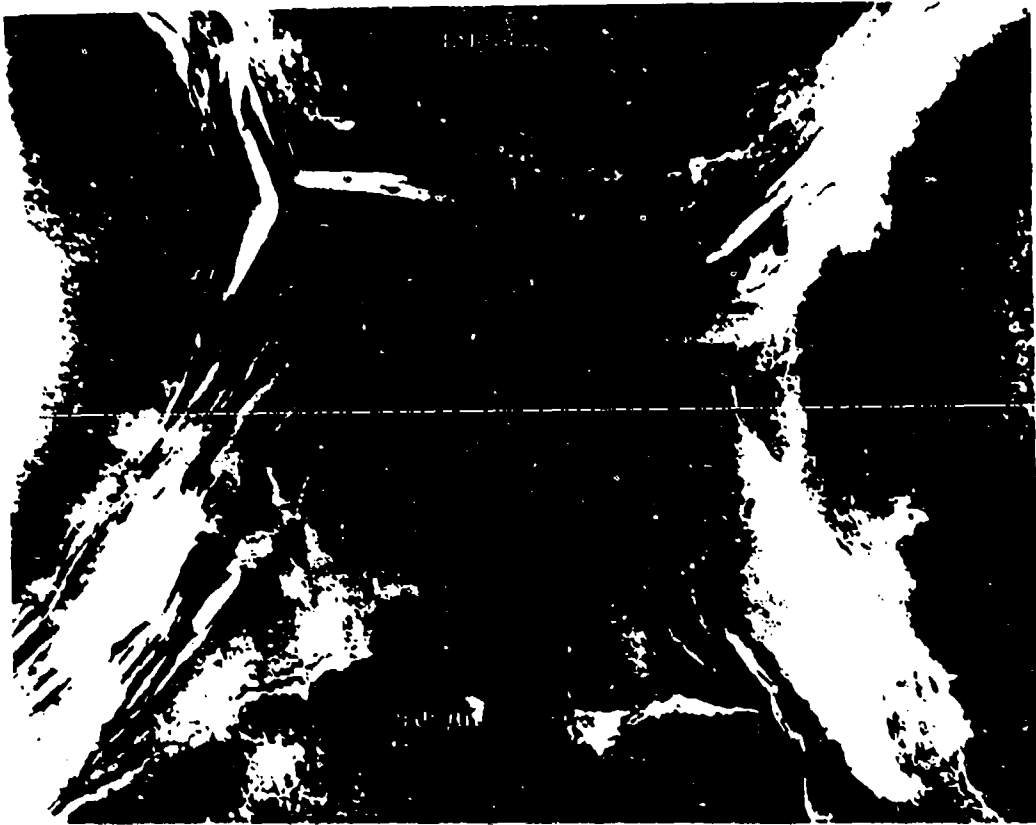
Figure --13. TEM Micrograph Showing the
Interfaces of CVI/Resin/Fiber
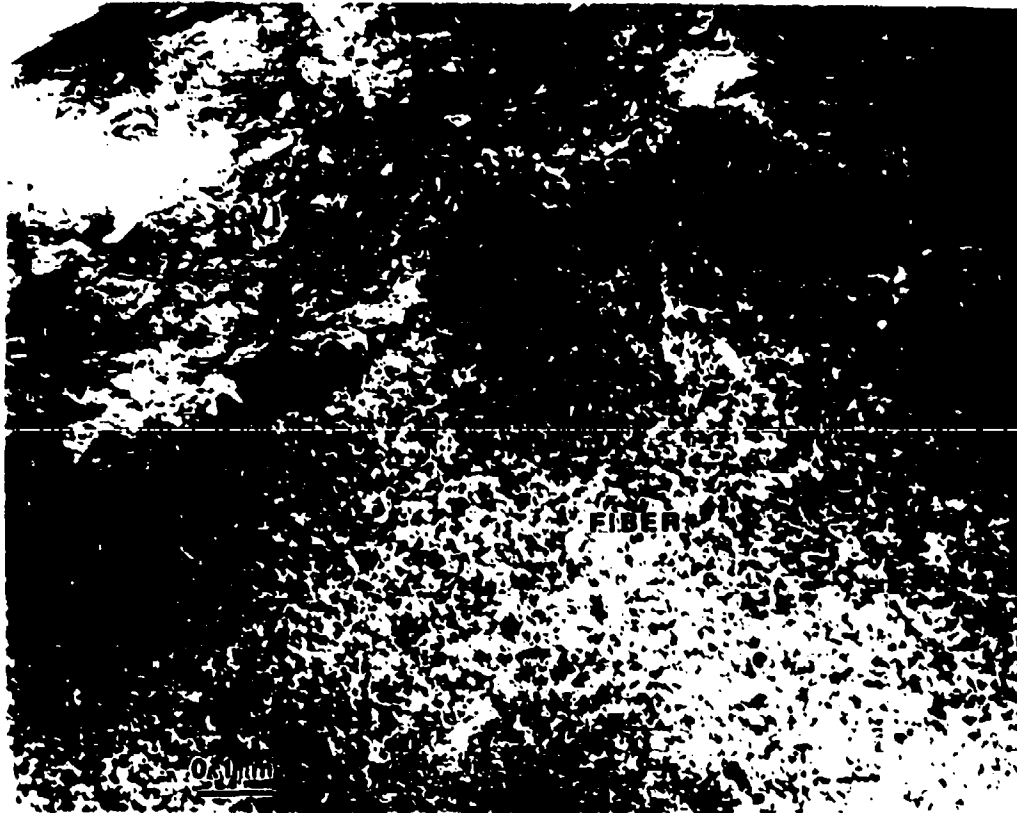
Figure 4-14. TEM Micrograph Showing the Interface of Fiber/CVI
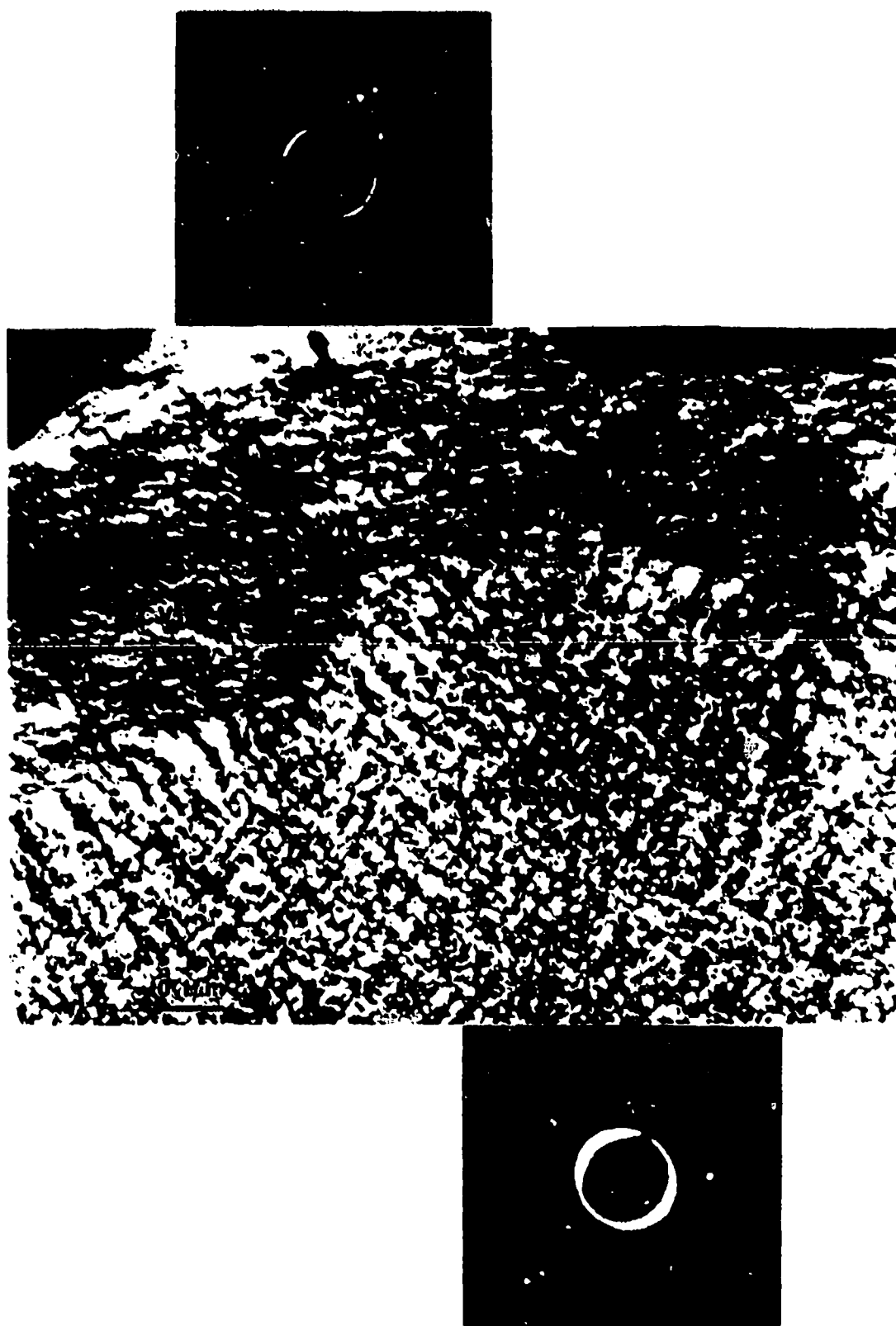
Figure 4-15. TEM Dark Field Micrograph Showing
the Same Area of Figure 4-14
Upper Left: SAD pattern from CVI portion
Upper Right: SAD pattern from fiber portion

Figure 4-16. TEM Micrograph Showing the Interface of Resin/CVI
Upper: SAD pattern from resin matrix portion
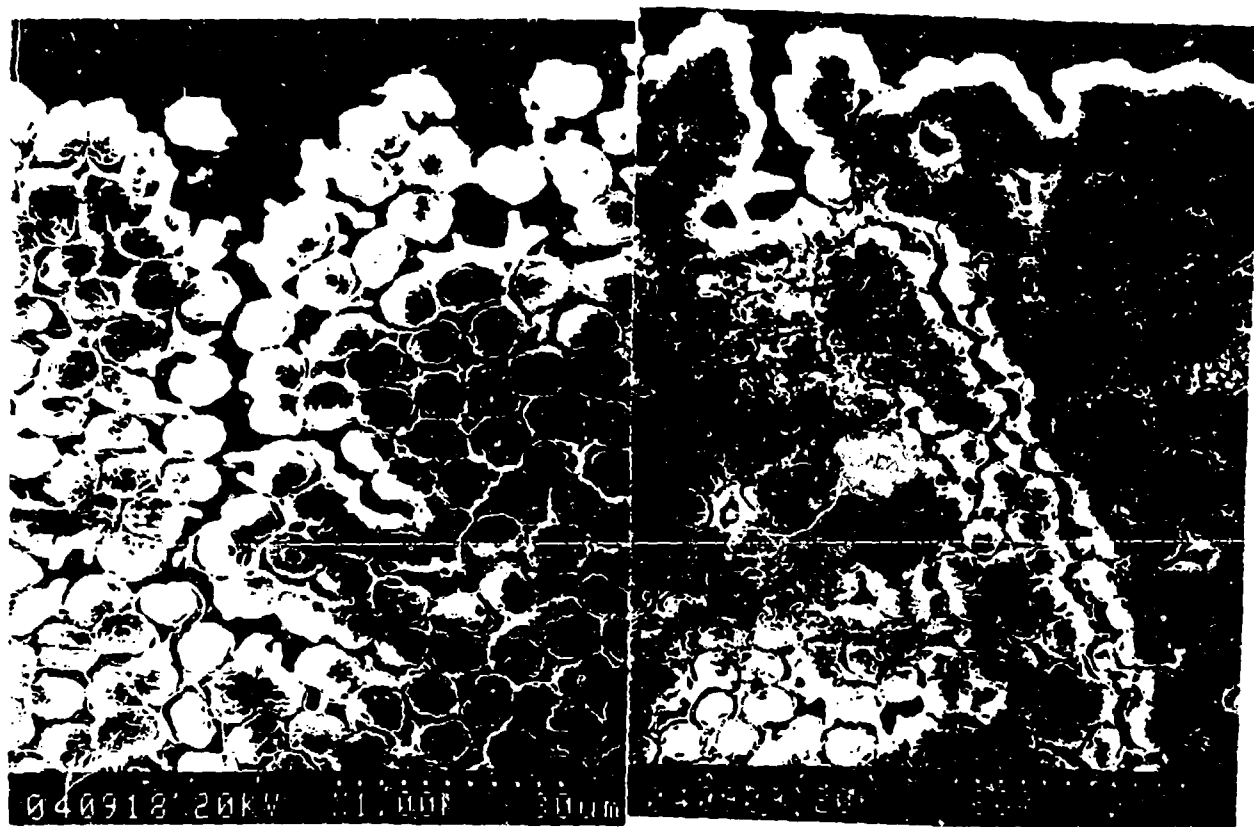
Figure 4-17. SEM Micrographs Taken from Surface Area of Two Specimens
with Different Processing History
Left: HT-D, 1050 °C, 15 torr
Right: HT-A, 1200 °C, 15 torr
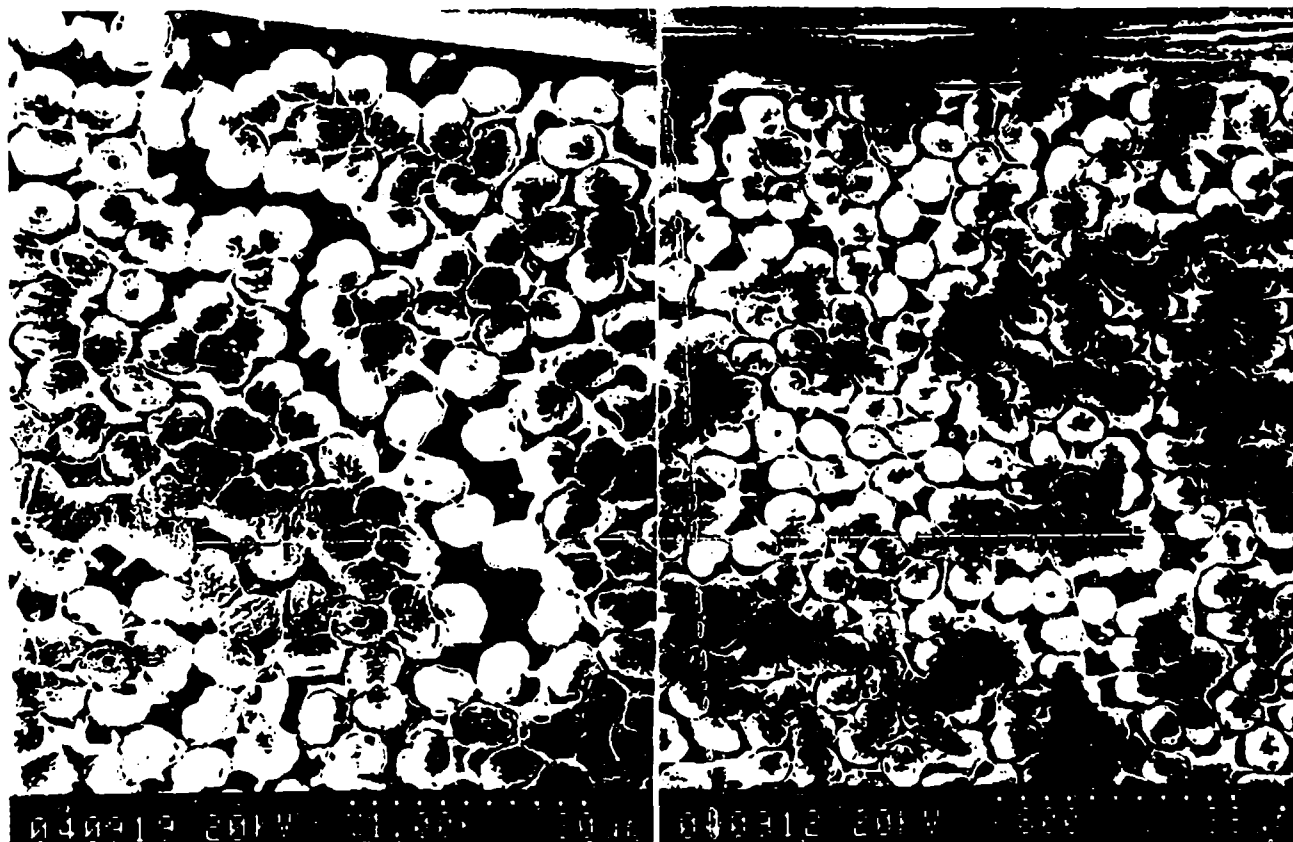
Figure —18. SEM Micrographs Taken from Center Area of Two Specimens
with Different Processing History
Left: HT-D, 1050 °C, 15 torr
Right: HT-A, 1200 °C, 15 torr

Figure 4-19. Polarized Optical Micrographs Showing CVI Carbon Effectively
Filling the Small Pores But Fail to Fill the Large Pores
1050°C 15 torr Processed Specemen (1000 X)
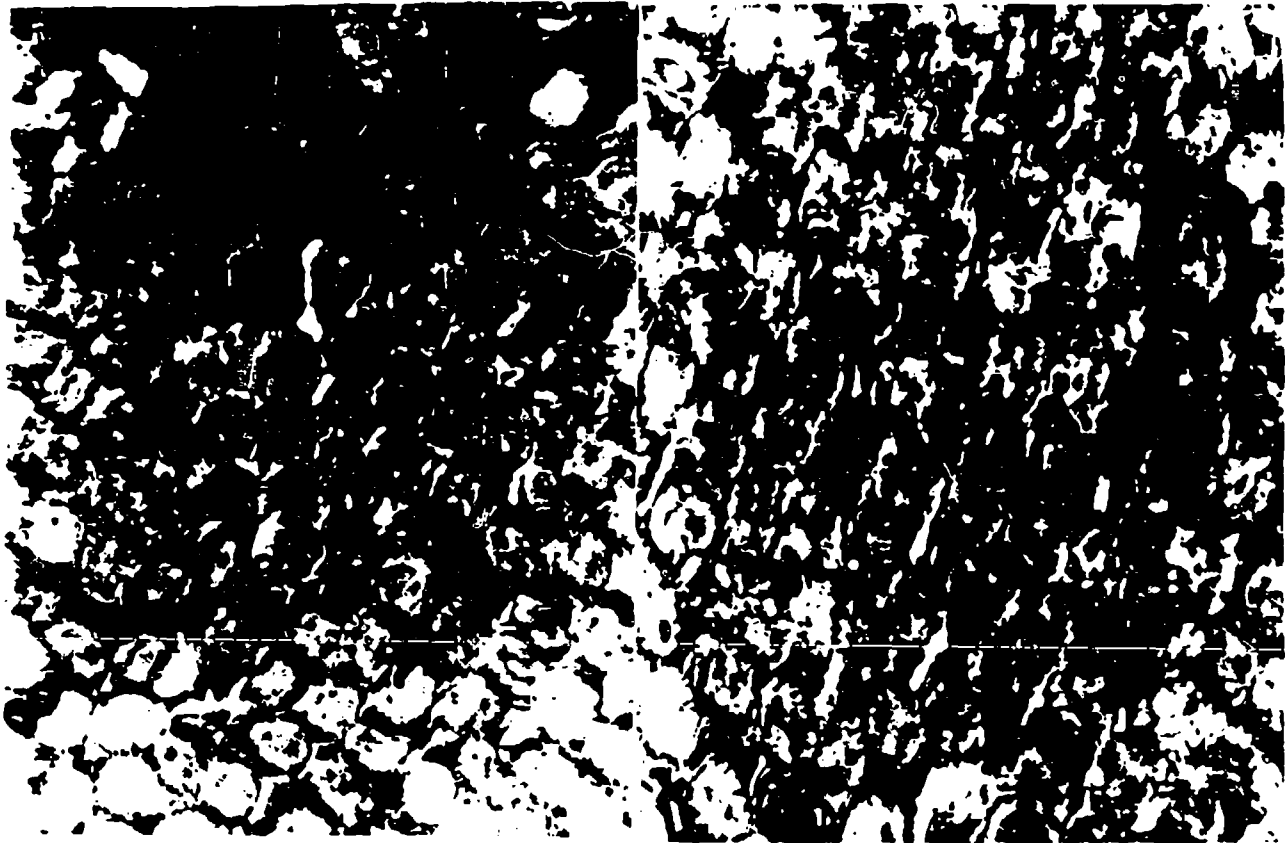
Figure 4-10. Polarized Optical Micrographs Taken from
the 1050°C, 15 torr Processed Specimen
Left: Surface (1300 X)
Right: Center (1300 X)

74
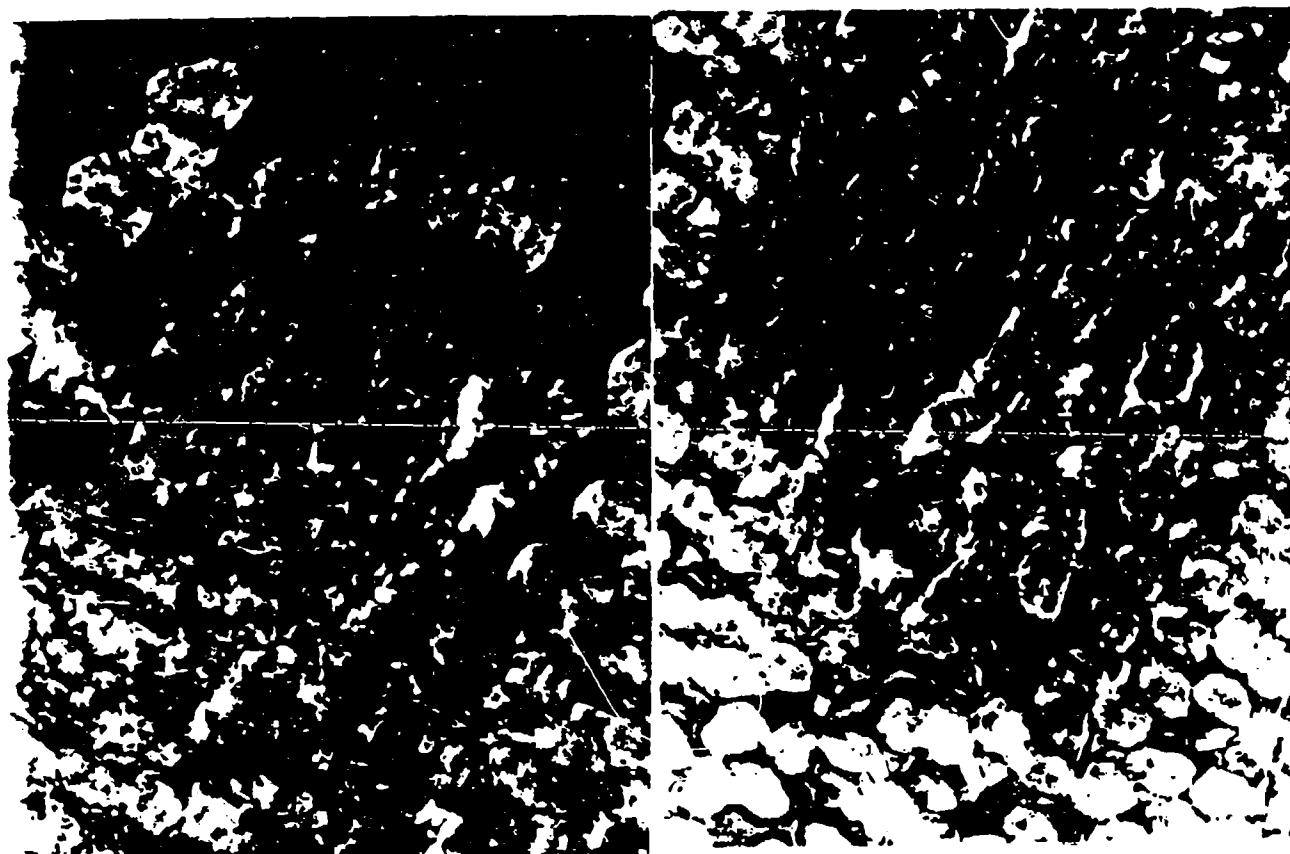
Figure 4-21. Polarized Optical Micrographs Taken from
the 1100°C/15 torr Processed Specimen
Left: Surface (1300 X)
Right: Center (1300 X)
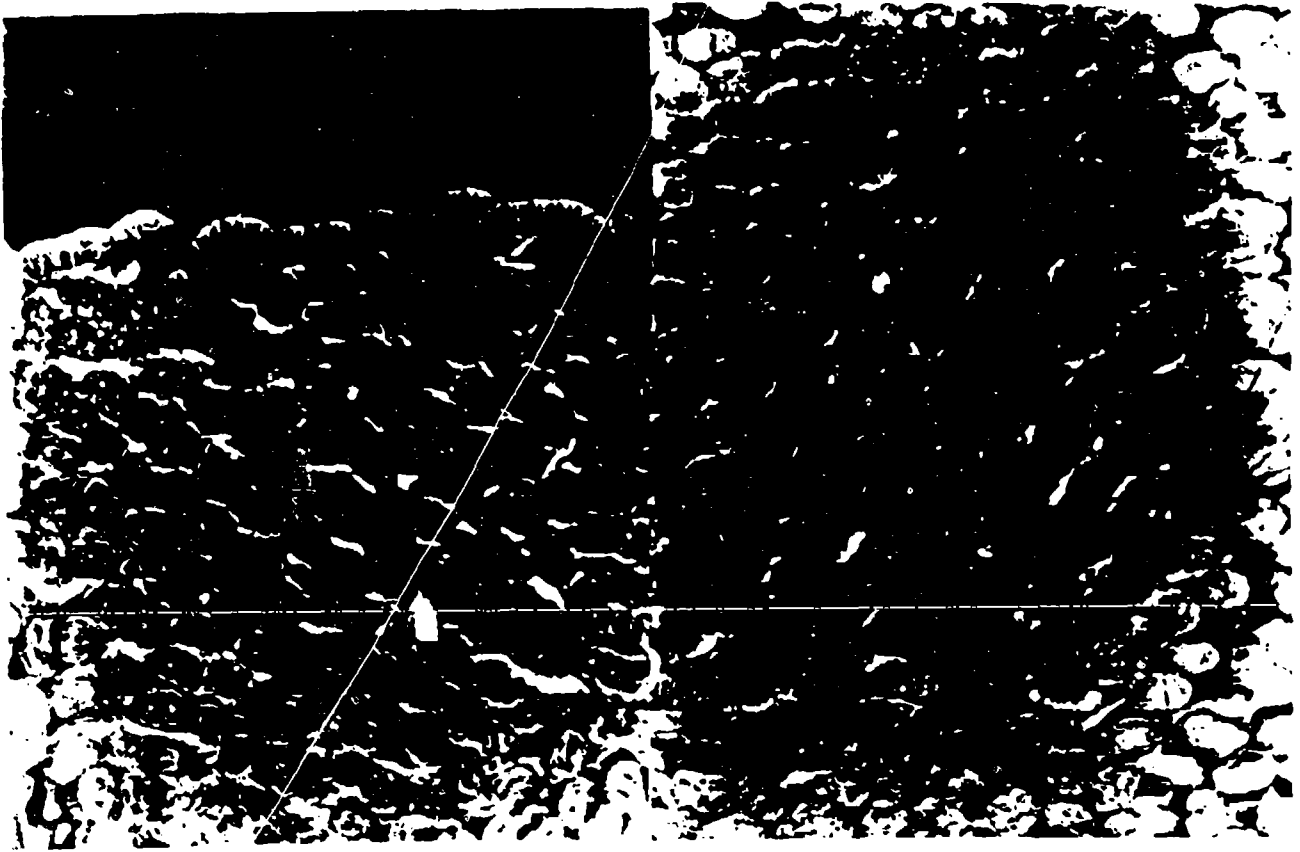
Figure 4-22. Polarized Optical Micrographs Taken from
the 1200°C 15 torr Processed Specimen
Left: Surface (400 X)
Right: Center (1000 X)

Figure 4-23. Polarized Optical Micrograph Showing Surface Crust Seals
A Large Crack at Surface of the 1200°C/15 torr Specimen (1000 X)

CHAPTER 5

DISCUSSION

CVI process can be considered as a subset of a more general class of dynamic chemical processes in which a flowing fluid passes through a volumetric region where chemical reactions involving the fluid occur. A thorough understanding of this process requires knowledge of different aspects of the processing system, including: (1) experimental variables such as temperature, pressure, and input gas composition; (2) system chemistry, including chemical species and phase composition, thermodynamic and kinetic properties, and reaction mechanisms; and (3) mass transport properties such as diffusion, thermal and forced convection. The complexity of this process is apparent.

The purpose of this study has focused on obtaining the best combinations of processing parameters in order to optimize the process. There are two essential requirements for the optimization of the CVI densification process: (1) uniform deposition of solid carbon in the interior of the composite, and (2) minimum processing time.

The result of CVI densification depends upon the competition between chemical reaction on the inner surfaces and the diffusion of precursor gases into the open porosity to reach these sites. High chemical reaction rate, as demonstrated by the CVI weight gain curves with steep slope and high initial CVI rate value, favors preferential near-surface deposition, since reactant gas depletion will be inevitable along the diffusion path into the open pores. This subsequently causes the formation of bottle-neck pores or a crust (surface coating) on the composite surface which hinders further infiltration. This

was confirmed by the density profile measurement and the microscopic studies. Therefore, the combined diffusion and reaction process must be kept in the chemical reaction limited regime to permit in-depth diffusion of the gaseous reactants. Experimental conditions have a strong influence on the kinetic steps as analyzed below.

5.1. Temperature

Better infiltration generally requires lower processing temperature, since reaction kinetics is a much stronger function of temperature than the diffusion process. To what degree a kinetic step depends on temperature can be quantitatively expressed by its activation energy. The transition from one mechanistic step to another can be analyzed using Arrhenius plot.

As shown in the Arrhenius plot in Figure 5-1, the activation energy for the chemical reaction estimated from the initial CVI weight slope (1000 °C to 1050 °C range) is approximately 124 kcal/mole. The activation energy estimated from the surface coating thickness measurement (1050 °C to 1100 °C range) is about 128 kcal/mole. Both are higher than the reported activation energy of thermal decomposition of methane, averaging 103 kcal/mole[7].

Assuming that (1) the rate limiting steps are either the chemical reaction on the internal surfaces or the diffusion of gaseous reactants reaching these sites over the experimental temperature range, and (2) both steps have temperature dependence in the form of

$$R = \exp\left(-\frac{E_a}{RT}\right) \qquad (5.1)$$

The overall rate R of the coupled reaction can then be expressed by[44]

$$R = \cfrac{1}{\cfrac{1}{R_{reaction}} + \cfrac{1}{R_{diffusion}}} \qquad (5.2)$$

Fitting equation 5.2 with the experimental data, the following expressions are obtained:

$$R_{reaction} = 10^{24.8} \exp\left(\frac{-152.4 \ kcal}{RT}\right) \qquad (5.3)$$

$$R_{diffusion} = 10^{2.87} \exp\left(\frac{-18.5 \ kcal}{RT}\right) \qquad (5.4).$$

The best fit curve is shown in the Arrhenius plot in Figure 5-2. This kind of temperature dependence was also observed by McAllister et. al.[30] on their carbon CVI study using propylene as a precursor. The activation energy for the chemical reaction obtained from this derivation, i.e. 152.4 kcal/mole, is even higher than that estimated directly. Diffusion limited processes gradually become predominant at high processing temperatures, as clearly revealed in the Arrhenius plot(Figure 5-2). The decrease in activation energy measured by surface thickening rate over the 1100 °C and 1200 °C temperature range is indicative of the formation of a boundary layer over the bulk specimen surface which limits the access of the reactant gases onto the bulk surface.

Analysis of the CVI weight gain curves showed that the higher the processing temperature, the higher the initial CVI rate would be, and also the stronger the tendency to close the open pores prematurely, as indicated by the early bend-over and level-off of

the curves.

5.2 Pressure

Temperature affects the CVI process through reaction kinetics, whereas pressure mainly contributes to the transport properties of the system. The CVI weight gain measurements suggest that higher pressure (15 torr in this study) will delay the bend-over, indicating the promotion of infiltration rather than surface coating. This is due to the fact that the increase in pressure will reduce the mean-free-path of the gas molecules, and therefore foster the effective in-depth diffusion of the reactant gas molecules into the open pores.

The mean-free-path of methane and hydrogen molecules in the pressure range under this investigation were plotted in Figures 5-3 and 5-4, respectively. The mean-free-path values in the intermediate temperature range between 1000 °C and 1200 °C lie in between the two borders set by these two temperature lines. Recall the criteria which distinguish molecular and Knudsen diffusion discussed in Chapter 2, and bear in mind the interbundle micropores vary around 1 to 5 μm in size, it is clear that Knudsen diffusion is predominate under the conditions employed in this study. The pressure dependence of the diffusive flux is demonstrated in Figure 5-5 by Satterfield [45]. This reveals that increasing the pressure will linearly increase the diffusive flux.

Care should be taken in applying high processing pressure, since high reactant concentration will also result in a high reaction rate. The reaction rate is linearly proportional to the concentration in the case of methane decomposition [24].

5.3 Preform Geometry

The geometry of carbon-carbon composites is complex, and it changes as the infiltration proceeds. The influence of the preform geometry on CVI process is two-fold. Firstly, it will affect the CVI rate through the change in total available surface area. Secondly, it affects the transport of both reactant and product gases.

Unlike the case of the CVI densification of the continuous fiber yarns, in which the total available surface area will definitely increase initially according to the overlap model proposed by Currier[8], the complex geometry of the preform in this study did not allow such an obvious prediction. The initial CVI rate increase as presented in Chapter 4 suggested a similar behavior. This indicates that the convex shaped surfaces in the original preform are larger than the concave shaped surfaces. As infiltration proceeds, even under the ideal chemical reaction controlled region, the overlap of the solid deposits will cause the decrease in total available surface area. This seems to be the case when low processing temperature is employed (1000 °C and 1050 °C) as confirmed by the microscopic study on thus densified specimens. When higher temperatures are used, the high deposition rate causes the reactant gases to deplete as they progress into the pores. This establishes a concentration gradient between the center and the surface of the preform, and thus results in the formation of bottle-neck pores and surface crust, and the premature closing of the pores, as indicated by the early bend-over of high temperature CVI weight gain curves.

Filling of the pore also changes the transport property. Larger pores are more easily infiltrated than smaller pores, especially in the Knudsen diffusion regime. The

expression of Knudsen diffusivity clearly demonstrates this point[36].

$$D_{Knudsen} = \frac{\bar{U}d}{3} \qquad (5.5)$$

where U is the average velocity of the gas molecules and d is the pore diameter. This property may also be partly responsible for the shape of the weight gain curves. Initially, when the pores are relatively large, high diffusive flux of reactant molecules keeps the overall reaction in the chemical reaction controlled regime; but when the pore sizes become smaller as the CVI process continues, the diffusivity decreases, causing a slower transportation of gaseous reactants to the reaction sites deep inside the pores: therefore the diffusion limited regime gradually takes over and becomes predominate. If tortuosity of the pores is taken into account, which is normally assumed to increase as porosity decreases [37], the decrease of the effective diffusive flux will be even faster. This reduction in reactive species transfer, coupled with decreasing total internal surface area, causes the bend-over of the weight gain curve.

The changing balance of the reaction-diffusion competition during the densification can be utilized to optimize the processing condition and minimize processing times. By imposing a temperature profile with higher initial temperature, and a gradually decreasing temperature, it is possible to keep the overall rate at the high end of the reaction controlled regime throughout the whole densification process, thus obtaining uniform densification in the shortest processing time.

Another concept also becomes explicit at this point: a preform with non-uniform porosity sizes is not likely to be fully densified using isothermal CVI technique, since

even under the best densification conditions, the even deposit thickness throughout the composites will not fully fill the large pores. Therefore, applying such hybrid process by pre-densifying the preform using liquid impregnation to fill up some of the large pores will certainly be beneficial.

5.4 Processing Efficiency

Based on the above analyses, low temperature and moderate pressure will promote uniform infiltration. However, the efficiency of the process should also be taken into account when choosing the fabrication parameters. At 1000 °C, it will take more than 25 days to achieve the same density which has been achieved by infiltration at 1050 °C for 5 days. In our case, a temperature around 1050 °C and a total pressure of about 15 torr seems to be the best combination. The optimum processing condition is also related to the geometry of the preforms being densified, therefore the unique characteristics of a certain kind of preform will affect the densification process. It should also be considered as a contributing factor when optimizing the processing conditions.

5.5 Preliminary Modeling Study

The modeling work conducted in this investigation utilized the "overlap concept" by Avrami[8]. Although the geometry of the resin-bonded preform is far more complicated than the fibrous yarn geometry used by Currier[8] to demonstrate the overlap concept, the recorded CVI rate curves all present in similar shape as predi   by the overlap model. To simplify the problem, the following assumptions are made which are in fact

only valid at low temperatures: (1) the overall rate of reaction is controlled by chemical kinetics only and the concentration of the gaseous species is uniform throughout the preform, and (2) the system is isothermal. Under these assumptions, the conversion of the solid can be expressed by

$$\rho_c \frac{dV}{dt} = k_s S C_0 \qquad (5.6)$$

where ρ_c is the density of pyrolytic carbon;

C_0 is the bulk gas concentration, as well as the gas concentration in the preform under the assumptions here;

k_s is the surface reaction rate;

S is the total available surface area;

dV/dt denotes the rate of solid volume increase;

V is the volume enclosed by the actual overlap system as discussed in Chapter 2.

Let the porosity at time t be $\epsilon(t) = 1 - V$;

the initial porosity at $t = 0$ be $\epsilon_{oi} = 1 - V_{0i}$;

the following relation is derived by Currier:[8]

$$\frac{\epsilon(t)}{\epsilon_{oi}} = \exp[-\tau(1 + \sigma\tau)] \qquad (5.7)$$

where the dimensionless quantities

$$\tau = \frac{k_S C_0 S_{0i} t}{\rho_c \varepsilon_0 i} \tag{5.8}$$

$$\sigma = \frac{\pi L_0 \varepsilon_{0i}^2}{S_{0i}^2} \tag{5.9}$$

To set a relation between Equation 5-7 and the experimental obtained weight gain data. it is written in the form

$$\frac{\varepsilon(t)}{\varepsilon_{0i}} = \exp(-at - bt^2) \tag{5.10}$$

Here a and b is related to Equation 5.8 and 5.9, and are temperature dependent through the surface reaction rate

$$a \propto k_S \propto \exp(-\frac{E_a}{RT}) \tag{5.11}$$

$$b \propto k_s^2 \propto \exp(-\frac{2E_a}{RT}) \tag{5.12}$$

Since the initial density

$$\rho_{0i} = \rho_c(1 - \varepsilon_{0i}) \tag{5.13}$$

the substrate density at time t

$$\rho(t) = \rho_c[1 - \varepsilon(t)] \tag{5.14}$$

the percentage weight gain can be expressed by

$$\% Wt. = \frac{\rho(t) - \rho_{0i}}{\rho_{0i}} = \frac{\varepsilon_{0i} - \varepsilon(t)}{1 - \varepsilon_{0i}} \qquad (5.15)$$

Incorporating Equation 5.10, we can establish a relation between the weight gain $\% Wt.$ and time t in the form of

$$\% Wt. = B[1 - \exp(-at - bt^2)] \qquad (5.16)$$

where B is a constant which relates to initial preform condition

$$B = \frac{\varepsilon_{0i}}{1 - \varepsilon_{0i}} \times 100 \qquad (5.17)$$

Fitting this relation with experimentally obtained weight gain data by using statistical methods, a weight gain vs. time relation can be obtained for each experimental condition. The comparison between the model curve and the experimental weight gain data is plotted as Figure 5-7. According to the model prediction, increasing the processing time to 200 hours in the 1050°C/15 torr case will increase the weight gain to about 18% and produce a specimen with about 1.67 g/cm³ density. In the case of the two 1100 °C runs. increasing the processing time beyond the actual experimental time will have virtually no effect on the specimen density and will just waste additional reactant gases and energy.

The a and b values obtained for under different experimental conditions do not obey the Arrehnius type of relationship as suggested by Equation 5.11 and 5.12. This is attributed to the fact that reaction control is not predominant in the investigated temperature range.

The calculated B value is 34.4, assuming 25.6% initial open porosity. However. the fitted B values range up to 18.3 in the case of 1050 °C, 15 torr run. This indicates

the evolution of close porosity during the densification; that volume portion becomes inaccessible to the reaction gases and therefore will not be filled.

Comparison of Rate Relations
Wt.Gain Rate/Surface Deposit Thickness
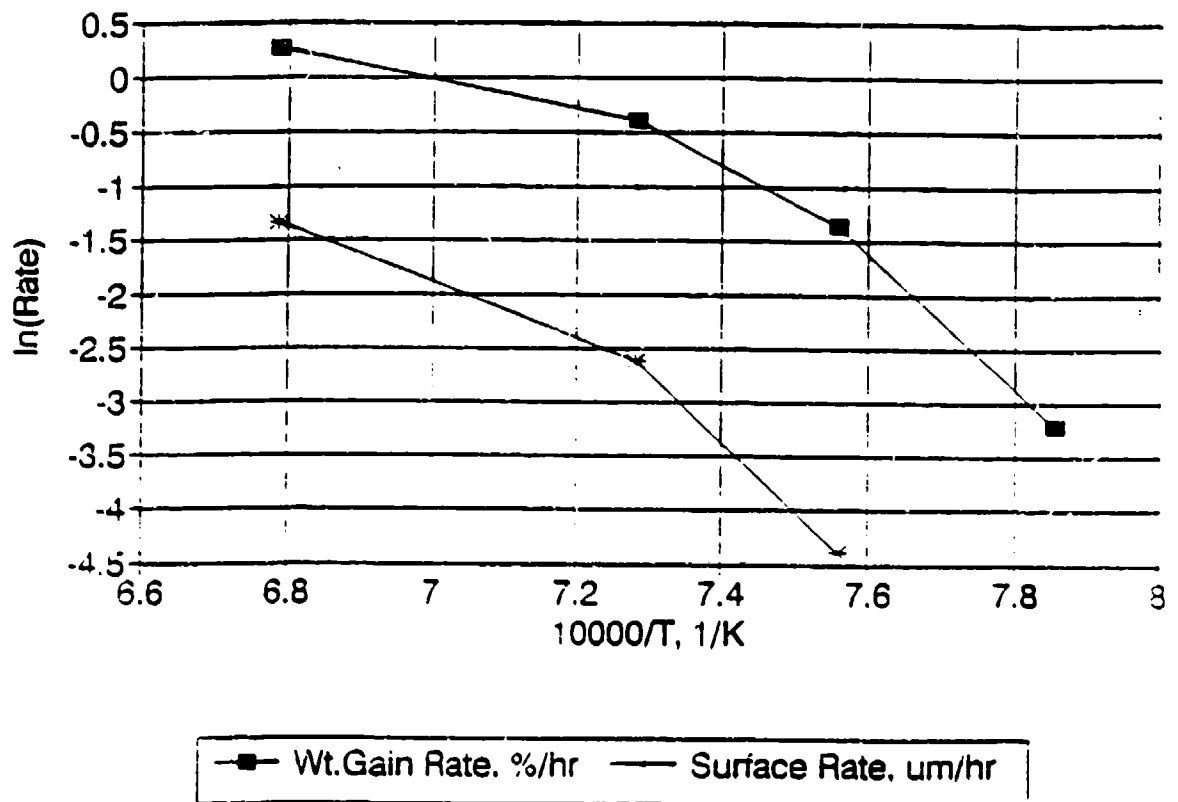
Figure 5-1. Comparison of Arrhenius Relation of CVI Rate
Obtained from Weight Gain Measurement and
Surface Deposit Thickness Measurement

Temperature Dependence of CVI Rate
(Arrhenius Plot)
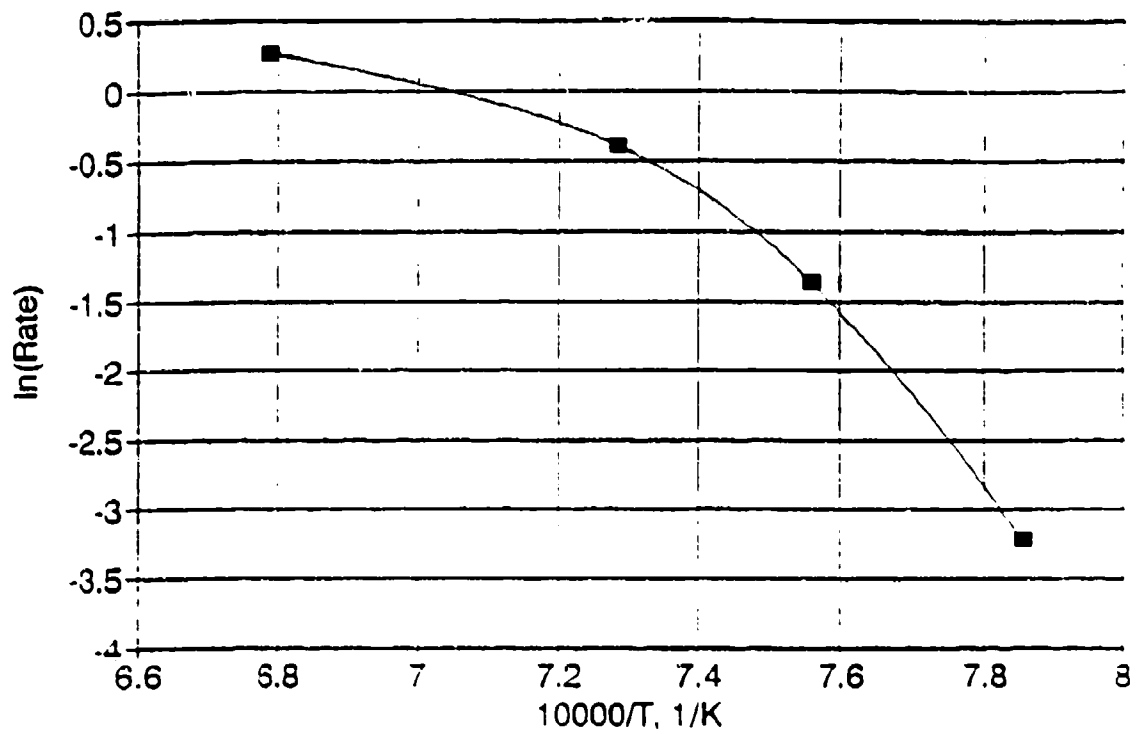
Figure 5-2. Arrhenius Plot of CVI Rate Showing Mixed Mechanism Control
as Suggested by Equation 5-

Mean Free Path for CH4
1000 C/1200 C
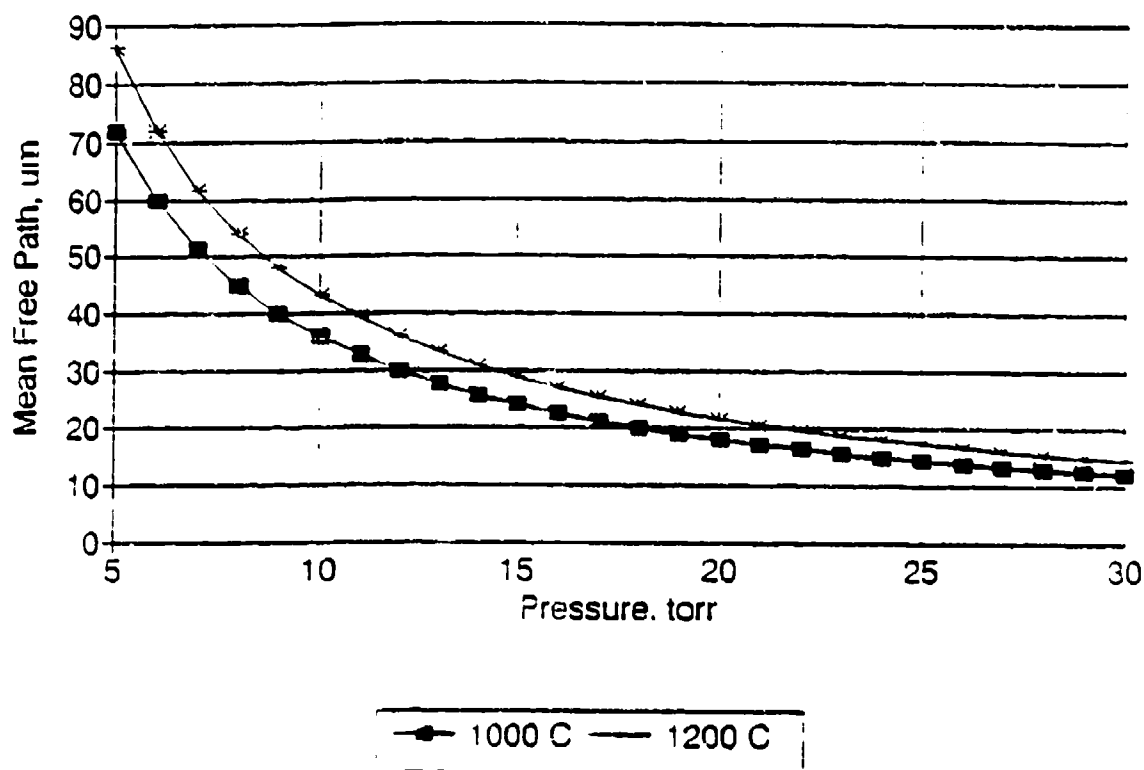
Figure 5-3. Mean-Free-Path of CH₄ Molecules in the CVI Experiment Range

Mean Free Path for H2
1000 C/1200 C
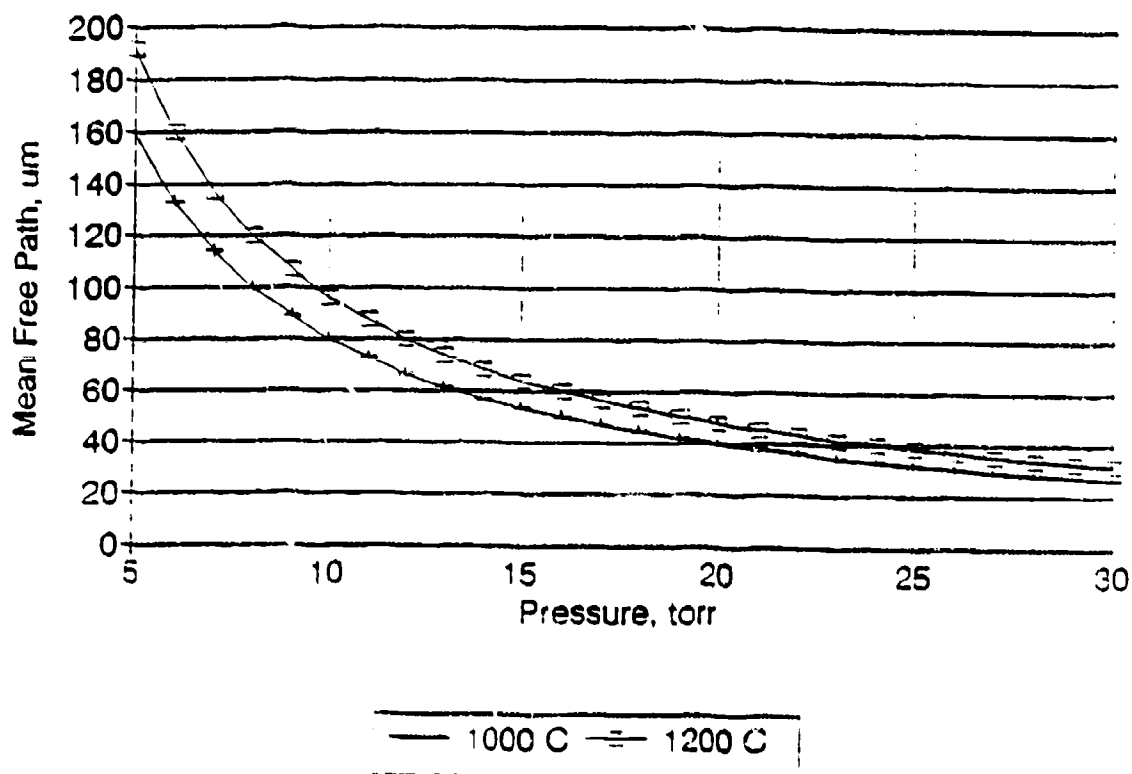
Figure 5-4. Mean-Free-Path of H_2 Molecules in the CVI Experiment Range
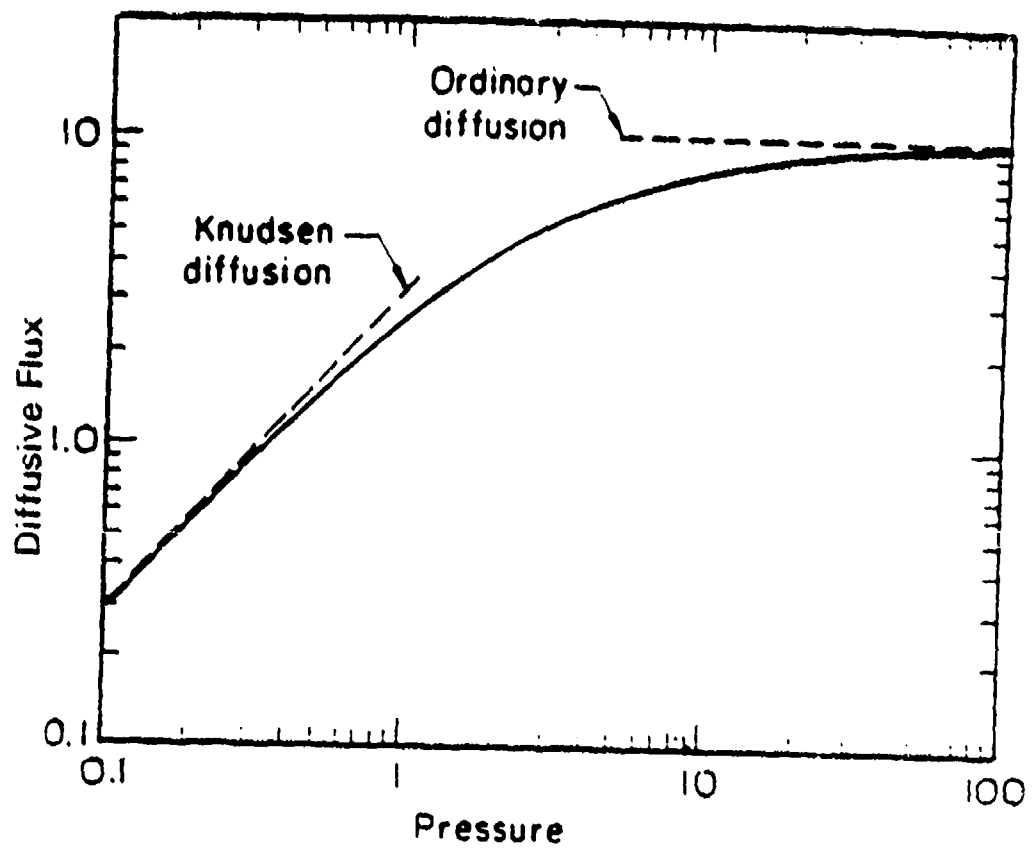
Figure 5-5. Pressure Dependence of Diffusive Flux
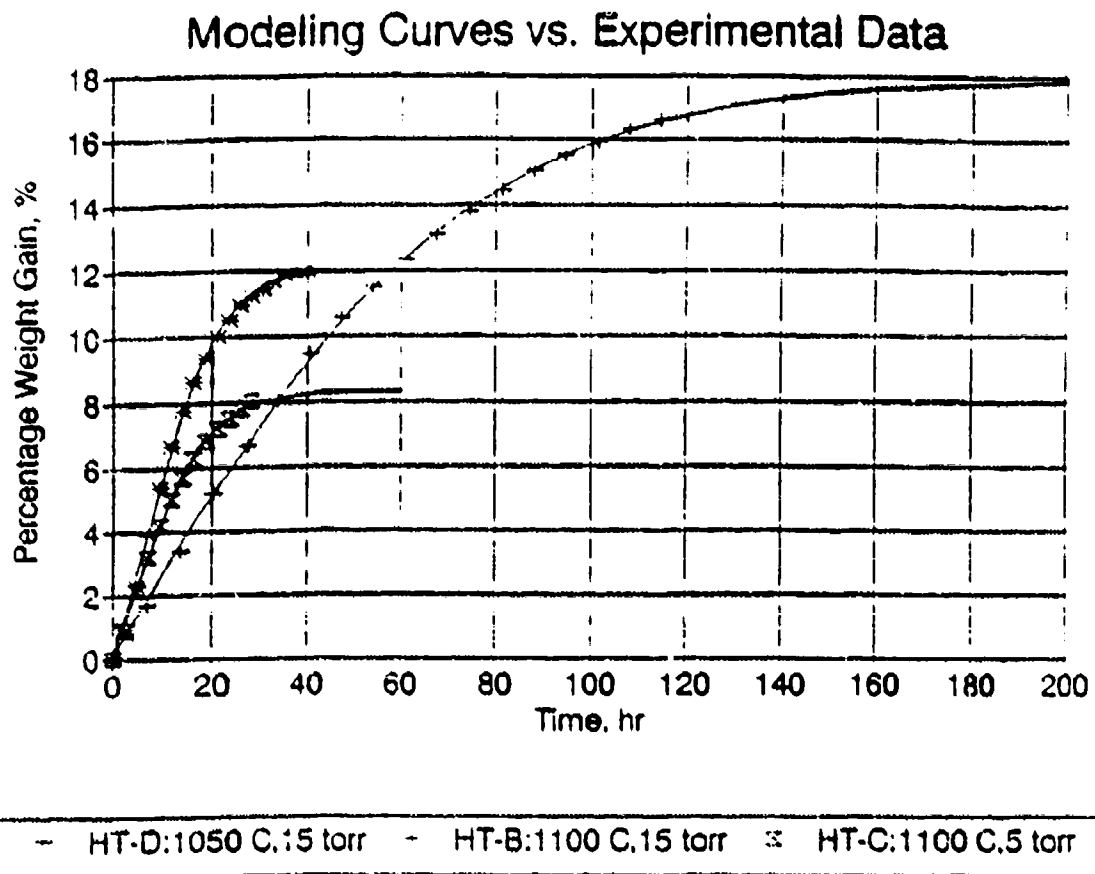
Figure 5-6. Comparison of Model Calculated Weight
Gain Curve with Experiment Data

CHAPTER 6

CONCLUSIONS

The overall objective of this thesis investigation has been focused on the better understanding of the isothermal CVI densification process of porous composite preforms. The first specific objective was to study the relationship between experiment parameters and the densification effect through a series of CVI experiments, which leads to the following conclusions:

(1)   The TGA on-line weight gain measurement has proven to be an effective technique to conduct kinetic study on the CVI processing.

(2)   The CVI process is mainly influenced by temperature, pressure, reactant gas concentration, and the preform geometry.

(3)   The CVI rate follows a typical trend: an initial increase, followed by a maximum value, and then a gradual decrease toward a minimum value beyond which no significant densification can be achieved; this trend is most significant when high temperature is employed.

(4)   High temperature results in a high initial rate and early bend-over of the weight gain curves, as well as a low composite density.

(5)   Pressure does not have much effect on initial CVI rate, but low pressure results in early bend-over of the weight gain curves.

(6)   Low temperature and moderate pressure promote infiltration.

The second objective was to characterize the microstructure of the densified specimens and correlate it with densification conditions, leading to the following

conclusions:

(7)   Bonding between CVI-matrix/fiber and CVI-matrix/resin-converted-matrix are good.

(8)   The CVI carbon is isotropic, whereas the high-temperature heat treated resin matrix is anisotropic.

(9)   Uniform densification is achieved on low-temperature/moderate-pressure processed specimens, the severity of non-uniformity increases as temperature increases.

(10)   Good densification cannot be achieved on preforms with wide porosity size distribution.

The third objective of this investigation was to perform kinetic and modeling studies, which shows:

(11)   The CVI process can be viewed as the competition between the chemical reaction kinetics on the open-pore surface and the diffusive transport of reactant gas molecules onto these sites.

(12)   Temperature influences CVI process through reaction kinetics, the reaction rate is a strong function of temperature (exponential terms), and the activation energy for the chemical reaction estimated 124 to 152 kcal/mole. High temperature causes the reactant gases to deplete as they progress into the open pores, thus establishing a concentration gradient between the surface and the center of the preform being densified, and resulting in the formation of the bottle-neck pores or even surface crust which hinders further infiltration.

(13) Pressure affects the process mainly through the transport steps. The small porosity size in the preform kept the diffusion mechanism in the Knudson diffusion range, where the diffusive flux increases nearly linearly with total pressure.

(14) Porosity size and geometry determine the value of the total available surface area and the ease of the diffusion step. The initial CVI rate increase was attributed to the increase in total available surface area. The shrinkage of the pore opening will decrease the Knudsen diffusivity, and may convert a originally surface reaction controlled process into diffusion limited process. The combination of the surface area decrease and pore openness shrinkage causes the CVI rate decrease at low temperatures.

(15) The CVI weight gain model incorporating overlap volume concept fits well with the experimental data, but the assumption this model is based on is oversimplified.

The fourth task of this investigation was to provide guidelines for optimizing the CVI process. The results are also represented in the above conclusions.

(16) The optimum CVI condition for the preform used in this study seems to be a temperature around 1050 °C, and a pressure of 15 torr.

(17) By imposing a temperature profile, similar densification effects may be obtained in reduced processing time.

CHAPTER 7

RECOMMENDATIONS

The following work should be conducted to further study the CVI process:

(1)   To continue the experimental study of CVI incorporating more variables, such as gas composition, flow rate, and preform geometry.

(2)   To continue the kinetic and modeling study with the ultimate goal of optimizing the CVI processing.

(3)   To study the chemistry of the system by full utilization of residual gas analyzer.

(4)   To conduct mechanical testing on densified specimens.

REFERENCES

1. E. Fitzer, in Proc. 3rd Annual Materials Technology Center Conf., M. H. Genisio, Ed., Southern Illinois University at Carbondale, 1986, pp.4-117.

2. J. Buckley, Am. Ceram. Soc. Bull., Vcl. 67, 2, 1988, pp. 364-68.

3. J. B. Donnet and R. C. Bansal, Carbon Fibers, 2nd ed., Marcel Dekker, inc., 1989, pp. 1-82.

4. R. J. Diefendorf, Engineered Materials Handbook, Vol. 1, ASM International, 1987, pp. 911-914.

5. Awasthi and J. L. Wood, Ceram. Eng. Sci. Proc., 9[7-8], 1988, pp. 553-560.

6. W.J. Lackey, in ENCYCLOPEDIA OF COMPOSITES, VCH Publishers. New York, 1990, pp. 318-332.

7. W. V. Kotlensky, in P. L. Walker, Jr., and A. Thrower, Ed., Chemistry and Physics of Carbon, Vol. 9, Decker, 1972, pp. 173-262.

8. R. Currier, J. of Am. Ceram. Soc., Vol. 73, 8, 1990, pp. 2274-2280.

9. N. Tai and T. Chou, J. of Am. Ceram. Soc., Vol. 72, 3, 1989, pp. 414-420.

10. G. Chung and B McCoy, J. Am. Ceram. Soc., Vol. 74, 4, 1991, pp. 746-51.

11. S. Middleman, J. Mater. Res., Vol. 4, 6[11-12], 1989, pp. 1515-24.

12. T. Starr, Ceram. Eng. Sci. Proc., Vol. 8, 7-8, 1987, pp. 951-957.

13. S. M. Gupte and J. A. Tsamopoulos, J. Electrochem. Soc., Vol. 137, 5, 1990, pp. 1626-38.

14. S. M. Gupte and J. A. Tsamopoulos, J. Electrochem. Soc., Vol. 137, 11, 1990, pp. 3675-82.

15. D. P. Stinton, et al., Am. Ceram. Soc. Bull., Vol. 67, 2, 1988, pp.350-355.

16. D. P. Stinton, et al., Am. Ceram. Soc. Bull., Vol. 65, 2, 1986, pp. 347-50.

17. J. Minet et. al., Comp. Sci. & Tech., Vol.37, 1990, pp. 79-107.

18. A. J. Caputo and W. J. Lackey, Ceram. Eng. Sci. Proc., 5[7-8], 1984, pp. 654-667.

19. Private communications with Dr. W. J. Lacky, Georgia Institue of Technology, Atlanta, Georgia, June, 1991.

20. K. Spear, Proc. 9th Int. Conf. on CVD, Electrochem. Soc. Inc, 1984, pp. 81-111.

21. K. Sugiyama and Y. Ohzawa, J. Materials Science, Vol. 25, 1990, pp. 4511-17.

22. K. Sugiyama, J. Materials Science, Vol. 24, 1989, pp. 3756-62.

23. R. L. Bickerdike et. al., Proceedings of 5th Conf. on Carbon, Vol. 1, Pergamon Press, New York, 1962, pp.575.

24. P. A. Tesner, in A. Thrower Ed., Chemistry and Physics of Carbon, Vol. 19, Decker, pp. 65-161. (USSR)

25. W. P. Hoffman et. al., Carbon, Vol. 23, 2, 1985, pp. 151-161.

26. W. P. Hoffman et. al., Carbon, Vol. 26, 4, 1988, pp. 485-499.

27. S. Marinkovic and S. Dimitrijevic, Carbon, Vol. 23, 6, 1985, pp. 691-699.

28. J. L. Kaae, Carbon, Vol. 23, 6, 1985, pp. 665-673.

29. S. M. Oh and Jai-Young Lee, Carbon, Vol. 24, 4, 1986, pp. 411-415.

30. P. McAllister et. al., Carbon, Vol. 28, 4, 1990, pp. 579-588.

31. I. M. K. Ismail et. al., Carbon, Vol. 29, 4/5, 1991, pp. 575-580.

32. A. Lachter et al, Carbon, Vol. 23, 1, 1985, pp. 111-116.

33. J. C. Bokros, in P. L. Walker Jr. Ed., Chemistry and Physics of Carbon, Vol. 5, Dekker, New York, 1969, pp. 1-118.

34. P. Lucas and A. Marchand, Carbon, Vol. 28, 1, 1990, pp. 207-219.

35. S. Marinkovic, Carbon, Vol. 29, 4/5, 1991, pp. 605-611.

36. A. L. Hines and R. N. Maddox, Mass Transfer - Fundamentals and Applications, Prentice-Hall, Inc, 1985.

37. P. McAllister and E. E. Wolf, Carbon, Vol. 29, 3, 1991, pp. 387-96.

38. S. M. Gupte and J. A. Tsamopoulos, J. Electrochem. Soc., Vol. 136, 1989, pp. 555.

39. J. Y. Rossignol, F. Langlais, and R. Naslain, Proc. 7th Int. Conf. on CVD, Electrochem. Soc. Inc, 1979, pp. 597-614.

40. J. Don, et. al., Proc. of 6th Materials Technology Center Annual Conference, M. H. Genisio, Ed., Southern Illinois University at Carbondale, 1990, pp. 146.

41. J. Don, et. al., Proc. of 7th Materials Technology Center Annual Conference, M. H. Genisio, Ed., Southern Illinois University at Carbondale, 1991, in printing.

42. E. Tatarzycki, ABS Report-4538216:#3, 10, 1990.

43. C. Ju, et. al., Proc. of 6th Materials Technology Center Annual Conference, M. H. Genisio, Ed., Southern Illinois University at Carbondale, 1990, pp. 71-76.

44. C. Wagner, Z. Phys. Chem., Vol. 64, 1969, pp. 69

45. C. Satterfield, Mass Transfer in Heterogeneous Catalysis, M.I.T. Press. Cambridge, 1957.

**OXIDATION PROTECTION SYSTEMS FOR CARBON-CARBON COMPOSITES
FORMED BY CHEMICAL VAPOR DEPOSITION AND
PLASMA ASSISTED CHEMICAL VAPOR DEPOSITION TECHNIQUES**

Section 2:

Oxidation Protection of Carbon-Carbon Composites
Using Pack Cementation

By

Jean L. Stojak

A thesis submitted in partial fulfillment of
the requirements for the degree of
Master of Science

ABSTRACT

Carbon fiber reinforced carbon matrix composites, otherwise known as carbon-carbon (C-C) composites, are structural materials that meet the heavy demands of many of today's high-tech design needs. C-C composites offer high strength, excellent strength retention at high temperatures, good resistance to thermal shock, chemical inertness, and a high heat of ablation. Unfortunately, C-C composites undergo severe oxidation at high temperatures in an oxidizing environment.

In an effort to protect carbon-carbon composites from oxidation, various coating systems are deposited onto the surface of the composite. However, these coatings tend to crack and spall off the surface of the C-C composite due to the mismatch in the coefficient of thermal expansion between the coating and the substrate.

Spalling of the surface coating can be eliminated by *converting the surface* of the substrate to a protective layer, instead of *depositing* the coating *onto the surface* of the substrate. This can be done using a technique called pack cementation.

This thesis investigates the effectiveness of pack cementation for the oxidation protection of carbon-carbon composites using refractory carbide conversion systems. The carbide conversion systems consist of combinations of boron carbide, silicon carbide and zirconium carbide.

TABLE OF CONTENTS

Page Number

LIST OF TABLES

LIST OF FIGURES

v

INTRODUCTION

Carbon materials reinforced with carbon fibers, otherwise known as carbon-carbon (C-C) composites, offer many advantages over traditional materials. Primarily, their high strength-to-weight ratio, and their high strength at high temperatures make C-C composites extremely attractive high temperature, structural materials. As shown in Figure 1, C-C composites surpass the superalloys and ceramic composites in strength-to-weight ratio at low temperatures.

While the strength of the superalloys and ceramic composites decreases with increasing temperature, C-C composites maintain and slightly increase in strength at temperatures well above the maximum usage temperatures of other materials. The fact that C-C composites are able to maintain room temperature strengths at temperatures above $2225^{\circ}C$[1], in addition to its lightweight, has far reaching applications, especially for the aircraft and aerospace industries. Unfortunately, before their full potential can be tapped, a major limitation must be overcome. C-C composites undergo severe oxidation when exposed to an oxidizing environment at temperatures above $370^{\circ}C$.[2]

In an effort to protect C-C composites from oxidation, various coating systems[1-14], which usually consist of one or more ceramic components, are deposited onto the surface of the composite, using one of several deposition techniques. Each of the deposition techniques has its advantages and
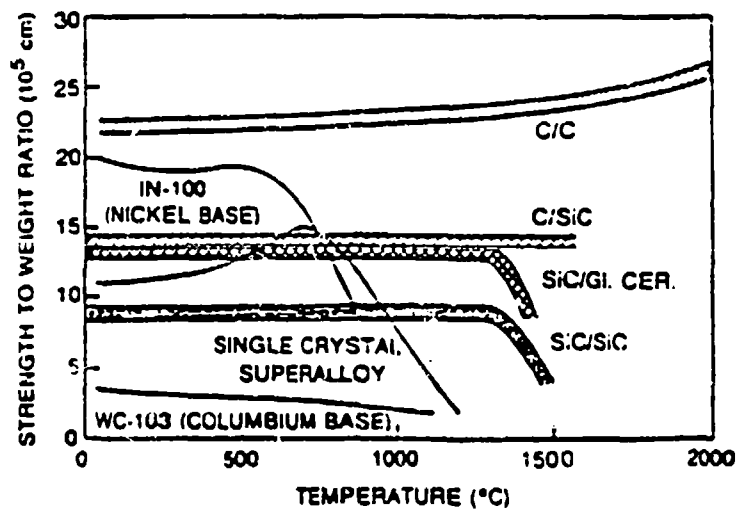
Figure 1. Comparison of strength to weight ratios as a function of temperature.[15]

limitations. The most common technique used to deposit protective coatings is chemical vapor deposition (CVD).

CVD is generally defined as "a chemical process which takes place in the vapor phase very near the substrate or on the substrate, so that a desired reaction product is deposited onto the substrate."[15] CVD techniques provide the ability to control the density, thickness, orientation, and composition of the deposit. These characteristics, added to the fact that a wide range of species can be deposited uniformly over large complex shapes, make CVD coatings attractive for the oxidation protection of C-C composites. Some of these characteristics may be enhanced by using modifications of the basic CVD system such as isothermal, pulse, thermal and pressure gradient.[16-18]

Protective coatings, which are deposited using one of the CVD techniques, have a tendency to crack and spall off the surface of the composite, due to the mismatch in the coefficient of thermal expansion between the coating and the substrate. Pack cementation is another technique used for the oxidation protection of C-C composites. It has the advantage over deposition techniques in that it converts a thin exterior layer of the composite into a protective coating, which does not spall off.

The purpose of this study is to investigate the oxidation protection of C-C composites, from 800 to 1800°C, using the pack cementation technique to obtain conversion coatings consisting of: (1) SiC, (2) SiC with B_4C, and (3)

SiC with ZrC. Included in this study are the following:

1. analysis of the microstructure of the base composite,

2. determination of the pack compositions* which will convert the exterior of the carbon substrate to silicon carbide (SiC) with boron carbide (B_4C) and SiC with zirconium carbide (ZrC),

3. determination of possible conversion mechanisms involved in the pack cementation process of the above conversion coatings,

4. determination of any difference in using the alpha or beta phase of SiC in the starting pack composition,

5. determination of the effect of alumina, in the starting pack composition, on the resultant conversion coatings and oxidation resistance.

---

* The SiC coating was obtained using a previously determined[11] pack composition of 60% SiC, 30% Si, and 10% Al_2O_3, by weight.

LITERATURE REVIEW

1.0 Oxidation Protection

Oxidation protection for C-C composites has become quite complicated. The reason for this is that there is no single coating that can provide reliable protection for the entire useful temperature range of C-C composites. As a result, multi-layer coating systems have been developed in an effort to provide adequate protection.[1-2,7-9]

Strife and Sheehan[2] have given a good overview of a general solution to this complex problem, as shown in Figure 2 and Figure 3. Above 370°C, C-C composites are susceptible to oxidation. Between the oxidation threshold and approximately 600°C, oxidation inhibitors have been dispersed in the matrix of the composite. These inhibitors protect the composite by acting as oxygen getters; tying up the oxygen so it won't degrade the composite. When and if these low temperature inhibitors are used, it is generally for temporary protection as the composite passes through the low end of the temperature scale, upon heating to the application temperature.

Matrix inhibitors are unable to protect the composite much above 600°C. Above this temperature, oxidation protection comes in the form of sealants. Sealants are typically ceramics which form a glass when oxidized at intermediate temperatures[5,13-14]. The glass is able to flow and seal the cracks of the outer high temperature coating,
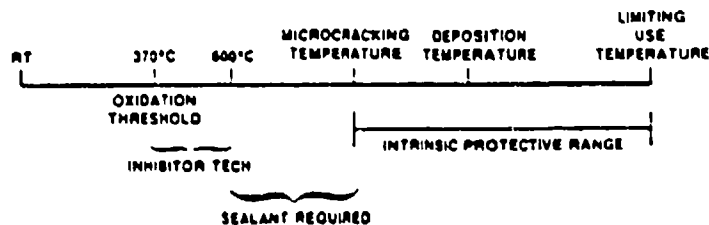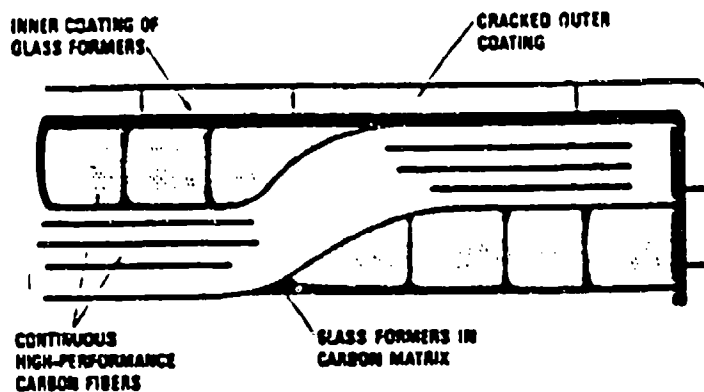
Figure 2. Oxidation protection at various temperatures.[9]

Figure 3. A schematic of an oxidation protection system as applied to a carbon-carbon composite.[9]

until the composite reaches the temperature range wherein the high temperature coating is able to form a glass and seal its own defects. Cracks in the coating originate during cooling from the coating deposition temperature, due to the thermal expansion mismatch between the coatings and the carbon composite. Sealants are generally used for temporary protection as the composite passes through the medium temperature range to reach the higher application temperatures.

Unfortunately, ceramics forming a glass at intermediate temperatures can not be used alone to protect the carbon substrate from oxidation, due to their volatility and oxygen permeability at high temperatures[19]. A high temperature coating, which is stable at the application temperature, is necessary to provide an effective barrier to oxidation. As the composite reaches the high temperature range, the high temperature coating oxidizes, forming a flowing glass oxide, which seals the cracks in the coating.

The above combination of coatings provide a general approach to the oxidation protection of C-C composites. This coating system is able to protect the carbon substrate from oxidation at temperatures below which the high temperature coatings are effective. They can also protect the carbon substrate from possible reaction with the carbide coating.

It is necessary to define the application of the composite before an effective, coating system can be

designed. Included in the application definition should be a description of the environment to which tne composite will be subjected; primarily, the temperature(s), pressure, flow conditions and contact gas compositions.

These applications can be broken down into two main categories: limited life applications (generally at very high temperatures) and extended life applications (generally at lower temperatures). Limited life applications (life expectancy of minutes to hours) have several inherent problems: thermal, flow erosion, coating spallation, and inherent protection capability. Extended life applications (life expectancy of weeks/years) also have difficulties with coating spallation, in addition to cracks in the coating, mechanical and chemical degradation and oxygen ingress over time.[7]

Spalling of the surface coating can be eliminated by converting the surface of the substrate to a refractory carbide instead of depositing the coating on the surface of the substrate. This can be done using the pack cementation technique[11-12] to convert an outer layer of the composite into a protective coating, as described below.

2.0 Pack Cementation

Pack cementation, sometimes refered to as conversion coating, diffusion coating, or vapor phase conversion, is a process by which the substrate is packed in a powder mixture

that reacts with the substrate, upon heating, to form a desired conversion layer.

The basic concept of this process was developed in the late 1950's and early 1960's, for the formation of alloy coatings by pack chromizing or siliconizing. In this process, iron or steel was placed in a container with chromium or silicon powder, an inert filler material, such as alumina, and a halogen-bearing material which reacted with the chromium or silicon powder to form volatile chromium or silicon compounds at elevated temperatures.[20]

The volatile compounds transported the silicon or chromium to the surface of the part where it then diffused into the part, and formed an alloy casing over the surface. These alloy coatings were used to protect jet engine turbine blades from oxidation.[20] These type of diffusion treatments are also used with carbon and nitrogen for carburizing or nitriding metals.[21]

For the oxidation protection of C-C composites, using the pack cementation technique, the composites are uniformly packed with ceramic powders into a graphite retort or crucible. The packed crucible is heated to a temperature where the desired species will be vapor transported to the surface of the composite. Although it is possible for the reactants to diffuse into the substrate to form a solid solution, it is prefered that the vapor species react with the carbon substrate; converting the surface to an oxidation protective ceramic coating.[11-12]

Rogers, et al.[12] studied the oxidation protection of C-C composites using the pack cementation technique, in conjunction with a slurry pack cementation technique. The slurry technique requires the pack powders to be mixed with isopropyl alcohol in proportions resulting in a slurry having a consistency that provides a smooth uniform coat when applied to the C-C composite.

Of the conversion compositions studied by Rogers, et al.[12] the best oxidation protection was obtained using a silicon based system and a Zr-B-Si system. The Si system in their study[12] was obtained using an initial slurry composition of 40% Si, 40% SiC, and 20% Al_2O_3 by weight, in isopropyl alcohol. The slurry pack process was followed by a standard pack cementation process using a powder mixture consisting of 30% Si and 70% SiC. The Zr-B-Si system used in their study[12] was obtained using an initial pack cementation process with 100% B powder at 3400°F (1871°C) for 2.5 hours, followed by a slurry coating consisting of 75% silicon and 25% zirconium in isopropyl alcohol. The substrate was then pack cemented in 100% silicon carbide at 3000°F (1648°C) for 4 hours. In the study by Rogers, et al.[12] it was determined that pack cemented materials provide better oxidation protection, at higher temperatures, than materials containing only inhibitors in the matrix.

Other oxidation protective coatings obtained using the pack cementation technique have also been patented[22-23]. Shuford[22] patented oxidation protective coatings using a

pack powder composition consisting of between 25-40% of silicon, 50-70% of silicon carbide, 1-15% of boron, and a minor amount of magnesium oxide to facilitate coating formation. He[23] also patented protective coatings which use the slurry pack cementation technique with an alkali silicate slurry applied over a substrate that has been powder pack cemented to form a silicon carbide coating. Unfortunately, no literature is available on the capabilities of the resultant coatings.

2.1 Conversion Mechanisms

Rogers, et al.[11] investigated the conversion mechanisms involved in a high temperature pack cementation process, which formed a hard silicon carbide conversion layer on the exterior surfaces of C-C composites. The process is used a pack powder mixture which consisted of 60% silicon carbide, 30% silicon, and 10% alumina. The researchers[12] dried the packed retorts at 400°F (204°C) for 16 hours before firing to 3100°F (1704°C) for 2 hours and 45 minutes.   Rogers, et al,[11] did not discuss the composition of the conversion layer in detail. However, they did mention that the converted layer thickness was a nominal 0.025 inch (635um) and that the silicon carbide fraction of the conversion layer was primarily the beta phase with only a slight amount of the alpha phase.

Rogers[11] also determined that the pack powders sinter during the cementation process, causing the pack to shrink

around the composite, maintaining intimate contact between
the two. This intimate contact was found to promote mass
transport of reactive pack materials into the C-C composite.
A large portion of the conversion layer is believed to be
formed from a gas phase reaction, based on visual evidence
of modular silicon carbide crystalline shapes.[11]

3.0 Protective Coatings

There are several coating compositions that can be used
in the general protective coating system, described above.
The limitations characteristic of each of the coatings
prevent each, in itself, from providing adequate oxidation
protection over the entire useful temperature range of the
C-C composite. However, the limitations of one coating may
be overcome with the capabilities of another coating or
combination of coatings. Previous work and information on
each of the coating constituents used in this study is
provided below. Table 1 lists some of the properties of the
coating constituents, and a comparison of the coefficients
of thermal expansion and the vapor pressures of these
coatings and their constituents is given in Figures 4 and 5,
respectively.

3.1 BORON

Elemental boron and boron containing compounds have
been used sucessfully to inhibit oxidation.[24-39] Lawerence,
et al.[24] patented the earliest use of a boron compound for

TABLF 1.

SELECTED PROPERTIES OF COATING COMPONENTS

CONSTITUENT	ATOMIC #	MELTING POINT, ^{O}C	DENSITY, g/cc
Si	14	1410	2.330
SiC		2700	
SiO_2		1723	
Zr	40	1852	6.506
ZrC		3540	
ZrO_2		2715	
ZrB_2		3000	
B	5	2079	2.340
B_4C		2350	
B_2O_3		450	
Al	13	660	2.699
Al_4C_3		2100	
Al_2O_3		2072	

COMPARISON OF THERMAL EXPANSION

TEMPERATURE (CELSIUS)
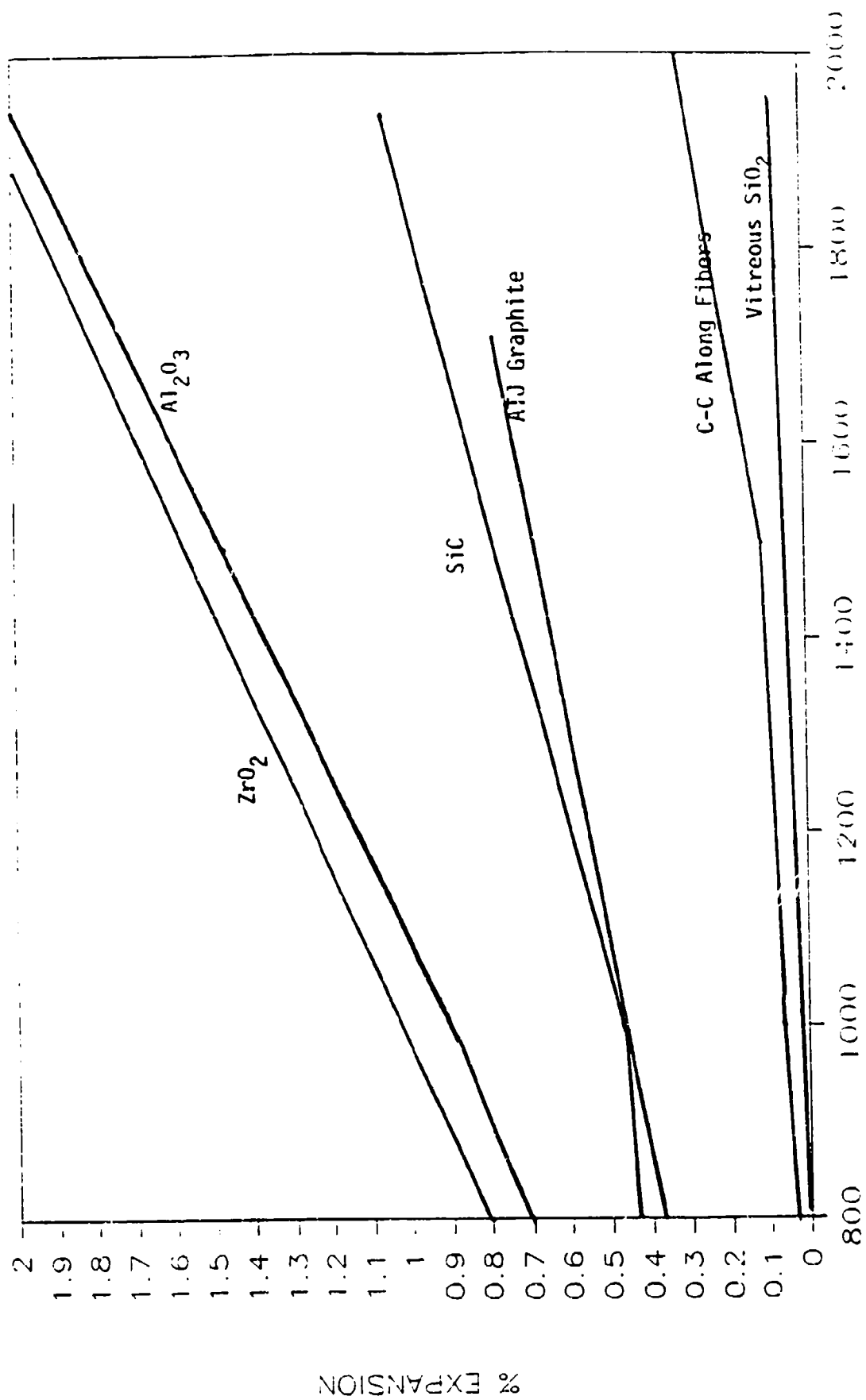
Figure 4. Comparison of CTE Values.

Figure 5. COMPARISON OF VAPOR PRESSURES OF SELECT GASES.

the oxidation inhibition of hydrocarbons in 1955. Woods et al.[25] give an overview on the use of boron compounds as oxidation stabilizers or antioxidants for various materials. It wasn't until the late 1970's, that boron containing compounds were seriously being used as an oxidation inhibitor for C-C materials.

Boron and boron carbide[5,13-14,27-39] form B_2O_3 glass when oxidized at intermediate temperatures. This glass acts as a sealant in the general oxidation protection system discussed above. It is able to flow across the surface of the C-C composite; sealing cracks in the higher temperature coatings that would otherwise lead to severe oxidation of the substrate.

McKee, et al.[33] found that above 450°C (the melting point of boron oxide), a glassy residue is formed which blocks the active sites on the carbon surface; protecting it from oxidation. McKee[33,37-38] and others[27-32,34-36] have found that compounds which form B_2O_3 when oxidized at intermediate temperatures, provide suitable protection from oxidation at temperatures up to 1000°C, for short term applications, and 600-800°C for long term applications.

Above 1000°C, the vapor pressure of B_2O_3 increases to the point where the glass volatizes, disrupting its surface and leaving the composite vulnerable to attack, see Figure 5. This is the reason sealants are used in conjunction with high temperature coatings, if the composite will be used at temperatures much above 800°C. In addition to its oxidation

protection, B_2O_3 increases the adherence of the higher temperature coatings and also protects the composite from possible reactions with high temperature coatings, such as SiC.

When B_2O_3 is used in conjunction with SiC, at temperatures above 1000°C, the volatilizing B_2O_3 may react with the silica glass, which forms when SiC is oxidized, as previously discussed, to form a borosilicate glass.[35] Borosilicate glass has a lower vapor pressure than B_2O_3 and a lower viscosity than SiO_2, which enables it to flow and seal cracks in the coating; thereby preventing the oxidation of the composite. The combination of B_2O_3 and SiC has been determined[39] to be a great improvement over coatings containing only silicon carbide for the oxidation protection of C-C composites used in a cyclic temperature environment.

Unfortunately, a major limitation to the use of B_2O_3 as a sealant is its reactivity with moisture; forming a hydrated species. The hydrated species have much higher vapor pressures than B_2O_3 and volatize at a faster rate. Thomas and Roscoe[40] found the reaction of B_2O_3 with moisture to have a catalytic effect on oxidation. McKee[33] later determined that although the oxidation protection of B_2O_3 decreases due to reactivity with moisture, it still inhibits the oxidation rate of C-C composites by a factor of about five. It is possible that McKee's findings are, in part, due to the use of a thicker coating of B_2O_3 than was used by Thomas and Roscoe[41]. The thicker coating provides more

oxide to react with the moisture, prolonging the oxidation protection of the substrate.[38]

3.2 Silicon Carbide

Because of its low oxygen diffusion[19] and thermal stability, silicon carbide has been used for oxidation protection in the temperature range between 1200-1700°C[2,7-13]. When deposited on the surface of the composite using CVD techniques, the source gas is usually silane or methyltrichlorosilane.[8] Pack cementation[11-12] has also been used to convert an outer layer of the composite to SiC, as discussed above. The SiC coating and conversion layer crack when cooled from the deposition/conversion temperatures, due to the mismatch in coefficent of thermal expansion between SiC and the ca.:on substrate, see Figure 4.

SiC does not start to oxidize significantly until temperatures around 900°C. SiC will oxidize and begin to form a protective silica film above 950°C; provided there is a plentiful supply of oxygen.[41] Above 1000°C, the silica glass is able to flow and seal surface cracks and defects. If there is excess Si in the SiC coating, it will begin to flow around 1425°C, filling any cracks or pits in the SiC coating. Elemental silicon will oxidize to form a protective silica film more readily than silicon carbide, especially at or above its melting temperature.[34] However, below 1000°C, it is necessary to use an intermediate

temperature sealant to provide adequate protection until temperatures are high enough to allow the silica glass to flow and seal the SiC coating.

Unfortunately, at temperatures above 1700°C, the vapor pressure of SiC becomes prohibitive; disrupting the protective oxide film, see Figure 5. It has been determined that a dual coating of SiC, in conjunction with a refractory carbide that has low vapor pressures, such as Hf or ZrC, reduces the overall vapor pressure of the coating and offers oxidation protection up to temperatures around 2000°C.[42]

SiC has another limitation when deposited directly onto the carbon substrate. At 1400°C, excessively high vapor pressure, primarily due to CO formation, as well as SiO, SiO_2, and CO_2 [5], disrupt the protective SiC coating. These gases result from the oxidation of the SiC coating and from the reaction between SiC and the carbon substrate.[19] Since ZrC does not react readily with carbon, it could be used as a separation layer between SiC and the substrate, to prevent this disruptive reaction.[2]

3.3 Zirconium Carbide

Zirconium carbide has been used primarily for high temperature oxidation protection. Chown, et al.[10] reported using conversion layers of ZrC to protect C-C for short periods of time up to 2200°C.

Although ZrC is attractive for oxidation protection because of its low carbon diffusivity and non-reactivity

with carbon,[2] it begins to oxidize at a dull red heat,[43] around 600°C, and forms zirconia (ZrO_2). Unfortunately, ZrO_2 doesn't melt until 2715°C. As a result, it is not able to flow and form a protective seal around the composite until it reaches the higher temperature regime. Additionally, ZrO_2 has a high oxygen permeability[2] at higher temperatures.

As mentioned above ZrC can be used as a barrier to prevent any reaction between the carbon substrate and its protective coatings, such as SiC. It has been used successfully with SiC to improve the oxidation resistance of SiC coatings above 1700°C[7], by forming zirconium silicide and zirconium silicate, which have lower vapor pressures than SiC and SiO_2.

EXPERIMENTAL PROCEDURES

1.0 The Substrate

Two carbon-carbon composite panels, provided by BP Chemicals Hitco Corporation, were used as the substrate material for the pack cementation process. The composite materials consisted of twelve layers of polyacrylnitrile (PAN) fibers, which had been woven into a cloth. Six of the layers, also called plies, were positioned warp face down with a 0, 90, 0, 90, 0, 90 degree orientation. The other six plies were positioned warp face up with a 90, 0, 90, 0, 90, 0 degree orientation.

The cloth lay-up was impregnated with a resin, containing boron particles as an oxidation inhibitor and carbon black particles as matrix "fillers". The C-C composite panels were then processed as follows:

- molded in autoclave
- carbonized
- pyrolization A
- pyrolization B
- chemical vapor deposition 1
- surface sanding
- chemical vapor deposition 2

The final densities of the two composite panels were reported by Hitco to be 1.704 and 1.715 grams/cubic centimeter.

1.1 Optical Reflective Microscopy

A sample of the as-received composite was cut using a low speed cut-off saw with a diamond tip blade. The cut sample was mounted in epoxy and ground to 600 grit, polished to 1um with diamond paste and finished to 0.05um with alumina slurry. The polished sample was analyzed with optical reflective microscopy(ORM).

1.2 Transmission Electron Microscopy (TEM)

Since specimens for TEM must be less than 500 Å thick, the following series of thinning steps were used.

1. A 1 mm thick slice was cut from the specimen using a low speed cut-off saw with a diamond tip saw blade.

2. The thin slice was mounted onto a polishing holder using a thin layer of wax. One side of the specimen was ground to 600 grit and polished on a 0.05um alumina polishing wheel.

3. The slice was removed from the polishing holder and secured, polished side face down, to a base plate using a thin layer of wax.

4. The base plate was positioned and clamped under a low speed drill and a 3 mm diameter disc was cut from the thin slice.

5. This disc was mounted onto a Dimpler sample holder with wax, polished side face down, and flat polished with 15um diamond slurry to an approximate thickness of 100um.

TABLE 2.

INFORMATION ON THE POWDERS USED IN THE PACK PROCESS

POWDER	COLOR	SIZE	% PURITY	SOURCE
Si	grey	< 100um	99.9	Alpha[*]
SiC				
alpha	yellow	1um	99.8	JMAG[**]
beta	grey	1um	99.8	JMAG
Zr	grey	+20 -60mesh	99.9	JMAG
ZrC	grey	3um	- - - -	Alpha
B	brown	-325mesh	92.0	Alpha
Al_2O_3	white	-325mesh	99.9	JMAG

* Alpha Products, P.O Box 8247, Ward Hill, MA 01835-0747

** Johnson Matthey Aesar Group. 892 Lafayette Rd.,
   P.O. Box 1087, Seabrook, NH 03874-1087

3.0 The Pack Cementation Process

The substrate material was cut into specimens, 15mm x 12mm x 6mm, all dimensions ± 1mm. The specimens were ground to 600 grit on all sides, rinsed in water and then rinsed in methanol and dried in a vacuum desiccator. After drying, the specimens were weighed, using a Mettler Balance, to determine the weight before pack cementation.

The powder composition was determined using weight percent of the starting powders and correspondingly weighed, ±2g. The powder mixture was then uniformly mixed by hand under a fume hood, before and during the packing process.

The one inch diameter graphite crucibles were loosely filled with the powder mixture which was then compressed by hand using the packing tool, as shown in Figure 6. This powder base was then compressed using a specimen mount press, to approximately 1273psi. The specimens were centered on the powder base in the crucible and the powder mixture was then carefully packed around the specimen using the same procedure.

The top of the specimen was packed in a similar manner; first compressing the powder mixture by hand until the desired thickness was achieved and then compressing the mixture under a 1000 lb force (1273psi). Finally, a graphite cover, with a small hole in the center to release excessive gas pressures, was cut to size and securely compressed into the crucible opening. The total weight of the packed crucible was measured, from which the specimen
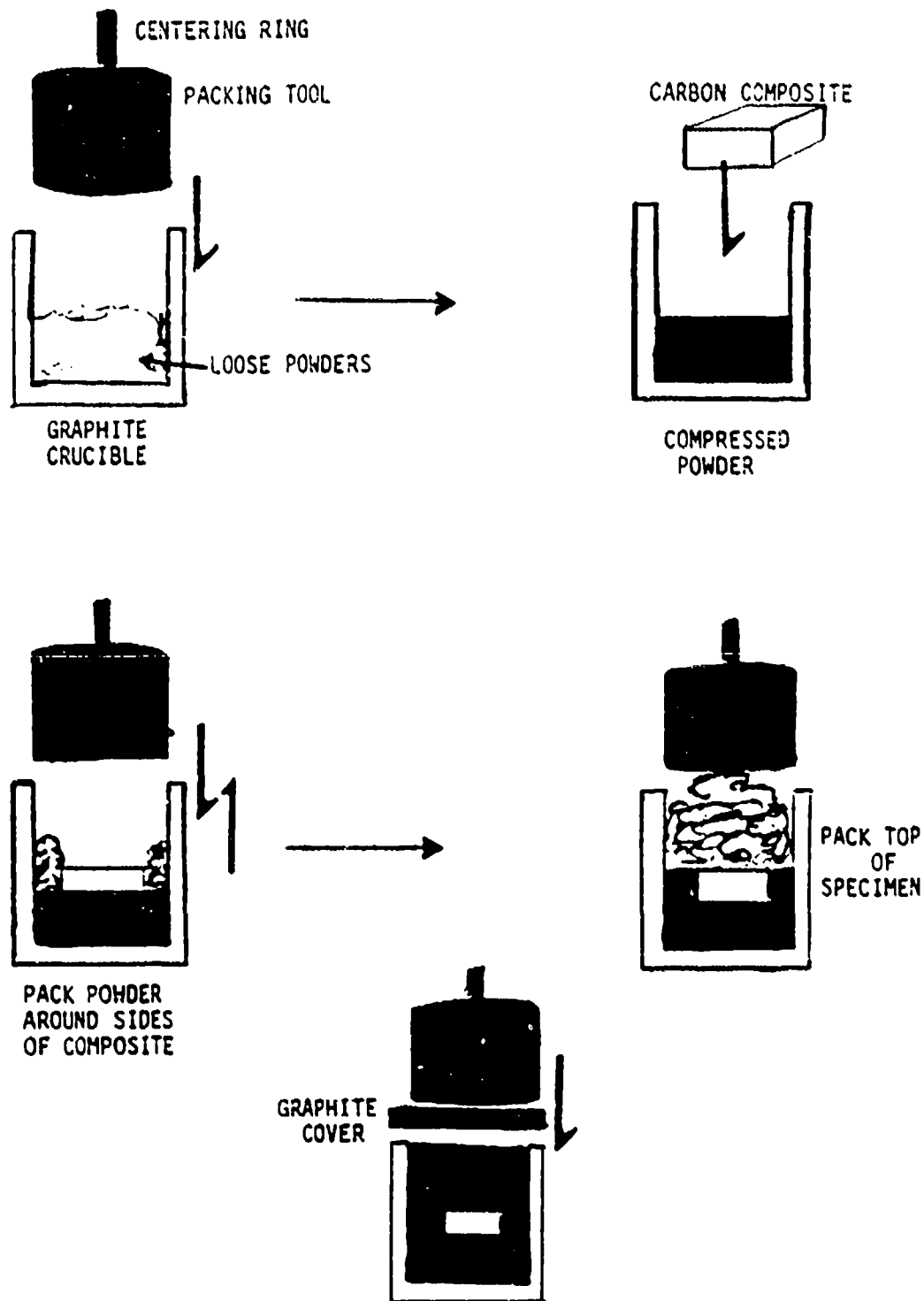
Figure 6. Sample Preparation in Pack Cementation

weight and the weight of the crucible and cover were subtracted to determine the amount of powder in the pack.

The packed crucibles were placed in a Centorr high temperature furnace. The furnace was pumped down to less than 100 millitorr and then purged with Ar to atmospheric pressure. This evacuation process was repeated two additional times. The furnace was then pumped down to a vacuum of less than 100 millitorr and the furnace power was raised to 2 % (approximately 400 ^{0}C). The crucibles were held at this temperature, under vacuum, for at least five hours to evacuate any residual moisture. The crucibles were again weighed to determine percent weight loss due to the low temperature volatiles.

The specimens were placed back into the furnace which was evacuated and purged three times, as previously described. After purging the furnace to a positive pressure of roughly 5psi, it was raised to the desired temperature and held at temperature for a predetermined amount of time. The time and temperature used for the pack cementation process were dependent on the desired thickness of the converted layer and the composition of the powder mixture, respectively. Pack powder mixtures containing ZrC were held at 1900^{0}C for 5 hours. Compositions without ZrC were held at 1700^{0}C for 3 hours.

The temperature was measured, to within ± 10^{0}C, with an optical pyrometer, as shown in Figure 7, and controlled

manually by adjusting the percent power of the furnace. The optical pyrometer was calibrated to 1900°C using a W + Re high temperature exotic thermocouple, under a vacuum environment. During the calibration process, the optical pyrometer was focused on a graphite crucible, as it is during a typical pack cementation process, Figure 8. The calibration curve is given in Appendix B.

After the pack cementation process, the specimens were carefully removed from the crucibles and lightly ground on 600 grit paper to remove any surface agglomerates. They were then rinsed in methanol, dried and weighed.

3.1 The Pack Cementation Coatings

Based on the review given in the previous chapter, an investigative study was initiated to determine the pack powder compositions which would form conversion coatings consisting of $SiC + B_4C$, $SiC + ZrC$. Due to the conflicting results in the literature, on the effect of Al_2O_3 in the pack[11-12,21] the above series of experiments were conducted with and without alumina. The pack compositions used in the initial series of pack cementation experiments are given in Table 3. Based on the results of the initial experiments and a previously reported SiC coating[11], the compositions listed in Table 4 were chosen for this study.

3.2 X-ray Diffraction

After the initial and final series of pack cementation
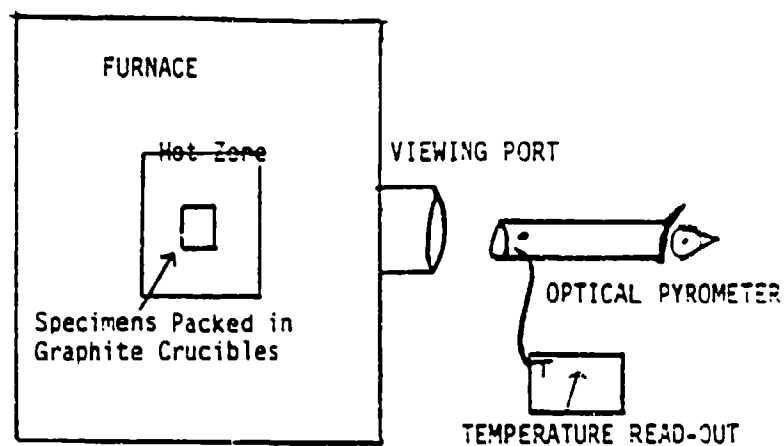
Figure 7. TEMPERATURE MEASUREMENT.
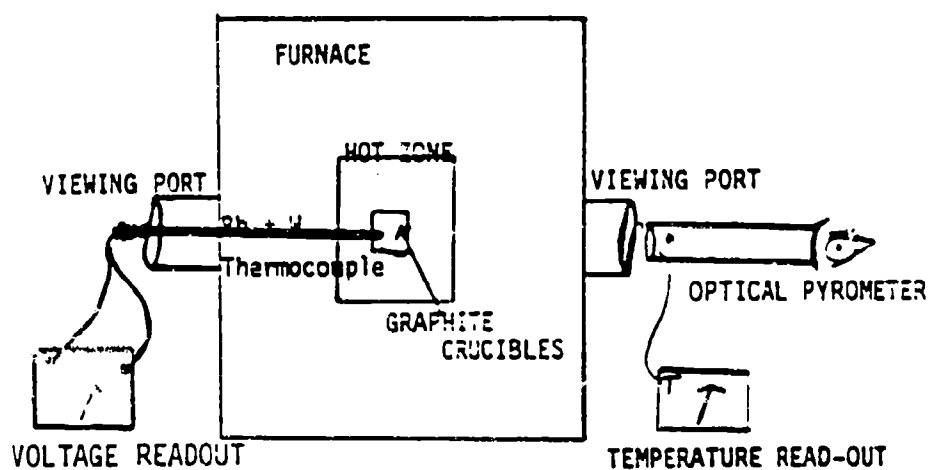
Figure 8. CALIBRATION OF OPTICAL PYROMETER.

TABLE 3.

THE INITIAL SERIES OF PACK CEMENTATION EXPERIMENTS

PACK COMPOSITION (% by weight)	TEMPERATURE (^{0}C)	TIME (Hr)
30 ZrC/30 SiC/40 Zr	1900	5
30 ZrC/30 SiC/30 Zr/10 Al_2O_3	1900	5
30 ZrC/30 SiC/40 Si	1900	5
30 ZrC/30 SiC/30 Si/10 Al_2O_3	1900	5
30 ZrC/30 SiC/40 B	1900	5
30 ZrC/30 SiC/30 B/10 Al_2O_3	1900	5
33 ZrC/33 SiC/11 Zr/11 Si/11 B	1900	5
30 ZrC/30 SiC/10 Zr/10 Si/10 B/10 Al_2O_3	1900	5
30 ZrC/30 SiC/20 Si/20 Zr	1900	5
30 ZrC/30 SiC/20 Si/20 B	1900	5
30 ZrC/30 SiC/20 Zr/20 B	1900	5
20 ZrC/20 SiC/25 Si/25 Zr/10 Al_2O_3	1900	5
60 SiC/20 B/10 Si/10 Al_2O_3	1900	5

Note: The silicon carbide used in the investigative series is the beta phase.

TABLE 4.

THE FINAL SERIES OF PACK CEMENTATION EXPERIMENTS

PACK COMPOSITION (% by weight)	TEMPERATURE (^{0}C)	TIME (Hr)
66 SiC/33 Si	1700	3
60 SiC/30 Si/10 Al_2O_3	1700	3
30 ZrC/30 SiC/40 Si	1900	5
30 ZrC/30 SiC/30 Si/10 Al_2O_3	1900	5
30 ZrC/30 SiC/40 B	1900	5
30 ZrC/30 SiC/30 B/10 Al_2O_3	1900	5

Note: The silicon carbide powder used in the final series is the alpha phase.

experiments, x-ray diffraction was conducted on one sample from each powder mixture. The experiments were conducted using a copper tube and a nickle filter, which resulted in a wavelength of 1.54178 Å. The samples were scanned from 10^0 to 90^0 at a rate of 2^0 per minute. The composition of the conversion layer was determined by calculating the d-spacings from the intensity vs 2θ angle results of the x-ray diffraction experiments. The calculations are discussed in Appendix C.

3.3 Optical Microscopy

One pack cemented sample, obtained from each of the compositions in the final series of pack cementation experiments, was mounted and prepared, as discussed in section 1.1. Optical Microscopy was used to identify the conversion layer.

3.4 Energy Dispersive Analysis by X-Ray (EDAX)

The specimens desribed in the previous section were analyzed using EDAX to identify the composition of each of the two phases present in the conversion layer. The two distinguishable phases were observed using optical microscopy, described in the previous section. The EDAX was a KEVEX 8000 used on an ETEC Autoscan scanning electron microscope. This system was unable to detect elements having an atomic weight lower than 14.

3.5 Conversion Layer Thickness Measurements

The thickness of the conversion layers of the mounted specimens, described in section 3.3, were measured using the optical scale on a microhardness tester. The measured values are ± 2um. Due to the nonuniformity of the conversion layers, the average conversion thickness was determined based on the measurements of a fairly continuous conversion layer. For a schematic example of the conversion thickness measurements, see Figure 9.

4.0 Oxidation Testing

For the oxidation tests, clean, dry specimens were weighed using a Mettler balance. The specimen to be tested was carefully placed in an alumina crucible and suspended from a thermogravimetric analyzer (TGA), which was constructed in-house, and centered inside an induction coil, as shown in Figure 10.

The force transducer in the TGA was connected to an AT compatible computer. The corresponding load needed to balance the sample, crucible, and suspending wire was directly input into a computer program developed in-house.

The initial load on the force transducer was manually adjusted to a value around -1.8. The relative scale range was between -2 and +2. When the sample was heated and it began to oxidize, a weight loss would correspond to less of a load on the force transducer, ie. a more positive scale

thickness of fairly continuous conversion layer

carbon

resin

crack

porosity

Fiber
Bundle
Parallel
to the
surface

Fiber
Bundle
Perpendicular
to surface
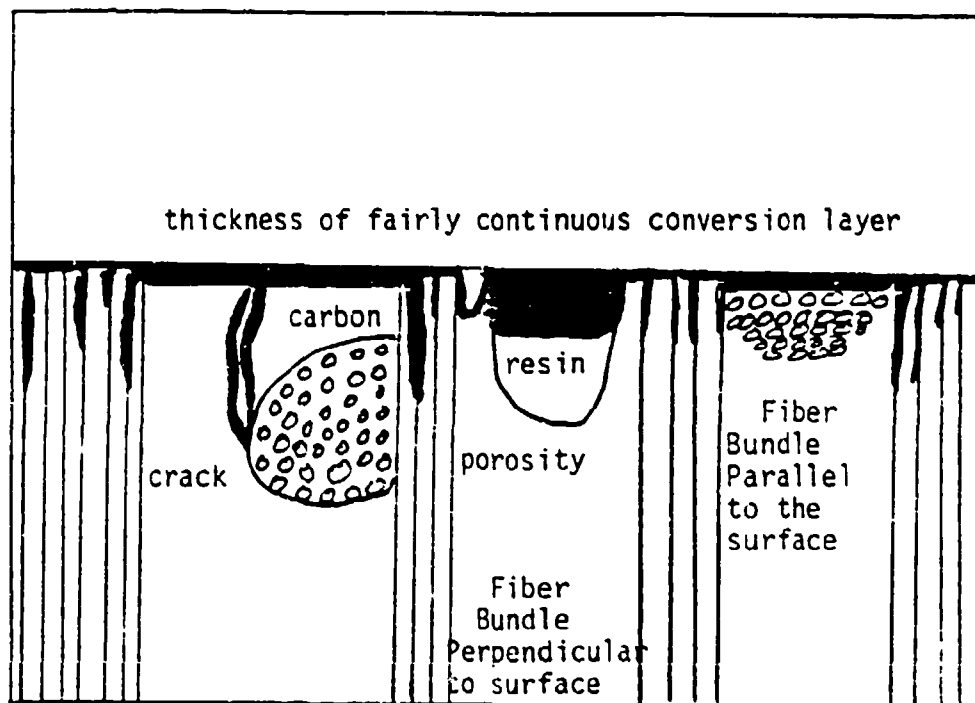
Figure 9.   Schematic of Conversion Layer Measurements.

OXIDATION UNIT WITH REAL TIME
DATA ACQUISITION (NOT TO SCALE)
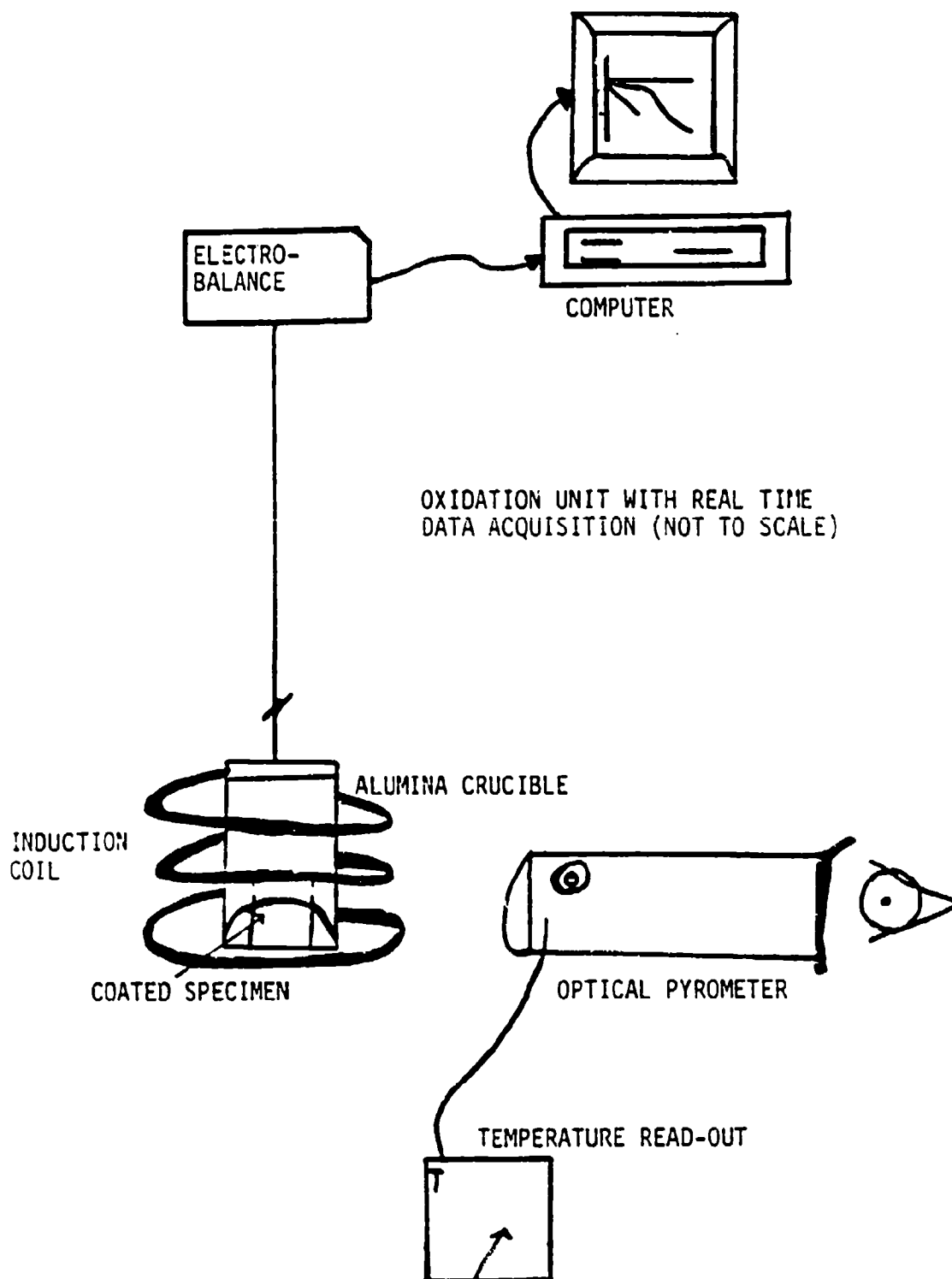
Figure 10.   Oxidation Unit.

value. Correspondingly, a weight gain would lead to a greater load on the force transducer, resulting in a more negative scale value.

The sample was quickly brought to the desired temperature for the oxidation test, using a 20 kilowatt Taylor Winfield induction heating unit, model number CE-2000. The RF field created by inductively heating the sample, altered the relative value of the TGA. Therefore, when the sample was at the desired temperature, as determined with an optical pyrometer, the resulting scale value was recorded as the initial TGA weight.

The samples were inductively heated in air until they had undergone approximately a 5 percent weight loss. The weight loss was 5 percent of the original weight measured with the Mettler balance. This amount was then added (indicating weight loss) to the initial TGA weight described above, to obtain the final allowable tga weight. When the sample reached this final TGA weight the induction field was quickly turned off. The specimen was cooled to room temperature and weighed using the Mettler balance to determine the actual weight loss of the specimen.

4.1 Scanning Electron Microscopy (SEM)

After the oxidation tests, the specimens were mounted onto SEM specimen stubs with carbon black paint, then sputter coated with palladium-gold. A Hitachi S-570

Scanning electron microscope was used to obtain the photomicrographs for the secondary electron images.
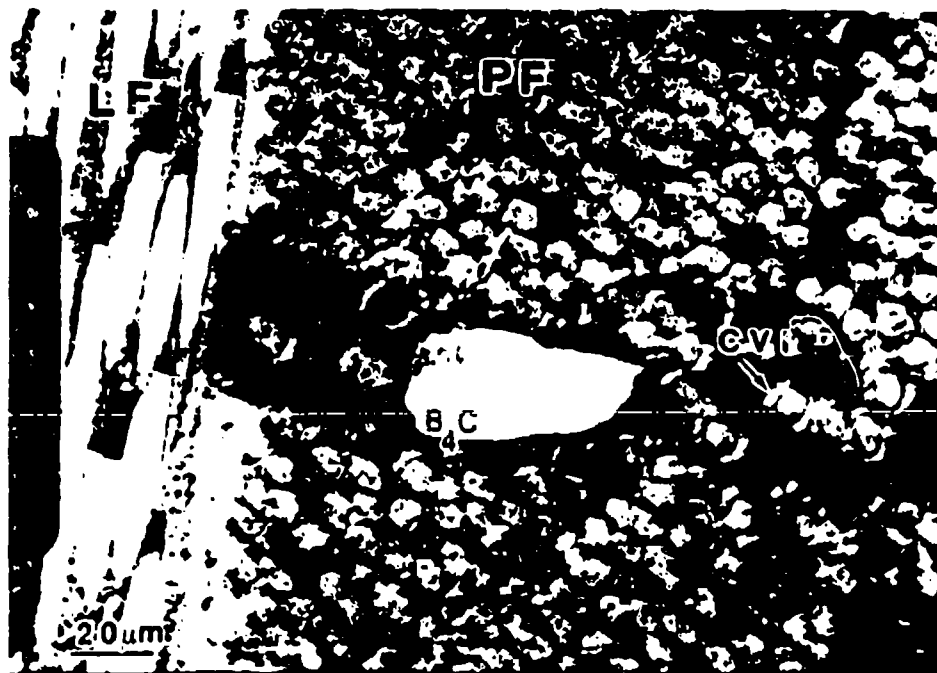
Figure 13. Optical micrograph of the as received composite,
showing a large boron carbide agglomerate.
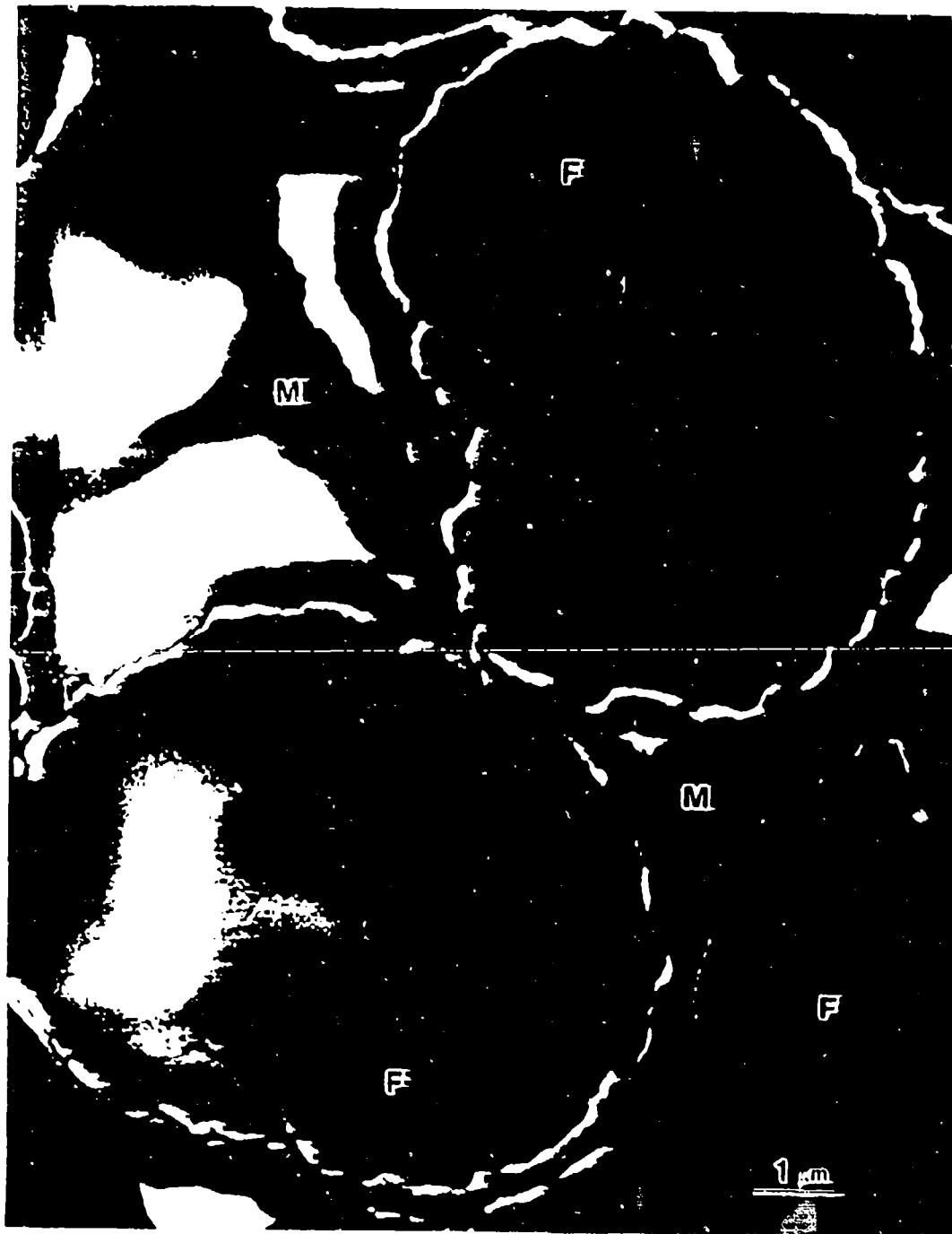
Figure 14. Transmission electron micrograph of the end-on
orientation of the fibers surrounded by matrix material.
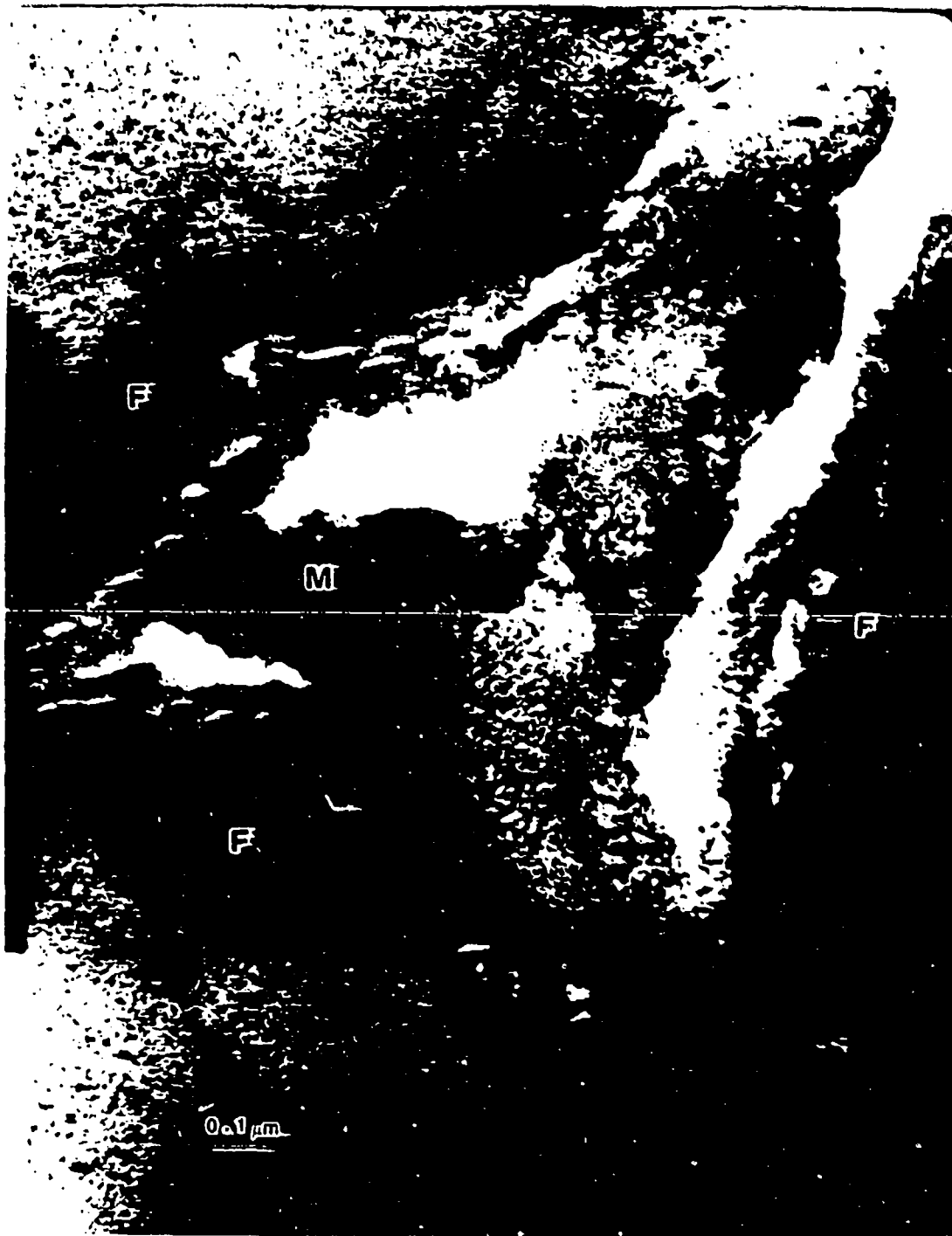
Figure 15. TEM of the carbon structure in the fibers, the fibers and matrix are identified as F and M, respectively.

A TEM micrograph showing a higher magnification of the inhibitor and the matrix is shown in Figure 16. An electron diffraction pattern of the inhibitor particles in the matrix, identifying them as B_4C, is also shown in Figure 16. For theory and sample calculations of the identifying d-spacings (plane spacings), the reader is referred to Appendix A.

2.0 The Pack Cemented Coatings

Based on the results of the initial pack compositions listed in Table 5, the following mixtures were chosen: 30 ZrC + 30 SiC + 40 Si, 30 ZrC + 30 SiC + 30 Si + 10 Al_2O_3, 30 ZrC + 30 SiC + 40 B, 30 ZrC + 30 SiC + 30 B + 10 Al_2O_3, in addition to the SiC pack composition used by Rogers, et al.[11] (60 SiC+30 Si+10 Al_2O_3) and a SiC pack composition without Al_2O_3 (66.67 SiC+33.33 Si). A final series of pack cementation experiments was conducted using the chosen pack compositions.

In the final series of experiments, alpha SiC was used in the pack composition, as opposed to the beta form used in the initial series. This was done to determine whether or not the phase of the SiC used in the starting pack composition has an effect on the conversion layer composition or quality. The resulting conversion layer compositions of the final series are listed in Table 6. When the results in Table 6 are compared to the initial

Figure 16. TEM diffraction pattern of the B_4C particle identified in the TEM micrograph. Carbon black particles are identified as CB.

TABLE 5.

X-RAY DIFFRACTION RESULTS OF THE INITIAL SERIES

PACK COMPOSITION (% by weight)	CONVERSION LAYER COMPOSITION*
30 ZrC/30 SiC/40 Zr	$\underline{SiC}$+ZrC+ZrSi$_2$**
30 ZrC/30 SiC/30 Zr/10 Al$_2$O$_3$	$\underline{SiC}$+ZrC+ SiC+ ZrSi$_2$+Al mixture
30 ZrC/30 SiC/40 Si	$\underline{SiC}$+ZrC
30 ZrC/30 SiC/30 Si/10 Al$_2$O$_3$	$\underline{SiC}$+Al mixtu· ZrSi$_2$+ . ,**
30 ZrC/30 SiC/40 B	$\underline{SiC}$+B$_4$C
·· ZrC/30 SiC/30 B/10 Al$_2$O$_3$	$\underline{B_4C}$+ $\underline{SiC}$+ZrB$_2$+ Al mix**+SiC**
33 ZrC/33 SiC/11 Zr/11 Si/11 B	$\underline{C}$+ SiC
30 ZrC/30 SiC/10 Zr/10 Si/10 B/10 Al$_2$O$_3$	$\underline{C}$+B$_4$C+Al mix
30 ZrC/30 SiC/20 Si/20 Zr	$\underline{SiC}$+C+ZrC+ZrSi$_2$**
30 ZrC/30 SiC/20 Si/20 B	$\underline{SiC}$+B$_4$C**
30 ZrC/30 SiC/20 Zr/20 B	$\underline{C}$+B$_4$C**+ZrB$_2$**+ SiC**
20 ZrC/20 SiC/25 Si/25 Zr/10 Al$_2$O$_3$	$\underline{SiC}$+ZrSi$_2$**
60 SiC/20 B/10 Si/10 Al$_2$O$_3$	$\underline{SiC}$+ $\underline{SiC}$+ $\underline{SiC}$+B$_4$C

Note: The silicon carbide used in the investigative series is the beta phase.
* Underlined components are the predominant composition, other phases are minor constituents listed in decreasing order.
**Present only in trace amounts.

TABLE 6.

X-RAY DIFFRACTION RESULTS OF THE FINAL SERIES

PACK COMPOSITION (% by weight)	CONVERSION LAYER COMPOSITION*
66 SiC/33 Si	$\underline{SiC}$+Si**
60 SiC/30 Si/10 Al_2O_3	$\underline{SiC}$+Al mixture
30 ZrC/30 SiC/40 Si	$\underline{SiC}$+ZrC+ SiC**
30 ZrC/30 SiC/30 Si/10 Al_2O_3	$\underline{SiC}$+Al mix+ZrC+ ZrSi$_2$
30 ZrC/30 SiC/40 B	$\underline{SiC}$+B$_4$C+ZrB$_2$**+ SiC**
30 ZrC/30 SiC/30 B/10 Al_2O_3	B$_4$C+ $\underline{SiC}$+ SiC‡ ZrB$_2$+Al mix**

Note: The silicon carbide powder used in the final series
is the alpha phase.
* Underlined components are the predominant composition,
other phases are minor constituents listed in decreasing
order.
**Present only in trace amounts.

results of the corresponding compositions in Table 5, no noticeable difference exists between the conversion compositions obtained using beta and those obtained using alpha SiC. The final pack compositions listed in Table 6, using the alpha phase of SiC, were used to prepare specimens for the oxidation tests.

Optical micrographs of a C-C composite that was pack cemented at 1700°C for 3 hours in a pack composition of 66.67 SiC + 33.33 Si, are shown in Figures 17a and 17b. The average depth of conversion is 29um. However, as shown in Figure 17a, the conversion layer is extremely non-uniform, having conversion depths up to 136um or more. The conversion depth of fiber bundles orientated perpendicular to the surface is very irregular. Although relatively uniform conversion occurs in the resin, the carbon matrix, and on fiber bundles orientated parallel to the surface, the depth of conversion in each of the different regions varies considerably.

X-ray diffraction has identified the conversion layer to consist predominantly of SiC with some free Si. Figure 17b shows the conversion layer to consist of two phases. EDAX determined both phases to contain Si, as expected. As discussed previously, the EDAX used in this study is unable to detect elements of low atomic weight, such as carbon, boron, and oxygen. Since the x-ray diffraction results determined SiC to be the dominant phase, the darker,
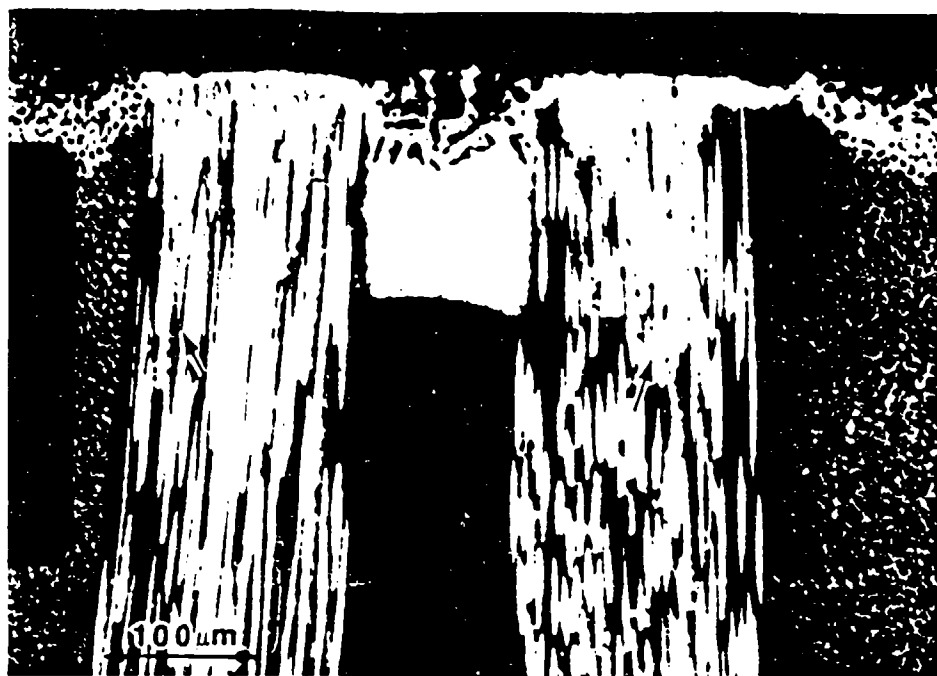
Figure 17a. Optical micrograph of composite pack cemented in 66.67% SiC + 33.33 Si at 1700°C for 3 hours.
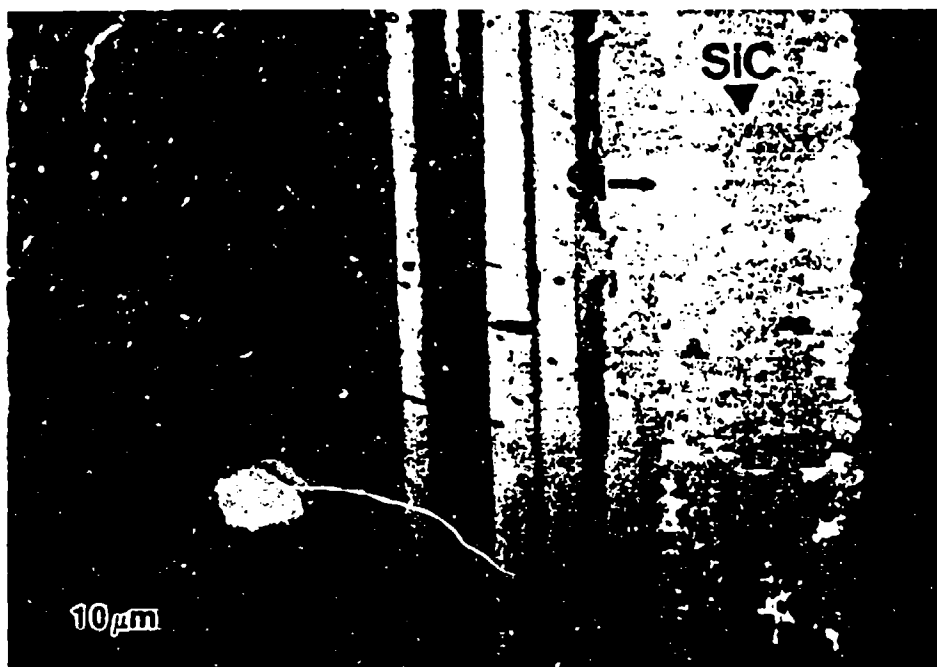
Figure 17b. Optical micrograph of composite pack cemented in 66.67% SiC + 33.33 Si at 1700°C for 3 hours.

predominant, phase in Figure 17b is probably SiC. The lighter, dispersed phase is probably free Si.

Figures 18a and 18b are optical micrographs of a C-C composite pack cemented at $1700^{\circ}C$ for 3 hours in a pack composition of 60 SiC + 30 Si + 10 Al_2O_3. The average depth of conversion is only 18um. A significant reduction in the conversion depth of the Si mixture has occured with the addition of Al_2O_3. However, it should be noted that the conversion depth for this mixture is also very nonuniform.

The conversion layer consists of SiC with only trace amounts of Al containing compounds, as determined by XRD. However, Figure 18b indicates there are two phases present in the coating. EDAX determined both phases to contain Si with trace amounts of an Al containing phase. It is obvious from the above results that the darker dominant phase is SiC and the lighter dispersed phase is free Si. In addition to having a thinner conversion layer, the pack cemented composite in Figures 18a and 18b, which contained Al_2O_3 in the starting pack, has less free Si dispersed in the SiC conversion layer than does the composite pack cemented without Al_2O_3.

A representative sample pack cemented at $1900^{\circ}C$ for 5 hours in a pack composition of 30 ZrC + 30 SiC + 40 Si, is shown in Figures 19a and 19b. The average conversion thickness is 18um. With this pack mixture, not only is the depth of conversion nonuniform, but the surface of the
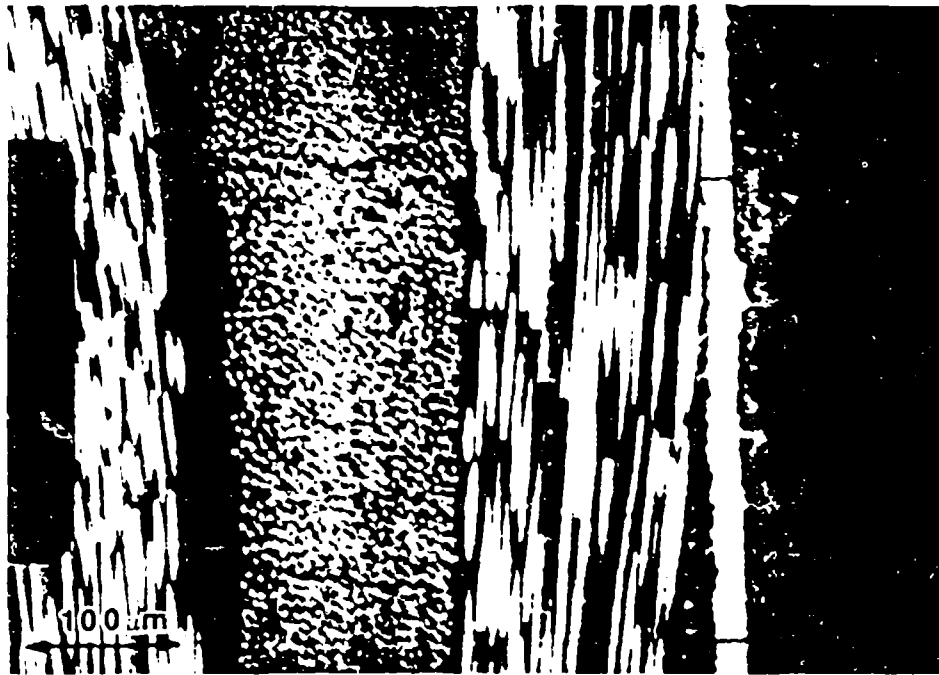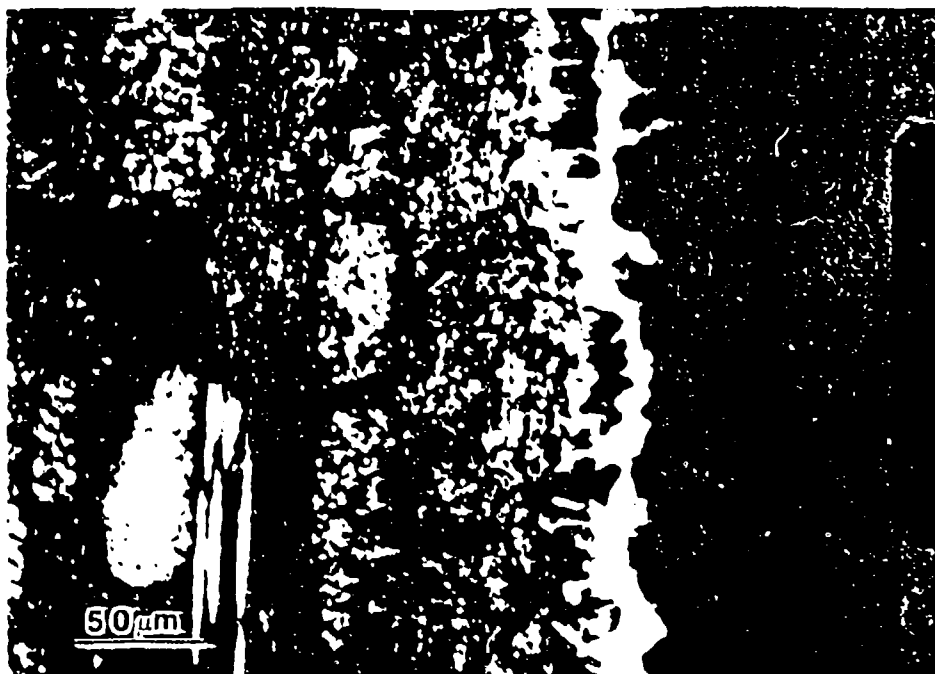
Figure 18a. Optical micrograph of the cross-section of a composite pack cemented in 60% SiC + 30% Si + 10% Al_2O_3 at 1700°C for 3 hours.

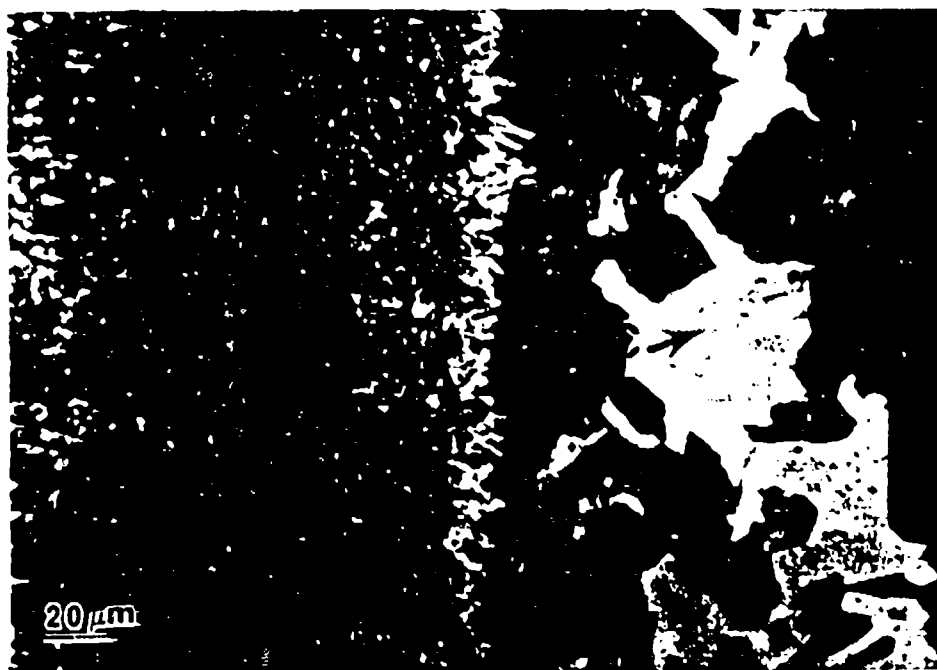Figure 18b. Optical micrograph of the cross-section of a composite pack cemented in 60% SiC + 30% Si + 10% Al_2O_3 at 1700°C for 3 hours.
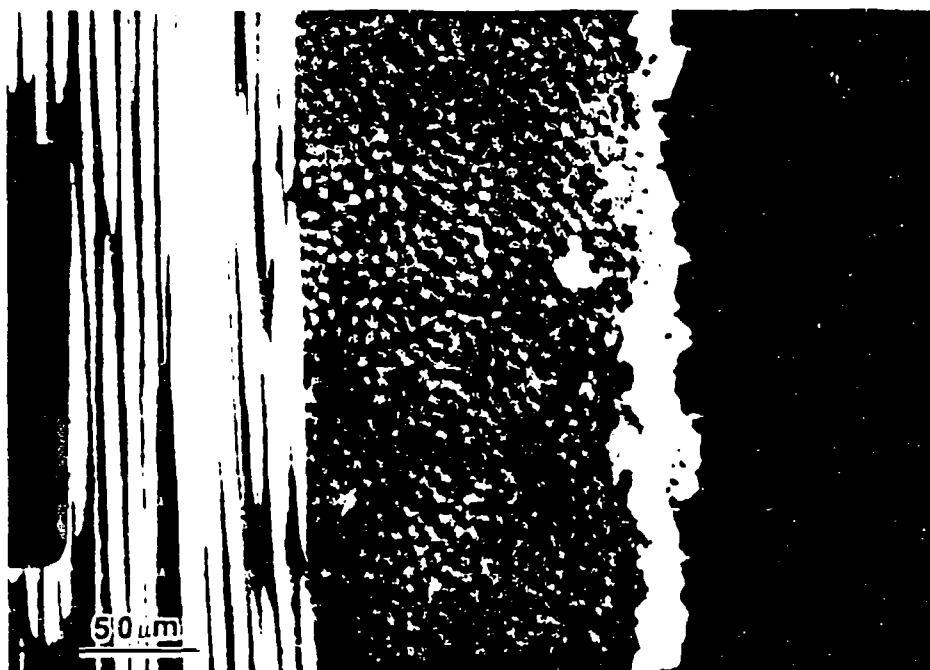
Figure 19a. Optical micrograph of the cross-section of a composite pack cemented in 30% ZrC + 30% SiC + 40% Si at 1900°C for 5 hours.
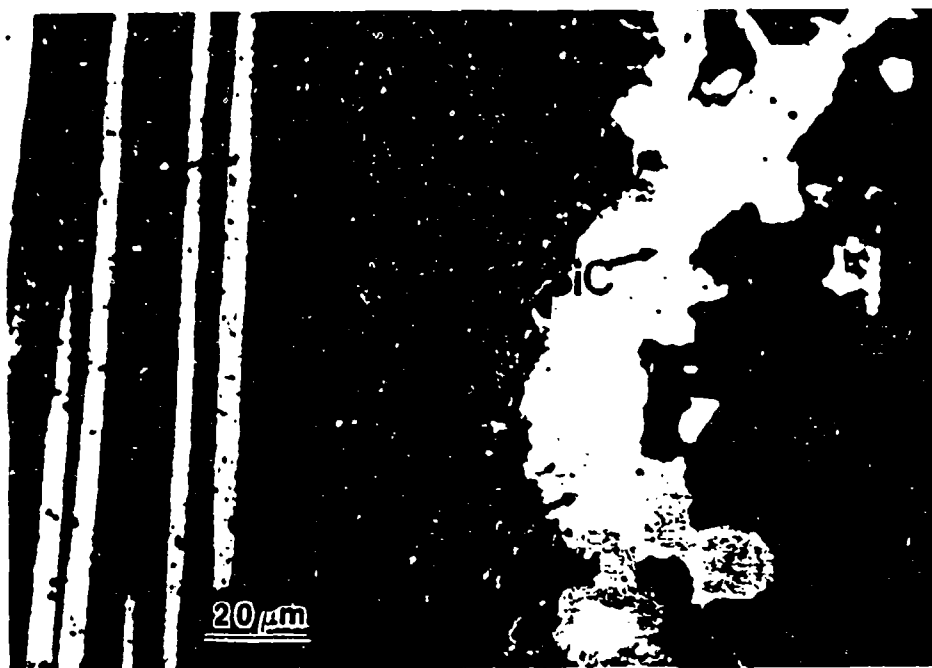
Figure 19b. Optical micrograph of the cross-section of a composite pack cemented in 30% ZrC + 30% SiC + 40% Si at 1900°C for 5 hours.

conversion layer is also irregular. XRD determined the conversion layer to consist predominantly of SiC, with a lesser amount of ZrC. EDAX determined the darker phase, shown in Figure 19b, to contain Si and the lighter phase to contain zirconium. The EDAX results, in conjunction with the XRD results, indicate that the dark phase is SiC, and the light, dispersed phase is ZrC. The ZrC is randomly dispersed in the SiC layer, occuring as agglomerated regions as opposed to small particulates.

Alumina additions to the above pack composition (30 ZrC + 30 SiC + 30 Si + 10 Al_2O_3) result in a thicker converion layer primarily consisting of SiC with lesser amounts of ZrC and only trace amounts of Al containing compounds, as determined by XRD. EDAX did not detect any Al containing compounds. It did confirm that the darker phase in Figures 20a and 20b is SiC, and the lighter phase is ZrC. Figure 20b shows a large SiC grain growing from the surface of the conversion layer.

Similar to the results of the previous composition, Al_2O_3 additions have decreased the amount of dispersed phase in the SiC, in this case the dispersed phase is ZrC. Unlike the previous composition, Al_2O_3 additions have increased the conversion depth considerably, 43um, compared to the conversion depth without Al_2O_3.

Figures 21a and 21b are optical micrographs of a carbon-carbon composite that was pack cemented in a starting

Figure 20a. Optical micrograph of the cross-section of a composite pack cemented in 30% ZrC + 30% SiC + 30% Si + 10% Al_2O_3 at 1900°C for 5 hours.
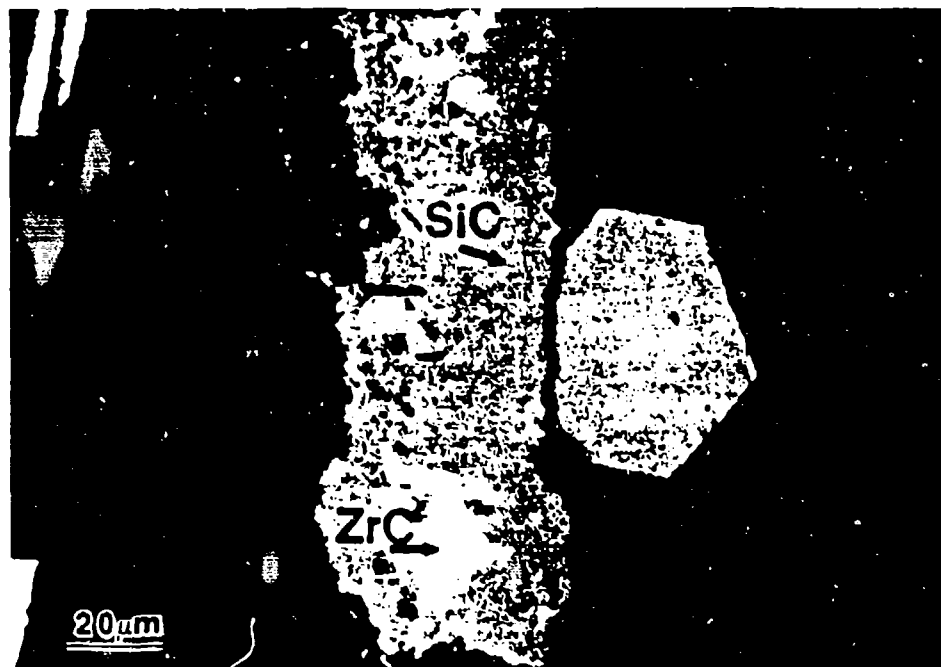
Figure 20b. Optical micrograph of the cross-section of a composite pack cemented in 30% ZrC + 30% SiC + 30% Si + 10% Al_2O_3 at 1900°C for 5 hours.
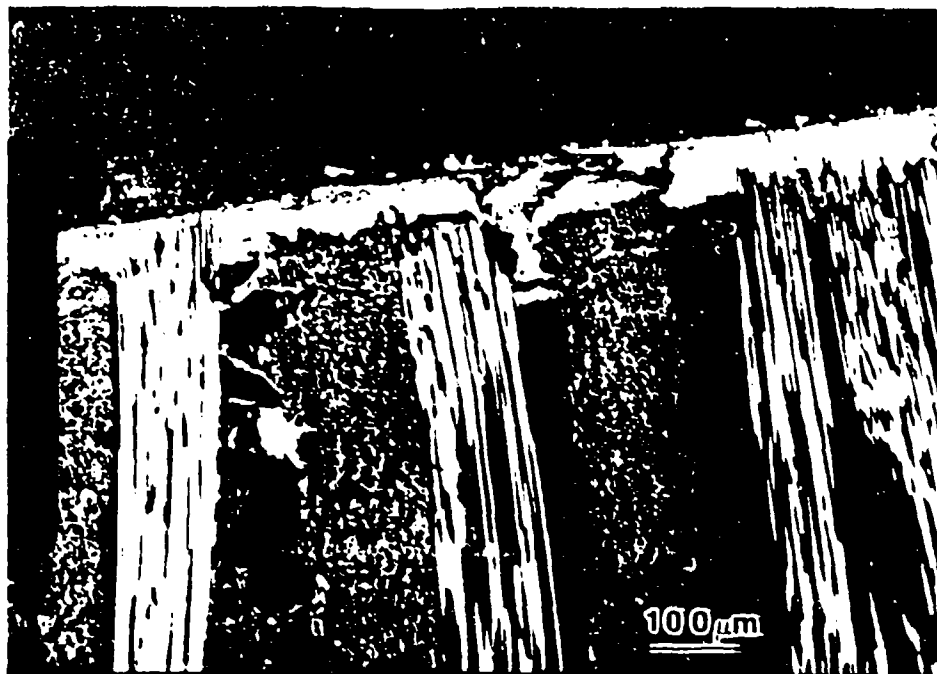
Figure 21a. Optical micrograph of the cross-section of a composite pack cemented in 30% ZrC + 30% SiC + 40% B at 1900°C for 5 hours.
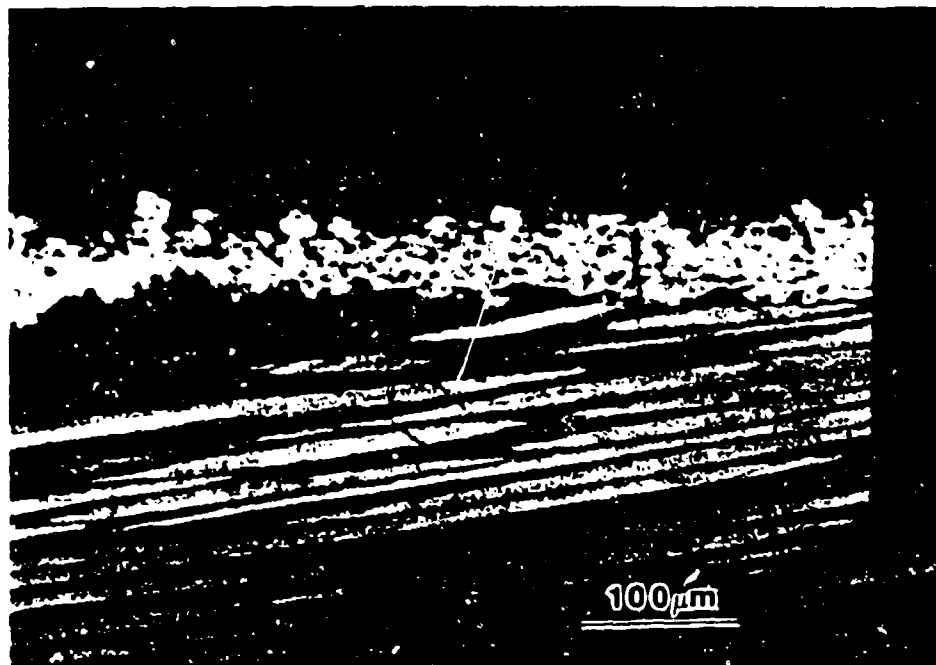
Figure 21b. Optical micrograph of the cross-section of a composite pack cemented in 30% ZrC + 30% SiC + 40% B at 1900°C for 5 hours.

pack composition of 30 ZrC + 30 SiC + 40 B. The average thickness of the conversion layer is 13um. Although, in Figure 21a it is clear that the conversion thickness is not very uniform; much thicker in some regions and quite thin in others. Fiber bundles orientated perpendicular to the surface and porosity lead to particularly irregular conversion depths.

In Figure 21b, it is evident that the conversion layer consists primarily of two phases. The XRD results identify the coating composition as predominantly SiC followed by B_4C and trace amounts of ZrB_2. EDAX determined both primary phases to contain Si and a minor phase to contain Zr.

Alumina additions to the ZrC/SiC/B system result in a larger average depth of conversion, 49um. XRD determined the composition of the conversion layer, in this case, to consist predominantly of B_4C, followed by SiC and some ZrB_2 with trace amounts or an Al mixture. EDAX identified the presence of Si with some Al in both the light and dark phases in Figures 22a and b. Again, the results of the XRD indicate the lighter phase is Si and the darker phase SiC. Determination of the distribution of B_4C was not possible using EDAX.

According to the XRD results, only trace amounts of Al containing compounds are present in the conversion layers that were obtained using Al_2O_3 in the starting pack composition. Optical microscopy on the cross-sections of

Figure 22a. Optical micrograph of the cross-section of a composite pack cemented in 30% ZrC + 30% SiC + 30% B + 10% Al_2O_3 at 1900°C for 5 hours.

Figure 22b. Optical micrograph of the cross-section of a composite pack cemented in 30% ZrC + 30% SiC + 30% B + 10% Al_2O_3 at 1900°C for 5 hours.

bundles with resin and CVI carbon. As a result, irregular pockets of open and closed porosity exists down the length of the fiber bundles which are readily accessible from the end of the fiber. Correspondingly, conversion of fiber bundles perpendicular to the surface is very irregular, as shown in Figure 17a.

Resin converts uniformly, see Figure 17a. The inhibited carbon matrix also converts uniformly, but to a lesser extent than the resin. It might be possible to obtain a more uniform conversion coating, if a uniformly dense carbon is deposited on the surface of the composite, a chemically vapor deposited coating, for example, before the pack cementation process. This approach has been used in industry with pack cementation and work has been published on its use with CVD coatings.[2]

3.0 Conversion Mechanisms

Identifying the mechanisms of conversion for any given system in itself requires a detailed investigation. This study does not attempt to cover every aspect in the conversion process. Its intent is to discuss the general mechanisms which are possible for conversion in the different pack powder compositions and temperatures used in this investigation. It should be noted that the possible mechanisms discussed below are based on thermodynamic calculations and the results of XRD, EDAX, and optical

microscopy, discussed above. Since no equilibrium conditions are realized in the process, it is possible for reactions with positive free energies to occur if the reaction products are removed as they are formed, such is possible for liquids and especially gases.[11]

The general conversion process follows similar steps as those followed in chemical vapor deposition. Initially, reactants are formed from the pack composition, unless the pack constituents are themselves reactants. These reactants need to be transported to the surface of the substrate. Chemical reactions with the composite occur, after which the gaseous by-products are transported away from the substrate.

Similar to reaction-formed ceramics[44], pack cementation uses mass transport of vapors and liquids to the substrate where they react, converting the exterior of the composite. Mass transport in pack cementation, as with reaction-formed ceramics, occurs over distances which correspond to the size of the substrate, in contrast to sintered or predensified bodies in which mass transport is restricted to the scale of the particle size.[44]

The carbon substrate can act as a reducing agent for the vapor, ie. a metal oxide, and in the reaction be converted to the metal carbide. The coating components may be dissolved by the substrate to form an alloy or solid solution. In this case, the activity of the coating component may be reduced significantly below unity, allowing

an otherwise unfavorable coating reaction to occur.[22] It is also possible for the substrate to react exothermically with the coating components to form a moderately or highly stable compound.[11]

3.1 SiC/Si System at 1700°C

Formation of reactants from the pack composition for this system, stem from the SiC and the inherent silica on the SiC and Si metal. The Si metal is, in itself, a reactant. However, the SiC must be converted to SiO SiO_2, or Si before it can react with the substrate. It is possible that the SiC is converted by the following reactions. Beta SiC is used in the calculations for the standard free energy of the reactions. Alpha SiC has approximately 2 kJ/mol higher standard free energy than the beta form.

$$SiC + SiO_2 \ _l \ ---> 2 \ Si_l + CO_2 \qquad (1)$$
$$\Delta G^\circ = +226.274 \ kJ/mol$$

$$SiC + SiO_2 \ _g \ ---> 2 \ Si_l + CO_2 \qquad (2)$$
$$\Delta G^\circ = -30.473 \ kJ/mol$$

$$SiC + 2 \ SiO_2 \ _g \ ---> 3 \ SiO + CO \qquad (3)$$
$$\Delta G^\circ = -402.163 \ kJ/mol$$

$$SiC + 2 \ SiO_2 \ _l \ -- > 3 \ SiO + CO \qquad (4)$$
$$\Delta G^\circ = +111.333 \ kJ/mol$$
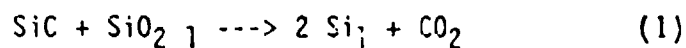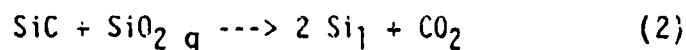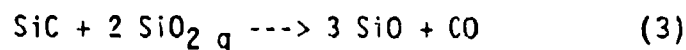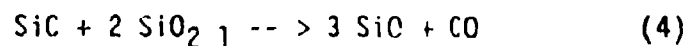
$$SiC + SiO_g \longrightarrow 2\ Si_l + CO_g \qquad (5)$$
$$\Delta G^* = +38.253\ kJ/mol$$
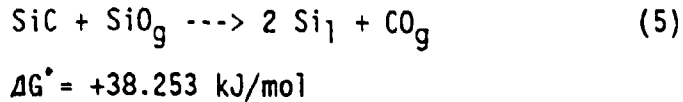
The SiC, whether it is the alpha or beta phase, must be broken down into the reactive species, SiO, SiO_2, and Si, before it will react with the carbon substrate to form the conversion layer. This is thermodynamically possible for both alpha and beta SiC starting powders.

Equations 6 through 10, below, are possible conversion reactions based on the reactive constituents. Equations 9 and 10 are not dependent on the initial breakdown of the SiC and probably occur more readily due to the availability in the pack composition.

$$SiO + 2\ C \longrightarrow SiC + CO \qquad (6)$$
$$\Delta G^o = -77.703\ kJ/mol$$

$$SiO_{2\ g} + 2\ C \longrightarrow SiC + CO_2 \qquad (7)$$
$$\Delta G^o = -146.429\ kJ/mol$$

$$SiO_{2\ l} + 2\ C -- \quad \ ^{..} \ l + CO_2 \qquad (8)$$
$$\Delta G = +110.319\ kJ/mol$$

$$C + Si_l \longrightarrow SiC \qquad (9)$$
$$\Delta G^* = -57.978\ kJ/mol$$

$$C + Si_g \longrightarrow SiC \qquad (10)$$
$$\Delta G^o = -219.29\ kJ/mol$$
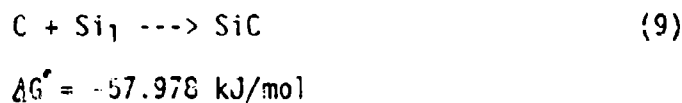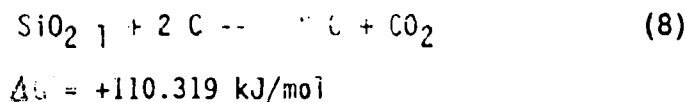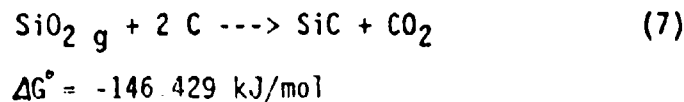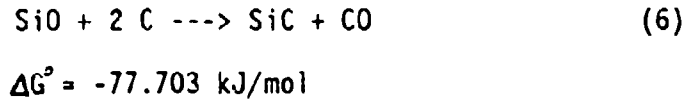
The formation of beta SiC is thermodynamically preferred over the formation of alpha SiC. Although there is only a 2kJ/mol difference in the standard free energy between the alpha and the beta phase, the reactions taking place in the conversion process strongly favor the formation of the beta form of SiC, as determined by XRD. The formation of beta SiC occurs regardless of which phase is used in the starting pack composition.

3.2 SiC/Si System with Alumina at 1700°C

Alumina additions to the pack composition may result in the following reactions.
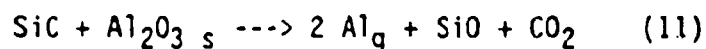
$$SiC + Al_2O_3 \; _s \;\text{--->}\; 2 \; Al_g + SiO + CO_2 \qquad (11)$$
$$\Delta G^o = -177.48 \text{ kJ/mol}$$

$$SiC + Al_2O_3 \; _s \;\text{--->}\; 2 \; Al_g + SiO_2 \; _l + CO \qquad (12)$$
$$\Delta G^o = -365.502 \text{ kJ/mol}$$

$$SiC + Al_2O_3 \; _s \;\text{--->}\; 2 \; Al_g + SiO_2 \; _g + CO \qquad (13)$$
$$\Delta G^o = -108.754 \text{ kJ/mol}$$

$$Al_2O_3 + 3 \; Si_l \;\text{--->}\; 2 \; Al_g + 3 \; SiO \qquad (14)$$
$$\Delta G^o = -298.545 \text{ kJ/mol}$$

$$2 \; Al_2O_3 + 6 \; C \;\text{--->}\; Al_4C_3 + 3 \; CO_2 \qquad (15)$$
$$\Delta G^o = -219.932 \text{ kJ/mol}$$

$$Al_2O_3 + 3\ C \longrightarrow 2\ Al_g + 3\ CO \qquad (16)$$
$$\Delta G^\circ = -426.390\ kJ/mol$$
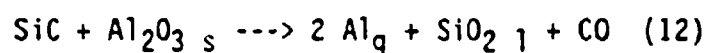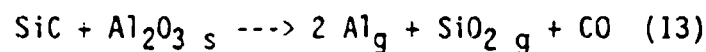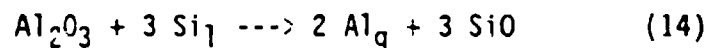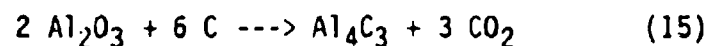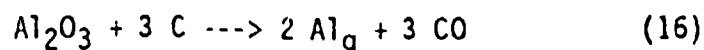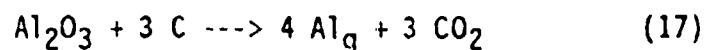
$$Al_2O_3 + 3\ C \longrightarrow 4\ Al_g + 3\ CO_2 \qquad (17)$$
$$\Delta G^\circ = -588.839\ kJ/mol$$

Alumina was originally used in pack cementation as an inert filler, as previously mentioned. Research later conducted by Rogers, et al.[11] indicates that Al_2O_3 may increase the amount of conversion by aiding the removal of the gaseous carbon by-product during conversion and increasing the vapor transport of Si to the surface of the composite.

From the above results of the SiC/Si system in this study, it appears that Al_2O_3 additions decrease the thickness of the conversion layer and reduce the amount of free Si in the SiC conversion layer. In this situation, the Al_2O_3 seems to be acting as a sintering aid, increasing the density of the SiC layer, but not the depth of the conversion. Alumina is sometimes used as a sintering aid, in the sintering of ceramics, since it segregates to the grain boundaries and inhibits the grain growth which increases the density of the sintered compact.

3.3 ZrC/SiC/Si System at 1900°C

The Si system takes part in the Zr and B systems described below. Therefore, it is necessary to identify the possible reactions in the SiC/Si system at 1900°C.
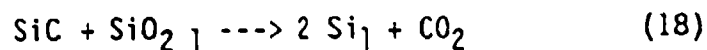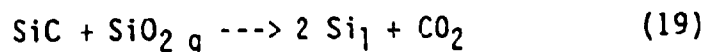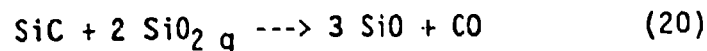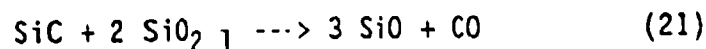
$$SiC + SiO_2{}_1 \longrightarrow 2\ Si_1 + CO_2 \qquad (18)$$
$$\Delta G^\circ = +192.313\ kJ/mol$$

$$SiC + SiO_2{}_g \longrightarrow 2\ Si_1 + CO_2 \qquad (19)$$
$$\Delta G^\circ = -32.496\ kJ/mol$$

$$SiC + 2\ SiO_2{}_g \longrightarrow 3\ SiO + CO \qquad (20)$$
$$\Delta G^\circ = -466.418\ kJ/mol$$

$$SiC + 2\ SiO_2{}_1 \longrightarrow 3\ SiO + CO \qquad (21)$$
$$\Delta G^\circ = -16.800\ kJ/mol$$

$$SiC + SiO_g \longrightarrow 2\ Si_1 + CO_g \qquad (22)$$
$$\Delta G^\circ = +34.945\ kJ/mol$$

$$SiO + 2\ C \longrightarrow SiC + CO \qquad (23)$$
$$\Delta G^\circ = -77.784\ kJ/mol$$

$$SiO_2{}_g + 2\ C \longrightarrow SiC + CO_2 \qquad (24)$$
$$\Delta G^\circ = -145.296\ kJ/mol$$

$$SiO_2{}_1 + 2\ C \longrightarrow SiC + CO_2 \qquad (25)$$
$$\Delta G^\circ = +79.513\ kJ/mol$$

$$C + Si_1 \longrightarrow SiC \qquad (26)$$
$$\Delta G^\circ = -56.400\ kJ/mol$$
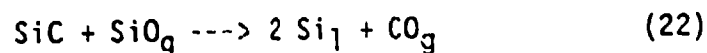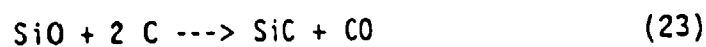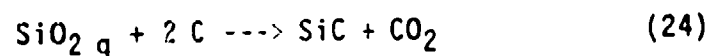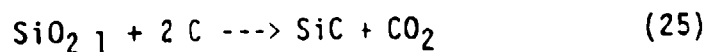
$$C + Si_g \longrightarrow SiC \qquad (27)$$
$$\Delta G^\circ = -189.439\ kJ/mol$$

Besides the possible reactions which can occur in the SiC/Si system, the following reactions are possible when ZrC is present in the pack composition, at 1900°C.
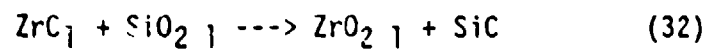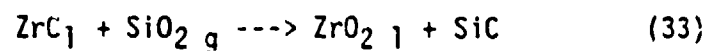
$$ZrC_l + SiO_g \longrightarrow ZrO_{2\ l} + SiC + Si_l \qquad (28)$$
$$\Delta G^\circ = -309.244 \text{ kJ/mol}$$

$$ZrC_s + SiO_g \longrightarrow ZrO_{2\ l} + SiC + Si_l \qquad (29)$$
$$\Delta G^\circ = -275.518 \text{ kJ/mol}$$

$$ZrC_l + SiO_g \longrightarrow ZrO_{2\ s} + SiC + Si_g \qquad (30)$$
$$\Delta G^\circ = -330.651 \text{ kJ/mol}$$

$$ZrC_s + SiO_g \longrightarrow ZrO_{2\ s} + SiC + Si_g \qquad (31)$$
$$\Delta G^\circ = -296.925 \text{ kJ/mol}$$

$$ZrC_l + SiO_{2\ l} \longrightarrow ZrO_{2\ l} + SiC \qquad (32)$$
$$\Delta G^\circ = -56.095 \text{ kJ/mol}$$

$$ZrC_l + SiO_{2\ g} \longrightarrow ZrO_{2\ l} + SiC \qquad (33)$$
$$\Delta G^\circ = -280.914 \text{ kJ/mol}$$

$$ZrC_l + SiO_{2\ g} \longrightarrow ZrO_{2\ s} + SiC \qquad (34)$$
$$\Delta G^\circ = -77.502 \text{ kJ/mol}$$

$$ZrC_l + SiO_{2\ g} \longrightarrow ZrO_{2\ s} + SiC \qquad (35)$$
$$\Delta G^\circ = -302.321 \text{ kJ/mol}$$

$$ZrC_s + SiO_{2\ l} \longrightarrow ZrO_{2\ l} + SiC \qquad (36)$$
$$\Delta G^\circ = -22.375 \text{ kJ/mol}$$

$$ZrC_s + SiO_{2\,g} ---> ZrO_{2\,l} + SiC \qquad (37)$$

$$\Delta G^\circ = -247.194 \text{ kJ/mol}$$

$$ZrC_s + SiO_{2\,l} ---> ZrO_{2\,s} + SiC \qquad (38)$$

$$\Delta G^\circ = -43.782 \text{ kJ/mol}$$

$$ZrC_s + SiO_{2\,g} ---> ZrO_{2\,s} + SiC \qquad (39)$$

$$\Delta G^\circ = -268.601 \text{ kJ/mol}$$

$$ZrO_{2\,g} + 3\,C ---> ZrC_l + 2\,CO \qquad (40)$$

$$\Delta G^\circ = -608.304 \text{ kJ/mol}$$

$$ZrO_{2\,g} + 3\,C ---> ZrC_s + 2\,CO \qquad (41)$$

$$\Delta G^\circ = -642.024 \text{ kJ/mol}$$

$$ZrO_{2\,l} + 3\,C ---> ZrC_l + 2\,CO \qquad (42)$$

$$\Delta G^\circ = -260.655 \text{ kJ/mol}$$

$$ZrO_{2\,l} + 3\,C ---> ZrC_s + 2\,CO \qquad (43)$$

$$\Delta G^\circ = -294.375 \text{ kJ/mol}$$

$$ZrO_{2\,s} + 3\,C ---> ZrC_l + 2\,CO \qquad (44)$$

$$\Delta G^\circ = -239.066 \text{ kJ/mol}$$

$$ZrO_{2\,s} + 3\,C ---> ZrC_s + 2\,CO \qquad (45)$$
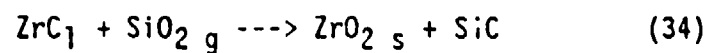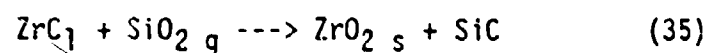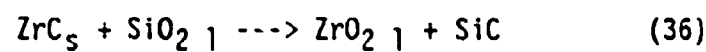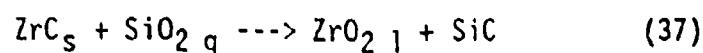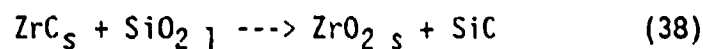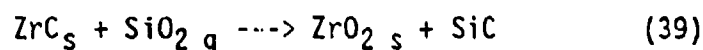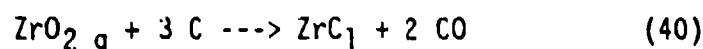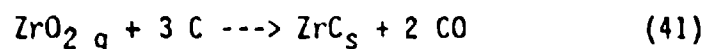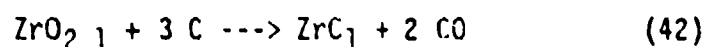
$$\Delta G^\circ = -272.786 \text{ kJ/mol}$$

There is a significant amount of ZrC in the dominant SiC conversion layer. Zirconium carbide does not react directly with carbon. To account for the presence of ZrC in

the conversion layer, it appears that ZrC initially reacts with SiO or SiO_2 in the pack composition to form ZrO_2. Although the formation of ZrO_2 gas is not thermodynamically possible in the system, the formation of ZrO_2 in the liquid and solid form is thermodynamically preferred. All phases of ZrO_2 readily react with the carbon substrate to form ZrC. Since ZrO_2 must be transported to the carbon substrate, it seems likely that the gas phase is the phase which results from the reaction between ZrC in the pack composition and SiO/SiO_2. As previously discussed, the pack cementation process does not take place at equilibrium. Therefore, it is possible for the formation of ZrO_2 gas to occur, even though it has a positive standard free energy, since it can be transported away from the reactions occuring in the pack and in turn can react with the carbon substrate.

3.4 ZrC/SiC/Si System with Alumina at 1900°C

The addition of ZrC to the Si system with alumina. has a significant effect on the conversion layer, as discussed in section 2. First, consider the reactions that may be taking place between the Si system and alumina at 1900°C.
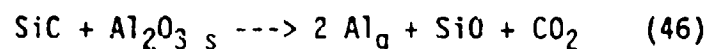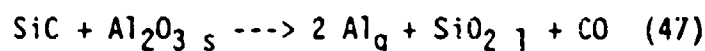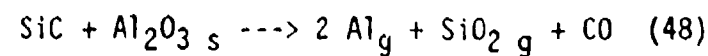
$$SiC + Al_2O_3 \text{ } _s \text{ } ---> 2 \text{ } Al_g + SiO + CO_2 \quad (46)$$
$$\Delta G^o = -252.645 \text{ kJ/mol}$$

$$SiC + Al_2O_3 \text{ } _s \text{ } ---> 2 \text{ } Al_g + SiO_{2 \text{ } l} + CO \quad (47)$$
$$\Delta G^o = -409.942 \text{ kJ/mol}$$

$$SiC + Al_2O_3 \text{ s} \dashrightarrow 2 Al_g + SiO_{2 \text{ g}} + CO \quad (48)$$
$$\Delta G^o = -185.133 \text{ kJ/mol}$$

$$Al_2O_3 + 3 Si_1 \dashrightarrow 2 Al_g + 3 SiO \quad (49)$$
$$\Delta G^o = -470.866 \text{ kJ/mol}$$

$$2 Al_2O_3 + 3 Si_1 \dashrightarrow 4 Al_g + 3 SiO_2 \quad (50)$$
$$\Delta G^o = -995.800 \text{ kJ/mol}$$

$$2 Al_2O_3 + 6 C \dashrightarrow Al_4C_3 + 3 CO_2 \quad (51)$$
$$\Delta G^o = -822.544 \text{ kJ/mol}$$

$$Al_2O_3 + 3 C \dashrightarrow 2 Al_g + 3 CO \quad (52)$$
$$\Delta G^o = -535.018 \text{ kJ/mol}$$
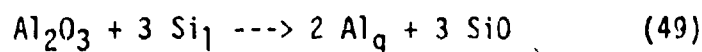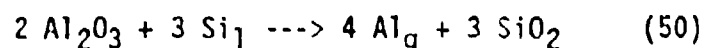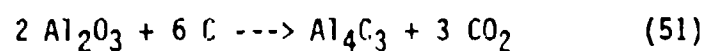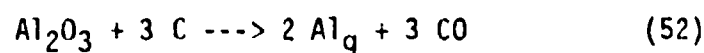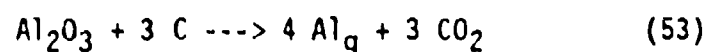
$$Al_2O_3 + 3 C \dashrightarrow 4 Al_g + 3 CO_2 \quad (53)$$
$$\Delta G^o = -690.744 \text{ kJ/mol}$$

In addition to the reactions that may occur between the ZrC and the SiC/Si system, and the reactions that may occur between the SiC/Si system and alumina, the following reactions may take place between the ZrC and the alumina.
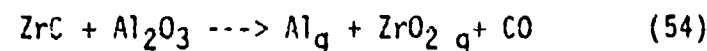
$$ZrC + Al_2O_3 \dashrightarrow Al_g + ZrO_{2 \text{ g}} + CO \quad (54)$$
$$\Delta G^o = +69.948 \text{ kJ/mol (using } ZrC_s)$$
$$\Delta G^o = +36.222 \text{ kJ/mol (using } ZrC_1)$$
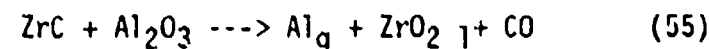
$$ZrC + Al_2O_3 \dashrightarrow Al_g + ZrO_{2 \text{ 1}} + CO \quad (55)$$
$$\Delta G^o = -277.701 \text{ kJ/mol (using } ZrC_s)$$
$$\Delta G^o = -311.421 \text{ kJ/mol (using } ZrC_1)$$

$$ZrC + Al_2O_3 \dashrightarrow Al_g + ZrO_{2\ s} + CO \qquad (56)$$
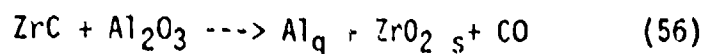
$\Delta G^o = -299.108$ kJ/mol (using ZrC_s)

$\Delta G^o = -332.828$ kJ/mol (using ZrC_l)

Contrary to the SiC/Si sy· ·m, the conversion layer of the ZrC/SiC/Si system with Al_2O_3 is, on the average, much deeper than the layer obtained without Al_2O_3. However, there is less ZrC in the SiC layer.

3.5 ZrC/SiC/B System at 1900°C

Besides the possible combinations of reactions between the ZrC and the Si system, boron may react with the other constituents through the following reactions.

$$4\ B + C \dashrightarrow B_4C_s \qquad (57)$$

$\Delta G^o = -52.610$ kJ/mol (using B_s)

$\Delta G^o = -37.563$ kJ/mol (using B_l)

$$4\ B + C \dashrightarrow B_4C_l \qquad (58)$$

$\Delta G^o = -29.825$ kJ/mol (using B_s)

$\Delta G^o = -14.737$ kJ/mol (using B_l)

$$4\ B_s + 3\ SiO_{2\ g} \dashrightarrow 2\ B_2O_3 + 3\ Si_l \qquad (59)$$
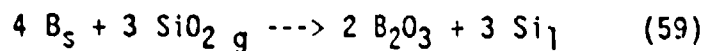
$\Delta G^o = -573.537$ kJ/mol (using $B_2O_{3\ g}$)

$\Delta G^o = -625.083$ kJ/mol (using $B_2O_{3\ l}$)
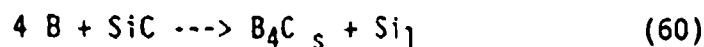
$$4\ B + SiC \dashrightarrow B_4C_s + Si_l \qquad (60)$$

$\Delta G^o = +3.749$ kJ/mol

$$4 \text{ B} + \text{SiC} \dashrightarrow \text{B}_4\text{C}_l + \text{Si}_l \qquad (61)$$
$$\Delta G^o = +26.575 \text{ kJ/mol}$$

$$2 \text{ B} + \text{ZrO}_{2 \ s} \dashrightarrow \text{ZrB}_{2 \ l} + \text{O}_2 \qquad (62)$$
$$\Delta G^o = +454.000 \text{ kJ/mol}$$

$$2 \text{ B} + \text{ZrO}_{2 \ g} \dashrightarrow \text{ZrB}_{2 \ s} + \text{O}_2 \qquad (63)$$
$$\Delta G^o = +50.410 \text{ kJ/mol}$$

$$4 \text{ B} + 3 \text{ ZrO}_{2 \ s} \dashrightarrow 2 \text{ B}_2\text{O}_{3 \ g} + 3 \text{ Zr}_l \qquad (64)$$
$$\Delta G^o = +596.000 \text{ kJ/mol}$$

$$4 \text{ B} + 3 \text{ ZrO}_{2 \ g} \dashrightarrow 2 \text{ B}_2\text{O}_{3 \ l} + 3 \text{ Zr}_l \qquad (65)$$
$$\Delta G^o = -562.180 \text{ kJ/mol}$$
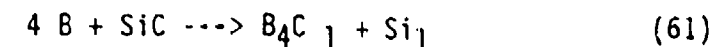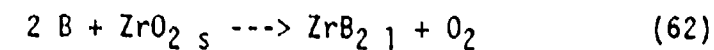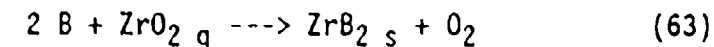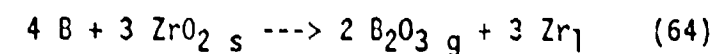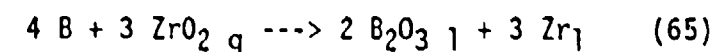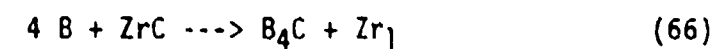
$$4 \text{ B} + \text{ZrC} \dashrightarrow \text{B}_4\text{C} + \text{Zr}_l \qquad (66)$$
$$\Delta G^o = +114.000 \text{ kJ/mol (using ZrC}_l)$$
$$\Delta G^o = +148.000 \text{ kJ/mol (using ZrC}_s)$$
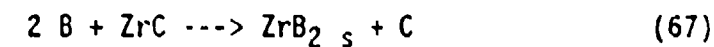
$$2 \text{ B} + \text{ZrC} \dashrightarrow \text{ZrB}_{2 \ s} + \text{C} \qquad (67)$$
$$\Delta G^o = -133.829 \text{ kJ/mol (using ZrC}_l)$$
$$\Delta G^o = -100.100 \text{ kJ/mol (using ZrC}_s)$$
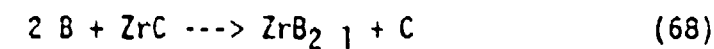
$$2 \text{ B} + \text{ZrC} \dashrightarrow \text{ZrB}_{2 \ l} + \text{C} \qquad (68)$$
$$\Delta G^o = -98.660 \text{ kJ/mol (using ZrC}_l)$$
$$\Delta G^o = -64.930 \text{ kJ/mol (using ZrC}_s)$$
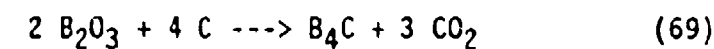
$$2 \text{ B}_2\text{O}_3 + 4 \text{ C} \dashrightarrow \text{B}_4\text{C} + 3 \text{ CO}_2 \qquad (69)$$
$$\Delta G^o = +328.000 \text{ kJ/mol}$$

3.6 ZrC/SiC/B System with Al_2O_3 at 1900^oC

With the addition of Al_2O_3, the following possible reactions are added to the ZrC/SiC/B system.

$$B + Al_2O_3 \longrightarrow AlBO_2 + AlO \qquad (70)$$
$$\Delta G^o = -411.344 \text{ kJ/mol}$$
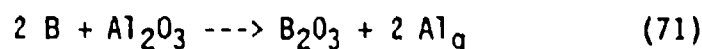
$$2 B + Al_2O_3 \longrightarrow B_2O_3 + 2 Al_g \qquad (71)$$
$$\Delta G^o = -381.555 \text{ kJ/mol}$$

Additions of Al_2O_3 increased the conversion layer thickness of the SiC + B_4C coating, as it did in the SiC + ZrC coating. However, it increased the amount of B_4C present in the converted layer.

4.0 Oxidation Protection

Specimens pack cemented using the six compositions discussed above were heated in air at 800, 1000, 1200, 1400, 1600, and 1800^oC to evaluate and compare the oxidation protection the resultant coatings could provide at a wide range of temperatures.

During the oxidation tests, the samples were held at temperature until approximately 5% weight loss was detected. Oxidation of C-C has a drastic affect on the structural properties for which it is used. Five percent was chosen as a rough maximum allowable oxidation to maintain the structural integrity of the composite.

It should be noted that five percent weight loss was
used to indicate the end of the oxidation test, as discussed
in the experimental procedures. Due to the nature of the
oxidation system, the weight recorded may not reflect the
actual weight loss. Some of the volatile compounds may
deposit on the inside of the crucible or on the supporting
wire, which would correspond to a lesser amount of weight
loss. As a result, some of the specimens had experienced
greater than five percent weight loss over the time of the
test. Table 7 lists the actual weight loss of each specimen
tested and the time at temperature.

The oxidation results for each of the compositions at
$800^{\circ}C$, in percent weight change over time, are shown in
Figure 23. Scanning electron micrographs of the surface of
each of these samples after oxidation, is presented in
Figures 24 through 29.

The coatings consisting of SiC with B_4C provided the
best oxidation protection at this temperature. Figures 24a
and 25a are scanning electron micrographs of the oxidized
surfaces of the composites of the SiC/B_4C coatings packed
with and without Al_2O_3. In these micrographs, the surfaces
are magnified 50 times, showing the coatings covering the
surface in a relatively uniform manner. Higher
magnifications, in Figures 24b and 25b, indicate that glass
formation has occured. At this temperature the glass
formation must be due to oxidation of the B_4C in the coating

TABLE 7.

ACTUAL WEIGHT LOSS DURING OXIDATION

PACK COMPOSITION (WEIGHT %) TEST TEMPERATURE	TIME AT TEMPERATURE (MINUTES)	ACTUAL WEIGHT LOSS (PERCENT)
30 ZrC/30 SiC/40 B		
800 ^{o}C	109	4.86
1000	60	5.43
1200	11	5.27
1400	3	7.33*
1600	1	11.14
1800	1	4.80
30 ZrC/30 SiC/30 B/10 Al_2O_3		
800 ^{o}C	91	5.39
1000	52	4.88
1200	80	5.04
1400	118	8.06
1600	7	9.71
1800	4	10.68*
66.7 SiC/33.3 Si		
800 ^{o}C	41	5.80
1000	104	6.79
1200	720	1.50
1400	380	8.43
1600	36	3.50
1800	37	12.3*
60 SiC/30 Si/10 Al_2O_3		
800 ^{o}C	69	5.00
1000	21	5.45
1200	92	6.86
1400	49	5.39
1600	8	6.45
1800	4	7.90

TABLE 7. (Continued)

ACTUAL WEIGHT LOSS DURING OXIDATION

PACK COMPOSITION (WEIGHT %) TEST TEMPERATURE	TIME AT TEMPERATURE (MINUTES)	ACTUAL WEIGHT LOSS (PERCENT)
30 ZrC/30 SiC/40 Si		
800 °C	35	5.97
1000	10	6.83
1200	56	6.89
1400	166	6.19
1600	16	5.66
1800	11	8.13
30 ZrC/30 SiC/30 Si/10 Al$_2$O$_3$		
800 °C	35	19.46
1000	14	10.19
1200	10	6.50
1400	26	5.84
1600	65	5.34
1800	24	10.29

* The sample broke when it was removed from the oxidation system. As a result, the measured weight loss is higher than the specimen experienced during the test.
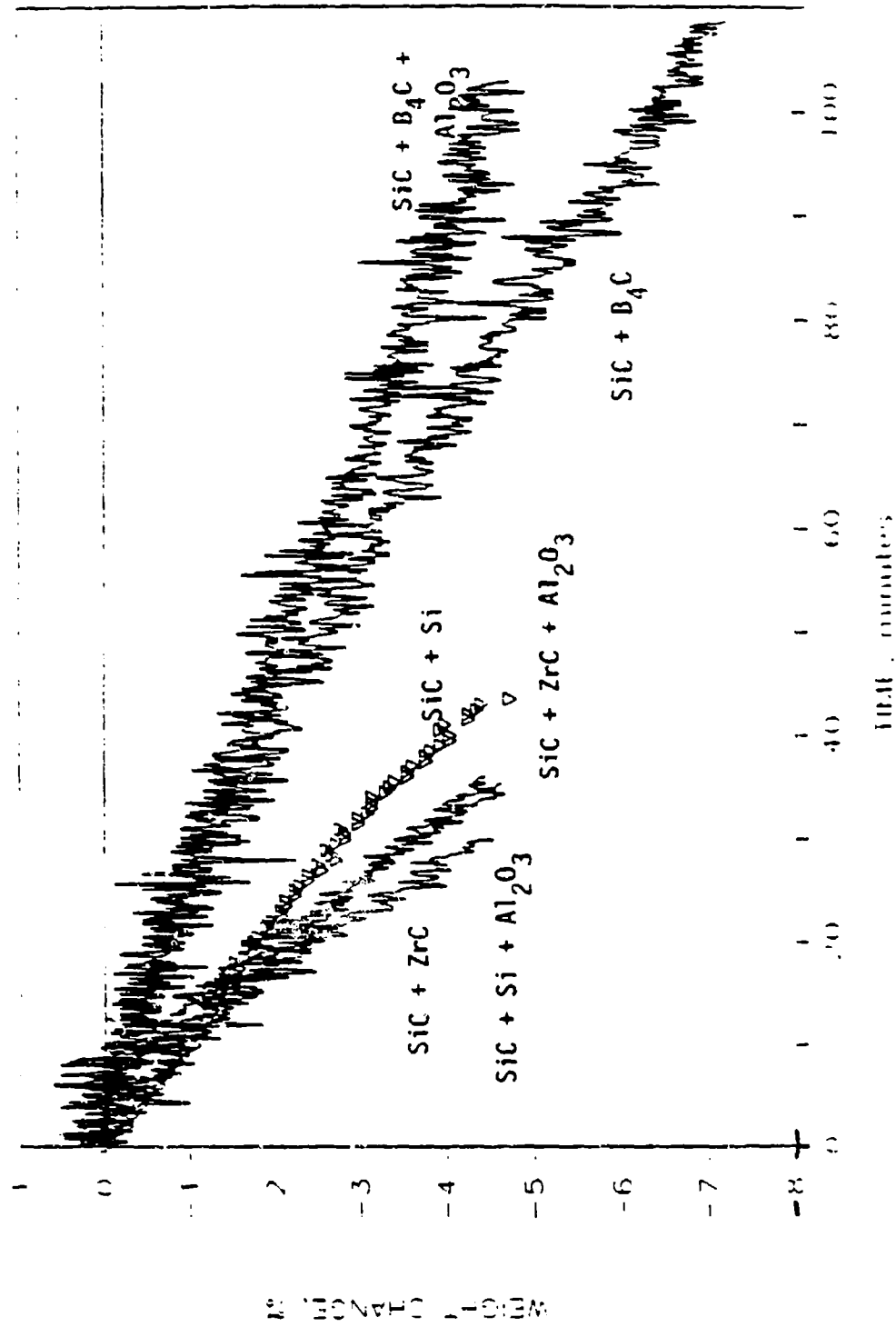
Figure 23. Comparison of Oxidation Results for All Mixtures Tested at 800°C.
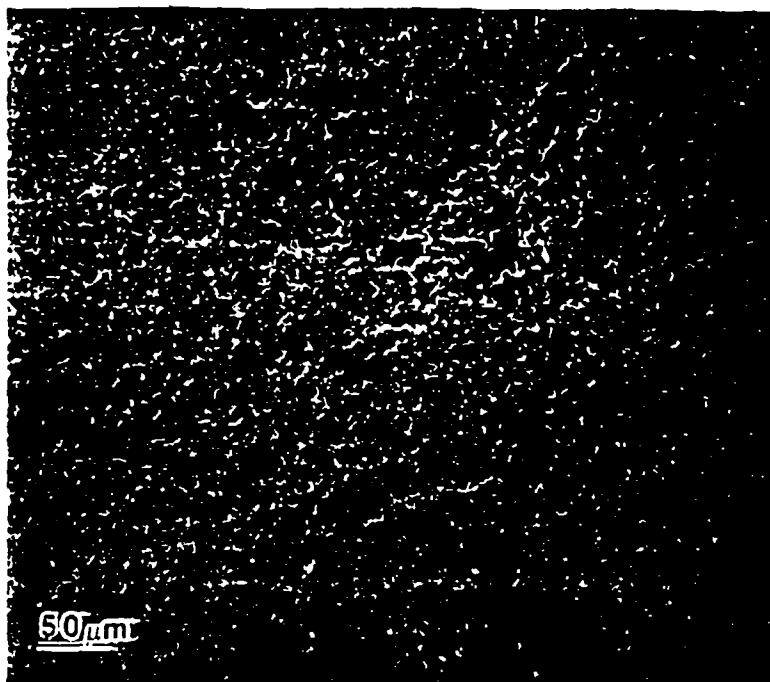
Figure 24a. SEM micrograph of an inhibited matrix composite packed cemented in the ZrC/SiC/B mixture and oxidized at 800°C.
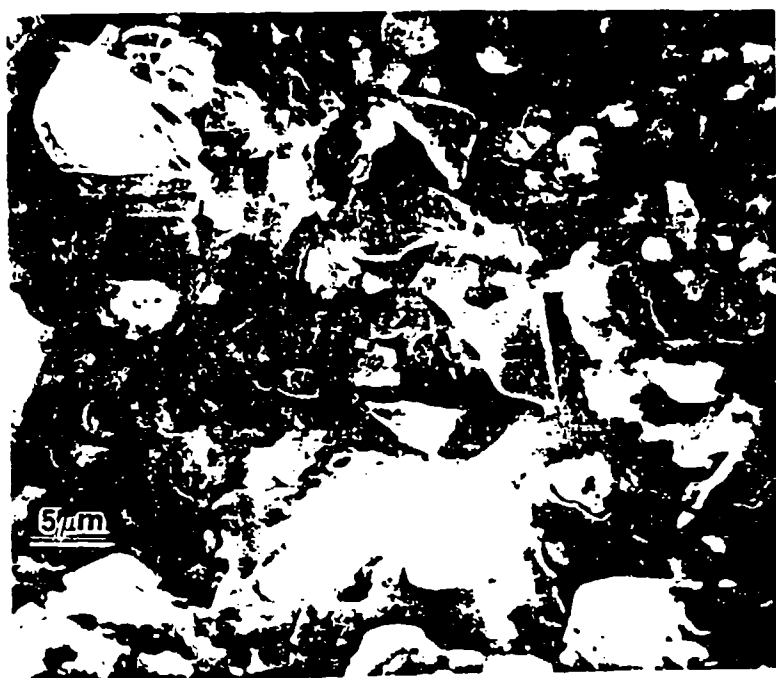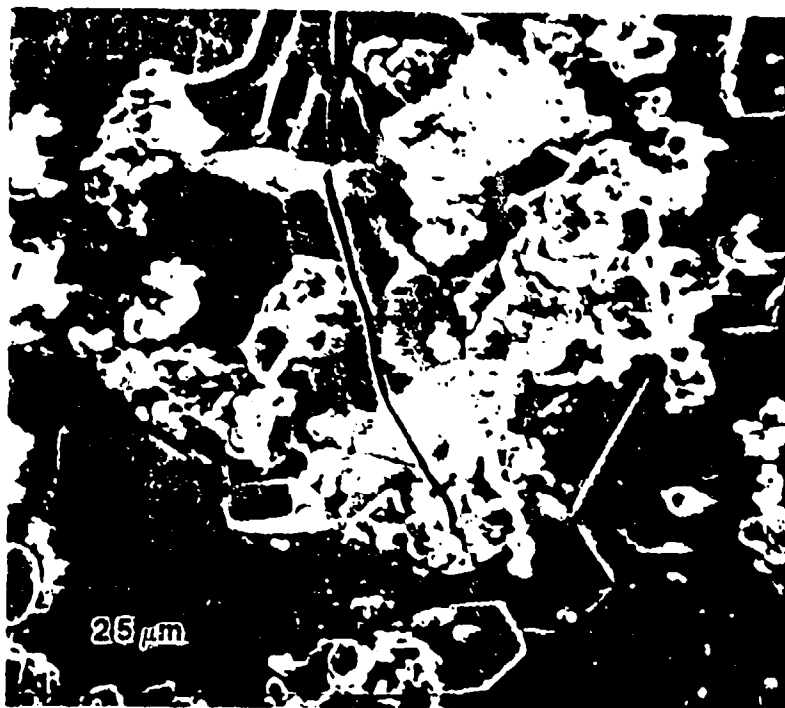

Figure 24b. SEM micrograph of an inhibited matrix composite packed cemented in the ZrC/SiC/B mixture and oxidized at 800°C.
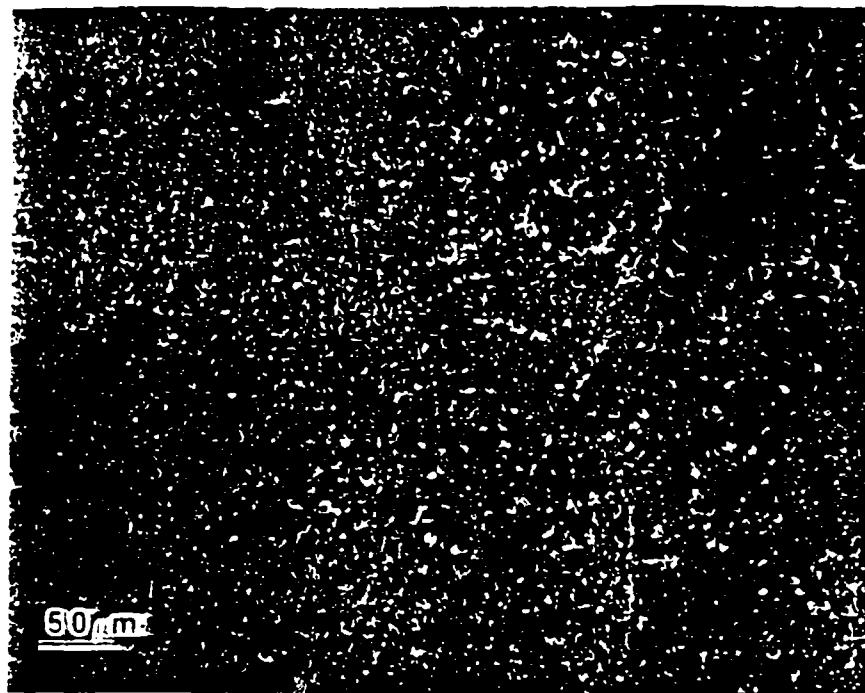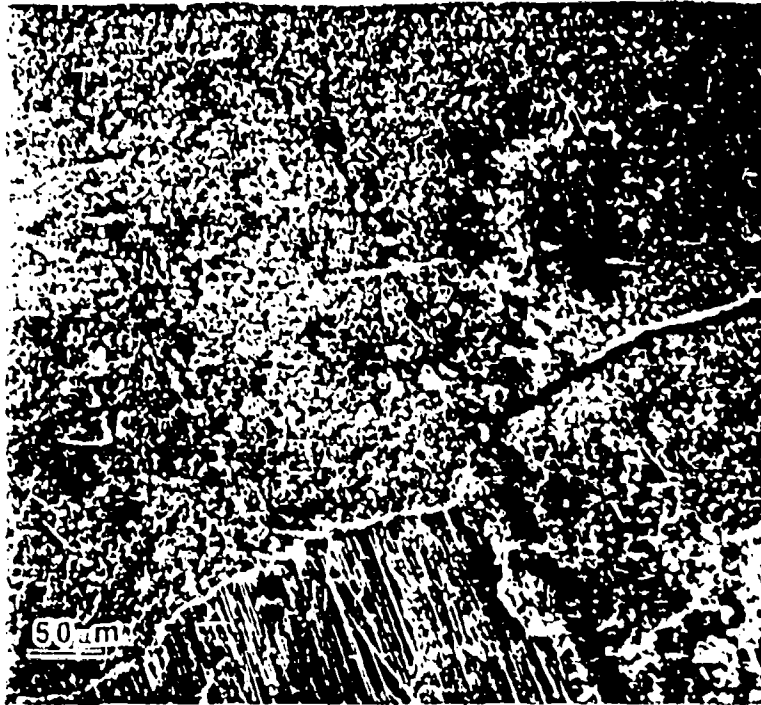
Figure 25a. SEM micrograph of an inhibited matrix composite packed cemented in the ZrC.SiC/B/Al$_2$O$_3$ mixture and oxidized at 800°C.
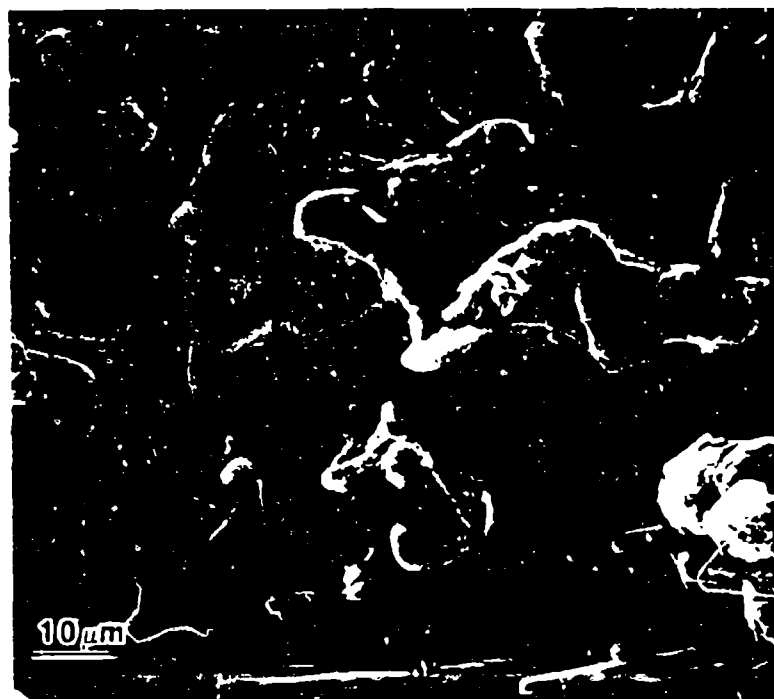
Figure 25b. SEM micrograph of an inhibited matrix composite packed cemented in the ZrC/SiC/B/Al$_2$O$_3$ mixture and oxidized at 800°C.
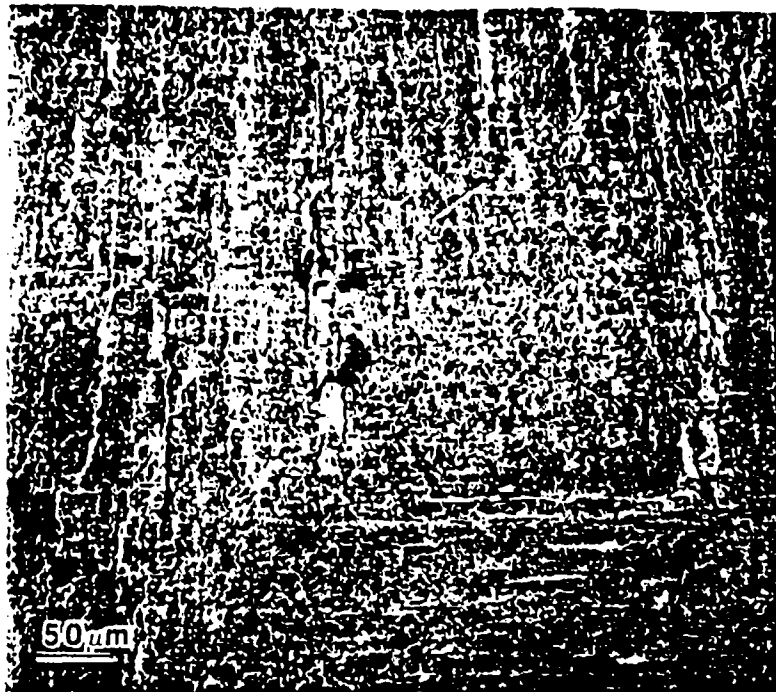
Figure 26a. SEM micrograph of an inhibited matrix composite packed cemented in the SiC/Si mixture and oxidized at 800°C.
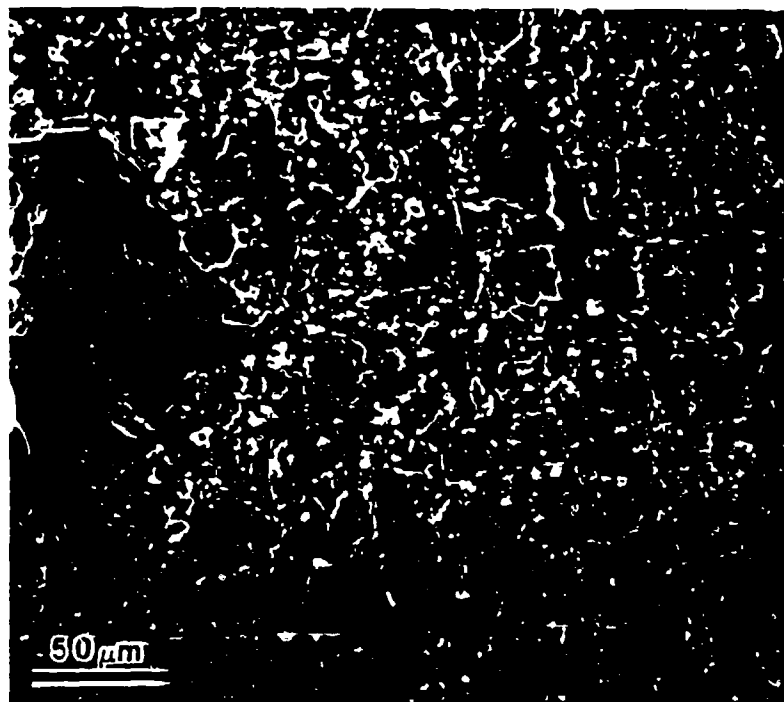
Figure 26b. SEM micrograph of an inhibited matrix composite packed cemented in the SiC/Si mixture and oxidized at 800°C.
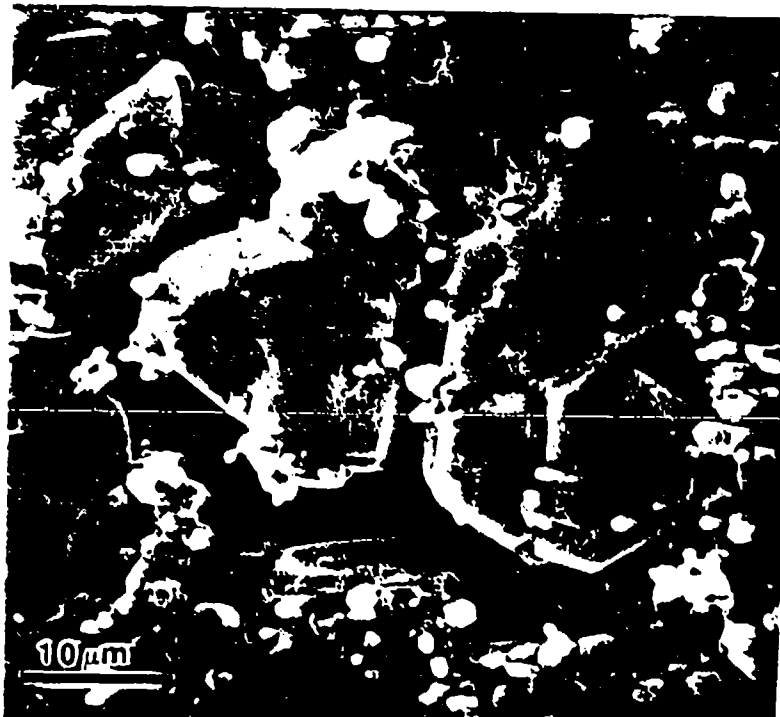
Figure 26c. Surface details of figure 26a, an inhibited matrix composite packed cemented in the SiC/Si mixture and oxidized at 800°C.
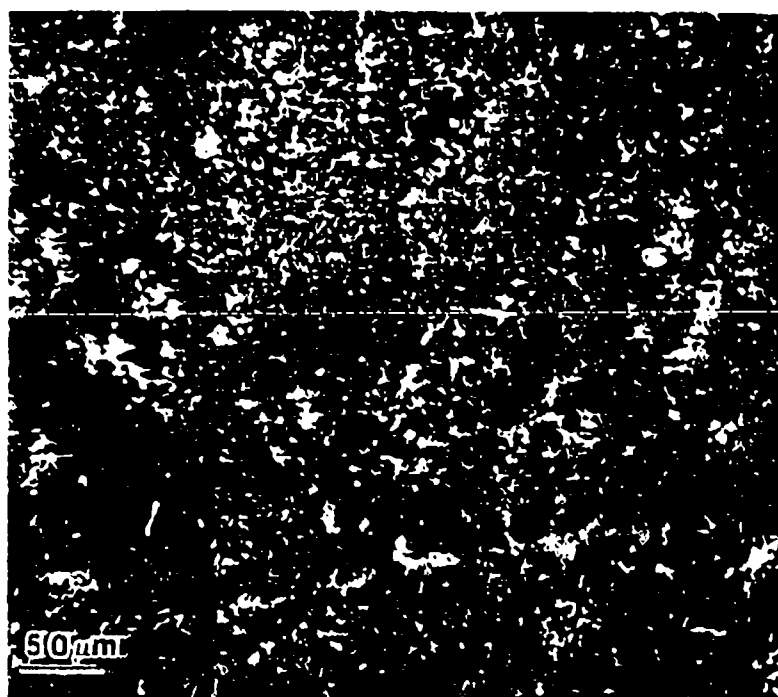
Figure 27a.   SEM micrograph of an inhibited matrix composite packed cemented in the $SiC/Si/Al_2O_3$ mixture and oxidized at 800 $^{\circ}$C.

Figure 28a. SEM micrograph of an inhibited matrix composite packed cemented in the ZrC/SiC/Si mixture and oxidized at 800°C.

Figure 28b. SEM micrograph of an inhibited matrix composite packed cemented in the ZrC/SiC/Si mixture and oxidized at 800°C.

Figure 29a. SEM micrograph of an inhibited matrix composite packed cemented in the $ZrC.SiC/Si/Al_2O_3$ mixture and oxidized at $800^\circ C$.

Figure 29b. SEM micrograph of an inhibited matrix composite packed cemented in the $ZrC/SiC/Si/Al_2O_3$ mixture and oxidized at $800^\circ C$.

to form B_2O_3. The particulates in the glass are probably SiC and perhaps some B_4C that has not yet oxidized.

At 800°C, the SiC coating does not oxidize appreciably to form a protective SiO_2 glass. Figures 26a and 27a are micrographs of the oxidized SiC coating without and with Al_2O_3, respectively. These low magnification micrographs show the cracks in the coating that were formed when cooling from the pack cementation temperatures. The higher magnifications, in Figures 26b and 27b, are representative of the coatings with and without Al_2O_3 and show the discontinuous SiC surface. Since the cracks and discontinuous structure are still present, it is evident that the coating was not able to provide adequate protection over the entire surface of the composite. For this reason, the SiC coatings were unable to provide better protection than the B containing coatings.

ZrC, in the coatings consisting of SiC with ZrC, oxidized readily at this temperature, forming a powdery ZrO_2 coating. This powdery coating easily spalled off the surface, as shown in Figures 28a and 29a, without and with Al_2O_3, respectively. The higher magnifications, Figures 28b and 29b, show the inability of the SiC portion of the coating to seal the surface. These coatings provided the least protection at this temperature, since part of the coating spalled off and the other part was unable to seal the exposed composite.

The overall results of oxidation at $1000^{\circ}C$ are shown in Figure 30, given in percent weight change over time. SEM micrographs of the oxidized surfaces are presented in Figures 31 through 36.

At $1000^{\circ}C$, the vapor pressure of B_2O_3 increases causing it to volatilize. As expected, the oxidation protection provided by the coatings containing SiC with B_4C decreases from the amount of protection provided at $800^{\circ}C$. Figures 31a and 32a show the oxidized surfaces of the coatings without and with Al_2O_3, respectively. The coatings are relatively uniform over the surface, except for the coating obtained with Al_2O_3. It has developed some uniformly spaced depressions in the coating. Higher magnifications, Figures 31b and 32b, indicate the formation of glass, as before, with more particulates present in the glass. This is probably due to the fact that B_2O_3 is volatilizing, leaving a greater percentage of particulates on the surface.

SiC oxidizes at this temperature to form a SiO_2 glass, which begins to flow at $1000^{\circ}C$. At this temperature, the SiO_2 glass is able to slowly flow and seal the cracks in the SiC coating. As a result, it provides better protection against oxidation at this temperature than at $800^{\circ}C$. Although the coatings obtained without and with Al_2O_3 are similar in appearance, as shown in Figures 33a and 34, respectively, the oxidation results are quite different, as shown in Figure 30. This is believed to result from the
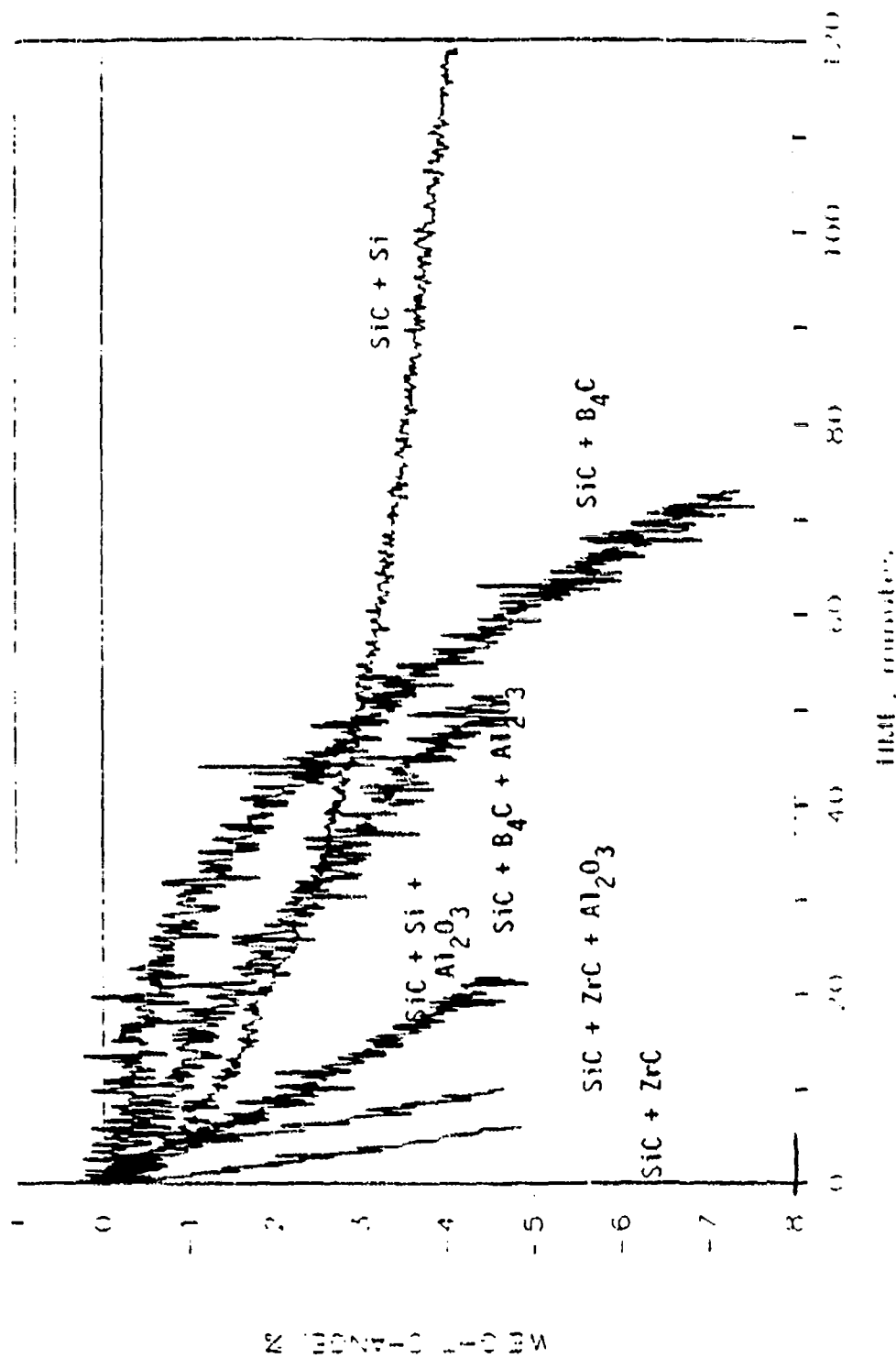
Figure 30. Comparison of Oxidation Results for All Mixtures Tested at 1000°C.
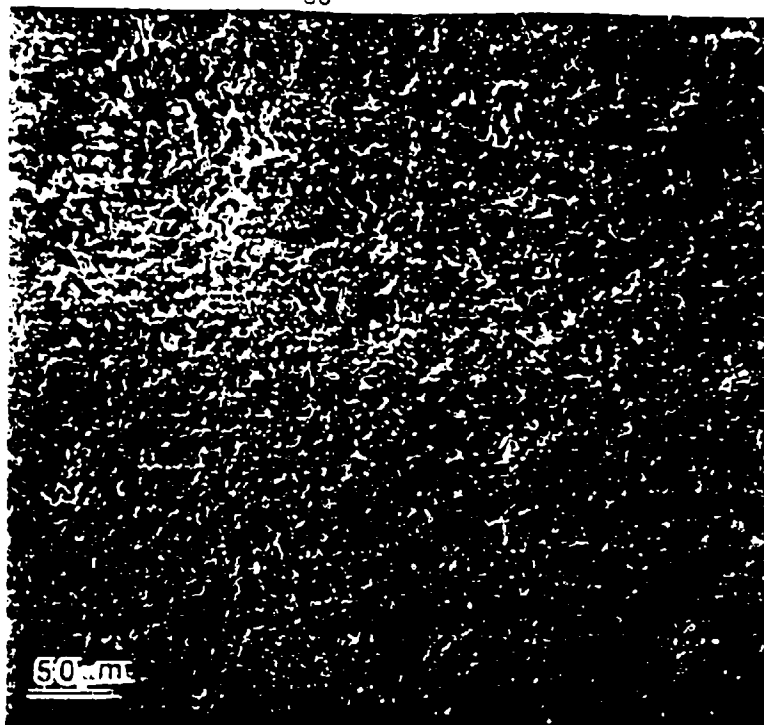
Figure 31a. SEM micrograph of an inhibited matrix composite packed cemented in the ZrC/SiC/B mixture and oxidized at 1000°C.
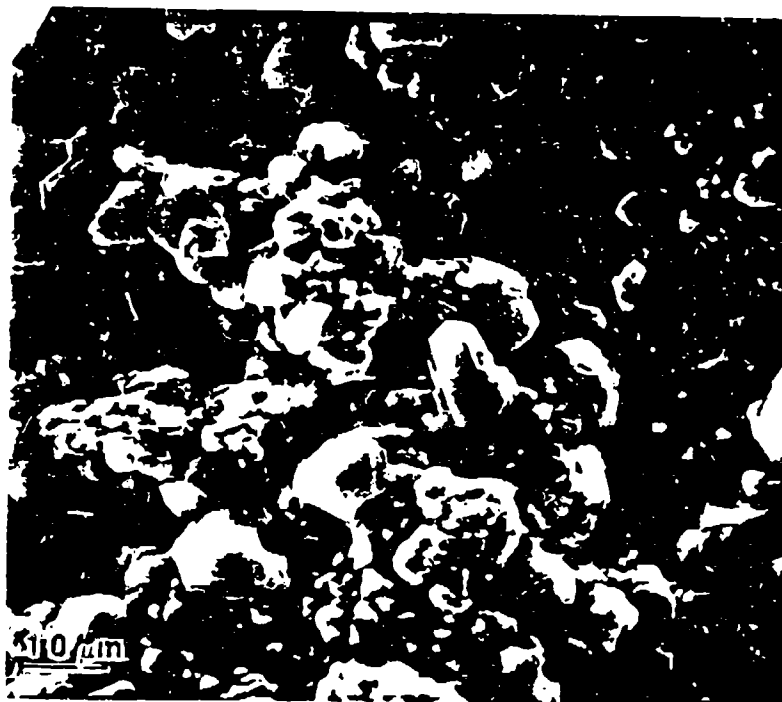
Figure 31b. SEM micrograph of an inhibited matrix composite packed cemented in the ZrC/SiC/B mixture and oxidized at 1000°C.
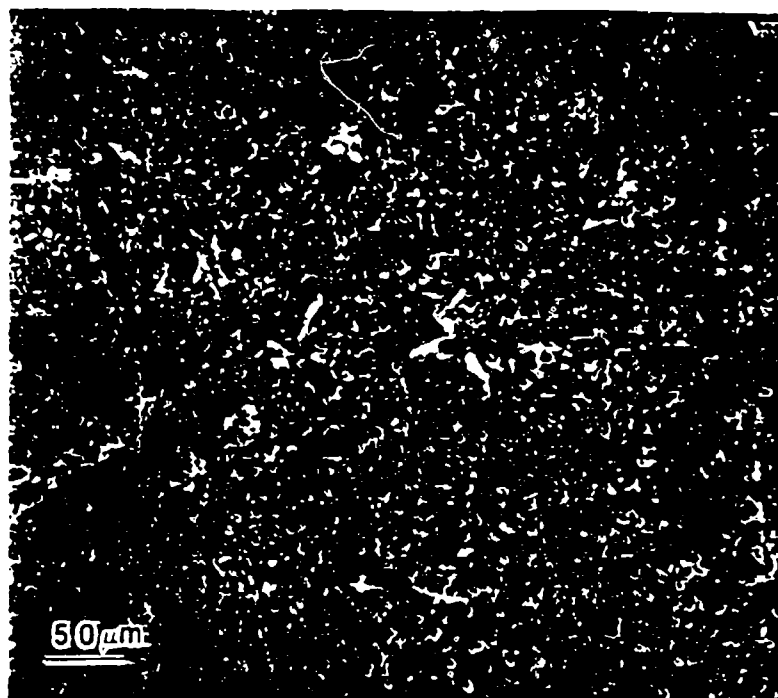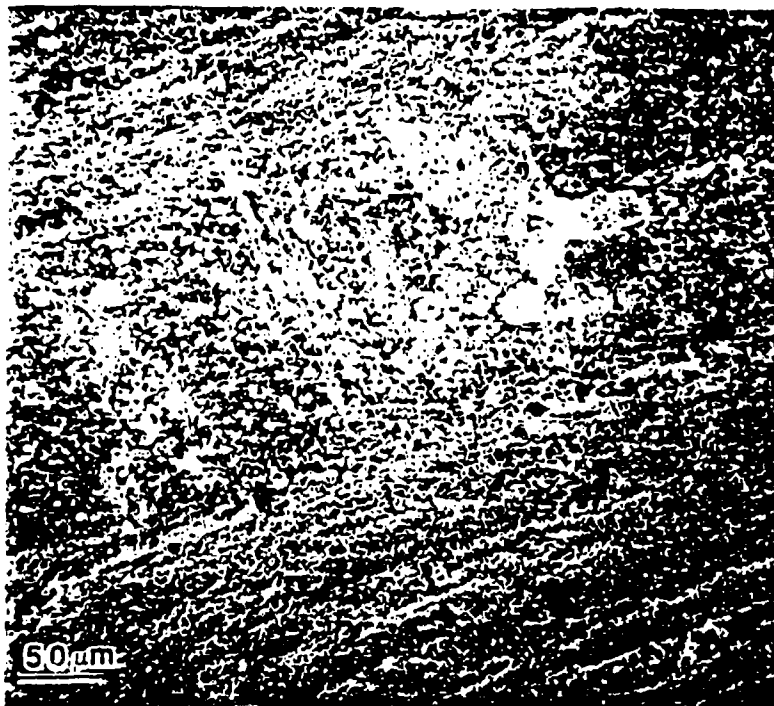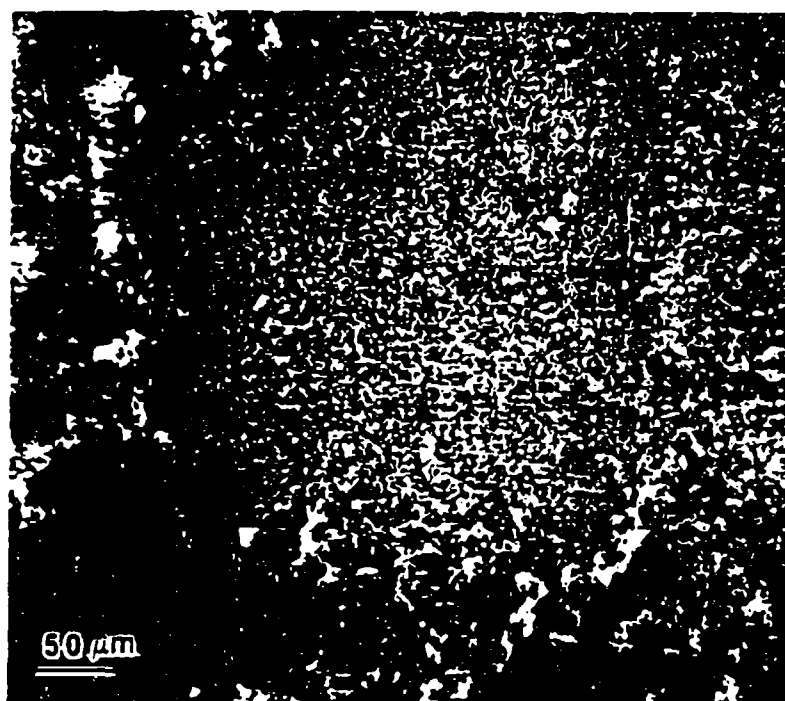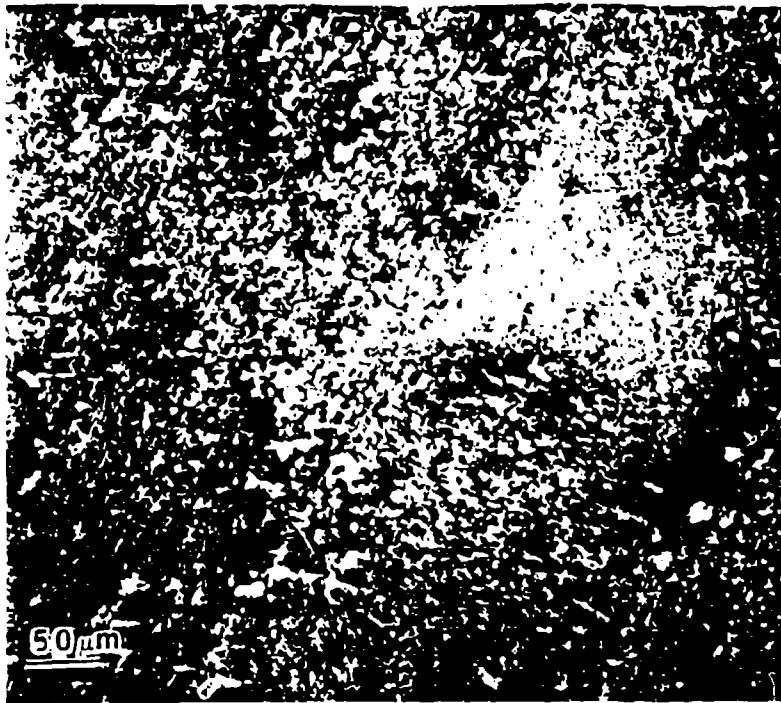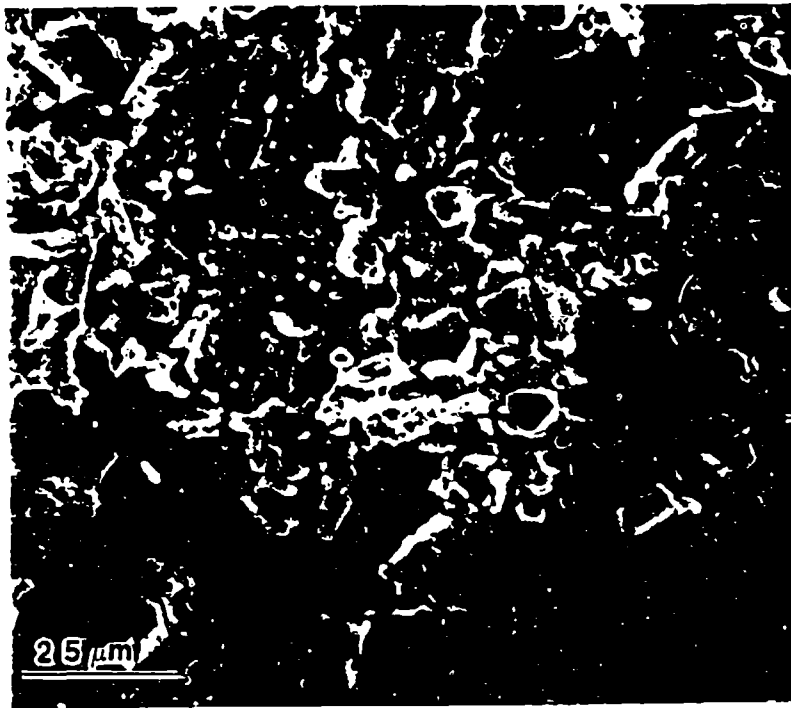
Figure 32a. SEM micrograph of an inhibited matrix composite packed cemented in the ZrC/SiC/B/Al$_2$O$_3$ mixture and oxidized at 1000°C.

Figure 32b. SEM micrograph of an inhibited matrix composite packed cemented in the ZrC/SiC/B/Al$_2$O$_3$ mixture and oxidized at 1000°C.

Figure 33a. SEM micrograph of an inhibited matrix composite packed cemented in the SiC/Si mixture and oxidized at 1000°C.

Figure 33b. SEM micrograph of an inhibited matrix composite packed cemented in the SiC/Si mixture and oxidized at 1000°C.

Figure 33c. Surface details of figure 33a, an inhibited matrix composite packed cemented in the SiC/Si mixture and oxidized at 1000°C.

Figure 34. SEM micrograph of an inhibited matrix composite packed cemented in the SiC/Si/Al$_2$O$_3$ mixture and oxidized at 1000°C.

Figure 35a. SEM micrograph of an inhibited matrix composite packed cemented in the ZrC/SiC/Si mixture and oxidized at 1000°C.

Figure 35b. SEM micrograph of an inhibited matrix composite packed cemented in the ZrC/SiC/Si mixture and oxidized at 1000°C.

Figure 36a. SEM micrograph of an inhibited matrix composite
packed cemented in the ZrC/SiC/Si/Al$_2$O$_3$ mixture and oxidized
at 1000°C.
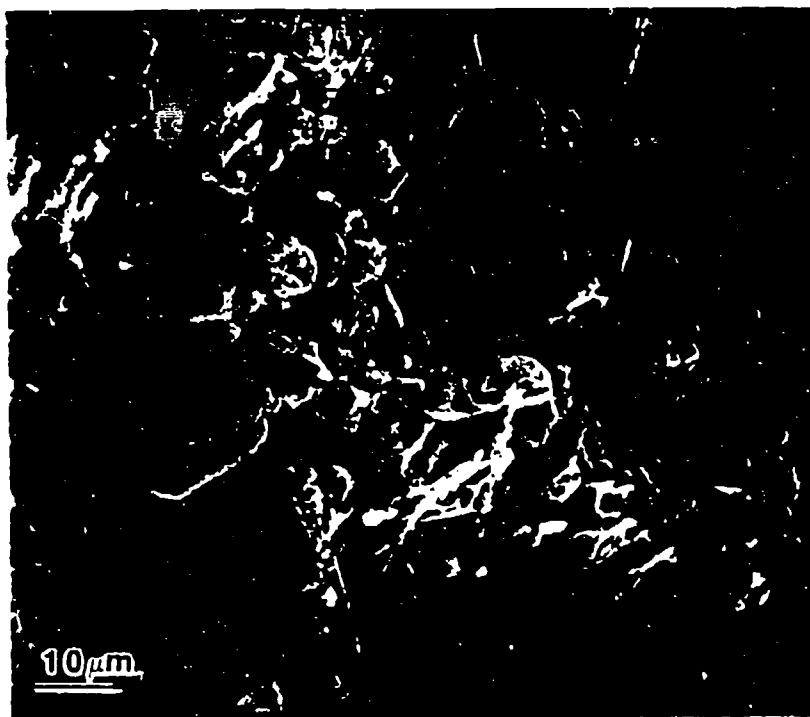
Figure 36b. SEM micrograph of an inhibited matrix composite
packed cemented in the ZrC/SiC/Si/Al$_2$O$_3$ mixture and oxidized
at 1000°C.

thinner layer of conversion on the SiC coatings obtained using Al_2O_3 in the pack composition. Even though there was a hole in the conversion layer of the coating obtained without Al_2O_3, as shown in Figure 33b, the thickness of the surrounding layer is able to provide SiO_2 glass to seal the defect.

ZrC also degrades the SiC coating at 1000^oC, as shown in Figures 35a and 36a. Although the SiC portion of the coating is able to form a glass, as shown in Figures 35b and 36b, it is not able to compensate for the spalled regions that occur from the powdery ZrO_2. Correspondingly, rapid oxidation occurs, as indicated in Figure 30.

Figure 37 shows the results of the oxidation tests conducted at 1200^oC. The corresponding micrographs of the oxidized surfaces are shown in Figures 38 through 43.

At 1200^oC, the vapor pressure of B_2O_3 increases to the point that the vapor begins to disrupt the surface coating in an attempt to escape. This effect can be seen in Figures 38 and 39a, which show the oxidized surfaces are beginning to be disrupted by the vapor pressure. Figure 39b is a higher magnification of a disrupted area, revealing major bubble formation.

The SiC coating, obtained without Al_2O_3, provides excellent protection at 1200^oC, as seen in Figure 37. After 12 hours at temperature, it maintained a steady 1% weight loss. The reason it again provided better protection than
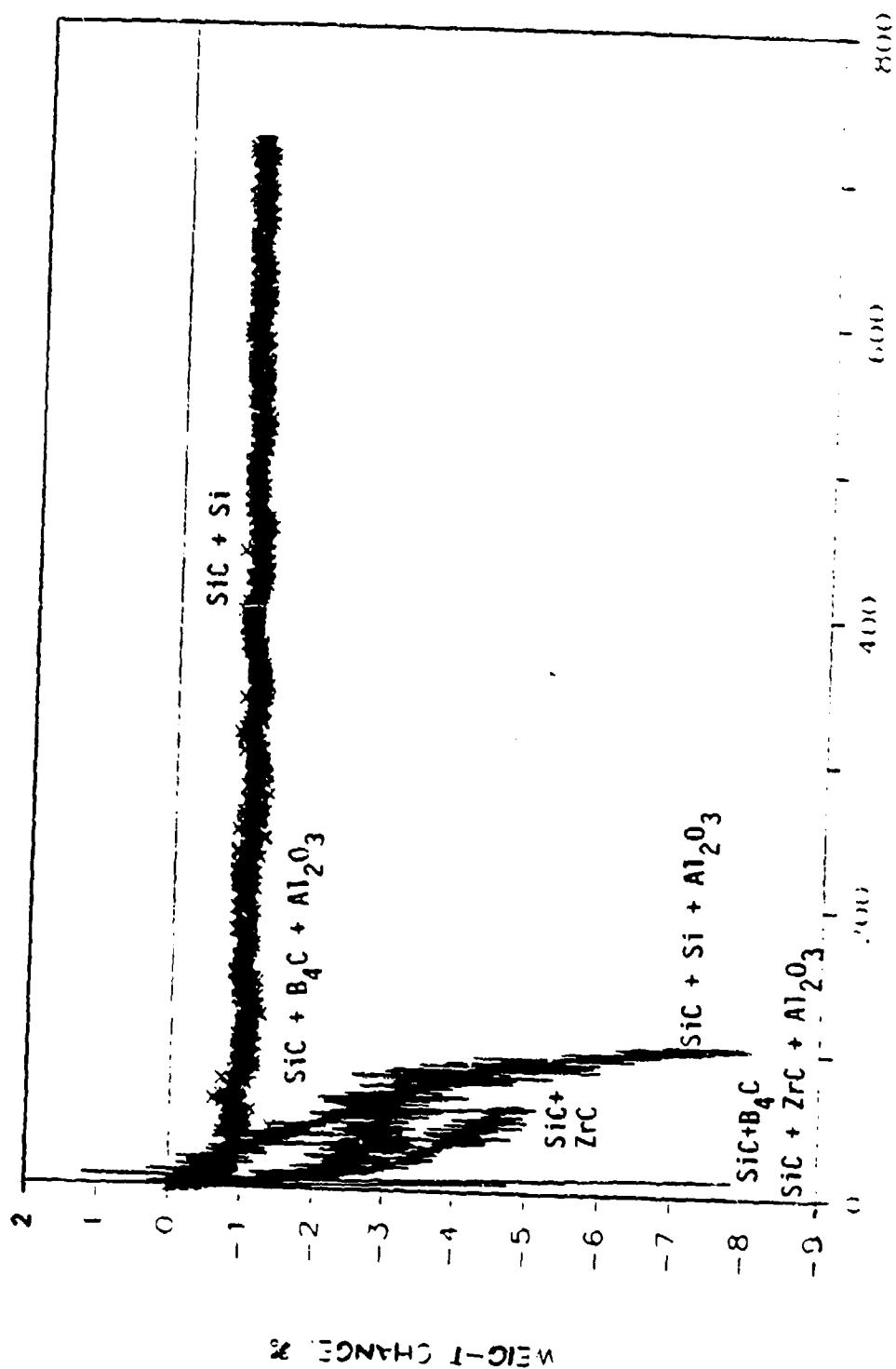
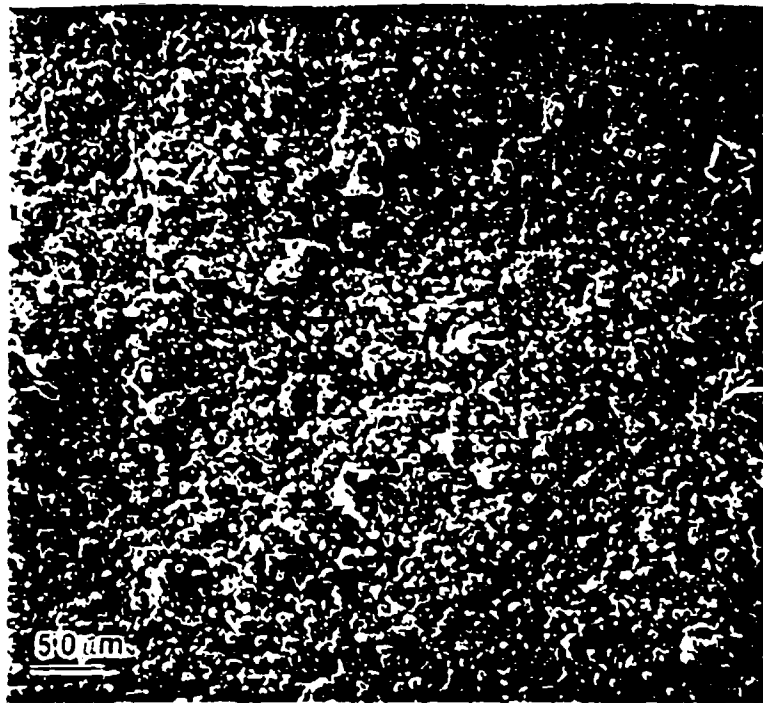Figure 37. Comparison of Oxidation Results for All Mixtures Tested at 1200°C.

Figure 38a. SEM micrograph of an inhibited matrix composite packed cemented in the ZrC/SiC/B mixture and oxidized at 1200°C.

Figure 38b. SEM micrograph of an inhibited matrix composite packed cemented in the ZrC/SiC/B mixture and oxidized at 1200°C.

Figure 40. SEM micrograph of an inhibited matrix composite packed cemented in the SiC/Si mixture and oxidized at 1200°C.
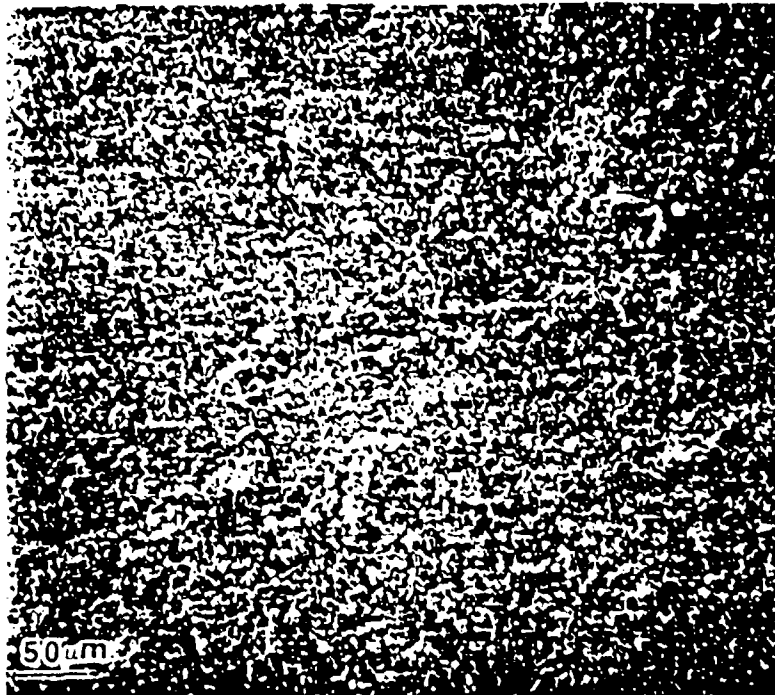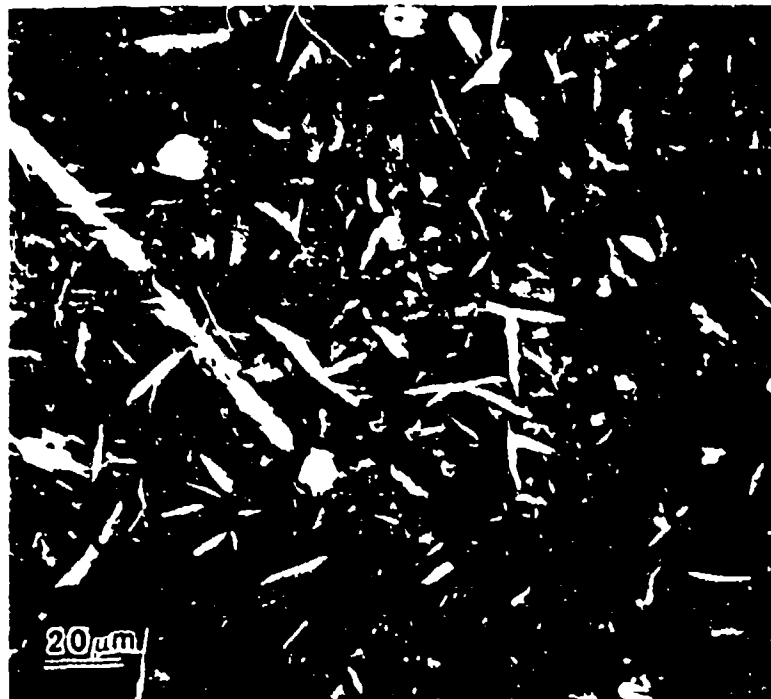
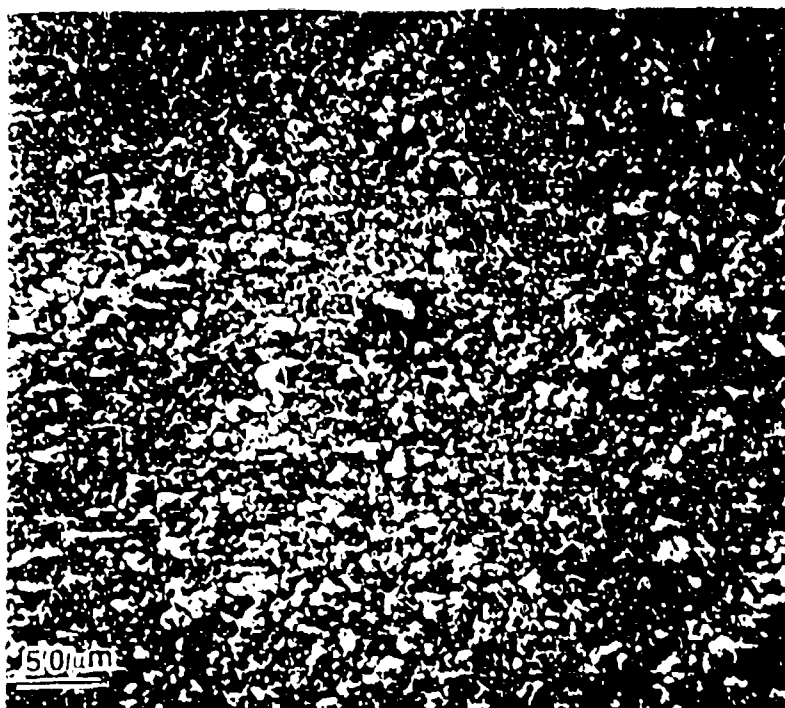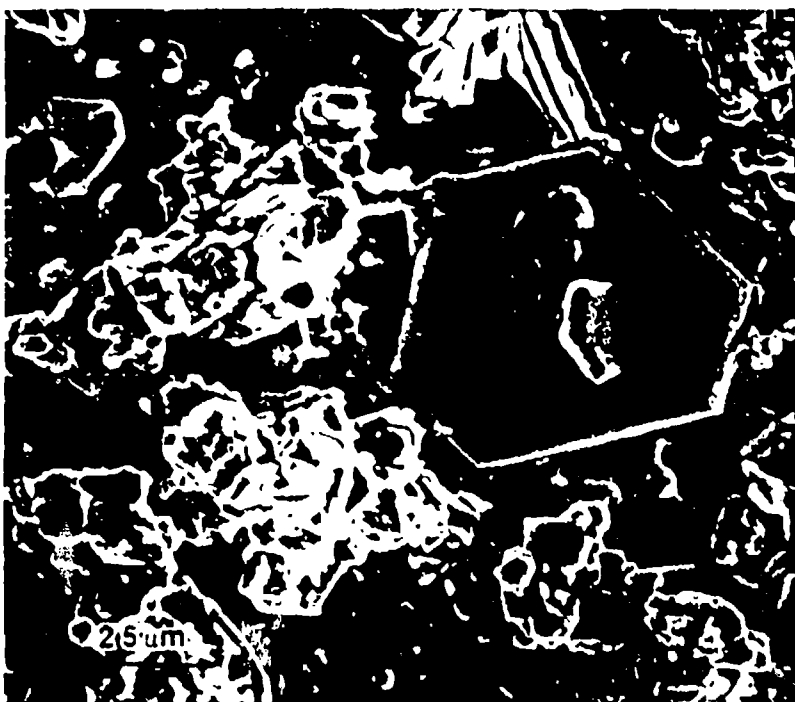Figure 41a. SEM micrograph of an inhibited matrix composite packed cemented in the SiC/Si/Al$_2$O$_3$ mixture and oxidized at 1200°C.

Figure 41b. SEM micrograph of an inhibited matrix composite packed cemented in the SiC/Si.Al$_2$O$_3$ mixture and oxidized at 1200°C.

Figure 42a. SEM micrograph of an inhibited matrix composite packed cemented in the ZrC/SiC/Si mixture and oxidized at 1200°C.
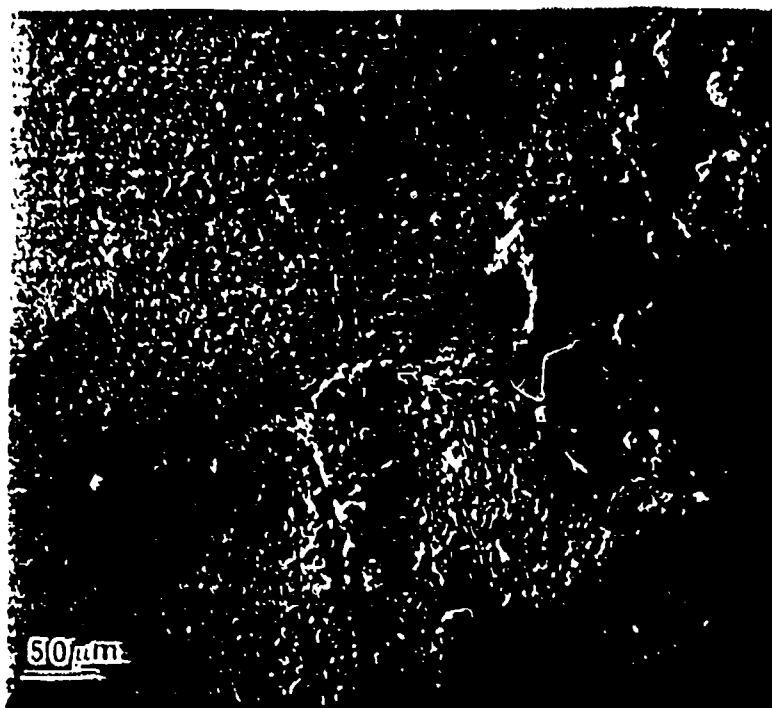

Figure 42b. SEM micrograph of an inhibited matrix composite packed cemented in the ZrC/SiC/Si mixture and oxidized at 1200°C.

Figure 43a.   SEM micrograph of an inhibited matrix composite packed cemented in the ZrC/SiC. Si/Al$_2$O$_3$ mixture and oxidized at 1200°C.
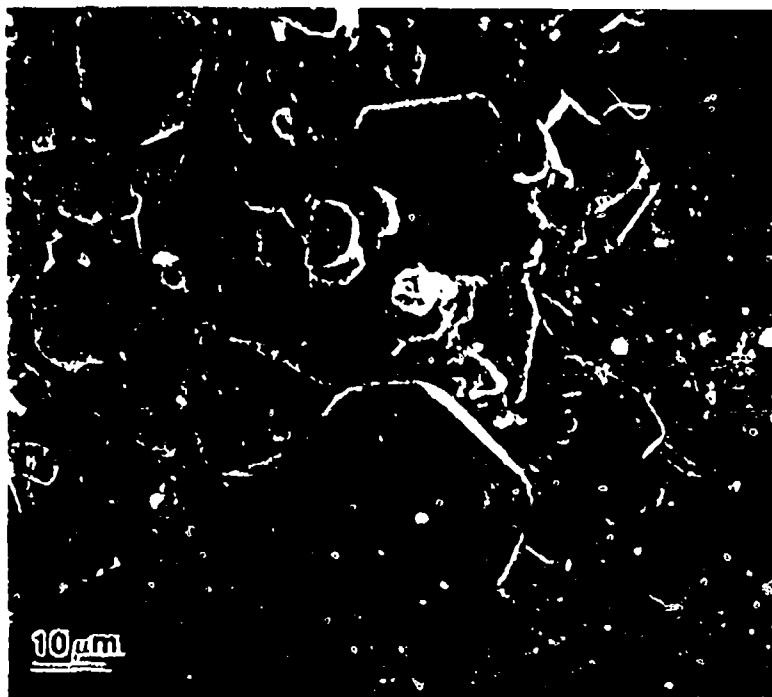
Figure 43b.   SEM micrograph of an inhibited matrix composite packed cemented in the ZrC/SiC. Si/Al$_2$O$_3$ mixture and oxidized at 1200°C.

the SiC coating obtained with Al_2O_3 is it has a thicker conversion layer, providing more coating with which to establish a protective seal over the surface of the composite. From the low magnification micrographs in Figures 40 and 41a, it appears that the oxidized surface of the composite without Al_2O_3 is more discontinuous than the composite with Al_2O_3. Which, based on earlier results, would indicate a coating that does not provide complete protection. However, in the higher magnification shown in Figure 41b, which is representative of the coatings obtained with or without Al_2O_3, it is evident that a glass layer has formed beneath the surface particles. Below the discontinuous surface, shown in Figure 40 is a protective glass seal.

The SiC in the SiC coating containing ZrC, is able to form a protective glass, which flows more easily at this temperature, to seal the surface of the composite before major spalling of the oxidized ZrC occurs. This results in a significant increase in its oxidation protection, as shown in Figure 37. Figures 42a and 43a show a more continuous coating than observed at the previous oxidation temperatures. The higher magnifications, Figures 42b and 43b, show the glass formation around the particulates.

The results of the $1400^\circ C$ oxidation tests are shown in Figure 44, with the corresponding micrographs of the oxidized surfaces shown in Figures 45-50. Although the
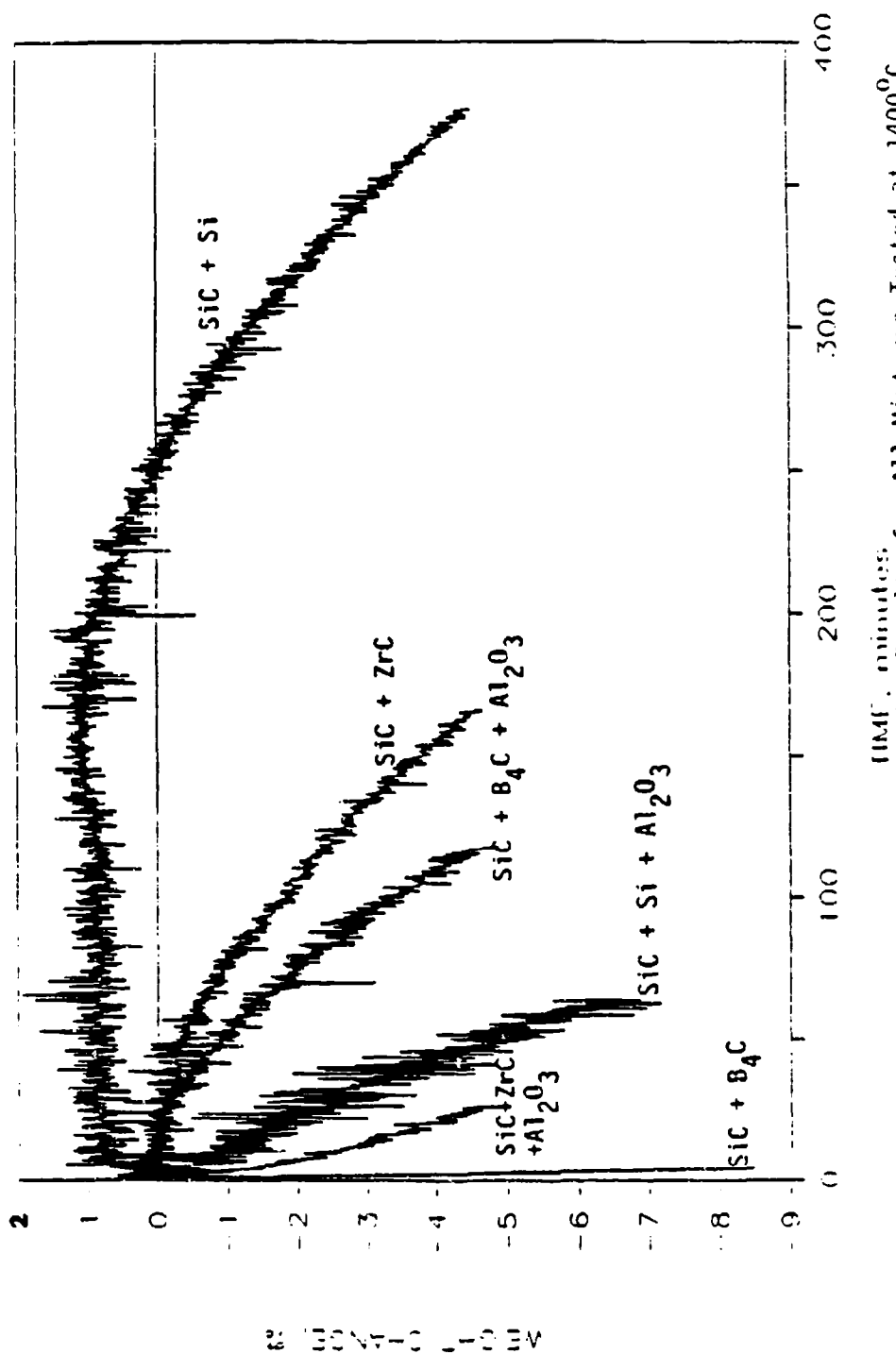
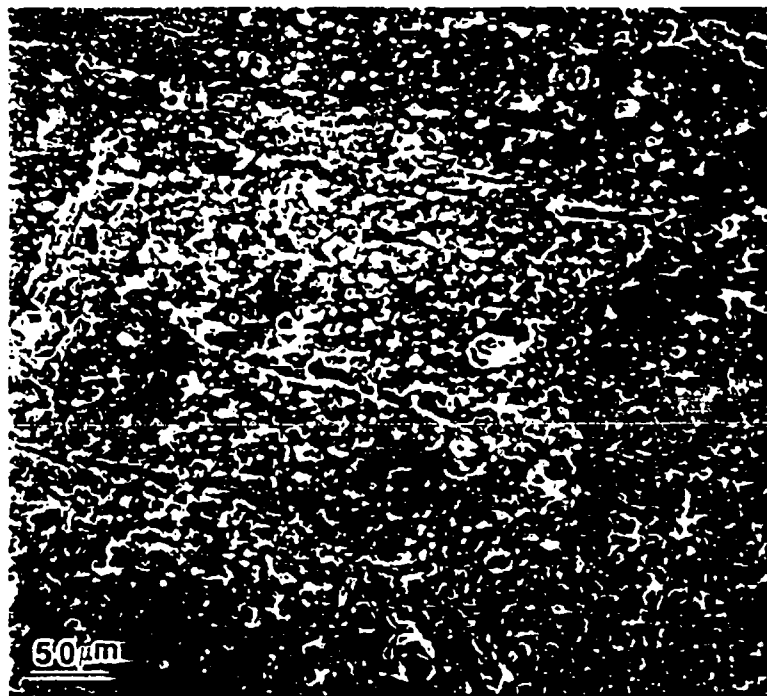Figure 44. Comparison of Oxidation Results for All Mixtures Tested at 1400°C.

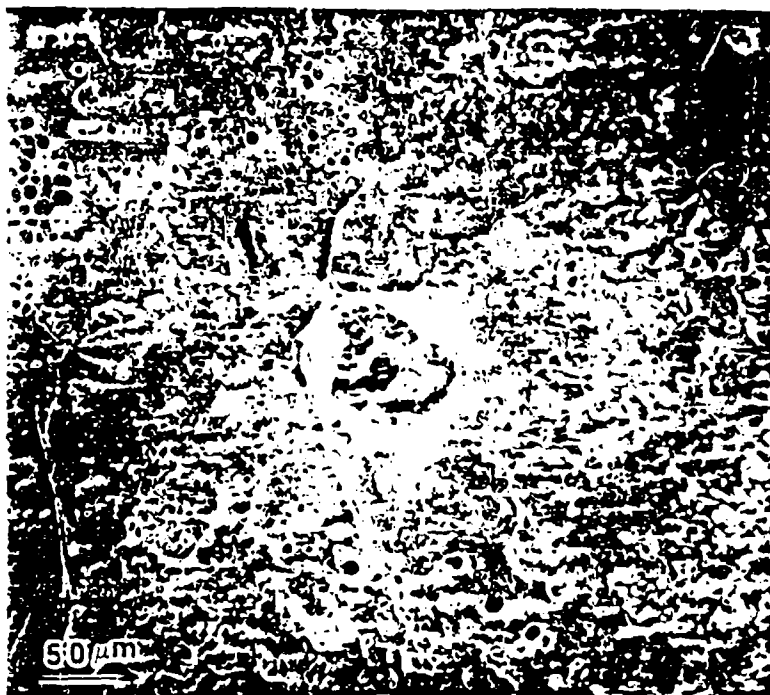Figure 45. SEM micrograph of an inhibited matrix composite packed cemented in the ZrC/SiC/B mixture and oxidized at 1400°C.

Figure 46a. SEM micrograph of an inhibited matrix composite packed cemented in the ZrC/SiC/B/Al$_2$O$_3$ mixture and oxidized at 1400°C.

Figure 46b. SEM micrograph of an inhibited matrix composite packed cemented in the ZrC/SiC/B/Al$_2$O$_3$ mixture and oxidized at 1400°C.
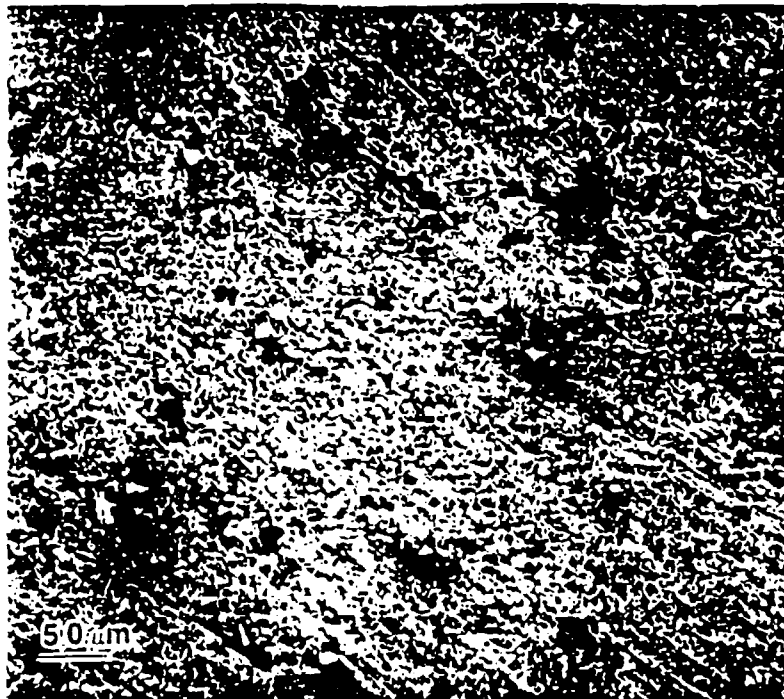
104

Figure 47a.   SEM micrograph of an inhibited matrix composite
packed cemented in the SiC/Si mixture and oxidized at
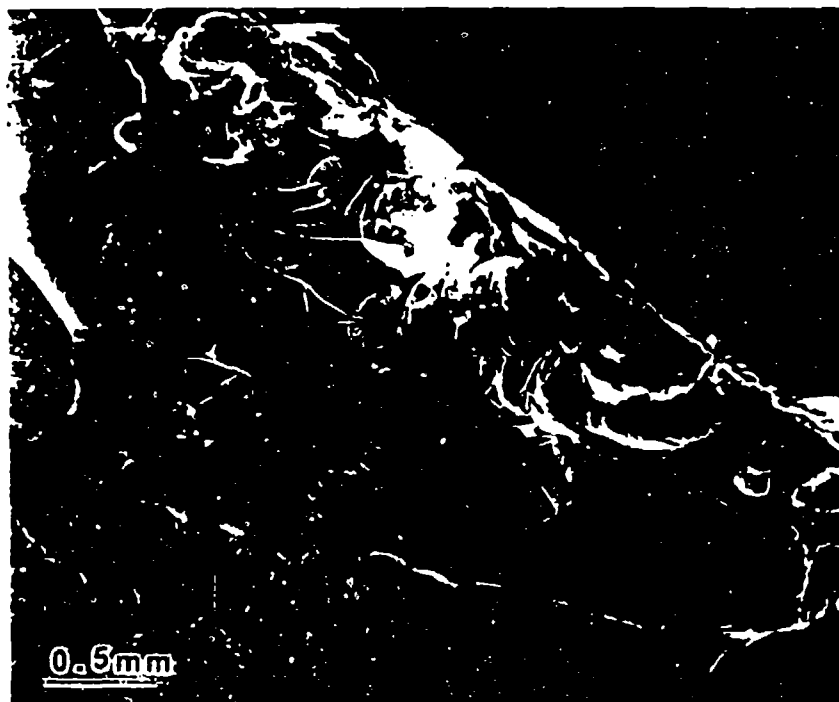1400°C.

Figure 47b.   SEM micrograph of an inhibited matrix composite
packed cemented in the SiC/Si mixture and oxidized at
1400°C.

Figure 48a.   SEM micrograph of an inhibited matrix composite
packed cemented in the SiC/Si/Al$_2$O$_3$ mixture and oxidized at
1400°C.

Figure 48b. Surface details of figure 48a, an inhibited
matrix composite packed cemented in the SiC/Si/Al$_2$O$_3$ mixture
and oxidized at 1400°C.

Figure 49a. SEM micrograph of an inhibited matrix composite
packed cemented in the ZrC/SiC/Si mixture and oxidized at
1400°C.

Figure 49b. SEM micrograph of an inhibited matrix composite
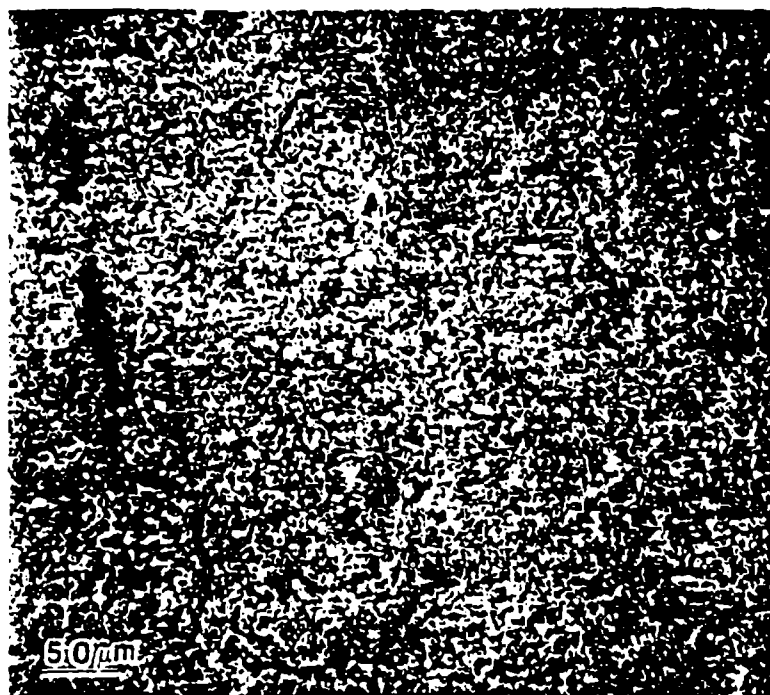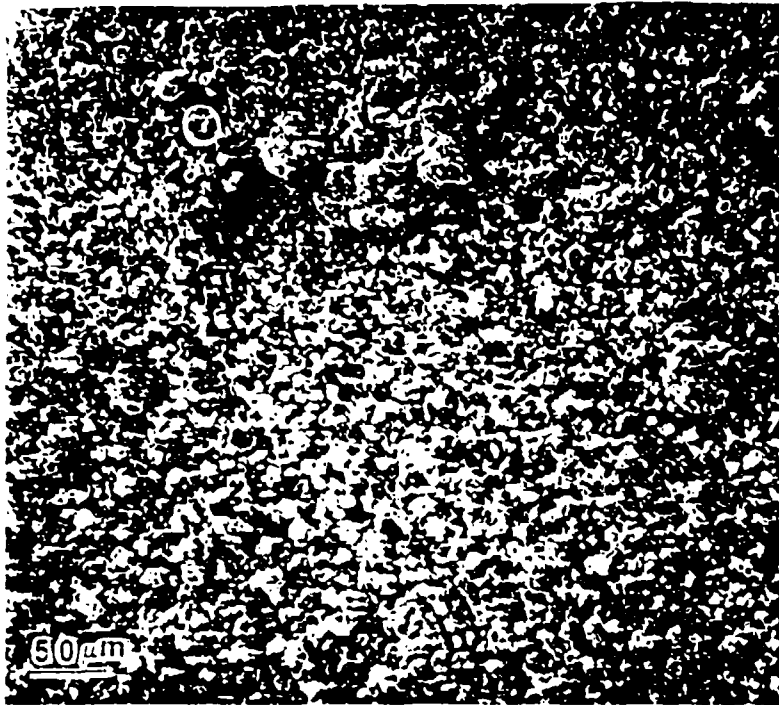packed cemented in the ZrC/SiC/Si mixture and oxidized at
1400°C.

Figure 50a. SEM micrograph of an inhibited matrix composite packed cemented in the ZrC/SiC/Si/Al$_2$O$_3$ mixture and oxidized at 1400°C.
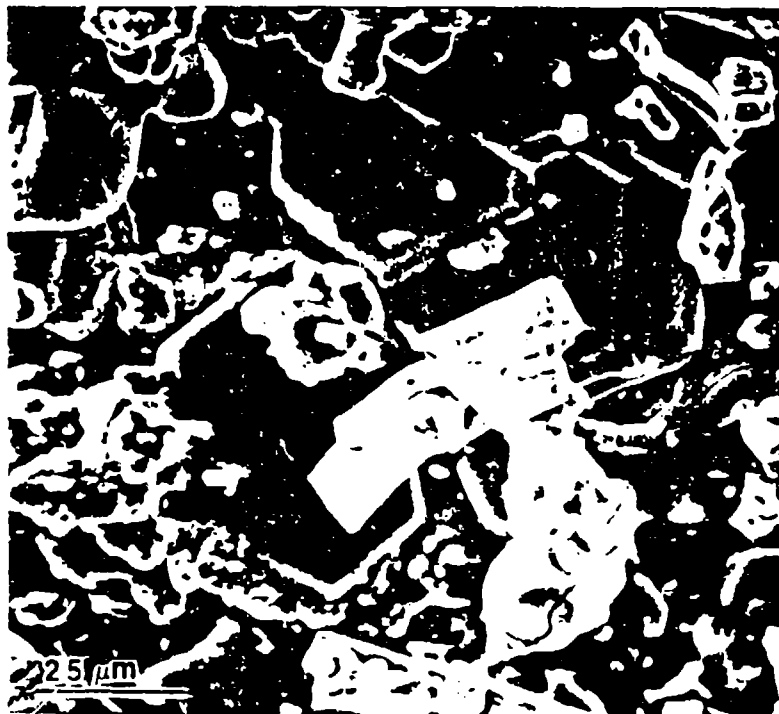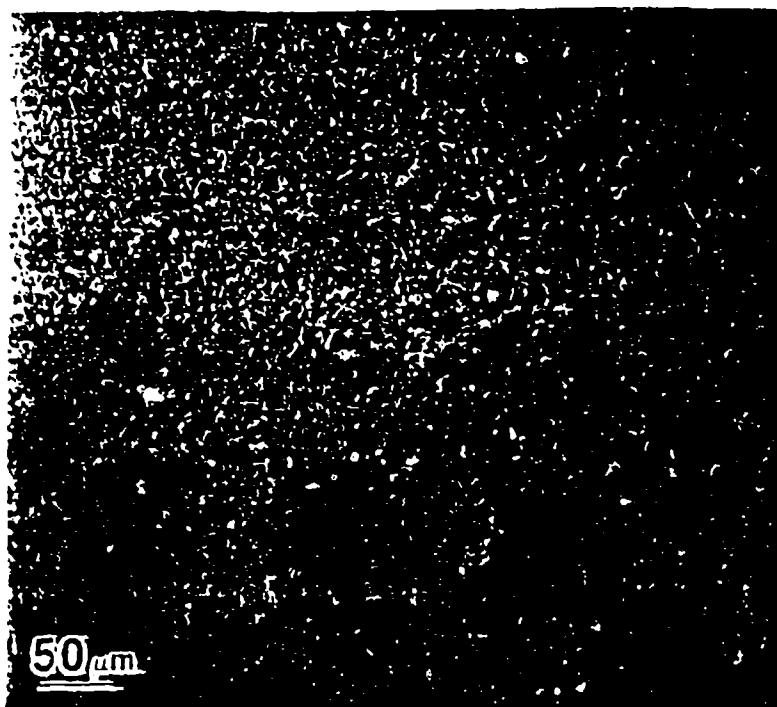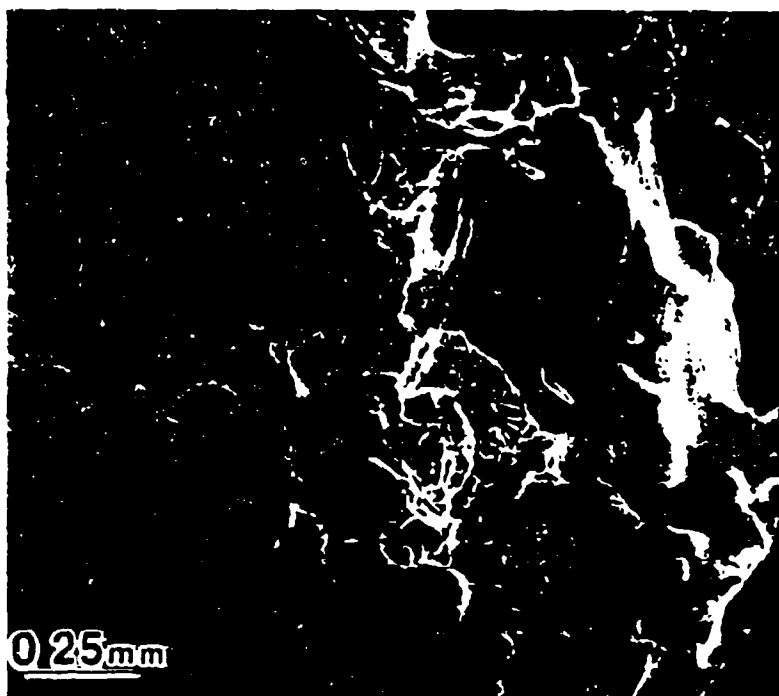

Figure 50b. SEM micrograph of an inhibited matrix composite packed cemented in the ZrC/SiC/Si/Al$_2$O$_3$ mixture and oxidized at 1400°C.

vapor pressure of B_2O_3 is prohibitively high at this
temperature, the SiC with B_4C obtained with Al_2O_3 provided
adequate protection for almost 150 minutes, see Figure 44.
The surface of this composite, as shown in Figure 46a, is
covered in a protective glassy film. This film is probably
a borosilicate glass, which has been reported to form at
this temperature from the reaction of B or B_4C with Si or
SiC.[36] Although bubble formation in the coating is present,
as shown in Figure 46a, a higher magnification of a bubble
broken after the test, Figure 46b, indicates there is a
continuous coating under the glassy film which would
oxidize, forming more of the protective oxide if the bubble
would have erupted during the test.

The SiC with B_4C coating obtained without Al_2O_3 was
thinner than the above coating, as mentioned previously.
The coating was probably too thin to provide enough material
for the borosilicate formation and protect the composite
until the glass did form. This resulted in an inferior
coating that left the composite exposed to oxidation, as
shown in Figure 45.

The SiC coating obtained without Al_2O_3, again provided
the best protection at this temperature, as shown in Figure
47. The thinner SiC coating obtained with Al_2O_3 provided
significantly lower protection, Figure 48.

The protection of the SiC with ZrC coatings improved
over 1200°C oxidation tests, as indicated by comparing

Figures 37 and 44. As before, the coating obtained without Al_2O_3 provided significantly better protection than the one obtained using Al_2O_3. The oxidized surfaces of both coatings at this temperature are similar to the oxidized surfaces at $1200^{\circ}C$, as seen in Figures 42-43 and 49-50.

Figure 51 shows the results of the oxidation tests conducted at $1600^{\circ}C$. Figures 52 through 57 are the micrographs of the oxidized surfaces.

The protection provided by the SiC with B_4C coatings decreases drastically from the $1400^{\circ}C$ tests. The oxidized surfaces shown in Figures 52 and 53 indicate that even though there was some glass formation, it wasn't enough to protect the composite. The vapor pressures at this temperature caused the surface coating to quickly volatilize.

The micrographs of the oxidized surfaces of the SiC coatings, shown in Figures 54a and 55a, indicate uniform coatings with protective glass formation. However, the results in Figure 51 reveal that the protection provided by these coatings has diminished from the protection at lower temperatures.

Although the protection of the SiC with ZrC coatings has also decreased from that provided at $1400^{\circ}C$, the coating obtained with alumina has provided the best protection at this temperature. Figures 56a and 57a indicate that in addition to glass formation, there is some bubble formation

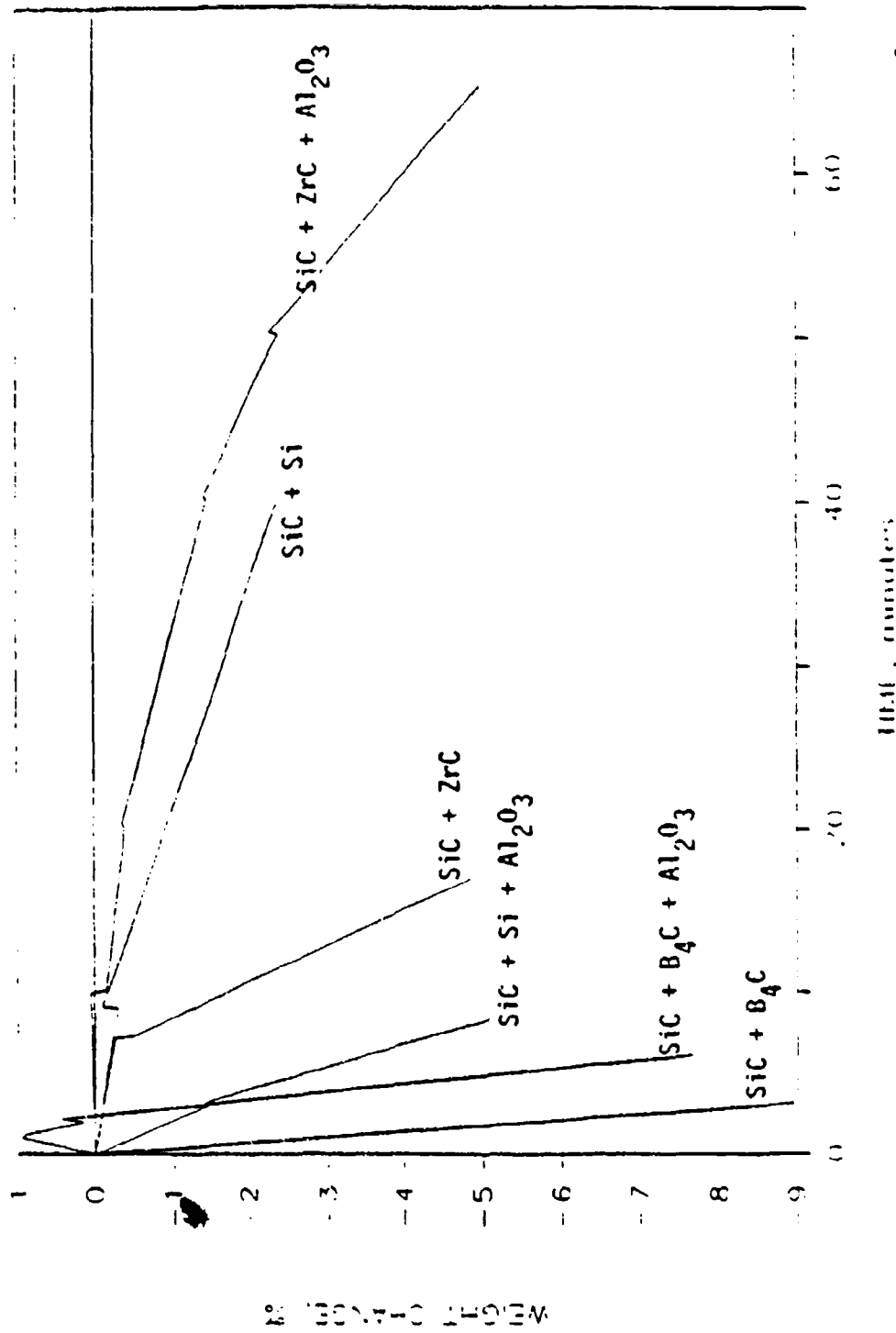Figure 51. Comparison of Oxidation Results for All Mixtures Tested at 1600°C.

111

Figure 52.   SEM micrograph of an inhibited matrix composite packed cemented in the ZrC/SiC/B mixture and oxidized at $1600^{o}C$.

Figure 53.   SEM micrograph of an inhibited matrix composite packed cemented in the ZrC/SiC/B/Al_2O_3 mixture and oxidized at $1600^{o}C$.

This page intentionally left blank.

Figure 54a. SEM micrograph of an inhibited matrix composite
packed cemented in the SiC/Si mixture and oxidized at
1600°C.

Figure 54b. SEM micrograph of an inhibited matrix composite
packed cemented in the SiC/Si mixture and oxidized at
1600°C.

Figure 55a. SEM micrograph of an inhibited matrix composite packed cemented in the $SiC/Si/Al_2O_3$ mixture and oxidized at $1600^{\circ}C$.

Figure 55b. Surface details of figure 55a, an inhibited matrix composite packed cemented in the $SiC/Si/Al_2O_3$ mixture and oxidized at $1600^{\circ}C$.
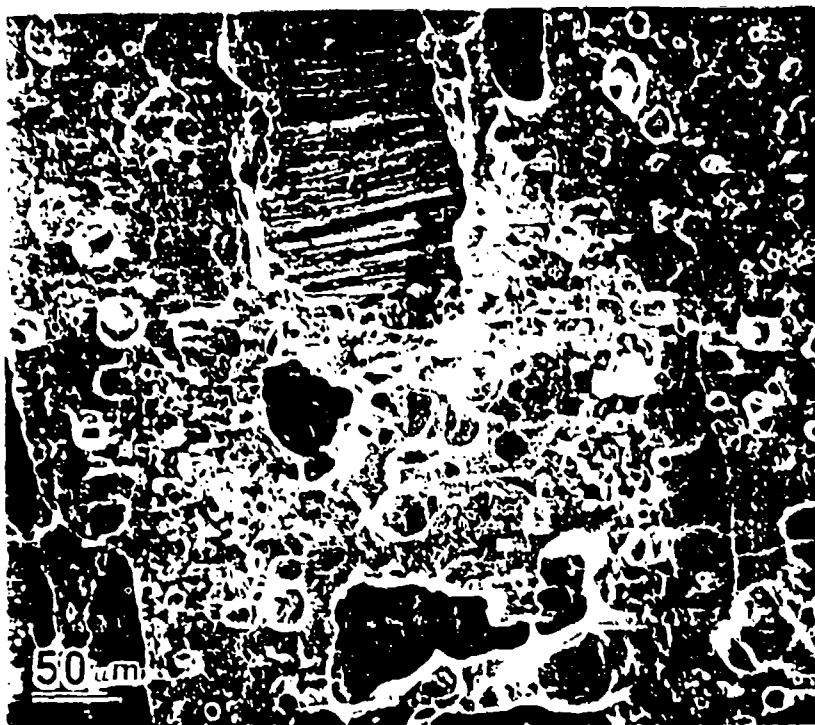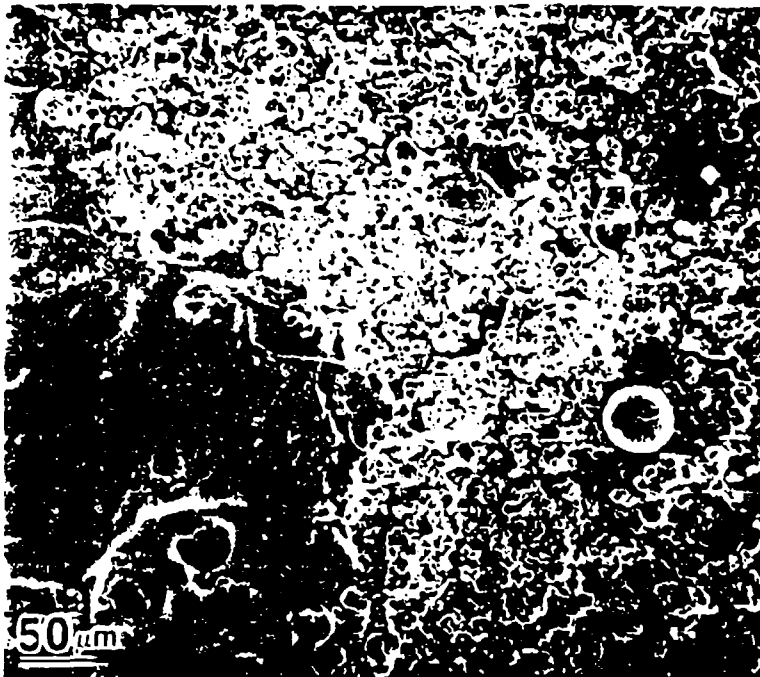
Figure 56a. SEM micrograph of an inhibited matrix composite packed cemented in the ZrC/SiC/Si mixture and oxidized at 1600°C.

Figure 56b. SEM micrograph of an inhibited matrix composite packed cemented in the ZrC SiC/Si mixture and oxidized at 1600°C.

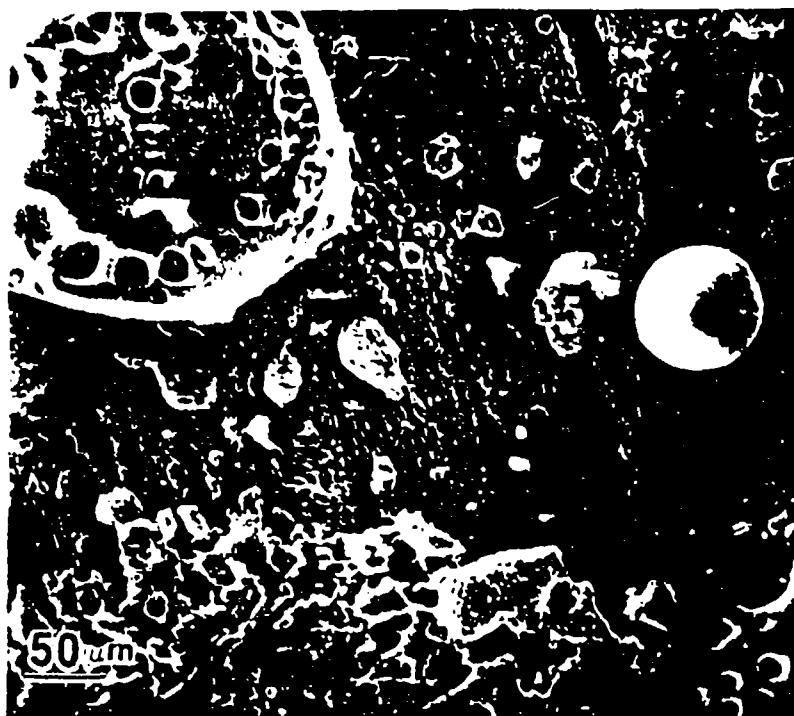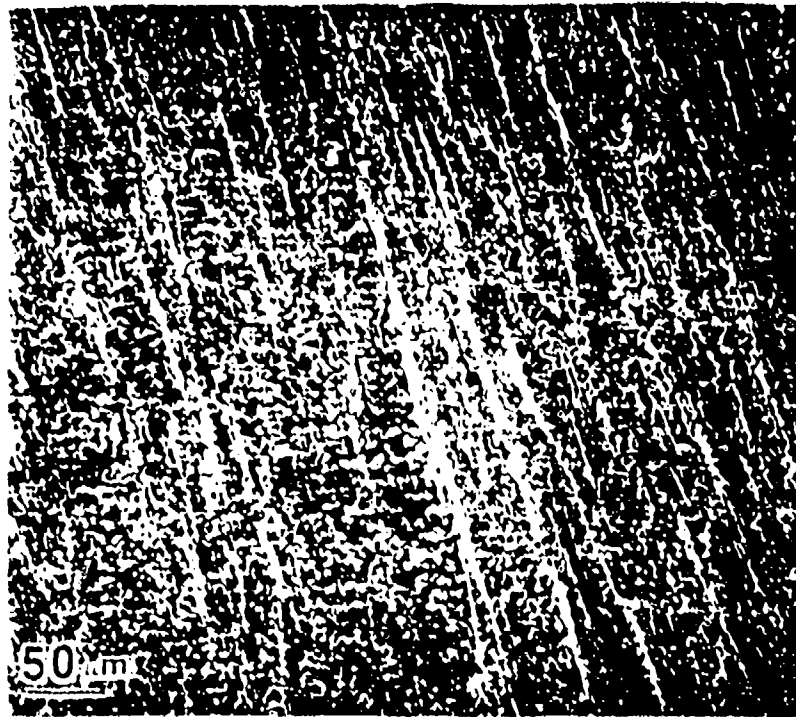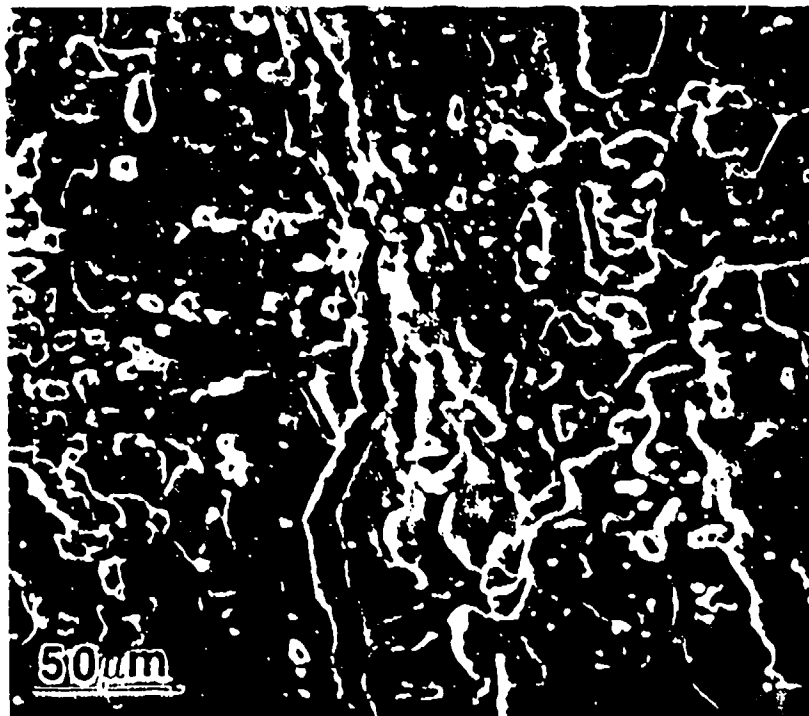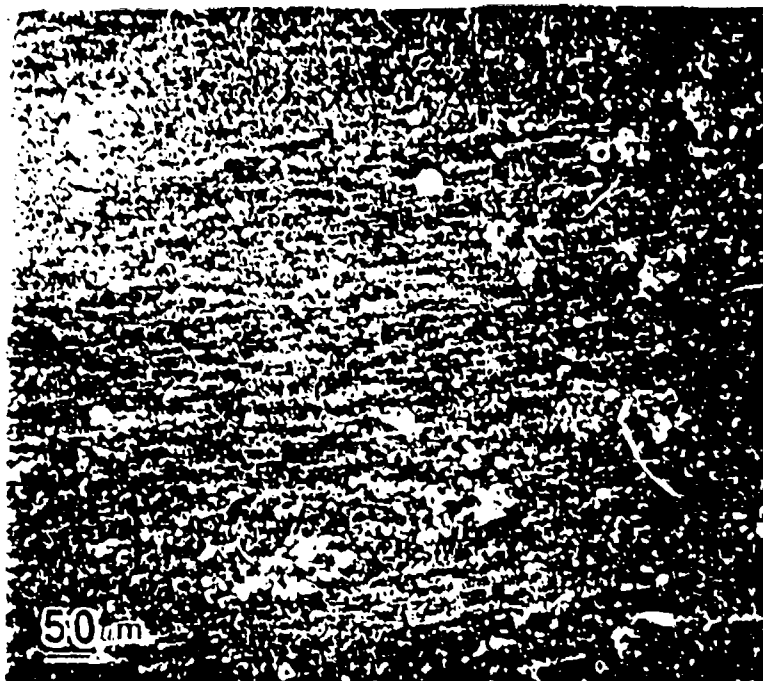Figure 57a. SEM micrograph of an inhibited matrix composite packed cemented in the ZrC/SiC/Si/Al$_2$O$_3$ mixture and oxidized at 1600°C.

Figure 57b. SEM micrograph of an inhibited matrix composite packed cemented in the ZrC/SiC/Si/Al$_2$O$_3$ mixture and oxidized at 1600°C.

begining in the coating. The bubble formation is clearer in the higher magnifications, given in Figures 56b and 57b.

Specimens of each composition were also oxidized at $1800^{\circ}C$. The results are presented in Figure 58. The oxidized surfaces are shown in Figures 59 through 64.

At $1800^{\circ}C$, the SiC + B_4C coatings quickly volatilize, leaving the surface of the composite open to rapid oxidation, as shown in Figures 59 and 60. The coating obtained with Al_2O_3 lasted twice as long as the coating obtained without. This is probaly due to the additional thickness of the coating obtained with Al_2O_3, as the results in Figure 58 indicate that both coatings failed in a matter of minutes.

At this temperature the SiC coatings, also volatilized leaving the composite vulnerable to oxidation. In Figure 61, the SiC coating obtained without Al_2O_3 is shown to have some glass formation and conversion layer still offering some protection to the composite. The lack of a protective layer shown in Figure 62 of the SiC coating obtained with Al_2O_3, readily explains the inferior protection provided by this coating.

The SiC + ZrC coating obtained without Al_2O_3, provided some protection. However, it too left large regions of the composite exposed, as shown in Figure 63. The thicker coating obtained with Al_2O_3 provided the best protection. Figure 64 shows the glassy film covering the composite.

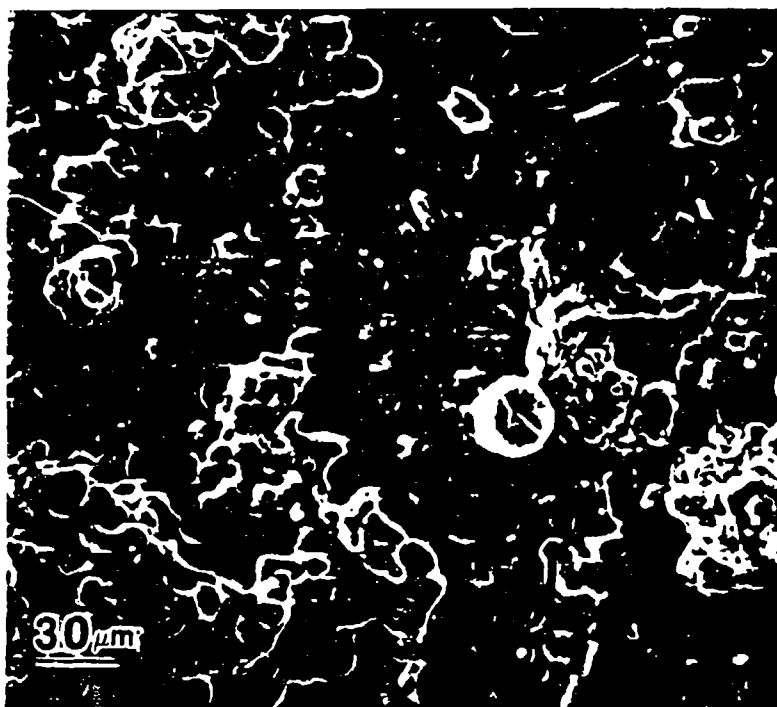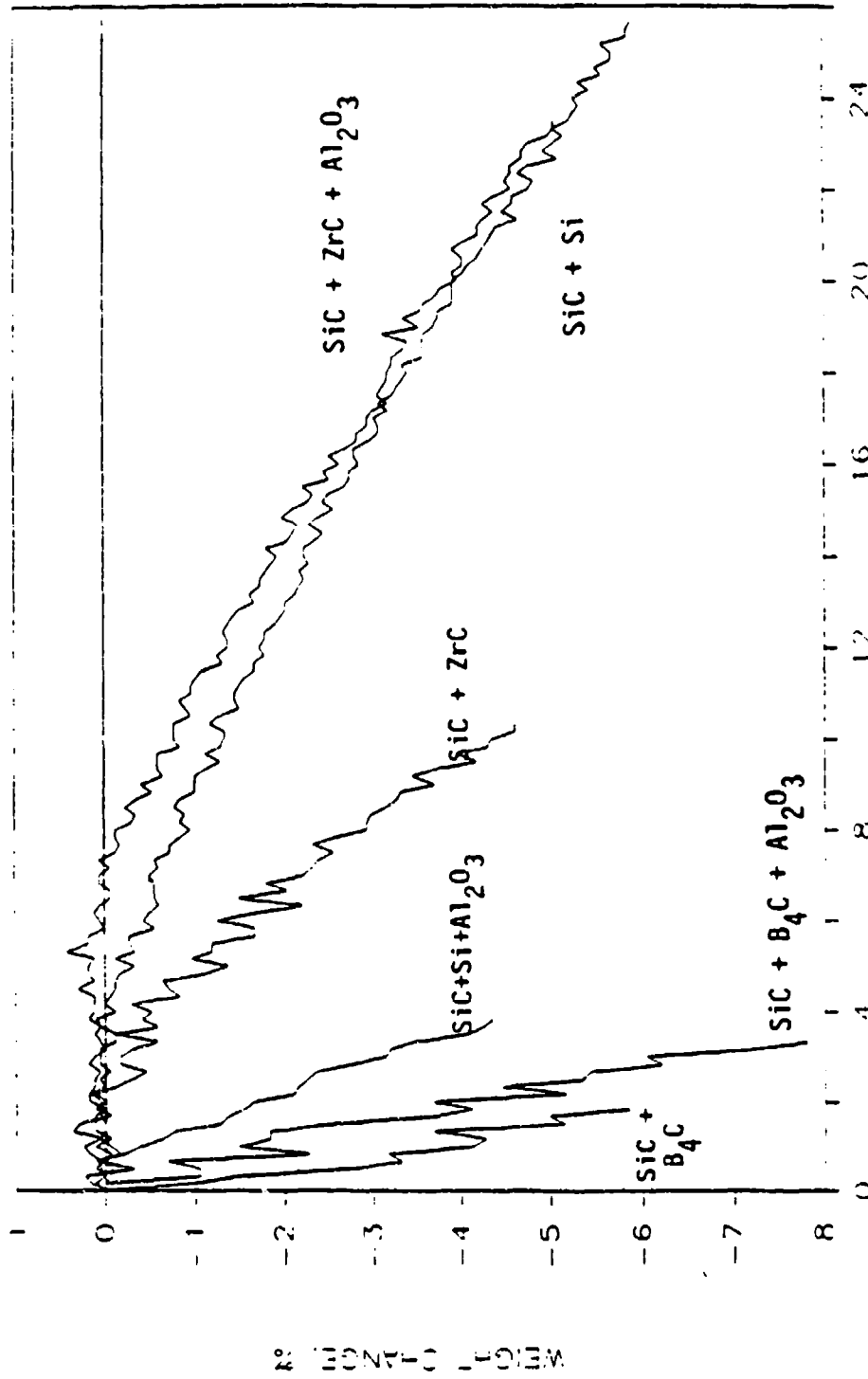Figure 58. Comparison of Oxidation Results for All Mixtures Tested at 1800°C.

Figure 59. SEM micrograph of an inhibited matrix composite packed cemented in the ZrC/SiC/B mixture and oxidized at 1800°C.

Figure 60. SEM micrograph of an inhibited matrix composite packed cemented in the ZrC/SiC/B/Al$_2$O$_3$ mixture and oxidized at 1800°C.

Figure 61. SEM micrograph of an inhibited matrix composite packed cemented in the SiC/Si mixture and oxidized at 1800°C.

Figure 62. SEM micrograph of an inhibited matrix composite packed cemented in the SiC/Si/Al$_2$O$_3$ mixture and oxidized at 1800°C.

Figure 63. SEM micrograph of an inhibited matrix composite packed cemented in the ZrC/SiC/Si mixture and oxidized at 1800°C.
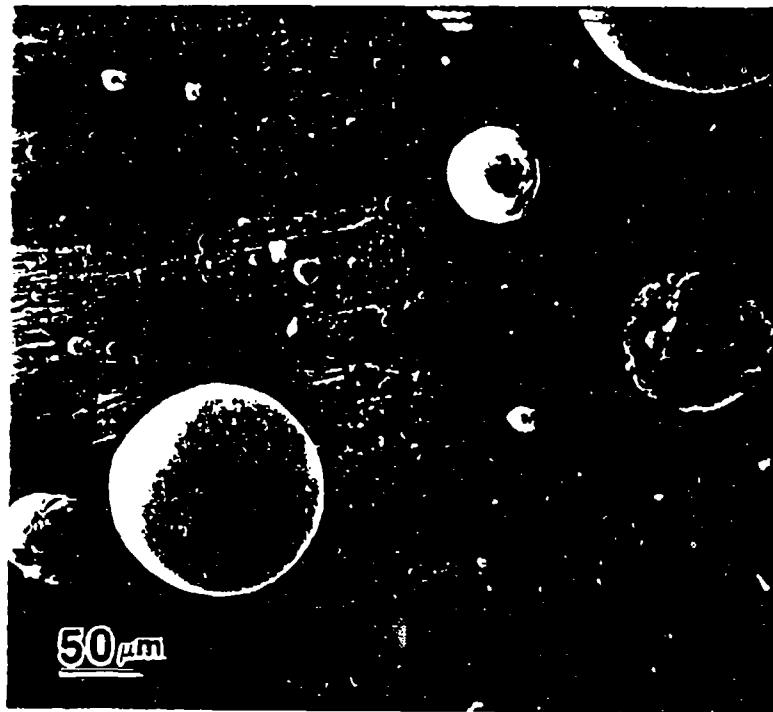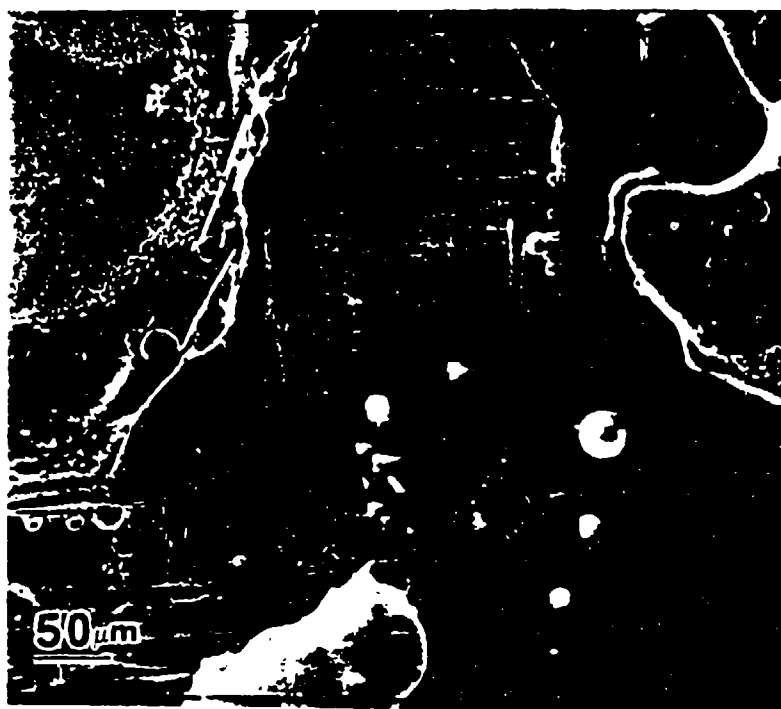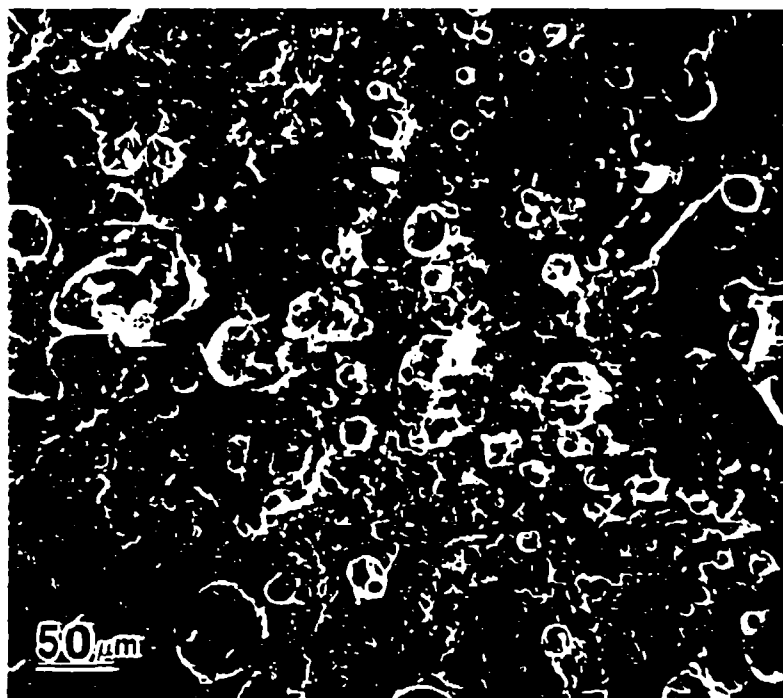

Figure 64. SEM micrograph of an inhibited matrix composite packed cemented in the ZrC/SiC/Si/Al$_2$O$_3$ mixture and oxidized at 1800°C.

Although significant bubble formation can be observed, this film completely covered the surface of the composite, without any exposed regions which were present on all the other composites tested at this temperature.

Figure 65 shows the oxidation results of the SiC + B_4C coatings obtained without Al_2O_3. The best protection available with this coating is at 800°C, where the B_2O_3 formed from the oxidation of the B_4C particles is able to flow and seal the surface cracks. The protection of this coating decreases with increasing temperature. Above 1000°C the vapor pressure of B_2O_3 becomes too high to provide much protection. As the temperature increases, the vapor pressure increases, providing less and less protection.

When Al_2O_3 is added to the pack composition for the SiC + B_4C coating, the thickness of the conversion layer increases. It was observed that the protection for this coating composition, as shown in Figure 66, was better at all the test temperatures than that obtained without Al_2O_3, as shown in Figure 65. The increase in protection is due to the increase in conversion thickness. However, it was more than a direct thickness relation. It is believed that the thicker coating allowed significant formation of borosilicate glass which resulted in greatly improved protection at 1200°C and 1400°C. This improvement is illustrated by comparing Figures 65 and 66. These results are in accord with earlier findings which used boron in conjuction with CVD SiC.
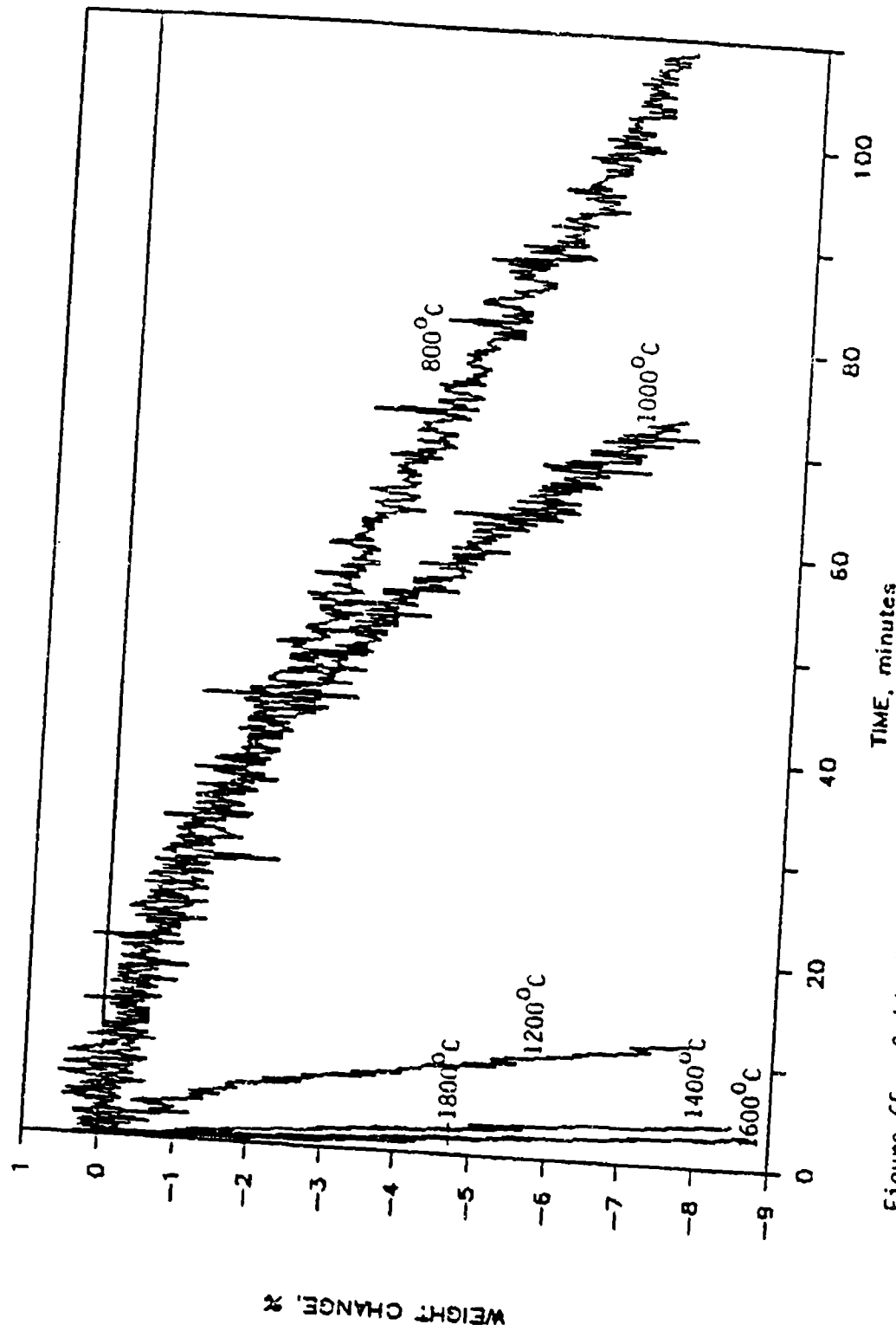
Figure 65. Oxidation Results at All Temperatures for the SiC+B$_4$C Coating.
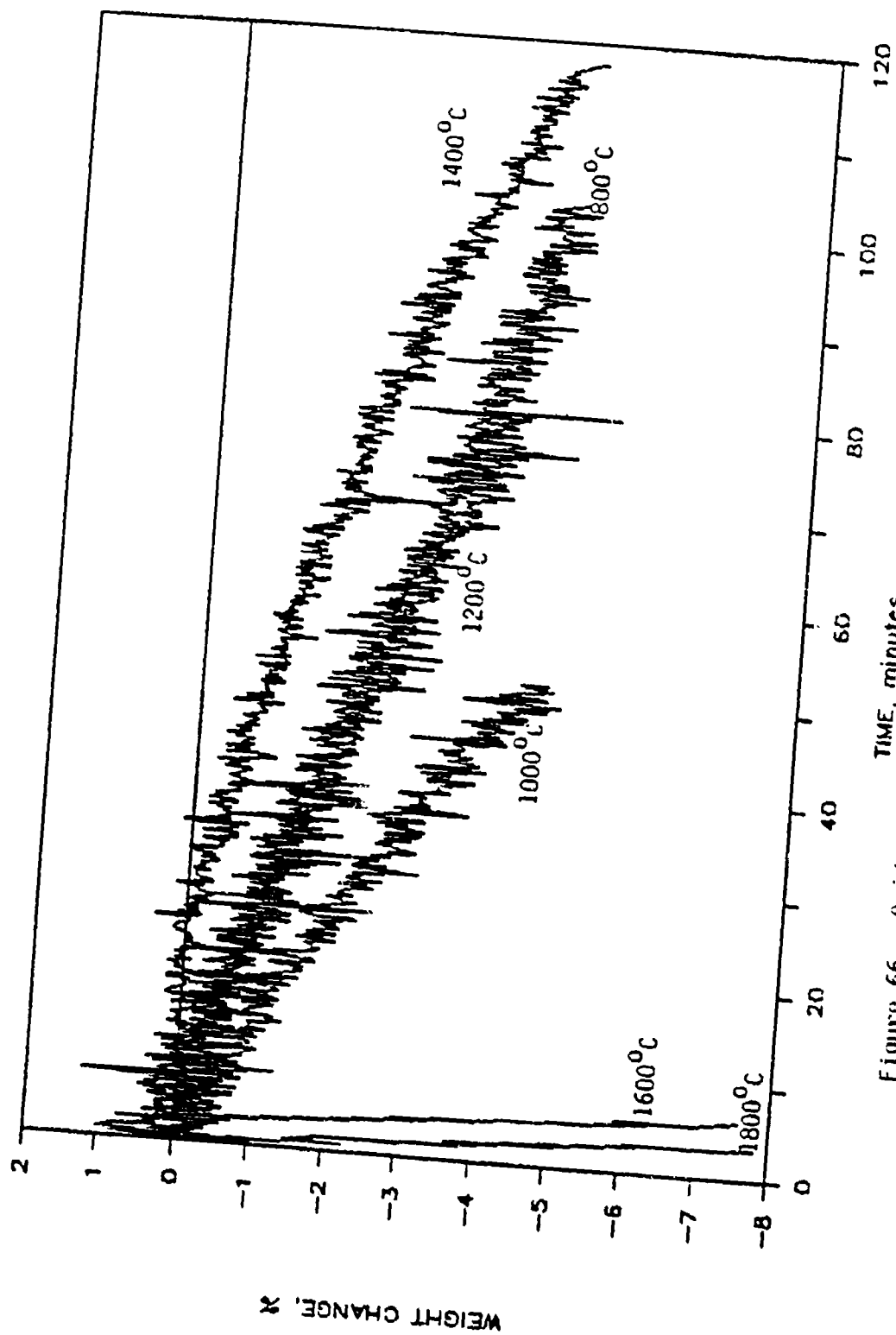
Figure 66. Oxidation Results at All Temperatures for the
SiC+B$_4$C Coating Obtained with Al$_2$O$_3$.

The SiC coatings obtained without Al_2O_3 performed as expected over the temperature range tested, see Figure 67. SiC offers its best protection around 1200^oC. At 1200^oC, the SiC has already oxidized to form a SiO_2 glass film which flows easily at this temperature to seal defects in the SiC coating, ie. cracks. The above is also true for the SiC coating at 1400^oC, however, the vapor pressures of primarily CO, as well as SiO, and SiO_2 start to be a problem. As a result, the coating doesn't provide as much protection at this temperature.

Although the protective SiO_2 film forms around 950^oC and begins to flow around 1000^oC, the glass is more viscous than it is at 1200^oC and is unable to seal as efficiently. This is the reason the SiC coatings do not protect as well at 1000^oC, as they do at slightly higher temperatures. At 800^oC, SiC does not oxidize readily to form SiO_2 glass. This leaves the cracks, which form due to the mismatch in coefficient of thermal expansion during cooling from the pack cementation temperatures, open, allowing the ingress of oxygen. As expected, SiC alone does not provide adequate protection at this temperature.

At 1600^oC and above, SiC begins to dissociate. The vapor pressures of SiC and SiO_2, become disruptive. Therefore, less protection is provided at these temperatures than at the $1200-1400^oC$ range, as shown in Figure 67.
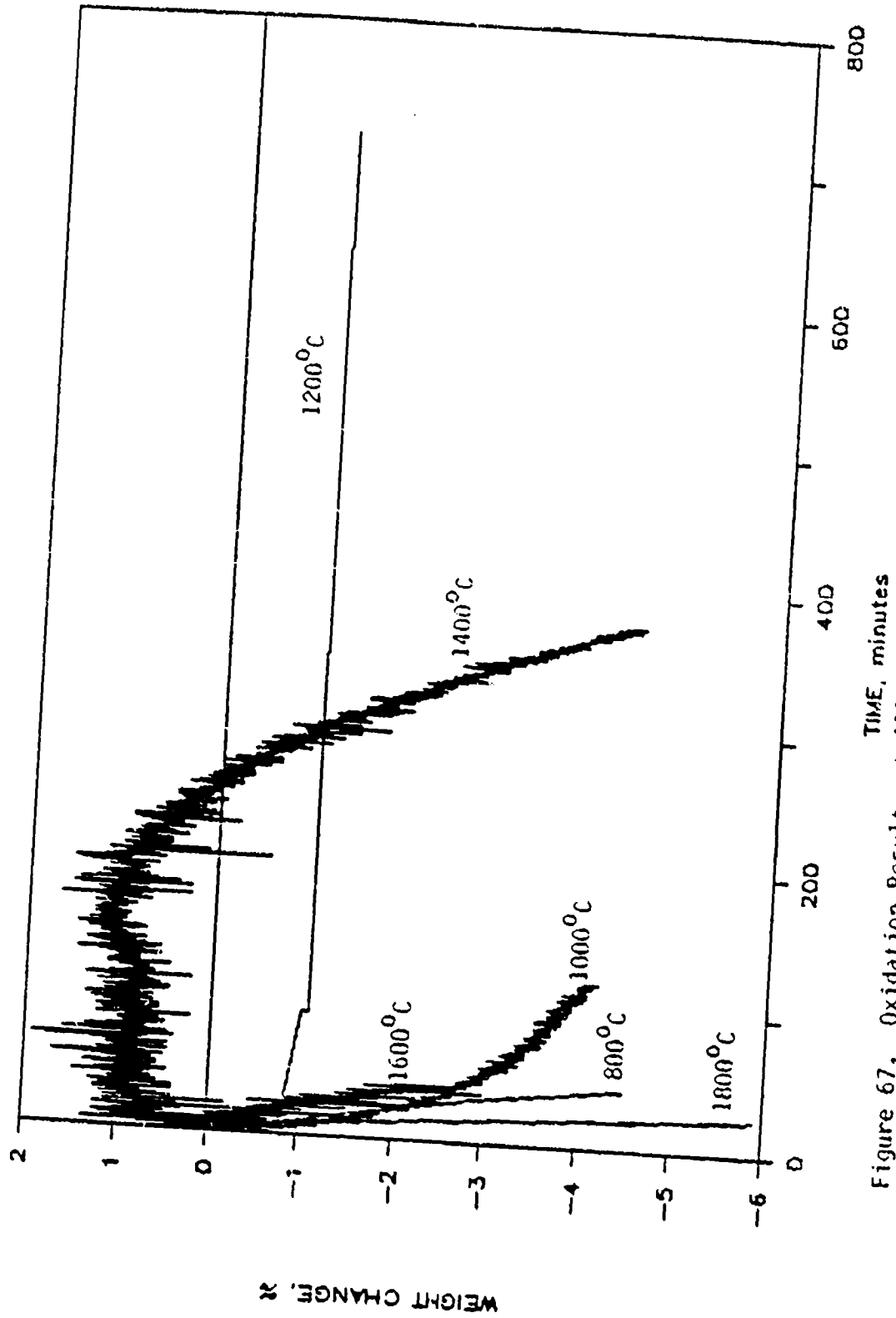
Figure 67. Oxidation Results at All Temperatures for the SiC Coating.

The above discussion for the SiC coatings obtained without Al_2O_3, is also true of the SiC coatings obtained with Al_2O_3. However, as previously noted, the coatings obtained with Al_2O_3 were thinner and, correspondingly, provided less protection from oxidation, as shown in Figure 68.

At lower temperatures, the SiC + ZrC coatings are not expected to provide noteworthy oxidation protection, since the SiC is not able form a protective glass at lower temperatures and ZrC forms an unprotective oxide. This is indeed what was observed for the coatings obtained with and without Al_2O_3, see Figures 69 and 70. The ZrC formed a powdery oxide that easily spalled off the surface, leaving the composite vulnerable to oxidation.

At the intermediate temeratures, SiC portion of the coating oxidizes to form a protective seal. ZrO_2 may react with the SiO_2 film to form zirconium silicate, which offers reasonable oxidation protection.

Although the SiC + ZrC coating oxidizes quickly at the high temperatures tested, it does appear that the ZrC additions improve the oxidation resistance of the SiC coating. This is possibly due to the reducing effect ZrC has on the vapor pressures of the silicon system, through the formation of the zirconium silicide and zirconium silicate.

Figure 71 presents a comparison of the final rates of

TIME, minutes
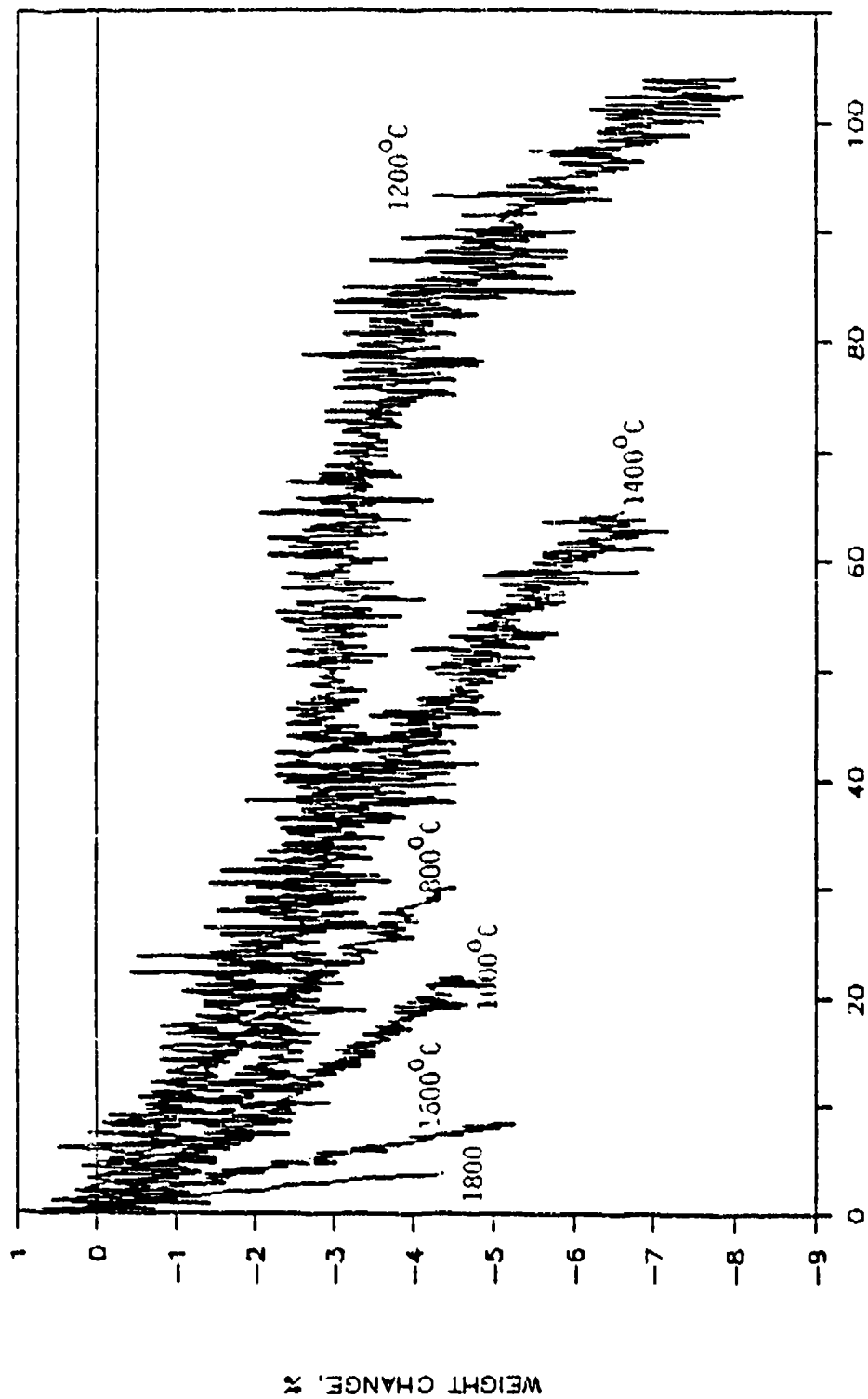
Figure 68. Oxidation Results at All Temperatures for the SiC Coating Obtained with Al_2O_3.
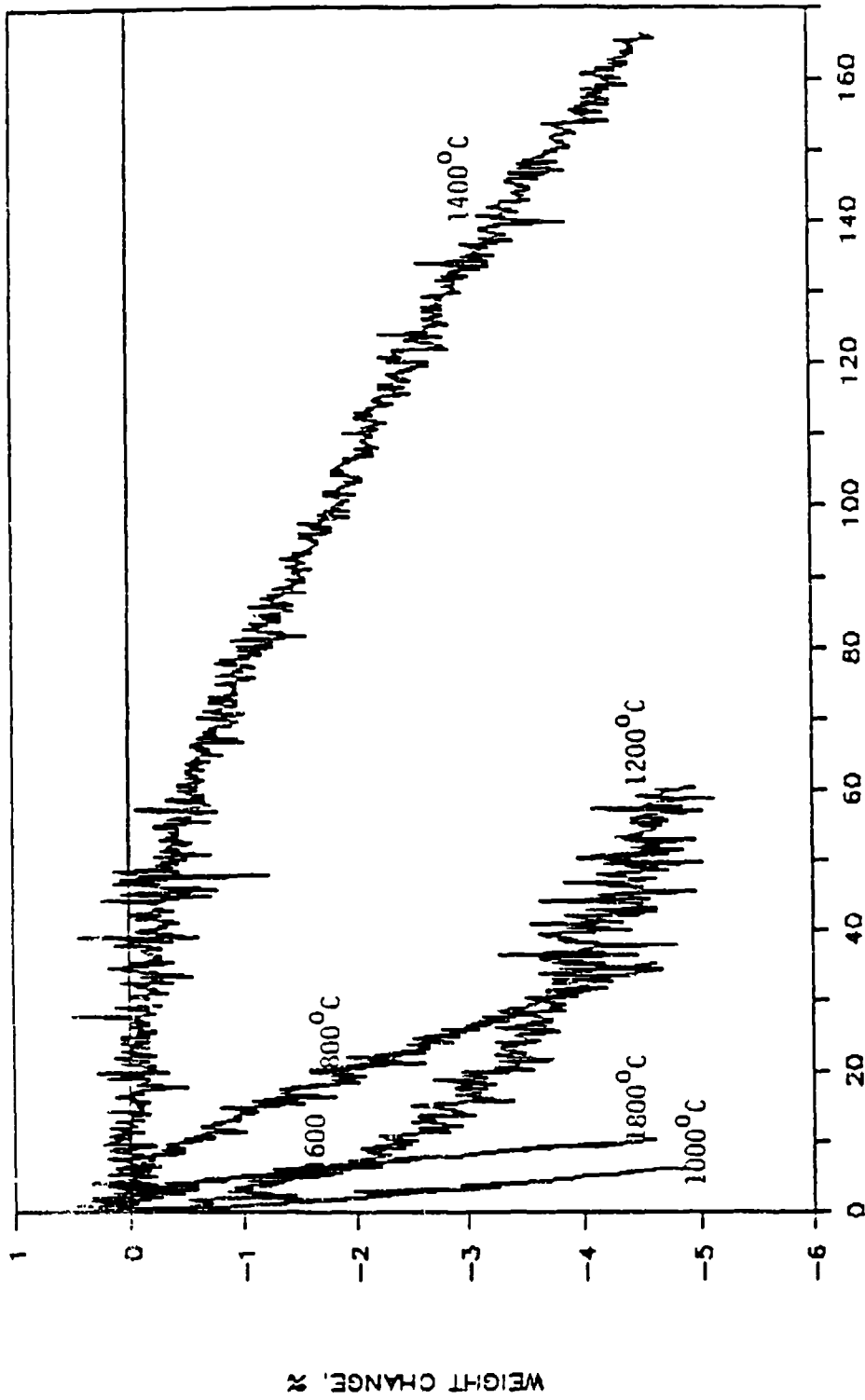
Figure 69. Oxidation Results at All Temperatures for the SiC+ ZrC Coating.
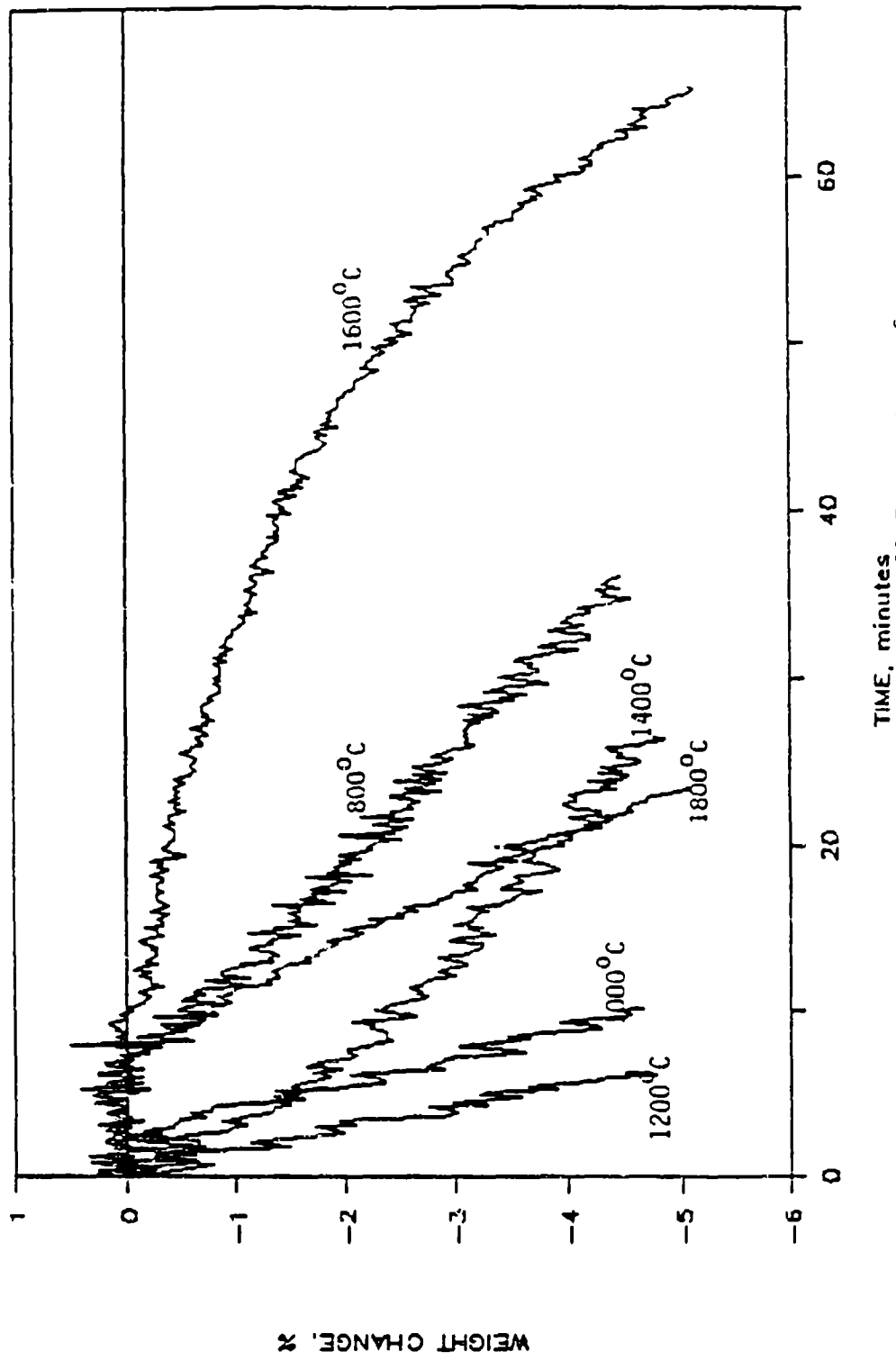
Figure 70. Oxidation Results at All Temperatures for the SiC+ZrC Coating Obtained with Al_2O_3.
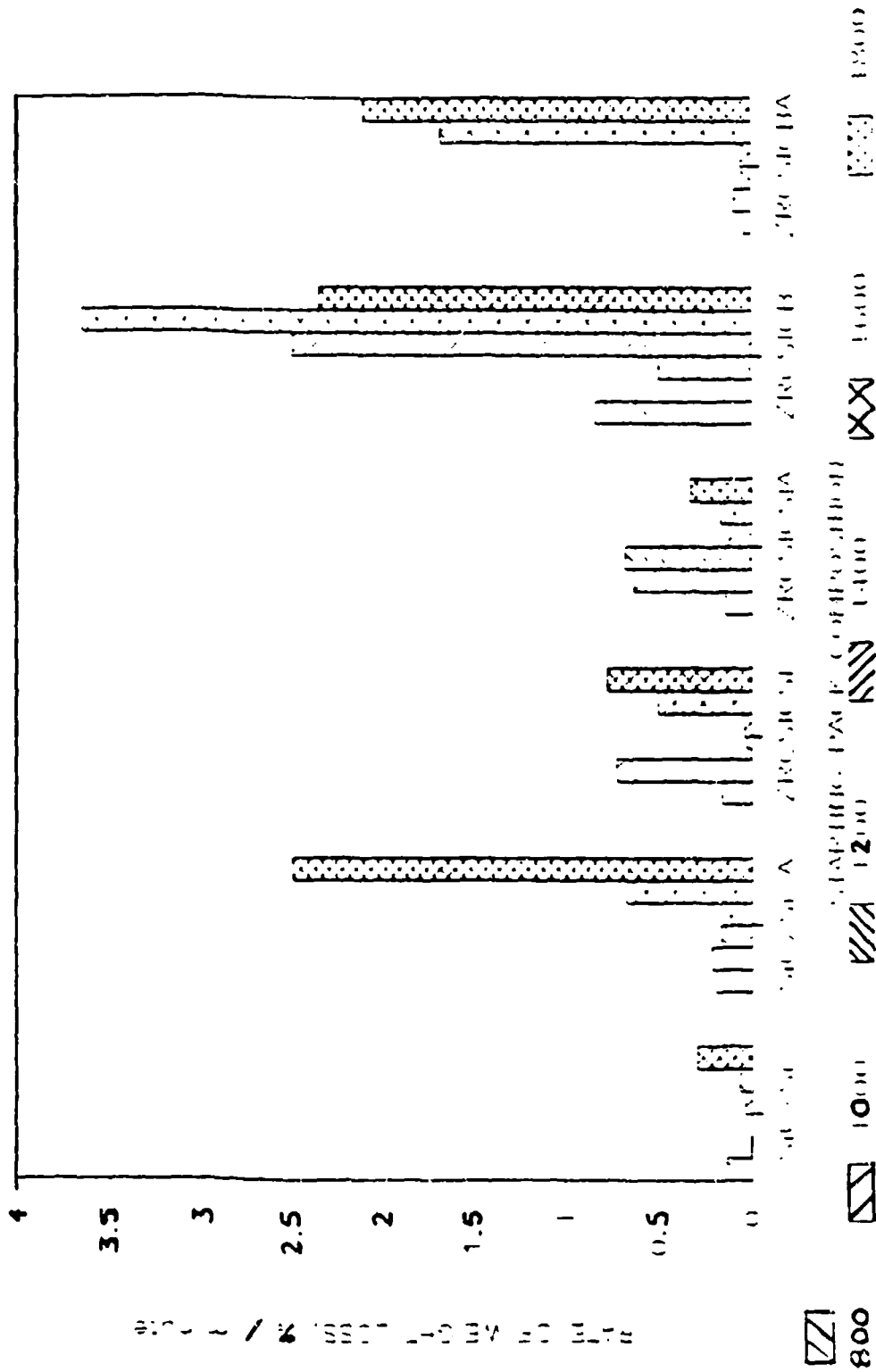
Figure 7.1   Comparison of the Final Rates of Weight Loss for All Mixtures.

weight loss of each composition for every temperature tested. The final rates were determined from regressed plots of the data. In this comparison, there appears to be a trend in the oxidation behavior of the coatings.

The rate of oxidation increases with temperature until the coating is able to form a protective glass, at which point the oxidation rate begins to decrease. The rate will continue to decrease with increasing temperature, until the glass reaches its optimum viscosity to provide the most efficient protection. When the temperature is increased above this temperature of optimum efficiency, the viscosity decreases too much, possibly causing the glass to flow off the surface of the composite, or the vapor pressure of the glass may increase significantly, causing the glass to volatize. As a result, the oxidation rate increases. The rate will then continue to increase with increasing temperature.

CONCLUSIONS

1. There is a uniform distribution of the oxidation inhibitors and fillers in the matrix. The B particulates in the matrix may react with the substrate to form B_4C.

2. Starting pack compositions consisting of 30%ZrC-30%SiC-40%Si and 30%ZrC-30%SiC-40%B result in conversion coating compositions of SiC + ZrC and SiC + B4C, respectively, when heated to 1900^0C for 5 hours.

3. The possible conversion mechanisms occuring in the pack cementation process are summarized below.

   SiC/Si SYSTEM AT 1700 AND 1900^0C

   $$Si + C \rightarrow SiC$$
   $$SiC + SiO_2 \rightarrow Si \text{ or } SiO$$
   $$SiO \text{ or } SiO_2 + C \rightarrow SiC$$

   ZrC/SiC/Si SYSTEM AT 1900^0C

   $$ZrC + SiO \text{ or } SiO_2 \rightarrow ZrO_2$$
   $$ZrO_2 + C \rightarrow ZrC$$

   ZrC/SiC/B SYSTEM AT 1900^0C

   $$B + C \rightarrow B_4C$$
   $$B + SiC \rightarrow B_4C$$
   $$B + ZrC \rightarrow ZrB_2$$
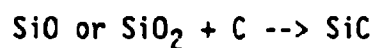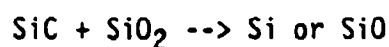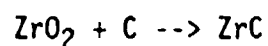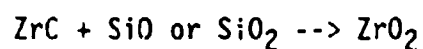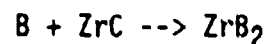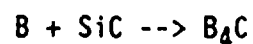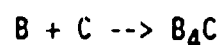
4. There is no significant difference on the conversion layer composition, thickness, or quality, between using alpha or beta SiC in the starting pack composition.

References

1. J. Buckley, "Carbon-Carbon, An Overview," Am. Ceram. Soc. Bull., 67 (2) pp. 364-68 (1988).

2. J. Strife, and J. Sheehan, "Ceramic Coatings for Carbon-Carbon Composites," Am. Ceram. Soc. Bull., 67 (2) pp. 369-74 (1988).

3. K. Luthra, H. Park, "Chemical Compatibility in Ceramic Composites," Materials Lab. Corporate Research and Development, G.E. Co., NY, (1987).

4. J.K. Weddell, "Screening Investigation of Materials for High Temperature Ceramic Composites," E.I. Dupont De Nemours and Co., Delaware, (1987).

5. LTV Aerospace and Defense Company, "High Temperature Composites Initiative Materials and Process Screening PRDA," Project FY1457-86-01132, Texas, (1987).

6. D.W. Richerson, "Modern Ceramic Engineering: Properties, Processing, and Use in Design, Marcel Dekker, Inc., NY, (1982).

7. L. Sheppard, "Challenges Facing the Carbon Industry," Am. Ceram. Soc. Bull., 67 (12) pp. 1897-1902 (1988).

8. D.P. Stinton, T.M., Besmann, and R.A. Lowden, "Advanced Ceramics by Chemical Vapor Deposition Techniques," Am. Ceram. Soc. Bull., 67 (2) pp. 350-55 (1988).

9. J. Sheehan, "Ceramic Coatings for Carbon Materials,"; in the Proceedings of The Fourth Annual Materials Technology Center Conference, Southern Illinois University, Carbondale, Il, (1987).

10. J.Chown, R.F. Deacon, N. Singer, and A.E.S. White, "Refractory Coatings On Graphite"; p.81 in Special Ceramics, Edited by P. Popper, Academic Press, (1963).

11. D.C. Rogers, D.M. Shuford, and J.I. Mueller, "Formation Mechanism of a Silicon Carbide Coating for a Reinforced Carbon-Carbon Composite," pg 319-336 in Proceedings of the 7th National SAMPE Technical Conference, (1975).

12. D.C. Rogers, R.O. Scott, and D.M. Shuford, "Material Development Aspects of an Oxidation Protection System for a Reinforced Carbon-Carbon Composite," pg 308-336 in Proceedings of the 8th National SAMPE Technical Conference, (1976).

26. G.Samsonov, L.Markovskii, A.Zhigach, M.Valyasho, "Boron, Its Compounds and Alloys," AEC-tr-5032 (books 1 and 2) U.S. Atomic Energy Commission, Division of Technical Information, Book 1 pp. 162-169, (1960).

27. A.Cochroan, J.Stephenson, J.Donaldson, "Boron and Boron Carbide Coatings by Vapor Deposition," J. Metals pp.37-40, (1970).

28. L.Vandenbulcke, G.Vuillard, "Chemical Vapor Deposition of Amorphous Boron on Massive Substrates," J. Electrochem. Soc.:Solid State Science and Technology, 123 2 pp. 278-285, (1976).

29. L.Ehrenreich, U.S. Patent # 4,119,189 (1978 to The Carborundum Co.).

30. R.Pierson, A.Mullendore, "Boron Coatings on Graphite for Fusion Reactor Applications," Thin Solid Films 63 pp. 257-261, (1979).

31. K.Saito, Y.Kogo, U.S. Patent # 4,197,279 (1980 to Toho Besion Co.).

32. R.Pierson, A.Mullendore, "The Chemical Vapor Deposition of Boron at Low Temperatures," Thin Solid Films 83 pp. 87-91, (1981).

33. D.McKee, C.Spiro, E.Lamby, "The Effects of Boron Additives on the Oxidation Behavior of Carbons," Carbon 22 6 pp. 507-511, (1984).

34. R.Hoizi, U.S. Patent # 4,515,860 (1985 to Dart Ind.).

35. T.Vasilos, U.S. Patent # 4,599,256 (1986 to Avco Corp.).

36. P.Ehrburger, P.Baranne, J.Lahaye, "Inhibition of the Oxidation of Carbon-Carbon Composite by Boron Oxide," Carbon 24 4 pp. 495-499, (1986).

37. D.McKee, "Borate Treatment of Carbon Fibers and Carbon-Carbon Composites for Improved Oxidation Resistance," Carbon 24 6 pp. 737-741, (1986).

38. D.McKee, "Oxidation Behavior and Protection of Carbon-Carbon Composites," Carbon 25 4 pp. 551-557, (1987).

39. K.Luthra, "Oxidation of Carbon/Carbon Composites-A Theoretical Analysis," Carbon 26 2 pp. 217-224, (1988).

40. J.Thomas, C.Roscoe, Proceedings of the 2nd Conference Industrial Carbon and Graphite, S.C.I., London, (1965).

ELECTRON DIFFRACTION

Identification of an unknown material is possible if the unique crystallographic information, the lattice spacings, can be identified. The determination of the lattice spacing between planes in an atom, is possible by analyzing the unique diffraction pattern which results when portions of an electron beam, passing through a thin material, are diffracted by the various planes in the crystal geometry.

The d-spacing is related to the diffracted angle by Bragg's Law: $d = \lambda / (2 \sin\theta)$. The wavelength of the electron beam, operating at 100keV, is 0.037 Angstroms. Bragg's Law, which must be met for diffraction to occur, is related to the camera length in the electron microscope through simple geometrical relations, see figure A1.

The camera length (L) is the distance between the sample and the plane of diffraction (the back focal plane of the microscope). The distance between the transmitted beam (T) and the diffracted beam (DB) is represented by R. This distance, R, is measured directly from the diffraction pattern on the negative of a micrograph. The camera length and the distance R are related by $R/L = \tan2\theta = 2\theta$, for very small angles.

Combining this relation with Bragg's Law gives:

$$L = Rd/\lambda.$$

The camera lengths of the microscope can be calibrated with

a known sample, commonly polycrystalline gold is used for this purpose. The camera length used to obtain the diffraction pattern in figure 16 was calculated with polycrystalline gold and determined to be 91.6 cm.

With the calculated camera length, and the measured distance, R, the above relation can be rearranged to give the d-spacing of an unknown, $d = \lambda L/R$. The distance between the diffraction spots and the transmitted beam in the diffraction pattern, figure 16, was measured to be 1.42cm. This results in a d-spacing of 2.387 Angstroms, which corresponds to boron carbide (021).

APPENDIX C

X-RAY DIFFRACTION

The x-ray diffraction experiments, conducted by Dr. Paul Robinson, were run using a copper tube with a nickle filter, which results in a wavelength of 1.54178 (Å). The samples were scanned at 2° per minute between 10°-90°. An example of the x-ray results is shown in Figure C1. The d-spacings or plane-spacings can be calculated using Bragg's Law, which states that the d-spacing is equal to the wavelength divided by 2 times the sine of the half angle, θ.

$$d = \lambda \ / \ (2 \ \sin\theta)$$

The peaks shown in the x-ray printout, Figure C1, are correlated to a given angle along the x-axis of the printout. This angle, in conjunction with the wavelength, identify the d-spacing of the particular peak.

After the d-spacings for the entire printout are identified, the relative intensities of each peak can be determined from the ratio of a peak's intensity to the maximum intensity. Below is a list of the d-spacing and relative intensities of the peaks in Figure C1, according to the value of 2θ. With the d-spacing information and the relative intensity, the card file of crystallographic information may be searched to find a match for the "unknown fingerprint". The other specimens were also indexed in this manner. The more constituents involved, the more complicated it becomes to match the d-spacing information.

2θ	D-Spacing, Å	Relative Intensity	Card File Match
28.50	3.13	8.44	Si
35.75	2.51	100	Beta SiC
41.50	2.17	14.9	Beta SiC
47.45	1.91	3.89	Si
60.00	1.54	54.5	Beta SiC
71.80	1.31	31.1	Beta SiC
75.55	1.25	3.24	Beta SiC
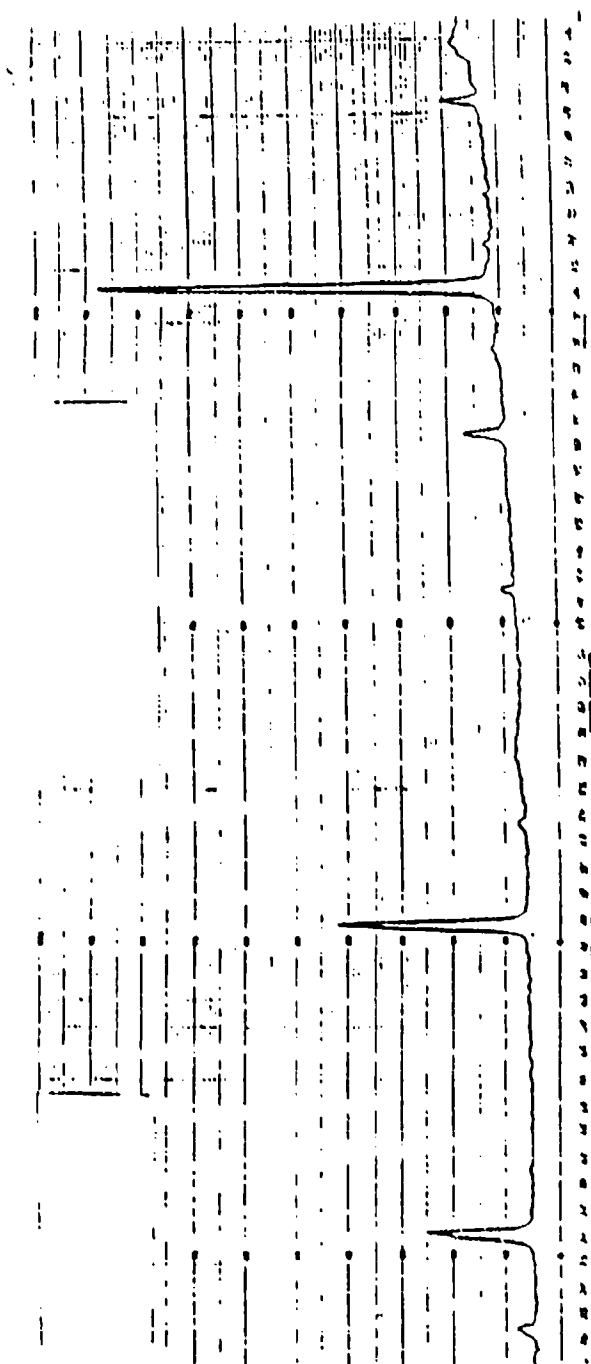
Figure C1. X-ray printout.

**OXIDATION PROTECTION SYSTEMS FOR CARBON-CARBON COMPOSITES
FORMED BY CHEMICAL VAPOR DEPOSITION AND
PLASMA ASSISTED CHEMICAL VAPOR DEPOSITION TECHNIQUES**

Section 3:

The Formation of Oxidation Protective Coatings on
Carbon-Carbon Composites Using a
Chemical Vapor Deposition (CVD) Technique

By

Jun He

A thesis submitted in partial fulfillment of
the requirements for the degree of
Master of Science

TABLE OF CONTENTS

I

TABLE OF CONTENTS (Continued)

ACKNOWLEDGMENTS

LIST OF FIGURES

LIST OF FIGURES

LIST OF FIGURES

LIST OF FIGURES

LIST OF FIGURES

ABBREVIATIONS

ABBREVIATION:

CVD --- Chemical Vapor Deposition.

CVI --- Chemical Vapor Infiltration.

TGA --- Thermogravimetric Analyzer.

SCCM --- Standard Cubic Centimeter per Minute.

SEM --- Scanning Electron Microscope.

TEM --- Transmission Electron Microscope.

OM --- Optical Microscope.

XRD --- X-Ray Diffraction.

CTE --- Coefficient of Thermal Expansion

μm --- Micron

MTS --- Methyltrichlorosilane

CHAPTER 1

INTRODUCTION

In popular literature, carbon fiber reinforced carbon matrix materials, otherwise known as carbon-carbon composites, are called miracle materials [1]. With characteristics such as light weight, high heat of ablation, good thermal shock resistance, and good strength and toughness at high temperatures, carbon-carbon composites offer high performance in extreme thermal and chemical environments [2,3]. Potential uses have not only been identified in military aircraft, advanced missile systems, various hypersonic aerospace vehicles, but also as a very promising replacement for asbestos in brake lining and disc materials [1]. Carbon-carbon composites are also applied in many other areas such as medical prostheses, and chemical plant heat exchangers [1].

Although having excellent high temperature physical, mechanical, thermal and chemical properties, carbon-carbon materials experience severe oxidation in oxidizing environments and can last only over a very limited period of time at elevated temperatures [1,2,3]. The development of oxidation protection for carbon has been the subject of research for more than 50 years. The first effort directed towards carbon-carbon composite oxidation protection was conducted in the early 1970's on components to be used on shuttle orbiter vehicles [1]. Since then, many types of protection techniques and systems have been developed for

carbon materials, for high and ultra-high temperature applications [2,3].

A successful oxidation-protection system should exhibit good mechanical and chemical stability under extreme thermal and oxidative environments. It should meet four main requirements: adequate adhesion between substrate and coating; maximum resistance to thermal shock and thermal cycling; good oxidation protection at both intermediate ($1000^{\circ}C$) and high ($>1500^{\circ}C$) temperatures; and good substrate oxidation resistance at moderate temperatures [2].

The objective of this investigation is to achieve effective high temperature oxidation resistance for carbon-carbon composites by applying both substrate treatments and surface coating techniques. Initially, carbon-carbon composites are heat treated in Si-bearing environments so that near-surface layers are converted to silicon carbide. This is followed by chemical vapor deposition to produce oxidation protective coatings. Prior to coating experiments, detailed thermodynamic calculations are performed. The result of these calculations is then used as a guide line to select appropriate experimental parameters, i.e., temperature, pressure and gas flow rates. Coating experiments are conducted by using a computer-controlled CVD reactor. Four types of CVD coating systems are to be investigated. They are: SiC monolayer, ZrB_2 monolayer, ZrB_2/SiC multilayer and graded ZrC/SiC coatings.

Following these coating experiments, characterizations of oxidation resistances and microstructures will also be performed. These characterization experiments include oxidation tests under isothermal and thermal cycling conditions and detailed microstructure analysis using optical microscopy, scanning electron microscopy, transmission electron microscopy, and X-ray diffraction.

CHAPTER 2

LITERATURE REVIEW

Since the sixties, significant efforts have been directed towards the oxidation protection of carbon-carbon materials [1]. The lack of oxidation resistance at high temperatures is attributed to the fact that carbon reacts with oxygen to give the gaseous products of CO and CO_2. Such oxidation reactions can occur on external surfaces as well as in numerous internal pores, which are usually introduced during the fabrication processes of the composite [4]. In order to use carbon-carbon composites as high temperature structural materials, oxidation protection methods need to be studied. In this chapter, oxidation of carbon material and oxidation protection methods reported in the literature will be discussed.

2.1 Oxidation of Carbon Materials

Oxidation of carbon-carbon may be controlled by one or more of the following steps [5,6]:

(1) Mass transport of gas molecules or products across a relatively stagnant boundary layer between the exterior surface of the solid and the main gas stream.

(2) Reacting gas diffusion from the exterior surface to an active site beneath the surface and mass transport of the products in the opposite direction.

(3) Chemisorption of reactant, wholly or in part; namely, rearrangement of chemisorbed species on the surface to desorbable product(s), and desorption of product(s) from

the surface.

The rate controlling step(s) varies from one type of carbon-carbon composite to another depending on the fabrication processes (carbonization, graphitization, raw materials, etc.), and on the characteristics of the composite (porosity, fiber, matrix and interface bonding) [5]. It also depends on the temperatures to which the carbon-carbon material is exposed [5]. Generally, the variation of oxidation rate with temperature can be divided into three zones [7], as shown in Figure 2-1.

(1) At low-temperatures, ZONE I, the reaction rate is controlled solely by the chemical reactivity of carbon (step 3). The activation energy, E_a, is equal to the true activation energy, E_t, of the gasification reaction.

(2) In the intermediate temperature range, ZONE II, the concentration of the reactant species gradually decreases to zero in the composite as a result of increasing chemical kinetics. In this regime, the reaction rate is controlled jointly by steps 2 and 3. The apparent activation energy, E_a, is approximately half of the true activation energy, E_t.

(3) At high temperatures, ZONE III, the reactant species are depleted at the exterior surface due to fast chemical kinetics of gasification. The depletion of the reactant species leads to the diffusion mechanism (step 1) dominating high temperature oxidation. Since gaseous diffusion generally has a low activation energy, the

apparent activation energy, E_a, of the carbon-carbon composites in ZONE III is also low [7].

2.2 Oxidation Protection of Carbon-Carbon Composites

Numerous techniques and various oxidation protection methods for c   on-carbon composites have been studied. Basically, these studies have focused on three major areas:

(1) Microstructural modification of carbon.

(2) Addition of inhibitors.

(3) Application of protective coatings.

2.2.1 Structural Modification of Fiber, Matrix, and Interface [8-10]

Since carbon-carbon composites are composed of reinforcing fiber and carbonaceous matrix, the microstructure (fibers, matrices and interfaces) has a great effect on the oxidation resistance of the composites. The microstructure of the individual components of the carbon-carbon composites is strongly dependent on the fabrication process and the control of the process parameters. For example, the porosity of a carbon-carbon composite is one of the key factors affecting the oxidation resistance. In industry, carbon-carbon manufacturers are trying in every direction to make composites as dense as possible so that the composites exhibit good mechanical properties and improved oxidation resistance. It has been reported [11-14] that high pressure carbonization, following well-controlled pitch or resin impregnation, results in a high coke yield and an ordered carbon

structure, which in turn increases the density and graphitizability of carbon-carbon composites.

On both laboratory and industrial scales, oxidation behavior of various fibers [8], matrices [15,16], and composites [17] has been studied. The processing procedures (carbonization, graphitization, etc.) and parameters (temperature, pressure, time, etc.) are being monitored and modified so that an optimum fabrication system can be found.

Improved interface structure is also important in the structural modification. Good chemical bonding at the fiber/matrix interface retards both oxygen diffusion and chemical reactivity along the interface. However, a strong fiber/matrix bonding degrades the mechanical properties of carbon-carbon composites by eliminating the crack deflection mechanism at the interface. for compromising the mechanical properties and the structural continuity of the composite, a weak bond, or the presence of a small fissure, along the le.. of fiber, is therefore desirable [14]. Numerous high resolution microstructural studies have been carried out for a better understanding of the structure and .he structure-processing relationship of various interfaces of the composites [4,18].

2.2.2 Oxidation-Inhibition Employing Boron and Phosphorus Additives

Carbon mat .u.'s experience different degrees of oxidation depending on their application temperatures.

Internal protection by matrix inhibition methods has been used to enhance the oxidation resistance of the bulk material. Materials such as boron, phosphorus, and their compounds are added during the fabrication of prepregs [19,20]. The benefits derived from the inclusion of elemental boron or boron compounds within various carbon composites are disclosed in some patents and papers [19-23]. According to the literature, there are also complications involved. Most of these reported additives produced oxidation inhibition effects at moderate temperatures and modified the surface character of the composite, but the segregation of these particulate additives may degrade the oxidation resistance because of delamination and swelling [24].

Chemical inhibitors display other advantages with respect to improving the oxidation resistance of composites. Many metal impurities are well known to catalyze the gasification reactions of carbon materials at temperatures less than $1000^{\circ}C$ [25]. To eliminate this catalytic effect, chemical inhibitors (e.g., chlorides) added to pitch precursors have shown some degree of success. Experimental results indicated that an additive such as $POCl_3$ promotes mesophase formation and lowers the reactivity of carbon in an oxidizing environment [26].

2.2.3. Internal and External Surface Coatings

Internal and external coating systems are the most popular and effective methods for the long term oxidation

protection of carbon-carbon composites in various high temperature applications. More details will be discussed in the next section.

2.3 Coatings for Protecting Carbon-Carbon Composites

The oxidation of carbon can, in theory, be retarded by the application of a coating to block oxygen from reaching the carbon material. In order to provide proper protection, this oxygen barrier itself must be stable in severe environments. A number of ceramic coatings based on the use of refractory metal carbides and borides have been studied for protecting carbon-carbon composites from oxidation because of their stability at high temperatures and compatibility with carbon [2,3,21,27-31].

2.3.1 Protective Mechanisms

As discussed above, an effective oxidation protection coating must have major constituents which act as efficient barriers to oxidation. However, flaws and defects often exist in the coating layer due to a thermal expansion mismatch. Therefore an effective coating must also be capable of self-healing these cracks and flaws [2].

The most efficient self-healing can be achieved by a glass sealant, which is formed upon the oxidation of the coating. SiC coating, for example, is one of the most efficient protective coatings for carbon-carbon composites up to $1700^\circ C$. When SiC is oxidized at high temperature, a thin SiO_2 glass film is formed since:

$$2SiC + 3O_2 \Longleftrightarrow 2SiO_2 + 2CO. \qquad\qquad \text{Eq. 2-1}$$

The glass starts to flow around 1200°C and becomes capable of filling cracks and pores at higher temperatures. Since SiO_2 has very low oxygen permeability and relatively low vapor pressure, it offers good oxidation protection for carbon-carbon composites.

2.3.2 Coating Techniques

Ceramic coatings can be obtained by many methods. Two types of coating methods for carbon-carbon composites will be discussed in this section. The first type involves the conversion of the surface carbon layer to ceramic, e.g., pack cementation and vapor treatment. The second one an external coating by CVD.

(1) Pack Cementation and Vapor Treatment

The purpose of applying conversion treatments, e.g., pack cementation and vapor treatment, to carbon-carbon substrate is to obtain a converted ceramic layer on the specimen surface. The advantages of these treatments include [27]:

(1) It provides SiC converted layer on internal pore and crack surfaces.

(2) It improves the adherence of the substrate to the external CVD coating.

(3) It helps to hinder internal oxidation by forming glass on internal surfaces during high temperature oxidation.

In the pack cementation process [27], a retort made of graphite was used to pack carbon substrates with a prepared

powder mixture. For silicon carbide coatings, a powder mixture of 60% SiC + 30% Si + 10% Al_2O_3 was used. After a low temperature baking process, the packed retort was fired up to 1705°C (3100°F) for 2 hours and 45 minutes in an inert gas environment. Following such pack cementation procedure, Rogers and the coworkers [27] observed that a surface layer of about 635 um was converted to B-SiC.

An SiC converted layer can also be obtained by reacting carbon substrates with SiO vapor [28] according to the reaction:

$$SiO + 2C ===> SiC + CO. \qquad \text{Eq. 2-2}$$

In this type of conversion process, the carbon substrate is placed above a powder mixture of Si and SiO_2. When both the powder mixture and the substrate are heated up to about 1200°C, SiO vapor is produced from the powder mixture according to the following reaction:

$$SiO_2 + Si ===> 2SiO. \qquad \text{Eq. 2-3}$$

The SiO vapor reacts with the carbon substrate to form an SiC coating layer on both internal and external surfaces.

Both of these processes can produce a converted thin surface layer on external and open internal surfaces. This coating layer provides appropriate substrate oxidation resistance and good coating adhesion.

(2) CVD Coatings

Currently, the most successful protective coating for carbon-carbon composite is CVD SiC. Coatings of either stoichiometric SiC or SiC with excess Si have demonstrated

successful oxidation protection up to $1700^{\circ}C$ [29]. When SiC oxidizes, a thin, viscous glass film of SiO_2, which exhibits a very low oxygen diffusibility, is formed. The thickening rate of the oxide layer is limited by diffusion and the parabolic rate constant is:

$K = 1.62 \times 10^{-6}$ EXP(-26,170cal/RT) cm^2/hour [30].
The protective film wets the carbon substrate very well so that it is capable of completely sealing the entire surface and retarding the access of oxygen to the composite interior. Since the parabolic rate constant of SiO_2 growth is very small, the growth of the SiO_2 layer would be expected to be very slow. For example, at $1727^{\circ}K$, the SiO_2 layer only grows 6.68×10^{-5} cm thick. Therefore, the maximum protection which SiC coating offers is not limited by the oxidation of SiC. Instead, the maximum protection is determined by the vapor pressures of SiO and CO. Based on thermodynamic calculations, the equilibrium vapor pressure of the CO + SiO associated with an SiC coating reaches 1 atm at $1760^{\circ}C$. Therefore, it has been suggested that the SiC coating fails to protect carbon materials above $1760^{\circ}C$ [2, 29, 31].

Although its performance in the 1100° - $1700^{\circ}C$ range is satisfactory, SiC coatings encounter considerable problems below $1100^{\circ}C$ and beyond $1700^{\circ}C$. At temperatures below $1100^{\circ}C$, the viscosity of silicon oxide glass is very high so that it can not seal off the cracks. To solve this problem, a boron containing compounds, e.g., ZrB_2, can be

used. Metal borides form metal oxides and borate glass during oxidation since:

$$2MB_2 + 5O_2 ===> 2MO_2 + 2B_2O_3 \qquad\qquad Eq. 2-4$$
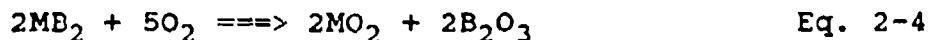
which gives the metal refractory oxide and the oxidation product B_2O_3. Since B_2O_3 has both a low melting point and a low viscosity [32], it provides sufficient sealing capability for the protection of carbon up to $1100^\circ C$, above which it evaporates and the protective layer is destroyed.

When the temperature exceeds $1700^\circ C$, SiC coatings fail because of the following problems:

(1) Vaporization:

At ultra-high temperatures, the vapor pressure of SiO and CO in the SiC + SiO_2 + C system could far exceed the ambient pressure so that bubbles are formed causing the disrupture of the coating. According to the calculation results obtained by Mieskowski, Mitchell and Heuer [33], if the ambient pressure is 1 atm, the internal pressures of SiO + CO for the formation of 20 micron- and 1 micron-sized bubbles are 1.3 atm and 7 atm, respectively. Thus, bubble nucleation should not represent a significant hindrance to bubble formation.

(2) Glass Viscosity:

The viscosity of SiO_2 decreases dramatically with increasing temperature and increasing content of impurities such as Fe, Na and B. When this happens, drastic flow of the glass film occurs which causes the protective layer to be spalled off from rotating parts or from entry vehicle

surfaces.

(3) Oxidation of Surface Coating:

As temperature increases, the permeability of oxygen through the SiO_2 film also increases because the permeability is inversely proportion to viscosity. Therefore, the surface coating might be rapidly consumed by oxidation. Consequently, catastrophic oxidation occurs due to the direct reaction of SiO_2 with carbon [34-36].

The problems discussed above cause SiC single-layer coatings for ultra-high temperature protection to be impractical. A number of approaches have been used in an attempt to solve these problems so that the carbon-carbon composites can be used at higher temperatures. Among these approaches, multilayer coatings and graded coatings have attracted the most attention.

2.3.3 Evaluation of Various Coating Systems

It is quite obvious that efficient coating systems should be designed and engineered according to application temperatures. Coatings suitable for ultra-high temperature applications may not be adequate for low temperatures. Described below are the coating systems aiming at three application temperature ranges: below 1500°C, from 1500°C to 1800°C, and above 1800°C.

Almost all successful coating systems designed to perform at temperatures below 1500°C contain boron [32]. The protection system Sheehan [2] developed, which contains a boron-inhibited matrix, an inner layer of borate glass

former and an overcoat of CVD SiC, was reported to withstand stressed oxidation tests and thermal cycling tests for hundreds of hours. During oxidation, borate glass formed and acted as an ternal glass sealant.

When the temperature exceeds 1500°C, boron oxide or borate glasses are reduced by carbon. The total CO pressure of the reaction:

$$2B_2O_3 + 7C ===> B_4C + 6CO \qquad \text{Eq. 2-5}$$

is greater than ambient pressure (as shown in Figure 2-2), causing the failure of the protective coating.

Since SiO_2 is stable with SiC at temperatures up to 1800°C [36] and B_2O_3 remains stable when in contact with B_4C at 1760°C [2], having a carbide inner layer to avoid the direct contact of carbon and oxide glasses increases the upper temperature limit by several hundred degrees. Addition of refractory metal elements in the oxide glass layer also improves long term oxidation protection in the temperature range from 1500°C to 1800°C [2].

At temperatures greater than 1800°C, a potentially effective coating system would contain a refractory oxide overcoat and an inner SiO_2 glass coating. The selection of oxide coatings is based on considerations of their thermal expansion coefficients, melting points, and vapor pressures. Sheehan [2] suggested that ZrO_2, HfO_2, TiO_2, TaO_2, Y_2O_3, and ThO_2, would all be suitable for overcoating for long-term use at temperatures over 2000°C. Since most of these oxides experience high oxygen permeabilities and

high viscosities, an inner SiO_2 glassy layer should be used to seal off cracks and retard oxygen diffusion.

2.4 Chemical Vapor Deposition Techniques

2.4.1 General Considerations

In the past several decades, various deposition techniques have drawn significant attention in many areas. Generally speaking, coatings are desirable, or may even be necessary, for a variety of reasons such as economics, materials conservation, unique combination of properties, protection against external damage, and so forth.

Chemical vapor deposition techniques have a wide range of application. They have been used to fabricate surface coatings and thin solid films for various purposes. For example, SiC, Si_3N_4, HfC, TiB_2 and B_4C coatings have been used as surface protective barriers against corrosion, oxidation and wear [37,38]. TiC, TiN, Al_2O_3 and diamond films have been used in the cutting tool industry for improved cutting performance. In the electronics industry, CVD has been employed to fabricate a thin films of semiconductors (e.g., GaAs and SiC) and insulators (e.g., SiO_2 and Si_3N_4), which have been used in integrated circuits. CVD has also been used to fabricate fibers, whiskers, and powders, as well as, various ceramic matrix composites [39,40].

"Coatings" can be formed by various processes, e.g., chemical vapor deposition (CVD), plasma-assisted chemical vapor deposition (PACVD), physical vapor deposition (PVD),

electro- and electroless deposition, plasma spraying, ion implantation, laser glazing, pack cementation, and so forth. (see Figure 2-3) [40]. Among these techniques, chemical vapor deposition, which is the major emphasis of this thesis, plays a very important roll in coating industries.

2.4.2 Chemical Vapor Deposition

CVD is a technique by which reactant gases are decomposed and reacted to form solid phase(s) on a heated substrate. The solid reaction product(s) is deposited on the heated substrate and forms a thin coating on the surface. Surface reactions may be activated by several different energy sources, such as thermal energy, DC, RF, microwave plasma and laser beam,... etc., as shown in Figure 2-4.

In the thermal CVD processes, the specimen is heated to a temperature which is high enough to activate chemical reactions in the surrounding gas environment. In plasma-assisted CVD, gaseous reactants are activated and ionized by an energetic electromagnetic wave or a strong electric field, so that enhanced chemical reactions can occur at relatively low temperatures [40]. Laser activated CVD processes are mainly used in the electronics industry where, micron-dimensional thin films are produced [41].

2.4.3 Components of CVD Apparatus

There are three major components in a CVD system: the source gases handling device, the reaction chamber, and the

exhaust system (Figure 2-5).

(1) Gas Precursor Feeding Device

Gases used for CVD coatings can be derived from gaseous, liquid or solid precursors. Gases such as H_2, CH_4, Ar, N_2 and SiH_4 are commonly used in the CVD of ceramic and metal coatings. Source gases derived from liquid or solid precursors need to be vaporized and carried into the reaction chamber by an appropriate carrier gas. For liquid precursors, e.g., $SiCl_4$ and $GaCl_4$, gas bubblers are used to feed reactant gases. In this case, carrier gas bubbles through a liquid container and transports the reactant vapor to the CVD reactor at the appropriate temperature. The bubbling rate and the vapor pressure of the liquid precursor determine the vapor flow rate in the reactor. Handling solid precursors such as $ZrCl_4$ and $HfCl_4$ is more complicated. Usually a vaporization furnace is employed to heat the powder in order to obtain an appropriate vapor pressure. Then, an inert carrier gas passes through the vaporizer and carries out the vapor. The entire passage channel from the vaporization furnace to the CVD reactor must be kept warm in order to avoid the condensation of the vapor.

(2) CVD Reactors

Many types of CVD reactors have been developed in the past 60 years. Generally, they can be categorized into two major types based on the method of heating and the arrangement of the reaction chamber.

a. Hot-Wall and Cold-Wall Reactors

The wall of a CVD reaction chamber can be either heated or cooled, depending upon the method of heating employed (Figure 2-6). In a hot-wall system, the substrate is placed in the heated chamber, which is usually heated by a resistance furnace. Since the reactor wall and the substrate are at the same temperature, deposition will take place on both the wall and substrate surfaces. This type of reactor allows accurate and uniform temperature control during the deposition. However, since deposition also occurs on the reactor wall, it can cause contamination, maintenance problems and lower efficiency [42,43].

In a cold-wall system, only the substrate is heated, either inductively or resistively, in the reaction chamber. In this type of reactor, a large temperature gradient is present between the substrate surface and the reactor wall. Chemical vapor deposition occurs only on the hot substrate surface. This minimizes particulate contamination and impurity problems associated with hot wall reactors. As a result, greater control over the deposition process is possible. However, the existence of the temperature gradient between the substrate and the reactor wall will induce complex buoyancy driven secondary flow in the reaction chamber, which makes kinetics and mass transport studies even more complicated [42,43].

b. Horizontal and Vertical Reactors

Another way of classifying CVD reactors is based on

the basic design of the chamber (Figure 2-6) [42].
Horizontal CVD reactors are mainly used in research
laboratories. Although the production scale is limited,
they are easy to set up. Gas flow is parallel to the
substrate surface, which is good for surface coating
because laminar gas flow is easy to maintain.

In vertical reactors, gas flow is perpendicular to the
surface. This provides better uniformity than the
horizontal geometry [44], but at the expense of low
reactant utilization [45].

(3) Exhaust System

Since many chemicals and reaction products associated
with CVD processes are toxic, corrosive or explosive,
disposal of by-products and partially converted reactants
must be handled with care. Depending on the type of
chemicals used, various treatment methods can be applied to
exhaust gases in order to prevent hazardous gases and
particles from being exposed to the atmosphere. For
example, gas scrubbers, activated alumina filters, aqueous
absorbents, various cold traps and in-line filters [40] can
be used to prevent the pollution problem. Obviously, each
CVD reaction has its own disposal/recycle problems whose
solution must be engineered into the system.

1.4 Fundamentals of CVD Processes

In a CVD process, one or more condensed phases are
produced as a result of gas-solid reactions. For a desired
deposition, complications may arise from the thermodynamic

feasibility of required reactions, the kinetics of reactions, and the morphology of solid products. The determination of optimum deposition parameters, in order to prepare desired products, requires a detailed understanding of the entire process. Such an understanding includes knowledge of the chemistry of the system, the equilibrium thermodynamic yields, possible rate-limiting mechanisms, and mass transport processes.

(1) Thermodynamic Considerations

The feasibility of a CVD reaction and the reaction driving force are determined by the thermodynamics of the system. In most CVD cases, laminar gas flow and high temperatures are required. This leads to a reasonable assumption that the chemical environment at the substrate surface is at or close to an equilibrium condition. In relatively simple CVD systems, thermodynamic analyses of equilibrium constants and the feasibility of depositing desired coatings have been previously examined [46-50]. Complex systems like M-X-H-Cl (where M-X = Ti-B, B-C, Nb-Ge and V-Si) [50], M-C-H-Cl and M-B-C-H-Cl (M = Si, Zr, Hf) [51,52] have also been studied. A number of computer programs, e.g., SOLGASMIX [53] and EQUICA [40], have recently become available for thermodynamic calculations. As a result, the feasibility of many proposed CVD reactions can be examined and the optimum range of processing parameters can be determined.

With the aid of CVD phase diagrams, which are based on

thermodynamic calculations using the free energies of formation of all of the compounds involved in the reactions [54], satisfactory predictions of possible coatings and deposition parameters can be achieved. As seen in Figure 2-7 which is a reported CVD phase diagram of $HfCl_4$-BCl_3-MTS (Methyltrichlorosilane) system, the deposition conditions for HfB_2 + SiC codeposition can be predicted [55].

(2) Mass Transport and Kinetic Study

The tendency of a CVD reaction to proceed is governed by two factors: thermodynamics, which considers the driving force of a reaction, and kinetics, which describes the rate-controlling mechanism(s) and, possibly, the microstructure.

Generally speaking, there are seven mechanistic steps involved in a CVD process (see Figure 2-8) [56]. They are described below:

a. Forced flow of reactant gases into the system.

b. Diffusion and bulk (viscous) flow of reactant gases through the boundary layer to the substrate.

c. Adsorption of gases onto the substrate.

d. Chemical reactions between adsorbed species.

e. Desorption of by-products from the substrate.

f. Diffusion and bulk flow of product gases through the boundary layer to the bulk gas.

g. Forced exit of gases from the system [56].

During a process, each step can occur individually or simultaneously with other ones. The rate-controlling step

may vary from one to another depending on the CVD
conditions (temperature, pressure, gas flow, substrate,
etc.). A thorough understanding of the rate-controlling
mechanism may help one to estimate the deposition rate and
predict the coating morphology.

The morphology and microstructure of CVD coatings vary
widely from single crystal films to amorphous deposits,
depending on deposition conditions. When supersaturation
and temperature are considered, the effect of deposition
conditions on the coating structure can be summarized as in
Figure 2-9 [57]. Generally, when supersaturation is low
and surface diffusion is fast, columnar, domed deposits
result. Slightly higher supersaturation and slower surface
diffusion lead to large, faceted grains with a preferred
orientation. Further increasing supersaturation and
decreasing surface diffusion produces fine, equiaxed grains
[57]. This type of structure is the most desirable coating
structure when strength and toughness are of concern.

During a CVD process, besides the effects of
supersaturation and deposition temperatures, the
deposition pressure also plays a very important role during
the process. Taking silicon coating as an example,
atmospheric pressure or soft vacuum are primarily used in
the CVD of epitaxial (i.e. single crystalline) silicon
films. Low pressure CVD, however, is the main production
tool for depositing polycrystalline silicon, dielectric and

passivation films used in the integrated circuit industry [42].

Based on thorough mechanistic studies, theories of modeling general CVD processes have been proposed. Kotechi [42] presented his calculated results as three-dimensional phase diagrams using the coordinates of flow rate, temperature and gas concentration. Comparison between his theories and experiments showed satisfactory consistency. He has also used these phase diagrams to demonstrate how to optimize deposition conditions in order to obtain desired coatings.

The development and stability of the boundary gas film over the substrate surface have significant effects on coating morphology. Rhee, Szekely and Ilegbusi [58] developed a modified CVD reactor, in which a point source gas inlet near the substrate surface was used in order to produce recirculatory flow. The recirculatory flow interfered with the development of the boundary layer in the gas phase. The experimental results show that a uniform, fine-grained coating of SiC was obtained.

2.4.5 Advantages and Limitations of CVD Techniques

The advantages and limitations of using CVD to obtain desired coatings can be summarized as follows [40]:

(1) Advantages:

a. CVD techniques can produce a large variety of coating materials (especially some of the less known refractory coatings) at near-theoretical density with good adherence.

Also, codeposition and graded deposition are possible.

b. Stoichiometry, morphology, crystal structure and crystal orientation can be tailored by controlling deposition parameters and by carefully preparing the substrate surface.

c. CVD techniques can be applied to deposit coatings on substantial contours. Compared to electroplating, CVD produces a more uniform film on complex-shaped surfaces (see Figure 2-10).

d. CVD processes are operated at a temperature, which is only a small fraction of the melting point of the coating materials. This saves tremendous energy and raw materials when depositing high melting point materials, such as most of the refractory metal carbides, nitrides and oxides.

e. CVD can also produce either thin (a few hundred angstroms) or thick (inch size) coatings with high purity. Both thickness and purity can be controlled reasonably well.

(2) Limitations

a. One of the essential requirements for a CVD process is to have a hot and stable substrate. The desired coating can not be deposited if the substrate temperature is not high enough for reactions to take place. Therefore, the substrate materials must be physically, chemically and thermally stable in a reaction chamber. In contrast, some other coating techniques can be done at room temperature (e.g., sputter coating and evaporating), or at low

temperatures (e.g. plasma-assisted CVD).

b. Suitable chemical reactions must take place in order to obtain the desired CVD coatings. Therefore, such reactions must be thermodynamically feasible at the desired temperature and pressure.

c. Due to the elevated temperatures required for CVD processes, thermal expansion mismatch between coating and substrate becomes an important factor on coating performance. Proper selection of coating and substrate materials is necessary in order to avoid cracking and spalling of the coating.

d. Since most chemicals involved in CVD reactions are hazardous (e.g., corrosive, toxic, and/or explosive), precautionary measures must be considered in designing a CVD apparatus.

CHAPTER 3

EXPERIMENTAL PROCEDURES

Substrate Material

The substrate material used in this study was a
proprietary 2-D carbon-carbon composite comprised of pitch
fiber within a resin/CVI carbon matrix. The carbon-carbon
composite had undergone two CVI of carbon cycles at $950^{\circ}C$
and a final high temperature ($2500^{\circ}C$) heat treatment in
order to obtain optimum densification for the composite.

3.2 Specimen Pretreatment

3.2.1 Substrate Pretreatment Apparatus

Figure 3-1a shows a schematic diagram of the equipment
used for both pack cementation and vapor treatment
experiments. The reactor consists of two components: a
reaction tube (Quartz, 65mm dia. x 953mm length) and a
cooling water jacket (Pyrex, 95mm dia. x 610mm length). An
induction furnace (GE, 20KW) was used as a heat source for
the reactor. The hot zone of the reactor is about 80mm
long. Two viewing ports were installed on both ends of the
quartz tube. Specimen temperature was measured by using an
optical pyrometer (Pyrometer Instrument Co., Inc., Model
No. 95), which was capable of measuring temperatures from
700 to $3200^{\circ}C$ (+/- $5^{\circ}C$ accuracy). The pyrometer was
calibrated by using a "Tungsten - 5% Rhenium vs. Tungsten -
26% Rhenium" thermocouple ($425^{\circ}C$ - $2320^{\circ}C$, +/- 1.0%) in a
graphite furnace. The calibration was conducted from $800^{\circ}C$
- $1800^{\circ}C$. It was found that the discrepancies measured by

the pyrometer and the Tungsten-Rhenium thermocouple were relatively linear, varying from $5^{\circ}C$ at $800^{\circ}C$ to $10^{\circ}C$ at $1800^{\circ}C$. The CVD reactor was evacuated and purged with Ar gas at least 3 times before each experiment started. Both pack cementation and vapor treatment experiments were conducted at atmospheric pressure under a steady flow of Ar. Since the reactor wall was cooled by water, the reaction chamber was capable of heating the carbon-carbon specimens up to $2000^{\circ}C$.

3.2.2 Specimen Preparation

Carbon-carbon specimens for both pack cementation and vapor treatment experiments were cut to 12.7mm x 15.9mm x 6.4mm in size by using an ISOMET diamond saw (Buehler LTD). Specimen surfaces were polished with 600 grit sand paper and then sonicated with methanol in an Ultramet III sonic cleaner (Buehler LTD). Cleaned specimens were dried in a vacuum dissector for at least 30 minutes before they were weighed by an electronic balance (+/- 0.01mg).

3.2.3 Pack Cementation Procedures

(1) Powder Preparation

The powder mixture used for pack cementation experiments contained 60% SiC (99.9%, -100 mesh), 30% Si (99.8%, 1μ) and 10% Al_2O_3 (99.9%, 1μ) by weight [27]. The powders were hand-mixed until a relatively uniform mixture was obtained. Finally, the powder mixture was dried at $300^{\circ}C$ for at least 5 hours.

(2) Packing Procedure

The graphite crucible used for pack cementation experiments is schematically illustrated in Figure 3-1b. The specimen was placed in the center of the crucible and firmly packed in the powder mixture.

(3) Pack Cementation

Initially, the reactor was evacuated and purged with Ar. After a suitable inert atmosphere was achieved, the specimen was heated at $500^{\circ}C$ for 20 minutes in order for residual moisture and volatiles to evaporate. Then the specimen was heat treated at $1700^{\circ}C$ for 3 hours so that the proper conversion reaction was achieved [27].

After pack cementation treatment, the specimen could be retrieved easily from the crucible. A typical gray-green conversion layer was obtained on the surface.

3.2.4 SiO Vapor Treatment

An alternative approach for obtaining an SiC converted layer was to heat a carbon substrate in an SiO vapor atmosphere. In this case, a carbon substrate was placed above a powder mixture which consisted of 50% SiO_2 (99.9%, -100 mesh)and 50% of Si (99.8%, 1μ)by weight [28].

The graphite crucible used for SiO vapor treatments is shown schematically in Figure 3-1b. The experiment was conducted at $1200^{\circ}C$, atmospheric pressure for 3 hours.

3.3 External Surface Coatings

Conventional thermal CVD techniques were employed in

this study. The reactor was of a horizontal, cold wall type. Most CVD experiments were done at $1200^{\circ}C$-$1300^{\circ}C$ and 2-10 torrs of pressure. Source gases used for various coating experiments were SiH_4, CH_4, $ZrCl_4$, BCl_3, H_2, and Ar.

3.3.1 CVD Apparatus

Figure 3-2 shows a schematic diagram of the chemical vapor deposition apparatus used in this study. There are four major components in the CVD apparatus: (1) a gas feeding system, (2) the chemical reaction chamber, (3) a gas disposing system, and (4) the computer control system.

(1) Gas Feeding System

In order to achieve the required gas flow control, four MKS flow meters and an MKS multi-gas-controller (MKS model 147) were used in conjunction with a computer. The flow rates of all four channels were monitored and controlled by the computer during the CVD experiments.

Since SiH_4 reacts violently with air, a check valve was installed at the outlet of the SiH_4 gas tank to avoid the back flow of air (Figure 3-2). CH_4 and H_2 are connected to the channels 2 and 3 flow meters. Ar was used as a carrier gas to transport $ZrCl_4$ vapor (Channel 3, Figure 3-2) and as a purge gas to purge gas lines in channels 1, 2, and 4 prior to each CVD experiment.

In this study, $ZrCl_4$ (99.6%) powder was used as a precursor for ZrC coating. Since it is in solid form under

normal conditions, a vaporization device was to be
installed in the gas feeding system. As illustrated in
Figure 3-2, the vaporization device contains a Varian type
tee adapter, in which $ZrCl_4$ powder was placed, and a
resistive furnace. When the appropriate vapor pressure of
$ZrCl_4$ was obtained, the Ar gas channel was turned on so
that it flowed through the tee adapter and carried the
$ZrCl_4$ vapor into the reaction chamber.

During CVD experiments, the temperature of the
vaporization chamber had to be determined by the
equilibrium vapor pressure of $ZrCl_4$. $ZrCl_4$ has a
sublimation point of $331^\circ C$. The temperature dependence of
$ZrCl_4$ vapor pressure is shown in Figure 3-3. Above $300^\circ C$,
the vapor pressure of $ZrCl_4$ dramatically increases. This
would make accurate control of $ZrCl_4$ virtually impossible.
On the other hand, at temperatures much below the
sublimation point, the vapor pressure becomes so low that a
sufficient amount of $ZrCl_4$ vapor can not be obtained.
Based on preliminary experiments, temperature in the range
from 260 to $280^\circ C$ was found most favorable for efficient
$ZrCl_4$ vaporization and accurate flow control.

In order to prevent the vapor from being condensed
before it reached the heated substrate, a tube furnace and
a heating tape were installed. Their temperatures were
measured by type K thermocouples and controlled at
approximately $310^\circ C$ by OMEGA controllers.

(2) Chemical Reaction Chamber

The CVD reaction chamber consists of a quartz tube with an inside diameter of 54 mm. An induction generator was used to heat the specimen. The hot zone was about 72 mm long and its length could be adjusted by changing the length of the induction coil. The entire hot zone was shielded with a metal cage to avoid interference of the electromagnetic field from the coil with electronic parts of the system. The specimen temperature was measured by using the calibrated optical pyrometer (Pyrometer Instrument Co., Inc., Model No. 95, +/- $5^{O}C$ accuracy). An MKS throttle valve, an MKS pressure sensor, and an MKS automatic pressure controller were used to control the total pressure of the reaction chamber. The sensing and the controlling of the pressure were both interfaced with the computer.

(3) Vacuum System

All deposition experiments in this study were done under low pressure conditions. Two mechanical pumps capable of pumping 300 liters of air per minute were used in parallel. This pumping capacity allowed CVD experiments to be performed at pressures ranging from 1 to 100 torrs. An Al_2O_3 filter was installed before the vacuum pumps in order to trap particulate reaction products, mild acids, and pump oil vapor.

(4) Computer Control System

In the CVD apparatus, data acquisition and control were all performed using an IBM AT micro-computer. The computer was interfaced with the upstream gas handling system and the downstream pressure control valve. The deposition pressure and the pattern of flow rate variation were easily controlled by keying in appropriate parameters.

3.3.2 External Coating Procedure

(1) Specimen Preparation

Pretreated specimens were lightly brushed and sonicated in methanol and then dried in vacuum dissector for 30 minutes. Dried specimens were weighed by an analytical balance (+/- 0.01mg).

(2) CVD Experiment

Coating systems investigated in this study were SiC, ZrB_2, SiC/ZrB_2 multilayer coating, and SiC/ZrC graded coating. Table 3-1 summarizes the gas precursors used for these coatings.

In order to obtain the desired coating systems, deposition parameters, such as temperature, pressure, time, and precursor composition, had to be optimized. Prior to each deposition experiment, a series of test runs were conducted in order to determine the optimum deposition conditions. The detailed description of deposition parameters for various coating systems is presented in Table 3-1.

Table 3-1 Gas Precursors

Coating	Raw Materials	Chemical Reaction
SiC	CH_4, SiH_4, H_2	$CH_4 + SiH_4 = SiC + 4H_2$
ZrB_2	$ZrCl_4$, BCl_3, H_2, Ar	$ZrCl_4 + 2H_2 = Zr + 4HCl$ $2BCl_3 + 3H_2 = 2B + 6HCl$ $Zr + 2B = ZrB_2$
$SiC+ZrB_2$	CH_4, SiH_4, H_2 $ZrCl_4$, BCl_3, Ar	All reactions above are involved.
SiC+ZrC	CH_4, SiH_4, H_2 $ZrCl_4$, Ar	$CH_4 + SiH_4 = SiC + 4H_2$ $CH_4 + ZrCl_4 = ZrC + HCl$

(1) SiC Coating

Based on the results of preliminary test runs, at temperatures below 1100°C, the deposition rates were very slow and SiC coatings were ⏤ thin to be able to protect the substrate against oxi⏤⏤on. On the other han⏤, deposition at above 1 ⏤°C ca ⏤ed spallation of the coating during cool down. T⏤ ⏤m CVD temperature was found to be about 1200°C. ⏤⏤ temperature, a fine polycrystalline SiC coating, good adhesion between coating and substrate, and proper coating thickness were obtained. The structure and chemical composition also depend on the deposition pressure and flow rates. A smooth, pure SiC coating layer was found to be deposited at 2 torrs of pressure ⏤nd an SiH_4/CH_4 ratio of ⏤3.

(2) ZrB_2 Coating

The source gases used for the ZrB_2 coating experiments were $ZrCl_4$, BCl_3 and H_2. Similar to the ZrC coating

experiments, Ar was used to carry the $ZrCl_4$ vapor into the reaction chamber. Based on the preliminary test runs, it was found that an Ar/BCl_3 ratio of 2:1 produces a pure ZrB_2 coating. Since chlorides were used as the primary source gases, a large amount of excess H_2 was needed to reduce the chloride gases. A series of test runs showed that a ZrB_2 coating could be deposited using 30 sccm of Ar, 15 sccm of BCl_3, and 420 sccm of H_2 at $1300^\circ C$ and 10 torrs of pressure.

(3) SiC and ZrB_2 Multilayer Coating

A pure ZrB_2 coating forms borate glass during oxidation at much lower temperature as compared with an SiC coating. However, a serious oxidation problem was encountered at higher temperature due to the vaporization of borate. In order to retard the vaporization of the borate glass, a SiC over coat was applied above the ZrB_2 coating. In this type of multilayer coating approach, a ZrB_2 inner layer and an SiC overcoat were deposited using the parameters described earlier in this section.

(4) SiC and ZrC graded Coating

A typical example of controlling gas flow rates for obtaining graded coating is illustrated in Figure 4-32b. Flow rates of H_2 and CH_4 were kept constant throughout the entire experiment. Flow rates of $ZrCl_4$, which was carried by the Ar carrier gas, and SiH_4 were varied in order to obtain the graded coating. With this type of flow control, it has been demonstrated that CVD experiments performed at

1300°C, 1.5 torr yielded the graded coating structure depicted in Figure 4-32a.

3.4 Oxidation Testings

Two types of oxidation tests were employed in this study: (1) isothermal tests, and (2) thermal cycling tests. Both types of tests were performed in air at atmospheric pressure.

3.4.1 Thermogravimetric Measurements

Two oxidation testing devices were used in this study. The first one was a thermal gravimetric analyzer (TGA) made by Dupont. The upper temperature limit of this analyzer is 1200°C. The testing chamber is a quartz made tube, 22.2 mm in diameter and 127 mm long. A maximum weight of 400 milligrams can be measured with an accuracy of +/- 0.02 milligram. Weight changes were continuously recorded on a chart recorder during oxidation tests.

The Dupont TGA can only operate at temperatures lower than 1200°C with limited specimen size. In order to expand the testing capability to higher temperatures on larger specimens, a high temperature TGA was designed and set up. As shown in Figure 3-4, the high temperature TGA consists of an induction coil and a force transducer. Oxidation tests can be conducted at temperatures up to 3000°C in static air. The force transducer (Vertek) measures the specimen weight and converts it linearly to an analog signal ranging from 0 to 5 volts. The analog signal is then recorded by an IBM personal computer through a data

acquisition interface.

3.4.2 Testing Procedure

The specimens for oxidation tests were cleaned in methanol and dried in a vacuum dissector for half an hour. The initial weight of each sample was measured using an analytical balance (+/- 0.01mg) before the oxidation tests were carried out.

(1) Dupont TGA Operation Procedure

Only one series of SiO vapor treated samples were tested using the Dupont TGA. The specimen size was about 15mm x 7mm x 1.5mm, which weighed less than 400 mg. A platinum wire basket was used as specimen holder. Air was introduced into the testing chamber at a flow rate of 50 sccm.

(2) High Temperature TGA Operation Procedure

Oxidation tests on pack cemented specimens and CVD-coated specimens were conducted by using the high temperature TGA apparatus. The specimen size was around 6.35mm x 12.7mm x 15.9mm and weighed approximately 2 to 2.5 grams. The specimen was placed in an alumina crucible, which was cut open near the bottom so that oxidation products would not be collected and measured. The crucible was carefully hung inside the induction coil using a thin tungsten wire which was connected to the force transducer. The tungsten wire was about 5mm above the induction coil. Therefore, during the oxidation tests, its temperature was much lower than the specimen temperature. After hundreds

of hours of oxidation tests, negligible weight loss occurred to the tungsten wire.

Before each test, the power supply of the force transducer was checked and adjusted. Then the cooling water and the power of the RF (radio frequency) generator was turned on. After warming up for more than 2 minutes, the coil power was turned on and slowly brought up to an appropriate level. During the test, the calibrated optical pyrometer was used to monitor the specimen temperature closely (+/- 5°C). The weight change was recorded by the computer and displayed on the monitor continuously throughout the test.

3.5 Microstructure Study

In this study, microstructural characterization of coated and oxidized composites were conducted by using an optical microscope (ORM), the scanning electron microscope (SEM), the transmission electron microscope (TEM), and the X-Ray diffraction (XRD).

3.5.1 Optical Microscopy

Conventional optical microscopy was employed with a magnification range of 50X to 1000X. Cross-sectioned samples were cut using a Buehler Isomet low speed saw to about 5mm x 12mm x 6mm size with a diamond wafering blade. Cut sections were then mounted in epoxy. Mounted samples were polished by using a Mini-Met polisher (Buehler). Polishing was done progressively from 600 grid to 1um diamond paste.

A Nikon Microphot microscope was used for optical microscopy work. Optical micrographs were taken using 35 mm color film. Black and white photographs were printed using Penalure printing paper.

3.5.2 Scanning Electron Microscopy

Samples for SEM studies were cut and mounted on SEM stubs with the use of a carbon cement. Since ceramic coatings and glasses are non-conductive, the surface of each specimen has to be coated with conductive substances such as carbon, gold or platinum. A sputtering device was used to apply a thin (about 300 Å) coating of platinum on the sample surface. This coating minimizes specimen charging so that the resolution of SEM image was greatly improved. SEM observations were conducted by using a Hitachi S-570 SEM. Polaroid PN-55 films were used to record SEM images.

3.5.3 Transmission Electron Microscopy

Since TEM foils have to be thinner than 2000 Å in order for electrons to penetrate, a special specimen thinning technique, e.g., atom milling, had to be used. Initially, thin slices (about 0.4 mm thick) were cut by using the Isomet low speed saw. Following cutting, each slice was polished down to 200 μm thick and core drilled into 3 mm diameter disks. Then, these discs were mounted on a dimpling platen in order to be dimpled by using a VCR dimpler. During dimpling, initially the surface of the specimen was flattened using 3 μm and 1μm diamond slurries.

hen a fine surface finish was achieved, the sample was
lipped over and the other surface was dimpled to a
hickness of about 10-20 μm. The dimpled specimen was then
arefully removed from the platen and rinsed with acetone
nd methanol.

The final perforation of TEM specimens was done in a
R Atom Miller. During atom milling, high energy Ar atoms
mbard both sides of the dimpled disc at low angles in
cuum. Such bombardment gradually removes surface atoms
e layer after another, and eventually, results in final
rforation. Normally, atom milling was conducted at
mperatures ranging from -70°C to -80°C in order to avoid
er heating, contamination, and non-uniform milling. The
celerating voltage was 5.5 KV, and the beam current was
proximately 1.5 mA. Initially a beam angle of 25° was
sed until perforation occurred. Then, the beam angle was
reduced to 15° and milling continued for additional four
urs.

TEM studies were conducted mostly using a Hitachi
H700-H TEM. TEM techniques of bright field imaging, dark
field imaging, and selecting area diffraction were employed
in the investigation.

3.5.4 X-ray Diffraction Analysis

The X-ray diffractometer used in this study utilized a
Cu-Ka irradiation in conjunction with a Ni filter. The X-
ray tube was operated at 35 KV, 15 mA. The monochromatic
wave length was 1.54178 Å. During each X-ray diffraction

experiment, the detector was scanned at an angular speed of 2 degrees per minute. The chart recorder used to record spectra was normally run at a speed of 2 cm per minute.

CHAPTER 4

EXPERIMENTAL RESULTS AND DISCUSSION

The experimental results and their interpretations and discussions are presented below based on three areas: (1) thermodynamic calculation of coating systems, (2) evaluation of coating microstructure, and (3) oxidation testing and characterization.

4.1 Results of Thermodynamic Calculation

The objective of using thermodynamic calculation was to study the feasibilities of desired coating systems and to determine optimum processing conditions. Although CVD processes inherently involve rapid changes of reacting species, it was still worthwhile to examine equilibrium conditions where very slow reactions were considered. Particularly, the following aspects were of primary interest: (1) What kind of gas precursors should be selected for a given coating system; (2) Under what conditions can the expected deposition be obtained; (3) Whether or not the variation of system temperature, pressure, and carrier gas have any effect on final deposition result?

4.1.1 Basic Principle

The basic principles on which thermodynamic calculations of the CVD phase diagrams was based were the "Law of Mass Action" and the standard free energy change of reactions [59]. They were used to calculate equilibrium phase boundaries as functions of state variables such as

temperature, pressure and gas composition in a given reaction system. The "Law of Mass Action" states that the rate at which a chemical reaction proceeds is proportional to the "active" masses of the reacting substances. The active mass of a mixture of ideal gases is the number density of each reacting species or, for a given temperature, it can be represented by its partial pressure.

Let us consider a typical chemical reaction:

$$v_a A + v_b B \iff v_c C + v_d D. \qquad \text{Eq. 4-1}$$
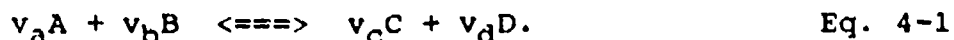
The "Law of Mass Action" states that:

$$\frac{(Pc)^{v_c} (Pd)^{v_d}}{(Pa)^{v_a} (Pb)^{v_b}} = K_p(T) \qquad \text{Eq. 4-2}$$

where P is partial pressure, v is a stoichiometric coefficient, and K_p is an equilibrium constant which is a function of temperature alone.

The equilibrium constant is related to standard free energy change by:

$$\Delta G^o = - RT \ln K_p \qquad \text{Eq. 4-3}$$

where R is the gas constant, T is the absolute temperature, and ΔG^o is the standard free energy change for the reaction. ΔG^o can be calculated by using thermodynamic data from JANAF Thermodynamical Tables [54] or from other thermodynamic data sources [60-62].

4.1.2 Simple Reaction System

Taking the decomposition of SiH_4 as an example, there are three predominant species involved in the reaction:

silane, silicon and hydrogen. Silane decomposes into elemental silicon and hydrogen according to the reaction:

$$SiH_4 \quad <===> \quad Si \; + \; 2H_2 \qquad\qquad \text{Eq. 4-4}$$

$$K_p = \frac{P_{H2}^2}{P_{SiH_4}} \qquad\qquad \text{Eq. 4-5}$$

$$\triangle G^O = - RT \ln K_p. \qquad\qquad \text{Eq. 4-3}$$

Taking the logarithm of Equation 4-5, one finds:

$$\ln K_p = 2\ln (P_{H2}) - \ln (P_{SiH4}). \qquad\qquad \text{Eq. 4-6}$$

Table 4-1 Thermodynamic Data for SiH4 Ideal Gas [54]

Temperature K	$\triangle G^O$ Kcal/mole	$\ln Kp = -\triangle G^O/(RT)$
500	17.254	-17.367
600	19.473	-16.334
700	21.763	-15.647
800	24.093	-15.157
900	26.449	-14.790
1000	28.816	-14.503
1100	31.190	-14.270
1200	33.564	-14.076
1300	35.934	-13.913
1400	39.302	-13.769
1500	40.663	-13.643
1600	43.016	-13.530
1700	45.476	-13.463
1800	48.534	-13.570

Using the data listed in Table 4-1, one can calculate K_p for a given temperature, and hence plot an equilibrium line in a $\ln P_{(H2)}$ vs. $\ln P_{(SiH4)}$ plot. The equilibrium lines for 1000°K and 1500°K are plotted in Figure 4-1. It is clear that by choosing the temperature and gas

composition, reaction direction can be determined. For
example, when gas composition is at the lower right region
of Figure 4-1, etching occurs. Namely, Si gasifies and
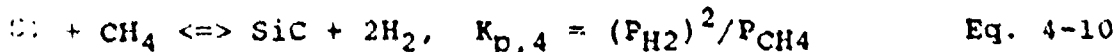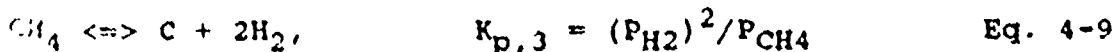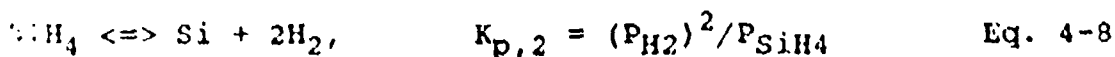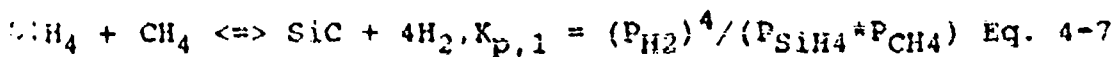forms SiH_4. On the other hand, when the gas composition
falls in the upper left region, SiH_4 decomposes and an Si
deposition layer forms.

4.1.3 Complex Reaction Systems

There are many source gases which can be used for CVD
SiC coating. Thermodynamic analysis for the $SiH_4-CH_4-H_2$
system were studied and the results are presented below.

In the $SiH_4-CH_4-H_2$ system, possible chemical reactions
and their equilibrium constants are:

$$SiH_4 + CH_4 <=> SiC + 4H_2, K_{p,1} = (P_{H2})^4/(P_{SiH4}*P_{CH4}) \quad \text{Eq. 4-7}$$

$$SiH_4 <=> Si + 2H_2, \quad K_{p,2} = (P_{H2})^2/P_{SiH4} \quad \text{Eq. 4-8}$$

$$CH_4 <=> C + 2H_2, \quad K_{p,3} = (P_{H2})^2/P_{CH4} \quad \text{Eq. 4-9}$$

$$Si + CH_4 <=> SiC + 2H_2, \quad K_{p,4} = (P_{H2})^2/P_{CH4} \quad \text{Eq. 4-10}$$

$$SiH_4 + C <=> SiC + 2H_2, \quad K_{p,5} = (P_{H2})^2/P_{SiH4}. \quad \text{Eq. 4-11}$$
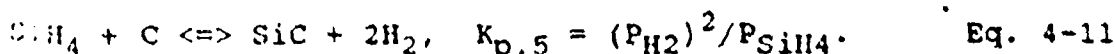
At a given temperature and total pressure, an
equilibrium line exists for each of the above equations.
Take Equation 4-7 for example, since

$$- \ln K_{p,1} = \ln (P_{CH4}/P_{H2}^2) + \ln(P_{SiH4}/P_{H2}^2) \quad \text{Eq. 4-12}$$

An equilibrium line which has a slope of -1 in a ln
(P_{CH4}/P_{H2}^2) vs. ln (P_{SiH4}/P_{H2}^2) plot can be determined if
$K_{p,1}$ is known. This equilibrium line depicts the phase
boundary between gas and SiC phase fields. After
determining all five equilibrium lines using the data
listed in Table 4-2, a CVD phase diagram, which is a map of

all stable phases at 1500°K, can be constructed. The calculated CVD phase diagram for the Si-C-H system at 1500°K is shown in Figure 4-2. It is clear that the expected deposition can be easily determined if the deposition parameters are known.

Table 4-2 Thermodynamic Data for Si-C-H System (1500°K)[54]

Reactions	$\triangle G^\circ$ (Cal)	$\ln K_p$
1 $SiH_4 + CH_4 \Longleftrightarrow SiC + 4H_2$,	3144	-1.0512
2 $SiH_4 \Longleftrightarrow Si + 2H_2$,	40663	-13.6430
3 $CH_4 \Longleftrightarrow C + 2H_2$,	17859	-5.9919
4 $Si + CH_4 \Longleftrightarrow SiC + 2H_2$,	25937	-8.7022
5 $SiH_4 + C \Longleftrightarrow SiC + 2H_2$,	43769	-14.6941

It is important to point out that the CVD phase diagram of Figure 4-2 has to satisfy the Phase Rule:

$$F = C - P + 2 \qquad\qquad \text{Eq. } 4\text{-}13$$

where F: degree(s) of freedom.

C: number of components.

P: number of phase(s).

If both temperature and pressure are constant, then the phase rule should be rewritten as:

$$F = C - P. \qquad\qquad \text{Eq. } 4\text{-}14$$

In our calculation, the number of components are three, i.e., $SiH_4 + CH_4 + H_2$. Therefore for single phase fields

where C = 3 and P = 1, two degrees of freedom should be expected. For two-phase equilibrium, only one degree of freedom exists.

Figure 4-2 shows four single phase fields with two degrees of freedom. Each of the five straight lines represents a two-phase equilibrium with one degree of freedom. Two triple-points where equilibrium lines met correspond to three-phase equilibrium, which have zero degree of freedom.

4.1.4 CVD Diagram for SiC and ZrC Codeposition

When there is a large number of species involved, the problem becomes very complicated. Using computers can make such complicated calculations possible and more efficient. In order to perform desired calculations for this study, a SOLGASMIX computer program [53] was revised and adapted to the IBM 370 mainframe computer [63]. This program iteratively minimizes the total free energy of the system by varying the amount of all possible compounds in the system. With the aid of this program, Zr-Si-C-H-Cl and Zr-Si-B-C-H systems were investigated. Results are presented as CVD phase diagrams in Figures 4-3 and 4-4.

Most CVD ceramic coatings are produced at high temperatures and some degree of vacuum in order to obtain optimum structure and properties. Also, since hydrogen is known to depress carbon formation, the use of hydrogen as a carrier gas was considered. As seen in Figure 4-3, the predicted concentration ratios of all four source gases for

the codeposition are similar to one another. This indicates that the deposition condition may be obtained without substantial difficulties.

4.1.5 CVD Phase Diagram of ZrB_2/SiC System

Figure 4-4 is a calculated phase diagram of a Zr-B-C-Si-H system at $1573^{O}K$ under a total system pressure of 0.1 atm. $Zr(BH_4)_4$, SiH_4 and CH_4 were used as gas precursors to obtain ZrB_2 and SiC codeposition [64]. The diagram shows that the simple two-phase field of ZrB_2/SiC did not exist at the composition range of our interest.

4.2 Results of Microstructural Studies and Oxidation Tests

4.2.1 Carbon-Carbon Substrate

Figure 4-5 shows an optical micrograph of the carbon-carbon substrate used in this study. Pitch fiber bundles are surrounded by a matrix composed of graphitized resin and CVI pyrolytic carbon. Cracks and porosity are observed in the fiber bundles interfaces as well as in the matrix. The density of this composite is about 1.7 g/cc.

TGA tests performed on the as-received carbon-carbon substrate resulted in rapid catastrophic oxidation at approximately $1000^{O}C$. For example, a rectangular specimen (15mm x 7mm x 1.5mm) lost 100% of its weight in 37 minutes under these conditions. This oxidation rate was obviously controlled by reaction kinetics, as indicated by the linear weight loss curve of line A in Figure 4-11.

4.2.2 Converted Coating

1. Pack-Cemented Coating

(1) Microstructure

After 3 hours of pack cementation at $1700^{\circ}C$, a uniform converted SiC layer was formed on the specimen surface (Figure 4-6a). The thickness of this layer was approximately 100-150 microns. The converted layer was formed not only on the surface of the specimen but also on open internal pores and crack surfaces. This indicates that the Si vapor diffused into porosity and cracks and reacted with all accessible surfaces, resulting in the formation of an SiC layer during the pack cementation experiments. In most reacted areas, fibers and matrices were both converted. However, since the matrix was more porous than the fibers, a preferential conversion reaction was usually found in the matrix. As a result, it is generally observed that non-converted or partially converted fibers were surrounded by converted SiC matrix (see Figure 4-6b). It is also seen in Figure 4-6b that micro-cracks were present in both converted fibers and matrix. This is due to the CTE mismatch between SiC and carbon.

Figure 4-7a is an X-ray diffraction spectrum of a pack cemented specimen. Indexing of the spectrum indicated that the converted layer was β-SiC. The detailed microstructure of the converted layer is shown in Figure 4-7b, which is a TEM micrograph of a pack cemented specimen. It was

observed that the β-SiC grains were equiaxed, with the grain sizes of about 1-5 microns. No preferred orientation in the SiC layer was found, regardless of the anisotropic nature of fibers and matrix.

(2) Oxidation tests results and discussion

Isothermal oxidation tests were done on the pack cemented specimens using the home-made TGA. The testing temperatures varied from $1000^{\circ}C$ to $1700^{\circ}C$.

Figure 4-8a is a computer recorded plot showing the weight changes of specimens oxidized at 1000, 1200, 1300, 1500, 1600, 1700 and $1800^{\circ}C$ in static air. Linear weight change curves were observed during all the tests. This indicated that reaction kinetics were the rate limiting step during oxidation. In order to obtain oxidation rates, linear regression was applied to the curves in Figure 4-8a. The results were plotted in Figure 4-8b, which shows the average oxidation rate (%/min) as a function of testing temperatures $(^{\circ}C)$. Oxidation rates obviously decreased with the increase of testing temperatures from 1000° to $1600^{\circ}C$. This is because that the SiO_2 glass formed and flowed more efficiently at higher temperatures. This effect enhances the oxidation resistance of the pack-cemented composite. The viscosity of the SiO_2 glass is very high at $1000^{\circ}C$ and gradually decreases as temperature increases. Better glass flow, i.e., lower viscosity, resulted in more efficient crack sealing and a lower

oxidation rate. The best oxidation protection result was obtained at 1600°C, as shown in Figure 4-8a and 4-8b. Higher oxidation temperatures, 1700 and 1800°C, resulted in catastrophic oxidation due to the formation and disrupture of glass bubbles. These events took place because the total equilibrium vapor pressures of CO and SiO were higher than the ambient pressure when SiO_2 was in contact with the carbon substrate at temperatures above 1600°C.

2. SiO Vapor Treated Substrate

   (1) Microscopy

   Figure 4-9 is an optical micrograph of a vapor treated composite. The thickness of the SiC conversion layer was not uniform, ranging from 80 microns to a few microns. SiO vapor penetrated much deeper through open porosity and cracks as compared with the results using the pack cementation process. It not only formed a thin layer of converted SiC on internal surfaces, but also produced fine whiskers in internal porosity. Figure 4-10 shows an SEM photograph of SiC whiskers obtained during the vapor treatment. These were submicron-sized SiC whiskers.

   (2) Oxidation Tests

   Since it was very difficult to obtain a uniformly converted coating using the SiO vapor treatment, the oxidation resistance of treated specimens was very poor. Figure 4-11 is a plot of weight loss curves for vapor treated specimens oxidized at 800°, 1000°, and 1200°C. All tested specimens suffered high weight loss after only short

periods of oxidation time. Line B is the weight loss curve of a vapor treated specimen oxidized at $1000^{\circ}C$. Comparing line B with line A (an as-received specimen oxidized at $1000^{\circ}C$), it was found that no oxidation resistance improvement was achieved by the vapor treatment technique.

Comparing the pack cementation and the SiO vapor treatment techniques, it is found that the pack cementation technique was more efficient in providing a uniform protective SiC layer than was the vapor treatment technique. As a result, pack cemented specimens showed much better oxidation resistance.

However, conversion coating obtained from either one of these techniques cannot be used independently as an efficient oxidation protection coating for high temperature applications, because:

(1) The converted layer is not a dense protective layer. It can slow down the oxidation process, but it can not achieve satisfactory protection by itself. Due to thermal expansion mismatch and structural differences, micro-cracks are produced which give access to oxygen during oxidation.

(2) Although a thicker SiC conversion layer could result in higher oxidation resistance, the thickness of the converted layer has to be limited in order not to degrade mechanical properties.

4.2.3 External CVD Coatings

In this investigation, the following external CVD coatings were produced: SiC, ZrB_2, SiC/ZrB_2 multilayer coating and SiC/ZrC graded coating. Results of CVD experiments, microstructural studies, and oxidation tests for these coatings are presented below.

1. SiC Coating

Based on the results of preliminary test runs at 1100°C, it was found that the deposition rates were very slow and that the SiC coatings obtained were too thin to be capable of protecting the substrate. On the other hand, deposition temperatures above 1400°C caused the coating to spall during cool down. The optimum temperature range for CVD was found to be between 1200 and 1250°C. The coating deposited at this temperature consisted of fine polycrystalline grains. Its adhesion to the substrate and deposition rate were both satisfactory.

The flow rate ratio of SiH_4 to CH_4 had a great effect on the final coating composition. Figure 4-12 shows typical flow rate curves for obtaining silicon carbide deposition. The flow rates of silane and methane were 25 and 75 sccm, respectively. Figure 4-13 is an X-Ray diffraction pattern of the SiC coating obtained using the gas flow condition described in Figure 4-12. In addition to the predominant phase of SiC, small amounts of free Si were also found in the coating. Figure 4-14a is an optical micrograph of a cross section of this SiC coating. The two

phase mixture (light and dark phases) was observed in the micrograph. The micro-hardness value of this coating was approximately 2700 kg/mm^2 on the knoop scale, which is consistent with the micro-hardness value of CVD silicon carbide. Good bonding between the pack cemented substrate and the CVD coating was also observed. SEM examination of the coating surface, Figure 4-14b, shows a polycrystalline surface morphology.

Figure 4-15a is a bright field TEM micrograph of the SiC coating. It is seen that the polycrystalline grains of B-SiC are about 2-10 microns in size and heavily twinned. Figures 4-15b and 4-15c are the bright field image and selecting area diffraction pattern, respectively, of the twin structures.

The addition of hydrogen in the mixture of reacting gases caused negative effects. Firstly, it lowered the coating efficiency since it forced the backward reactions in Equations 4-6 and 4-7 to occur. Secondly, it caused the formation of a large amount of free Si in the coating. Thus, a substantial drop of the micro-hardness value to about 800 kg/mm^2 resulted.

Isothermal and thermally cycled oxidation tests were conducted on SiC-coated carbon-carbon specimens which were obtained by using flow rates shown in Figure 4-12. Figure 4-16 is a TGA thermogram of isothermal oxidation tests carried out in air at 1500° and 1700°C. After 10 hours of

tests, the specimen oxidized at 1500°C gained 3.5% of its initial weight whereas the specimen oxidized at 1700°C showed less than 1% weight gain. Figure 4-17 compares the results of the isothermal test and the thermal cycling test at 1700°C. In the thermal cycling test, the temperature was cycled between room temperature and 1700°C, with a residence time of 0.5 hour at 1700°C and a 3-minute period between each cycle. The thermal cycling test showed no significant weight change in the initial 8 cycles. Then, the specimen started to lose weight. After 10 hours of the cycling test, the specimen showed about 4.4% weight loss. The weight loss during the thermal cycling test was a linear function of time, which indicated that the oxidation was reaction-controlled.

Figure 4-18 is a cross section optical micrograph of an SiC-coated composite after 10 hours of isothermal oxidation at 1700°C. A thin glass layer was found covering the entire surface of the specimen. A wavy, continuous dark layer was found lying underneath the glass film. This dark layer is probably a carbon layer which is formed as a result of the interaction of the SiO_2 glass and the SiC coating because:

$$SiC + O_2 \Longleftrightarrow SiO_2 + C. \qquad\qquad \text{Eq. 4-15}$$
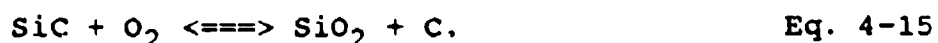
Figure 4-19 is an SEM photograph of an SiC-coated specimen which was oxidized at 1500°C. No significant damage of the coating was found. However, oxidation at 1700°C caused bubble formation in a short period of time. As shown in

Figure 4-20, bubbling was observed after 3 hours of oxidation at 1700°C.

2. ZrB_2 Coating

In addition to the Si-carrying compounds, such as the glass formers of SiC and Si_3N_4, metal diborides have also been reported to be good candidates for oxidation protection. ZrB_2 was selected in this study because it tends to form borate glass at high temperatures. Figure 4-21a shows a typical flow rate pattern for obtaining a ZrB_2 coating. After a series of test runs, it was found that the optimum condition for depositing ZrB_2 was: 1300°C, 30 sccm of Ar ($ZrCl_4$ carrier gas), 15 sccm of BCl_3, 420 sccm of H_2, and 10 torrs of pressure.

An X-Ray diffraction spectrum of a ZrB_2 coating obtained by using the coating conditions described above is shown in Figure 4-21b. The diffraction pattern shows that the predominant phase in the coating is ZrB_2, along with a small amount of B_4C. Figure 4-22 is an optical micrograph of this ZrB_2 coating, which shows very good coating adhesion. However, the number of thermal cracks was found to be higher than in the case of the SiC coating. This is because of the fact that the CTE of ZrB_2 (4.6×10^{-6} °C^{-1}) is higher than that of SiC (3.6×10^{-6} °C^{-1}) [65].

Although ZrB_2 is quite refractory, the oxidation results of ZrB_2 coating were not encouraging. As shown in Figure 4-23, the ZrB_2-coated specimen started to smoke

badly at about 1000°C and suffered severe weight loss when the temperature reached 1500°C. The oxidized specimen surface was partially covered with white powdery residue. X-ray diffraction performed on this residue showed that it was predominantly ZrO_2, as demonstrated in Figure 4-24.

In order to find out how and why ZrB_2 fails to protect carbon-carbon composite, an oxidation test was interrupted after 10 minutes and the specimen was examined by SEM. As shown in Figure 4-25a, it was found that the glass sealant of B_2O_3 bubbled and ruptured easily, leaving particulate residue, presumably ZrO_2, where the bubbles ruptured. The remaining B_2O_3 glass, i.e., the background phase in Figure 4-25a, also started to degrade. Micro-cracks began to develop due to the vaporization of B_2O_3 releasing the pressure of forming additional bubbles. Eventually, the structure of the ZrO_2 residue shown in Figure 4-25b resulted. The events which occurred during the oxidation of the ZrB_2 coating indicated that Zr was not involved in forming a passive Zr-containing borate glass. The oxidation reaction of ZrB_2 seemed to be:

$$ZrB_2 + 5/2 \ O_2 \Longleftrightarrow ZrO_2 + B_2O_3. \qquad \text{Eq. 4-16}$$
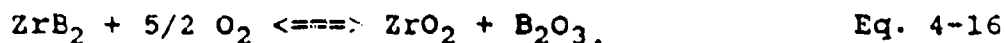
The B_2O_3 product was vaporized quickly since it was only a low melting point compound (449°C [65]).

Although ZrB_2 was not qualified as an independent protective coating, it was interesting to note that this coating started to form B_2O_3 glass at a temperature lower than 1000°C. It may help to improve the protection of

carbon-carbon composites at intermediate temperatures. Therefore, if ZrB_2 is used in conjunction with SiC coating, better thermal cycling properties should be expected. This leads to the approach of SiC + ZrB_2 multilayer coating.

3. SiC and ZrB_2 Multilayer Coating

The multilayer coating of SiC + ZrB_2 consisted of an inner layer of ZrB_2 and an overcoat of SiC. As described earlier, this composite coating is expected to offer good oxidation protection at both intermediate and high temperatures.

The coating conditions for obtaining the multilayer coating were adopted from the previous SiC and ZrB_2 deposition experiments. Three hours of SiC coating was followed by another three hours of ZrB_2 deposition in order to form the desired multilayer coating.

Since efficient protection is expected to cover a wide temperature range in this multilayer approach, the thermal cycling test was of primary interest in the study of this approach. In particular, a new type of 2-stage thermal cycling test was designed, which included residence time periods at both intermediate and high temperatures in a cycle. Figure 4-26 is a TGA result of a 2-stage thermal cycling test performed on a multilayer-coated composite. During the test the temperature was cycled from room temperature to $1000^{\circ}C$ for half an hour followed by $1500^{\circ}C$ for another half hour. After 25 hours of testing, the

specimen showed a uniform, reflective, glassy surface without any trace of oxidation damage. The total weight loss of the specimen was less than 1%. SEM observations showed that a few chipped areas caused by prior CVD cool down were all perfectly covered with glass (Figure 4-27). Apparently, glass flowed efficiently at $1000^{\circ}C$ and remained stable at $1500^{\circ}C$. It indicated that B_2O_3 and SiO_2 reacted readily, leading the formation of borosilicate glass which provided good protection over a wide temperature range. Additionally, no evidence of ZrO_2 was found. This implies that Zr was contained in the glass and it may have offered an advantageous effect to the glass.

4. SiC and ZrC Graded Coating

Figure 4-28 illustrates a schematic diagram which demonstrates the concept of the graded coating approach. The area indicated by "A" represents a pretreated substrate whose internal and external surfaces are converted to refractory metal carbide. The converted carbide layers should provide proper oxidation resistance at intermediate temperatures while maintaining a low CO pressure at high temperatures. The layer shown by "B" is a refractory carbide layer (e.g., ZrC, HfC). This layer limits carbon diffusion and exhibits good mechanical and chemical compatibility with the carbon substrate. The transition from refractory metal carbide to silicon carbon, indicated by "C", is gradual. The graded layer minimizes thermal stresses so that spalling and cracking would then be

suppressed. The SiC interlayer, labeled by "D", serves as a glass former. When the viscous glass flows and seals off the crack, it reacts with the refractory metal carbide overcoat, layer "E", which forms a high viscosity silicate. The high viscosity silicate is expected to have lower evaporation rate and act as a barrier against erosion and oxygen diffusion.

Figure 4-29a shows curves of the gas flow which were used in an attempt to produce the ZrC + SiC graded coating. At the beginning and near the end of the deposition, large amounts of $ZrCl_4$ vapor were carried into the CVD reactor by high flow rates of the He carrier gas. Hydrogen and methane flow rates were kept constant at 50 and 30 sccm throughout the experiment. Silane flow rate started from zero and was gradually increased to 15 sccm while $ZrCl_4$ was absent. Subsequently, silane flow gradually decreased to zero where as $ZrCl_4$ flow slowly increased to its initial value. An optical photograph of the coating thus obtained is shown in Figure 4-29b. A ZrC predominant phase was observed through the coating thickness. This indicated that the $ZrCl_4$ flow was too high, and that the silane flow rate should be increased.

In order to promote SiC formation and suppress ZrC formation in the middle section of the coating, maximum silane flow during the middle hour of the CVD experiment should be increased and the initial and final $ZrCl_4$ flow

rates should be decreased. Figure 4-30a shows the modified flow rate pattern which was used for the purpose of promoting SiC formation. The cross-section optical micrograph of the coating obtained is shown in Figure 4-30b. It shows a multilayered coating of ZrC and SiC. Obviously, however, the deposited layers shown in Figure 4-30b were not graded, since the transition between the layers of ZrC and SiC is abrupt. This coating tends to spall and crack due to the CTE mismatch between ZrC ($7.54 \times 10^{-6} \; ^{\circ}C^{-1}$) and SiC ($3.6 \times 10^{-6} \; ^{\circ}C^{-1}$). This mismatch is responsible for poor oxidation protection performance of the coating. Figure 4-31 shows an SEM micrograph of the multilayer-coated specimen after oxidation at $1500^{\circ}C$. Spalling and cracking of the protective layer obviously occurred during oxidation. The cracked coating also caused severe bubbling in the SiO_2 glass layer. This is because the SiO_2 layer found access to the carbon substrate, yielding high CO and SiO pressure, since:

$$SiO_2 + C \; <===> \; CO + SiO. \hspace{3cm} \text{Eq. 4-17}$$

Excessive formation of these bubbles was attributed to the failure of the coated composite after 1 hour of oxidation at $1500^{\circ}C$.

In order to achieve a gradual transition from ZrC to SiC layers, a small amount of silane was introduced at the beginning of the deposition. Figure 4-32a shows the graded coating obtained by controlling gas flow rates according to the flow rate curves shown in Figure 4-32b. As shown in

the micrograph, the fraction of fine SiC grains gradually increases as the layer thickness increases. It appears that the use of low SiH_4/CH_4 and high $ZrCl_4/CH_4$ flow rate ratios yielded a fine-grained two phase mixture of ZrC and SiC. This is consistent with the calculated CVD phase diagram of Figure 4-3.

Isothermal oxidation tests at $1500^{\circ}C$ in air were performed on a specimen obtained by using the gas flow rates shown in Figure 4-32b. After 10 hours the specimen showed no weight loss. Instead, a weight gain of 1% was observed. The SEM micrograph (Figure 4-33a) shows that the surface of the oxidized specimen contained a two phase mixture of SiO_2 glass and a fine crystalline phase, presumably a zirconium-containing silicate. Figure 4-33b shows the cross-section micrograph of the specimen. A uniform protective glass layer was found on the specimen surface.

Figure 4-34 shows the control of gas flow rates which proved to be the best of the flow rate conditions for SiC/ZrC graded deposition. An oxidation test performed on the coated specimen obtained showed no appreciable weight loss after 100 hours of testing at $1500^{\circ}C$ in air. The TGA result is shown in Figure 4-35, as compared with the oxidation of pack-cemented specimens.

Oxidation tests at $1700^{\circ}C$ were also performed on this type of coated specimen. After 10 hours of oxidation at

$1700^{\circ}C$, the specimen showed no evident damage, as shown in Figure 4-36. The coating gradually degraded after prolonged oxidization at $1700^{\circ}C$. As seen in Figure 4-37, after 21 hours of oxidation, moderate bubbling was observed. Nevertheless, no evidence of appreciable damage on the surface was observed.

The results of TEM observation are presented in Figure 4-38 in order to reveal the detailed microstructure of the glass layer. Figure 4-38a is a TEM bright field image of the surface glass formed during oxidation. The associated selecting area diffraction pattern is shown in Figure 4-38b. It is evident that the glass also contained small crystals which were 0.01 - 0.02 microns in size. The SAD pattern, along with X-ray diffraction pattern of Figure 4-39, proved that these tiny crystals were $ZrSiO_4$. Although the viscosity and the structure of the glassy phase are yet to be investigated, the morphology of the glass layer seemed to indicate that the protective surface layer is capable of providing a reasonable resistance to both oxygen diffusion and erosion.

The CVD phase diagram shown in Figure 4-3 indicates that when the molar ratio of $ZrCl_4/CH_4$ is greater than about 20, while keeping the ratio of SiH_4/CH_4 low, ZrC should be the predominant deposition phase. In practice it is difficult to correlate the flow rates of the Ar carrier gas and the actual amount of $ZrCl_4$ vapor being carried into the reaction chamber. However, the presence of the ZrC

layer shown in Figure 4-30b demonstrates that by supplying 60 sccm of argon, 30 sccm of CH_4, and 40 sccm of H_2 into the CVD reaction chamber, the gas composition required to form ZrC is provided. This implies that the gas composition over the substrate surface falls into the ZrC phase field in the calculated phase diagram (Figure 4-3). When $ZrCl_4$ vapor ceases to enter the reaction chamber and the flow rate ratio of SiH_4/CH_4 is 1 (Figure 4-30b), SiC should result according to the CVD Phase diagram. The SiC interlayer shown in Figure 4-30b indicates that the prediction was satisfactorily met.

CHAPTER 5

CONCLUSIONS

1. Thermochemical calculations performed using a modified SOLGASMIX program were consistent to certain degrees with experimental results.

For obtaining the SiC coating, the flow rate ratio of CH_4/SiH_4 should be slightly larger than 1 and smaller than 4. 20 sccm of Ar as a carrier gas for $ZrCl_4$, 40 sccm of BCl_3, and 500 sccm of H_2 were used to produce the ZrB_2 coating. For the ZrC coating, 60 sccm of Ar and 40 sccm of CH_4 were found to be successful.

2. Converted coating experiments demonstrated that the SiC pack cementation technique provided a thicker and more uniform converted layer than the vapor treatment did. As a result, pack cemented specimens showed better oxidation resistance.

The SiO vapor treatment experiments showed deeper Si vapor penetration through internal porosities. As a result, it may improve internal oxidation protection because more internal pore and crack surfaces were converted into SiC. Gas phase nucleation resulted in SiC whisker formation during the vapor treatment. The whiskers were present on the specimen surfaces as well as in the internal porosities.

3. The SiC coating protected carbon-carbon composites against oxidation at 1500°C and 1700°C for 10 hours without any weight loss in isothermal tests. The thermal cycling

test at 1700°C showed no significant weight change in first 8 cycles, and 4.4% weight loss in the next 8 cycles. These results indicate that SiC coating is capable of protecting the carbon-carbon substrate in a oxidizing atmosphere up to 1700°C.

4. ZrB_2 coating can not protect carbon-carbon substrate from oxidation at 1500°C. It formed a low melting point, high vapor pressure boron oxide glass, which evaporated at the testing temperature and destroyed the coating layer because of bubbling and spallation.

5. ZrB_2/SiC multilayer coating greatly improves the oxidation resistance of carbon-carbon composites at both intermediate (1000°C) and high temperatures (1500°C). The thermal cycling test showed that this coating formed low viscosity glass at a temperature lower than 1000°C. The glass sealed off cracks and spalled areas during oxidation. SiC and ZrB_2 together formed borosilicate glass which also protected the carbon-carbon substrate from oxidation at higher temperatures.

6. Graded coating system

A ZrC-SiC graded coating can be obtained by using flow rates shown in Figure 3-34. A graded ZrC and SiC coating with fine-grained structure offers good oxidation protection for carbon-carbon composites because it enhances both chemical and mechanical stabilities. A gradual transition from ZrC to SiC reduces the chance of interface delamination, while a fine, polycrystalline structure is

more resistant to thermal cracking as compared to a coarse, columnar coating. This graded coating survived a 100-hour isothermal oxidation test in air at 1500°C with only a 0.61% weight loss. An isothermal oxidation test at higher temperature, 1700°C, shows less than a 1% weight loss after 21 hours. A glass phase as well as zirconium silicate were identified by microscopy study. No evidence of appreciable damage of the coating or gasification of the carbon-carbon substrate was observed.

CHAPTER 6

FUTURE WORK

1. Oxidation Testings in Controlled Environments

So far, isothermal and thermal cycling tests have been conducted in static air. A series of oxidation tests in controlled environments needs to be carried out where pressure, temperature and moisture level can be controlled in order to stimulate real application environments, e.g., NASP (National Aero Space Plane) environments.

2. Theoretical Studies

Although lots of studies have been performed on coating systems and their oxidation resistances, further kinetics and mass transport behaviors need to be studied in order to obtain a better basic, theoretical understanding of coating processes. This will help us to achieve better coating process control and to obtain better deposition in terms of uniformity, morphology, structure and efficiency.

3. Mechanical Testing

As one of the most important factors, the mechanical properties of coated composites, have significant effects on their final performance. Mechanical testings such as tensile, bending and coating adhesion tests at both room temperature and high temperatures can provide valuable information in the evaluation of each coating system.

4. Other Coating Systems

More coating systems, such as other refractory carbides (HfC, TaC, TiC, ...), refractory borides (HfB$_2$,

TiB_2, ...) and oxides (SiO_2, Al_2O_3, Ta_2O_5, ...), should be studied in order to extend the oxidation resistance and mechanical properties of carbon-carbon composite to a wider temperature range.

5. Whisker Reinforced Coating

The whisker formation during the vapor treatment experiments needs to be further studied, so that the results can be applied to the concept of whisker reinforced coatings.

6. Microscopy Studies

Detailed structural and chemical studies of coated and oxidized carbon-carbon composites are necessary to help us understand the processing/property relationship and the protection/degradation mechanisms of coatings.

REFERENCES

1. E. Fitzer, "Carbon Fibres and Their Composites". Published by United Nations Financing System for Science & Technology for Development (UNFSSTD), based on papers presented at the International Conference on Carbon Fibre Applications, Brazil, 5-9 Dec. 1983.

2. J. E. Sheehan, "Ceramic Coatings for Carbon Materials". Proceedings of the Fourth Annual Materials Technology Center Conference on Recent Research into Carbon Composites, 1987. pp. 369-374.

3. J. R. Strife, J. E. Sheehan, "Ceramic Coatings for Carbon-Carbon Composites". Ceramic Bulletin, Vol. 67, No.2, 1988.

4. J. Don, "Microstructure Study of Carbon-Carbon Composite", Proceeding of 11th Int. Conf. on Advanced Composite Materials, Cocoa Beach, Florida, 1987.

5. H. Chang and R. M. Rusnak, "Oxidation Behavior of Carbon-Carbon Composites", Carbon, Vol. 17, pp.407-410, 1979.

6. G. W. Smith, "Oxidation Resistance of Pyrolytically Grown Carbon Fibers", Carbon, Vol. 22, No.6, pp 477-479, 1984.

7. D. D. Eley, P. W. Selwood, "Advantages in Catalysis and Related Subjects", Vol. XI, pp. 165, 1959.

8. E. Fitzer, K.-H. Geigl, W. Huttner and R. Wiess, "Chemical Interactions Between the Carbon Fibre Surface and Epoxy Resins", Carbon, Vol.18, pp. 389-393, 1980.

9. M. A. Forrest, H. Marsh, "The Effects of Pressure on the Carbonization of Pitch/Carbon Fibre Composite", J. Mater. Sci., Vol. 18, pp. 978-990, 1983.

10. G. W. Weber, K. R. Young, A. J. Taylor and T. J. Curci, "Densification of Carbon-Carbon Composite at 30 KSI", Proceedings and Program of XVIIth Biennial Conference on CARBON. pp. 68, 1985.

11. J. B. Donnet and R. C. Bansal, "Carbon Fibers", published by Marcel Dekker, Inc. 1985.

12. J. H. Cranmer, I. G. Plotzker, L. H. Peebles,Jr., and D. R. Uhlmann, "Carbon Mesophase-Substrate interactions", Carbon, Vol.21, No.33, pp. 201-207, 1983.

13. B. Rand, "Carbon Fibres from Mesophase Pitch", Handbook of Composites, Vol. 1, pp.497-575, 1985.

14. M. A. Forrest, H. Marsh, "Structure in Carbon/Carbon Fibre Composites as Studied by Microscopy and Etching With Chromic Acid", J. Mater. Sci., Vol. 18, pp. 973-977, 1983.

15. H. W. Chang and S. K. Rhee, "Oxidation of Carbon Derived from Phenolic Resin", Carbon, Vol.16, pp. 17-20, 1978.

16. L. S. Penn and R. C. T. Chou, A. S. D. Wang and W. K. Binienda, "The Effect of Matrix Shinkage on Damage Accumulation in Composites", J. Comp. Mater., Vol. 23, pp. 570-586, June 1989.

17. P. Ehrburger and J. Lahaye, "Characterization of Carbon-Carbon Composites - II, Oxidation Behavior", Carbon, Vol. 19, pp. 7-10, 1981.

18. C. P. Ju, J. Don, "Basal Plane Orientation of PAN Fibers in a Commerial PAN/Pitch Carbon-Carbon Composite", Mater. Sci. Eng., in Press, 1990.

19. D. W. McKee, C. L. Spiro and E. J. Lamby, "The Inhibition of Graphite Oxidation By Phosphorus Additives", Carbon, Vol. 22, No. 3, pp. 285-290, 1984.

20. D. W. McKee, "Borate Treatment of Carbon Fibers and Carbon/Carbon Composites for Improved Oxidation Resistance", Carbon, Vol. 24, pp. 737, 1986.

21. D. C. Rogers, R. O. Scott, D. M. Shuford, "Material Development Aspects of an Oxidation Protection System for a Reinforced Carbon-Carbon Composite", Proceedings of the 7th National SAMPE Technical Conference. pp. 308, 1976.

22. M. K. Saito, and Y. L. Kogo, "Carbon Fiber Having Improved Thermal Oxidation Resistance and Process For Producing Same", U.S. Patent 4,197,279, April 8, 1980.

23. T. Vasilos, "Self Healing Oxidation Resistant Carbon Structure", U.S. Patent 4,559,256, July 8, 1986.

24. M. Maeda, K. Nakamura, and M. Yamada, "Oxidation Resistance Evaluation of Silicon Carbide Ceramics with Various Additives", J. Am. Ceram. Soc., Vol. 72 [3], pp. 512-514, 1989.

25. P. L. Walker Jr., M. Shelef and R. A. Anderson, "Catalysis of Carbon Gasification", Chem. Phys. of Carbon, Vol. 4, pp. 287, 1968.

26. N. Murdie, E. J. Hippo, "Improved Oxidation Resistance of Carbons By Addition of Chemical Inhibitors to Pitches", Proceedings of Materials Technology Center 15th Annual Conference, pp.137-147, April, 1988.

27. D. C. Rogers, D. M. Shuford, "Formation Mechanism of a Silicon Carbide Coating for a Reinforced Carbon-Carbon Composite", Proceedings of the 8th National SAMPE Technical Conference, pp308, 1976.

28. GMELIN Handbook of Inorganic Chemistry, "Si, Silicon Carbide", Springer-Verlag, W. Germany, 1986.

29. R. A. Rapp and G. R. St. Pierre, "New Options for the Protection of Carbon/Carbon Composites", presented at the High Temperature Composites Initiative Materials Compatibility Meeting, Dayton, Ohio, Oct. 1985.

30. K. Motzfeldt, "On the Rates of Oxidation of Silicon and of Silicon Carbide in Oxygen, and Correlation with Permeability of Silica Glass", Acta Chem. Scand. 18, pp. 1596-1606, 1964.

31. G. H. Schiroky, J. L. Daae and J. E. Sheehan, "High Temperature Oxidation of CVD Silicon Carbide", Proceeding of the 87th Annual Meeting of the American Ceramic Society, May 1985.

32. D. W. McKee, C. L. Spiro and E. J. Lamby, "The Effects of Boron Additives on the Oxidation Behavior of Carbons", Carbon, Vol. 22, No. 6, pp. 507-511, 1984.

33. D. M. Mieskowski, T. E. Mitchell, and A. H. Heuer, "Bubble Formation in Oxide Scale on SiC", Comm. Amer. Ceram. Soc., Jan., C-17, 1984.

34. C. Wagner, "Passivity During the Oxidation of Silicon at Elevated Temperatures", J. Appl. Phys., 29, pp. 1295-1297, 1958.

35. F. W. Hinze and H. C. Graham, "The Active Oxidation of Si and SiC in the Viscous Gas-Flow Regime", J. Electrochem. Soc., 123, pp. 1066-1073, 1976.

36. D. E. Rosner and H. D. Allendorf, "High Temperature Kinetics of the Oxidation and Nitridation of Pyrolytic Silicon Carbide in Dissociated Gases", J. phys. Chem., 74, pp. 1829-1839, 1970.

37. E. Fitzer, D. Hegen, H. Strohmeier, "Chemical Vapor Deposition of Silicon Carbide and Silicon Nitride and Its Application for Preparation of Improved Silicon Ceramics", Proceedings of the 7th International Conference on Chemical Vapor Deposition, pp. 525-535, 1979.

38. L. R. Newkirk, R. E. Riley, H. Sheinberg, F. A. Valencia and T. C. Wallace, "Preparation of Fiber Reinforced Titanium Diboride and Boron Carbide Composite Bodies", Same above, pp. 515-524, 1979.

39. T. Buljan, A. E. Pasto and H. J. Kim, "Ceramic Whisker- and Particulate-Composites: Properties, Reliability, and Applications". Ceram. Bulle., Vol. 68, NO. 2, pp. 387-394, 1989.

40. Bunshah, "Deposition Technologies for Films and Coatings", Noyes Publications, 1982.

41. D. E. Kotechi and I. P. Herman, "A Real Time Monte Carlo Simulation of Thin Film Nucleation in Localized-Laser Chemical Vapor Deposition", J. Appl. Phys., Vol. 64 (10), pp. 4920, 1988.

42. K. F. Jensen, "Micro-Reaction Engineering Applications of Reaction Engineering to Processing of electronic and Photonic Materials", Chem. Eng. Sci., Vol. 42, No. 5, pp. 923-958, 1987.

43. A. Sherman, "Chemical Vapor Deposition for Microelectronics, Principles, Technology, and Applications", Noyes Publications, 1987.

44. D. Foster, A. Learn and T. Kamins, "Silicon Films Deposited in a Vertical Flow Reactor", Solid State Technol., Vol. 29, No. 5, pp. 227-232, 1986.

45. U. Kaempf, "Computer aided control of integrated circuit manufacturing process", Proc. Am. Control Conf., pp. 763-774, 1984.

46. H. Schafer, "Chemical Transport Reactions", Academic Press, NY 1964.

47. K. E. Spear, "Chemical Transport Reactions, A Relevant Area of Research", J. Chem. Ed., 49, pp. 81-86, 1972.

48. K. E. Spear, "High Temperature Reactivity, Treatise on Solid State Chemistry", Vol.4, pp.163. Plenum Press, NY 1976.

49. A. Reisman and T. O. Sedgwick, "Chemical Vapor Deposition and Solid-Vapor Equilibria", Phase Diagrams, Vol. IV, pp. 1. 1976.

50. K. E. Spear, "Applications of Phase Diagrams and Thermodynamics to CVD Proceedings from the 7th International Conference on Chemical Vapor Deposition", pp. 1-16, 1979

51. J. Don, "Thermodynamic Calculation of CVD Phase Diagrams", Materially Speaking, Material Technology Center, SIU-C, 1987.

52. J. Don, "Calculation of Deposition Conditions for ZrC and SiC Multilayer coating for Oxidation Protection of Carbon-Carbon Composite Materials", submitted for publication.

53. G. Eriksson, "Thermodynamic Studies High Temperature Equilibria XII SOLGASMIX; a computer program for calculation of equilibrium composition in multiphase systems", Chem. Scr., 18, 100, 1975.

54. "JANAF Thermodynamical Tables", Second Edition, National Burear of Standards, NSDRS-NBS 37, 1971.

55. W. J. Lacky, A. W. Smith, D. M. Dillard and
    D. J. Twait, "Codeposition of Dispersed Phase Ceramic
    Composites", Proceedings of the 7th International
    Conference on Chemical Vapor Deposition. pp.1008-1027,
    1979.

56. K. E. Spear, "Thermochemical Modeling of Steady-State
    CVD Processes", Proceedings of the Conference on
    Chemical Vapor Deposition. pp.81, 1984.

57. D. P. Stinton, T. M. Besmann, and R. A. Lowden,
    "Advanced Ceramics by Chemical Vapor Deposition
    Techniques", Ceram. Bulle., Vol. 67, No. 2, pp. 350-
    354, 1988.

58. S. Rhee, J. Szekely, and O. J. Ilegbusi, "On Three-
    Dimensional Transport Phenomena in CVD Processes", J.
    Electrochem. Soc.: Solid-State Sci. & Techno., Vol.
    134, No.10, pp. 2552-2557, Oct. 1987.

59. S. Glasstone, "Textbook of Physical Chemistry",
    Princeton, Nj. D. Van Nostrand, 1946.

60. E. Storms, "The Thermodynamics of Refractory Materials.
    Fundamentals of Refractory Compounds", ED. by H. H.
    Hausner, M. G. Bowman, Plenum Press, New York, 1968.

61. Steinitz, "Physical and Mechanical Properties of
    Refractory Compound", Academic Press, New York and
    London, 1966.

62. H. L. Schick, "Thermodynamics of Certain Refractory
    Compounds", Vol. I, Discussion of Theoretical Studies.

63. Private Communication with Dr. Jarlen Don.

64. G. W. Rice and R. L. Woodin, "Zirconium Borohydride as a Zirconium Boride Precursor", J. Am. Ceram. Soc., Vol. 71 [4], pp. C-181-C-183, 1988.

65. "Handbook of Chemistry and Physics", 54th Edition, CRC Press, 1973-1974.
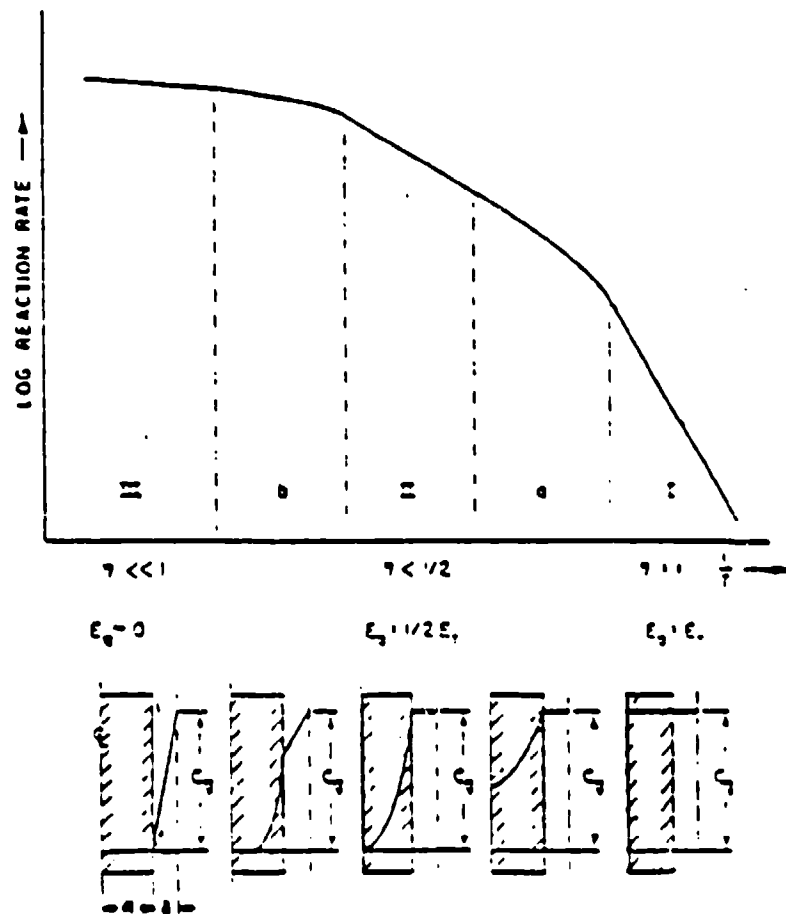
Figure 2-1. The curve which shows three zones of carbon oxidation as a function of inverse temperature. The corresponding oxygen concentration profiles are also shown below [7].
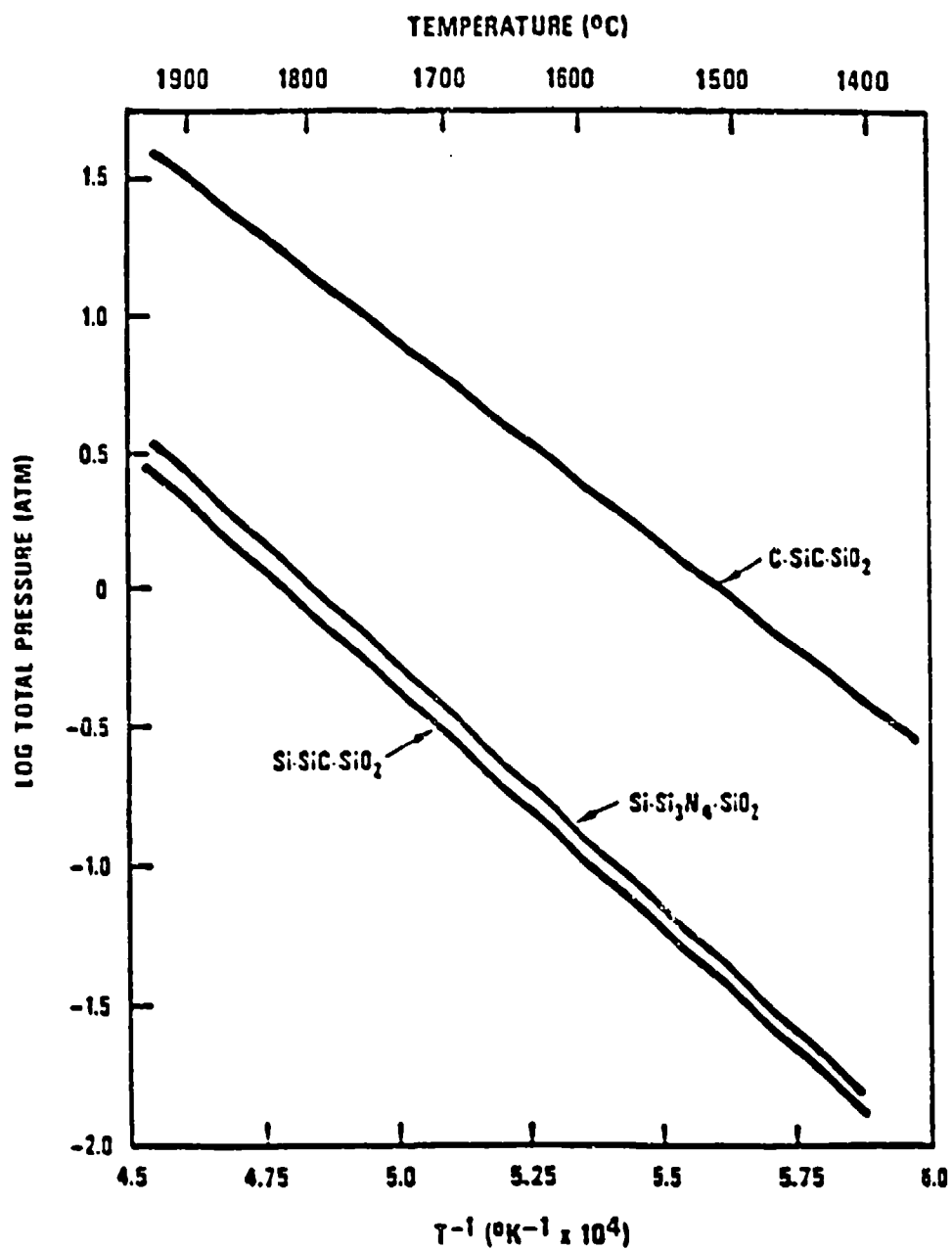
Figure 2-2.   Reduction of SiO_2 by SiC.

.

Table 1.1: Methods of Fabricating Coatings

Atomistic Deposition	Particulate Deposition	Bulk Coatings	Surface Modification
Electrolytic Environment	*Thermal Spraying*	*Wetting Processes*	*Chemical Conversion*
Electroplating	Plasma Spraying	Painting	Electrolytic
Electroless Plating	D-Gun	Dip Coating	Anodization
Fused Salt Electrolysis	Flame Spraying	*Electrostatic Spraying*	(Oxide)
Chemical Displacement	*Fusion Coatings*	Printing	Fused Salts
Vacuum Environment	Thick Film Ink	Spin Coating	*Chemical-Liquid*
Vacuum Evaporation	Enameling	*Cladding*	*Chemical-Vapor*
Ion Beam Deposition	Electrophoretic	Explosive	Thermal
Molecular Beam	*Impact Plating*	Roll Bonding	Plasma
Epitaxy		Overlaying	Leaching
Plasma Environment		Weld Coating	*Mechanical*
Sputter Deposition			Shot Peening
Activated Reactive			*Thermal*
Evaporation			*Surface Enrichment*
Plasma Polymerization			Diffusion from
Ion Plating			Bulk
Chemical Vapor Environment			*Sputtering*
			Ion Implantation
Chemical Vapor Deposition			
position			
Reduction			
Decomposition			
Plasma Enhanced			
Spray Pyrolysis			
Liquid Phase Epitaxy			

Figure 2-3. Methods of fabricating coatings.

$$e^-, \ CH_4^*, \ H, \ H^+,$$

$$CH_4 \ ==> \ C + 2H_2 \qquad\qquad CH_3, \ radiation, \ \ldots$$

a. Thermal   b. Laser   c. Plasma

```
      --------->:  _____  :--------->
      Gas        :         _:___:_      :  Gas
      Feeding    :  _____     :  Disposal
```
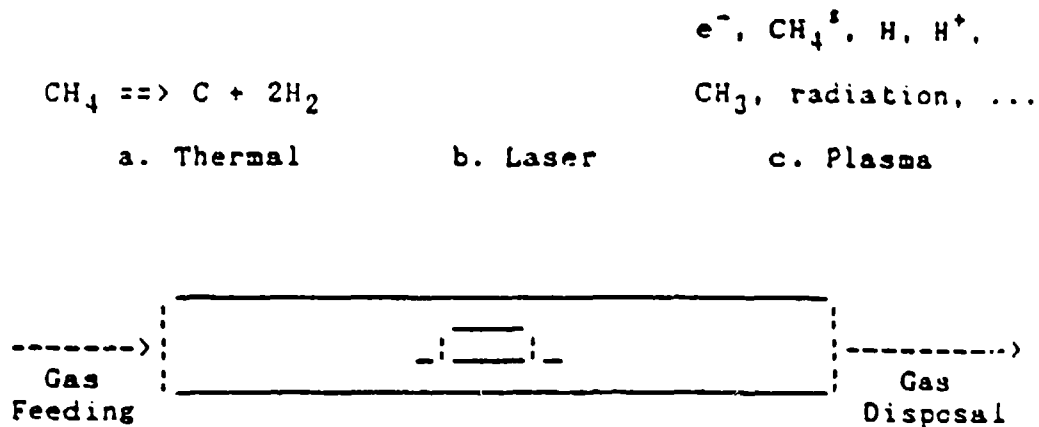
REACTOR

Figure 2-4.   Schematic diagram showing various methods
which can be used to activate CVD reactions.

```
: Gas Feeding :::::: CVD Reactor :::::: Exhaust :
      ..                ..                ..
      ..                ..                ..
      ..                ..                ..
      ..                ..                ..
```

tanks   horizontal   pump

bubbler   vertical   scrubber

furnace   AP or LP

                 hot-wall

                 cold-wall
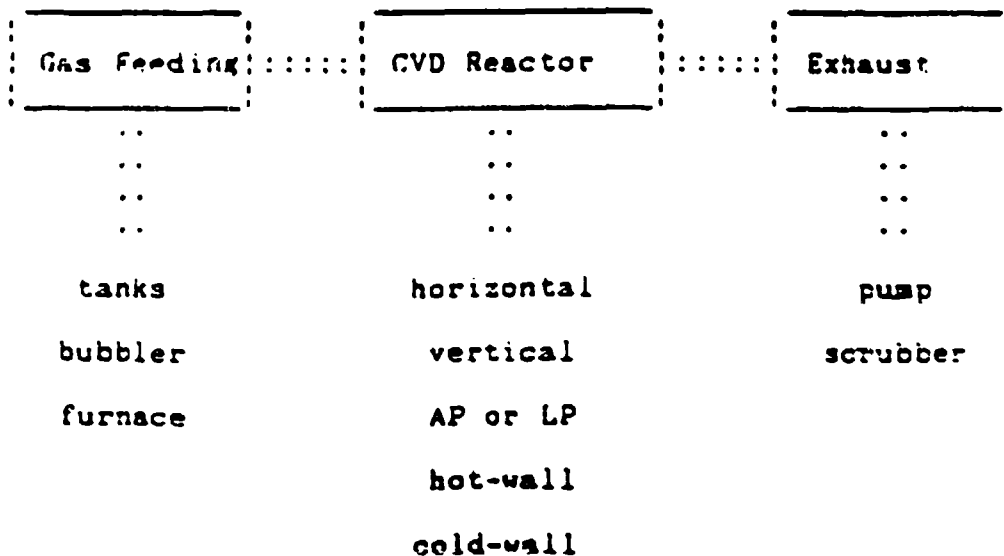
Figure 2-5   Three major components in a CVD system.
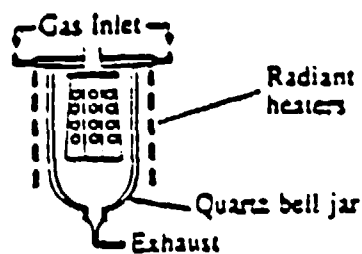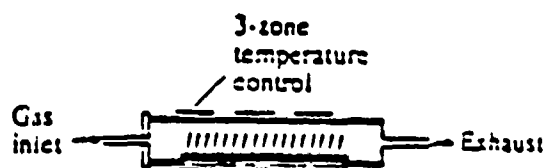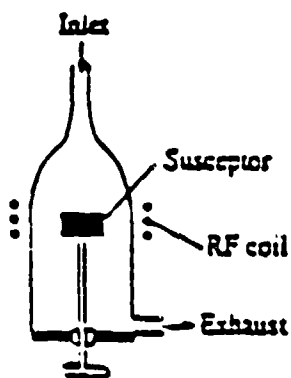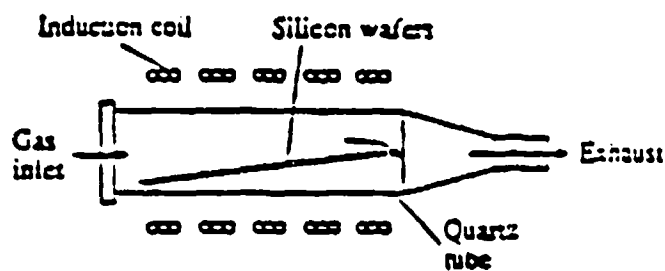
Figure 2-6   Common CVD reactors
          a. Vertical reactor with radiant heater.
          b. Horizontal reactor with radiant heater.
          c. Vertical reactor with induction heater.
          d. Horizontal reactor with induction heater.
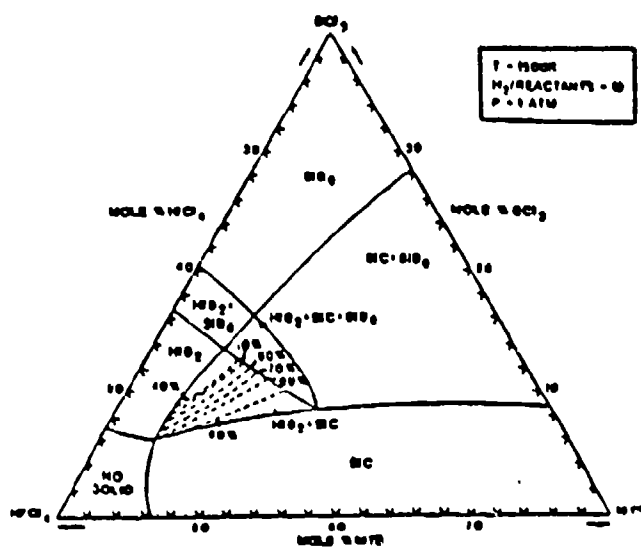
Figure 2-7   CVD phase diagram for the $HfCl_4$-BCl_3-MTS system
at 1500^OK.   The dotted lines show the contours of constant
SiC contents in the two phase region of HfB_2 + SiC.
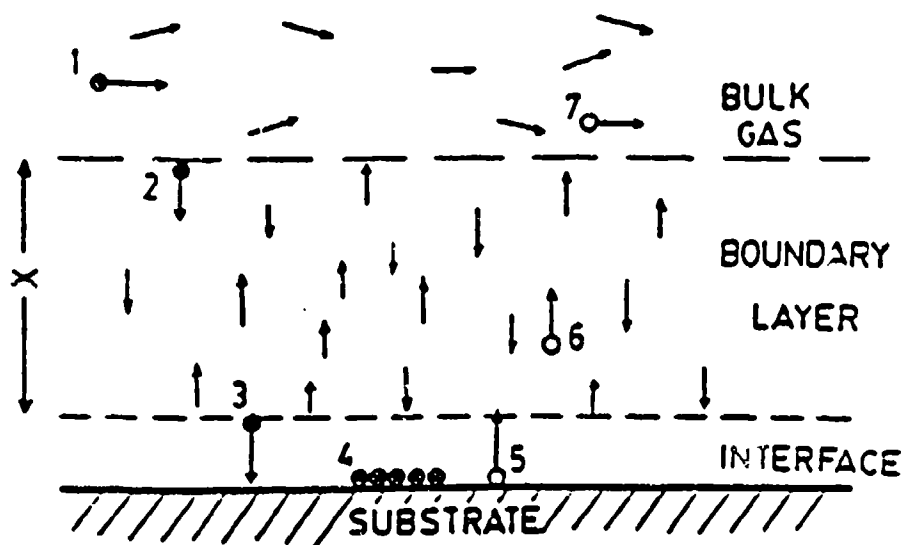
Figure 2-8.   Schematic diagram showing the seven steps
which occur during a CVD process.

```
                                          Approaches equilibrium
                                            condition(25)

                  ::                          /\
                  ::   Epitaxial Growth        ::
                  ::   Platelets               ::
Effect of         ::   Whiskers                ::   Effect of
Increased         ::   Dendrites               ::   Increased
Supersat-         ::   Polycrystals            ::   Temperature
  uration         ::   Fine Grained Polycrystals ::
                  ::   Amorphous Deposits       ::
                  ::                           ::
                  \/                           ::

         Deviates from

      equilibrium condition
```

Figure 2-9. Effect of supersaturation and temperature on the structure of CVD coatings.

electroplating   CVD coating
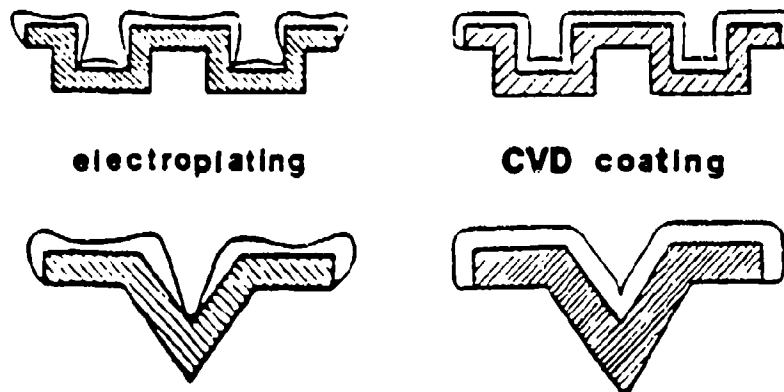
Figure 2-10. Comparison electroplating and CVD coating structures.
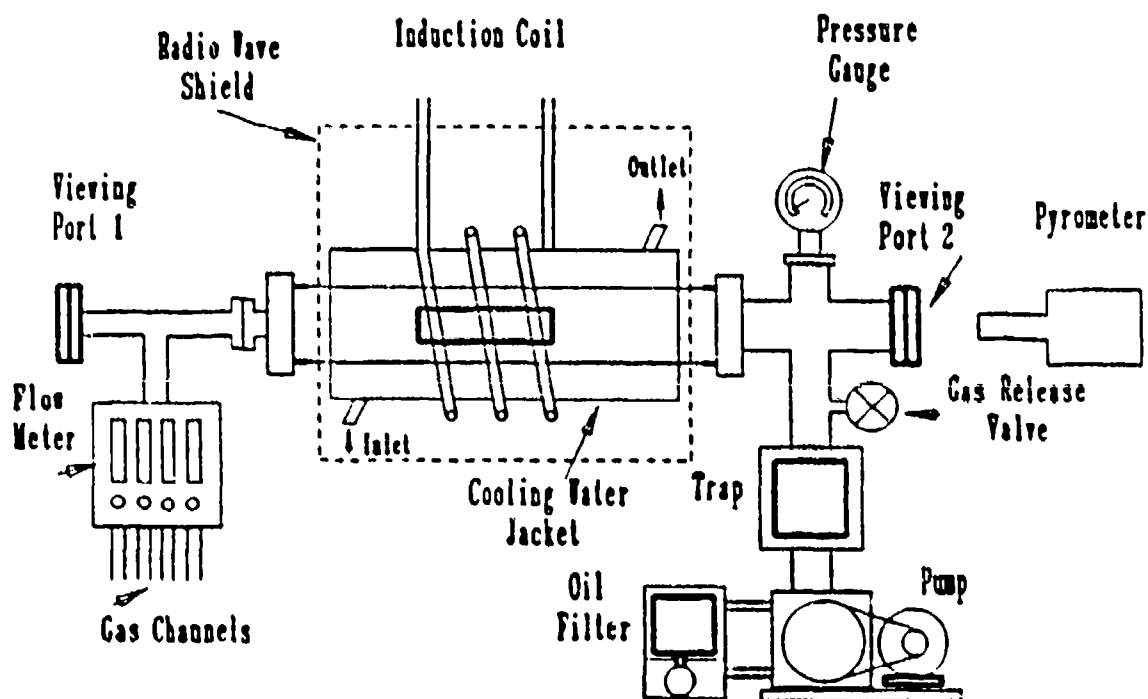
Figure 3-1a. Schematic diagram showing the induction
furnace used for pack cementation and SiO vapor treatment.
The cooling water jacket around the reactor tube makes heat
treatment temperature in excess to 2000°C possible.
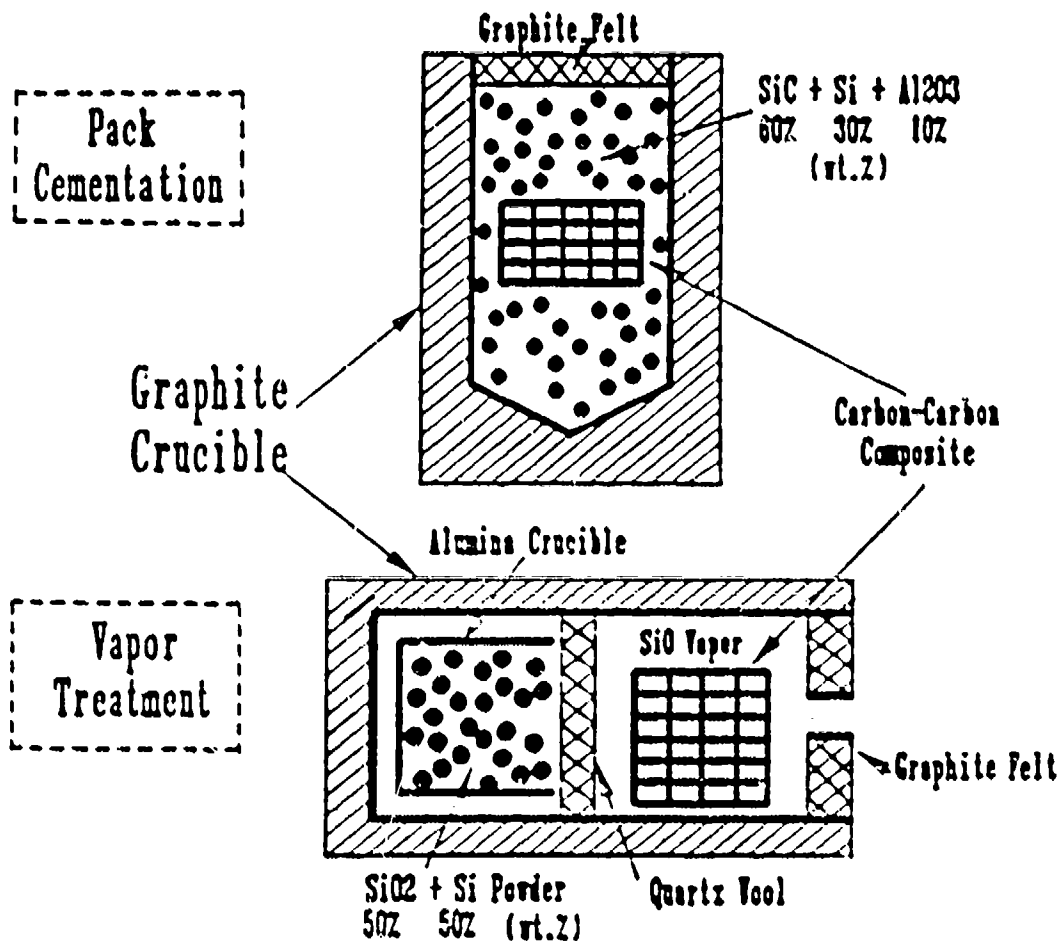
Figure 3-1b. Schematic diagram of reactors for pack cementation and SiO vapor treatment experiments.
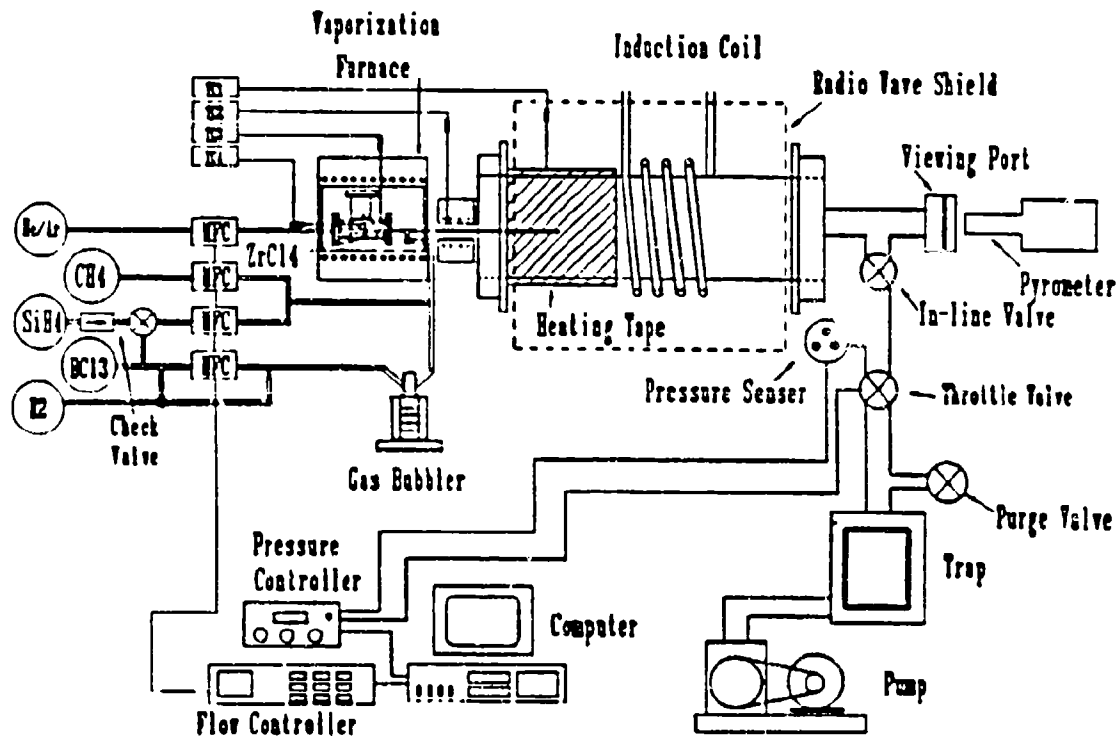
Figure 3-2. Detailed design of the computer-controlled CVD device used in this study. Note that the sensing/control of pressure and flow rates are both interfaced with the computer.
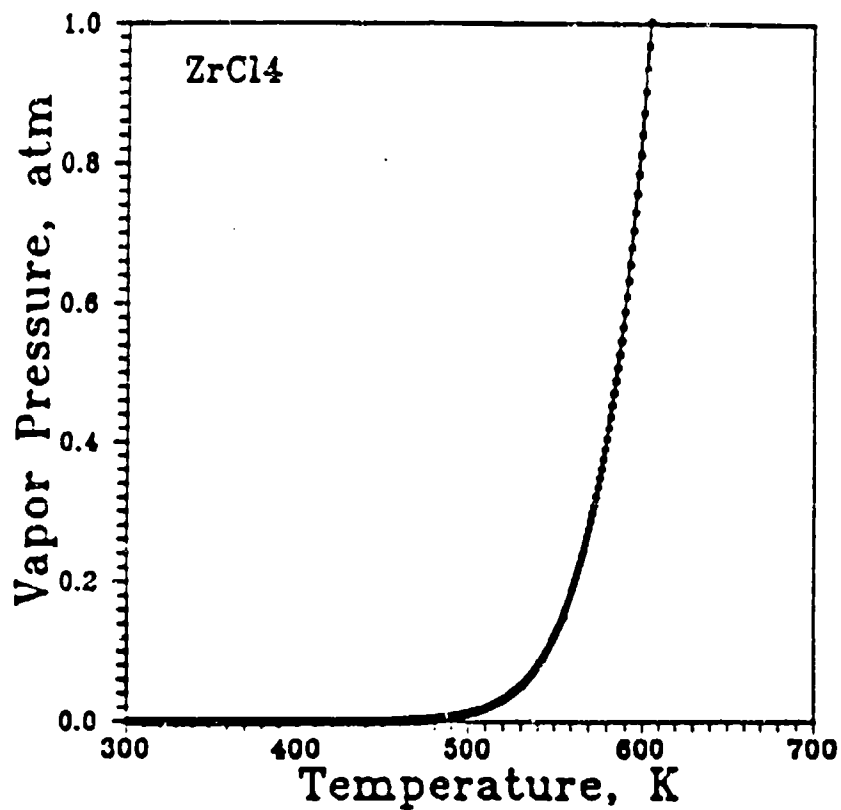
Figure 3-3. Calculated equilibrium vapor pressure of $ZrCl_4$ as a function of temperature. Note the vapor pressure increases drastically near the sublimation point of $ZrCl_4$, 604^OK (331^OC).
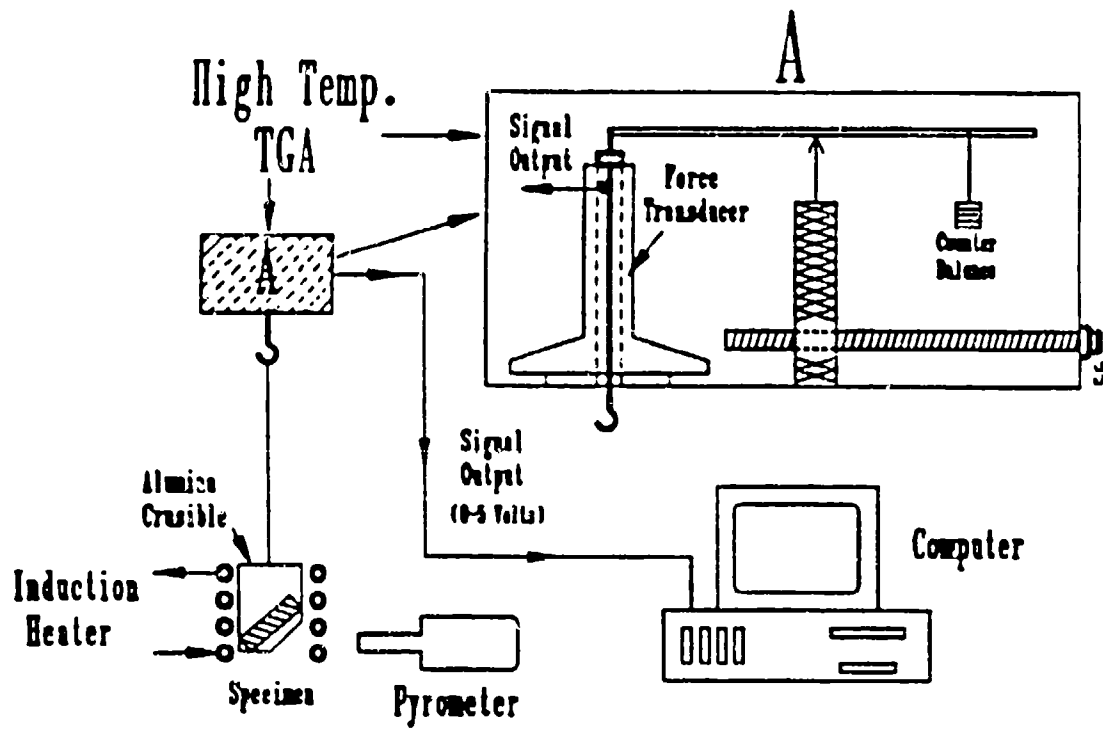
Figure 3-4. Schematic diagram showing the design of the high temperature TGA used in this study.

Silane (SiH4) Decomposition Phase Lines
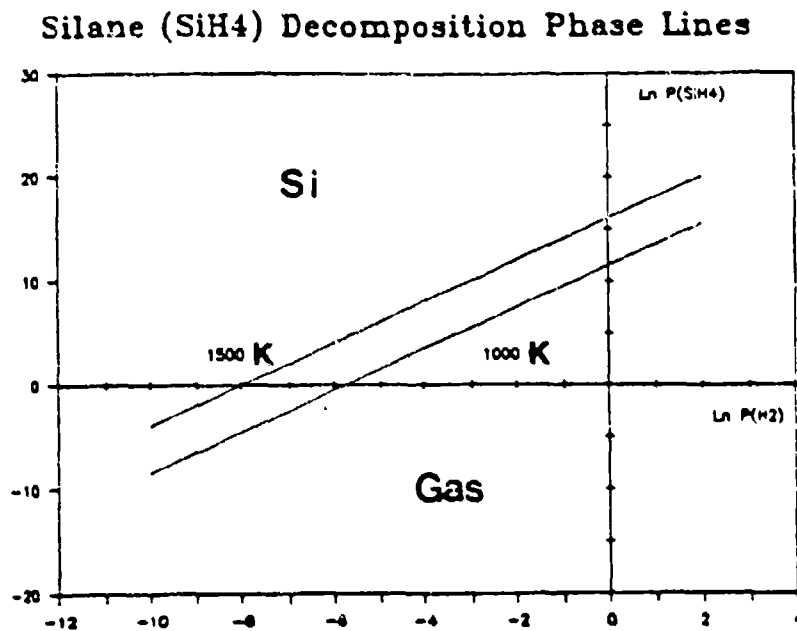
Figure 4-1. Calculated equilibrium lines in SiH_4-H_2 system at $1000^\circ C$ and $1500^\circ C$.
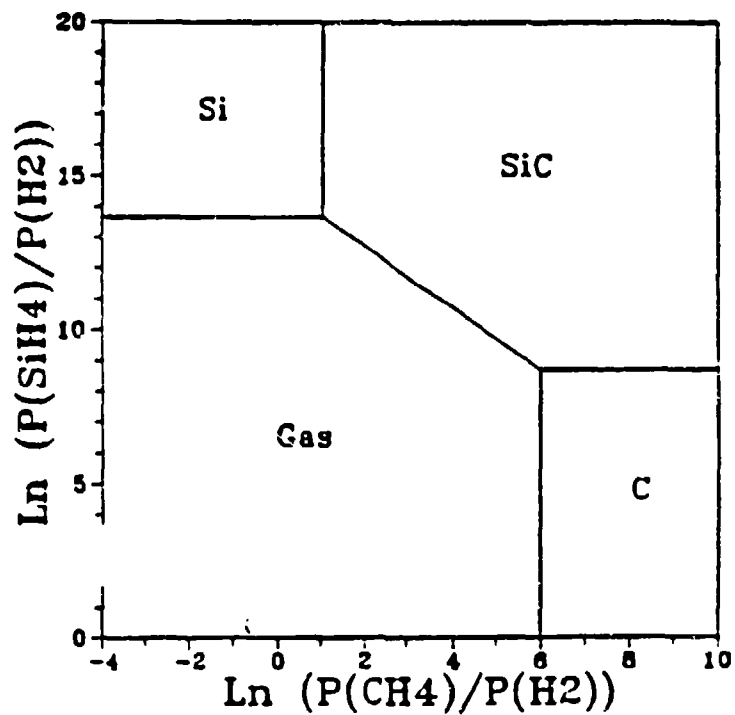
Figure 4-2. Calculated CVD phase diagram for CH_4-SiH_4-H_2 system at $1227^\circ C$.
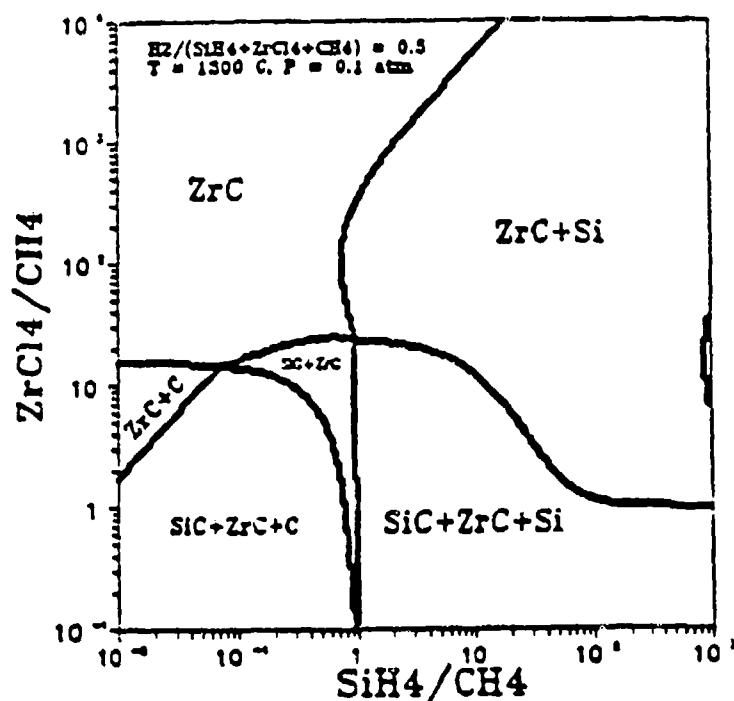
Figure 4-3. CVD phase diagram of the $ZrCl_4$, SiH_4, CH_4 and H_2 system at $1300^\circ C$, 0.1 atm.
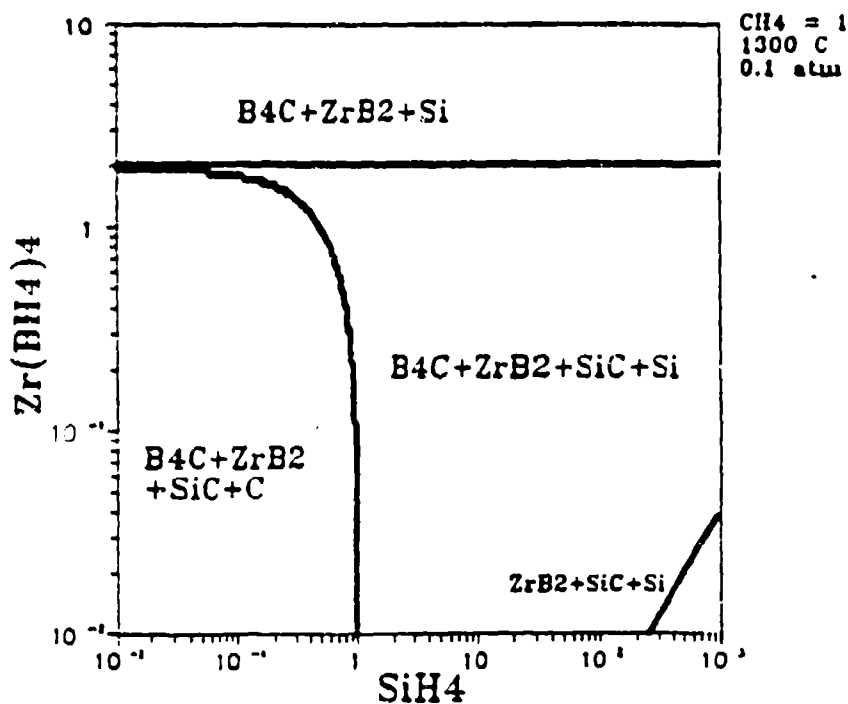
Figure 4-4. CVD phase diagram of SiH_4-$Zr(BH_4)_4$-CH_4 system at $1300^\circ C$, 0.1 atm.
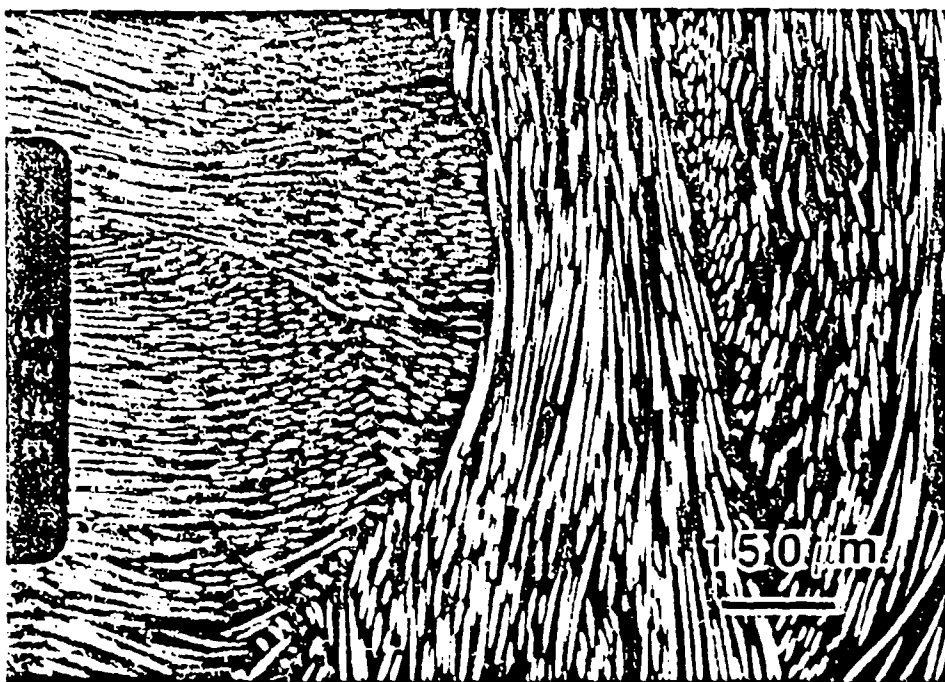
Figure 4-5. Optical micrograph of the as-received carbon-carbon composite.
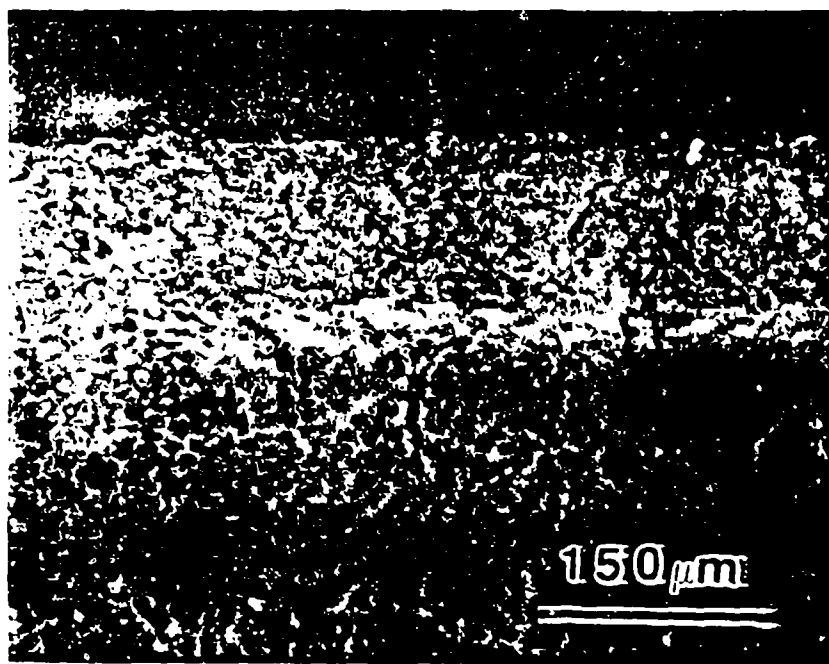
Figure 4-5a. Optical micrograph showing the cross section of a pack-cemented composite. The converted layer is about 150 µm.

Figure 4-6b. Optical micrograph of a pack-cemented composite at higher magnification. Note that fibers are less reactive during pack cementation process.
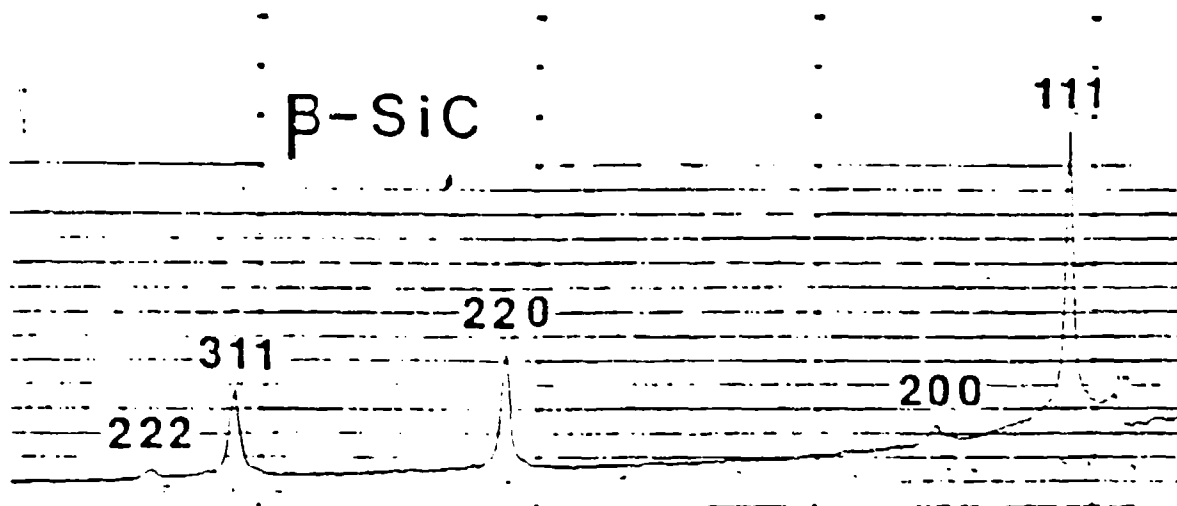
Figure 4-7a. X-ray diffraction spectrum of a pack cemented specimen.
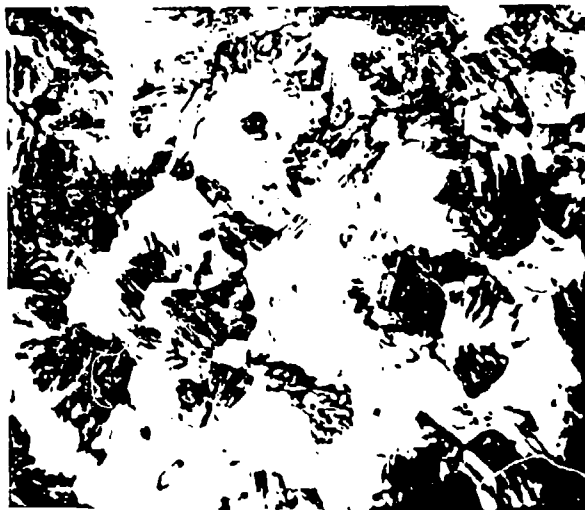
Figure 4-7b. TEM bright-field image of the converted SiC in pack-cemented specimen.

Pack Cementation Oxidation Tests
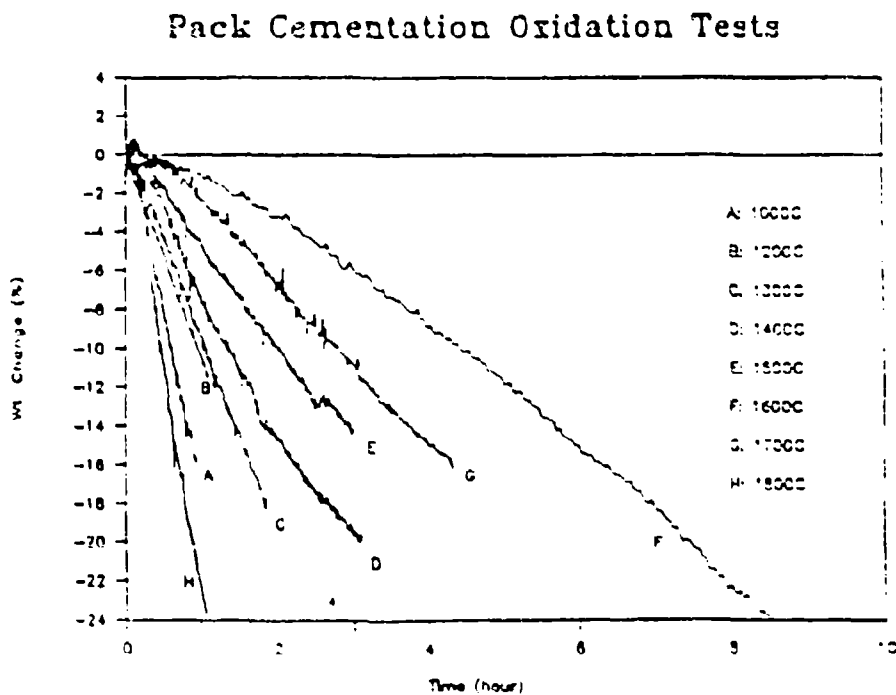
Figure 4-8a. TGA results of pack-cemented specimens.

96

Pack Cementation Oxidation Test Result
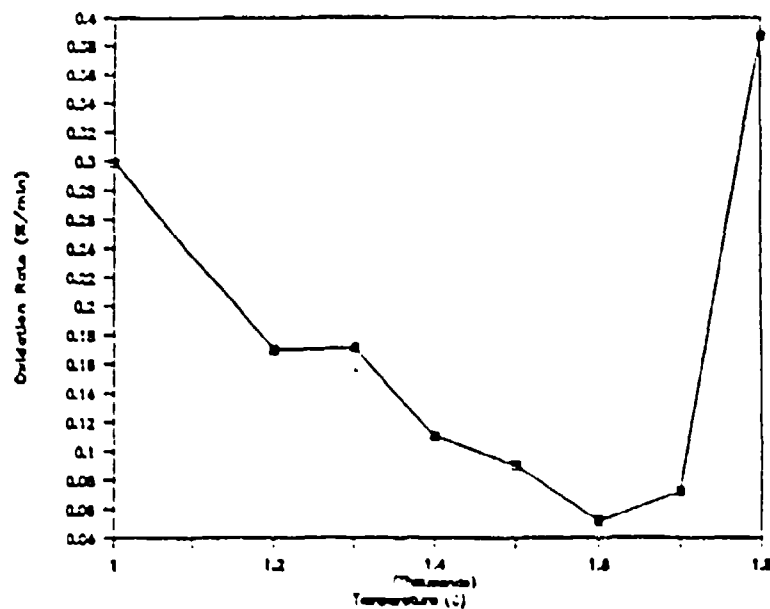
Figure 4-8b. Measured oxidation rates vs. oxidation temperature plot of the oxidized pack-cemented specimens.
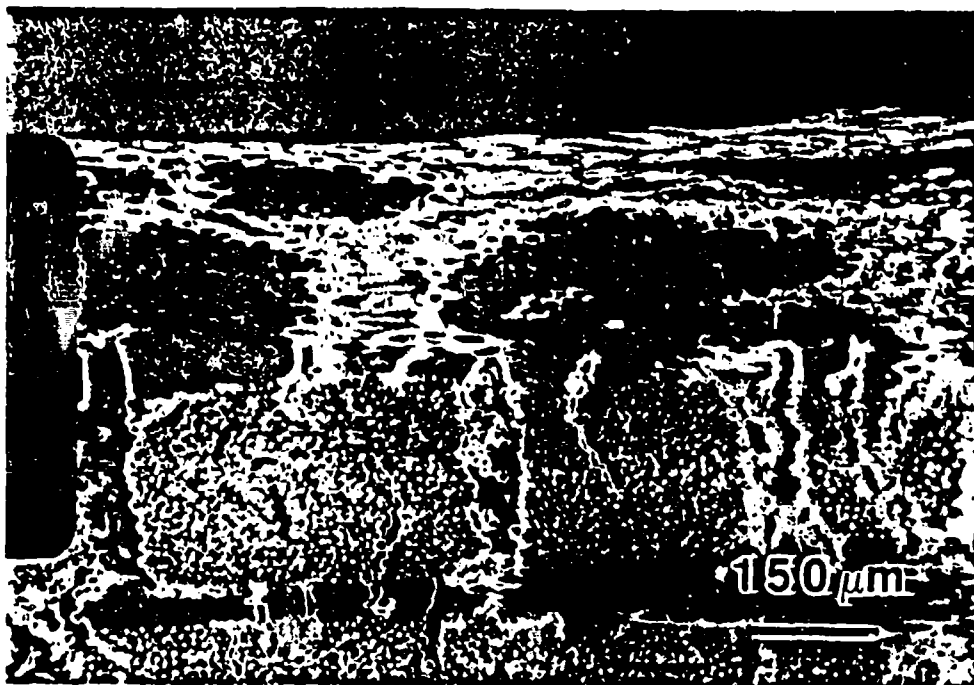
Figure 4-9. Cross-section optical micrograph of a SiO vapor treated specimen. Deeper penetration of SiC was observed.
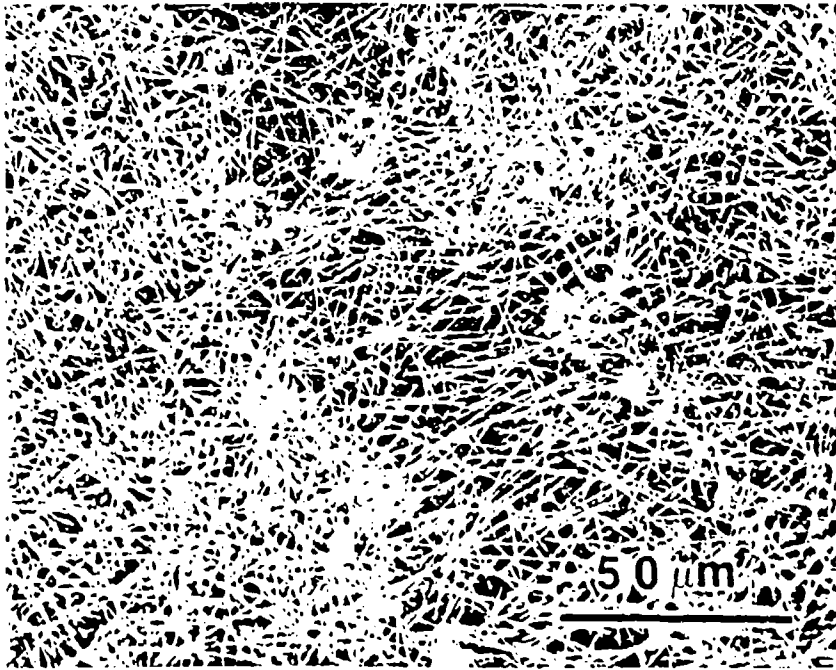
Figure 4-10. SEM micrograph of SiC whisker formed on carbon substrate surface during SiO vapor treatment.
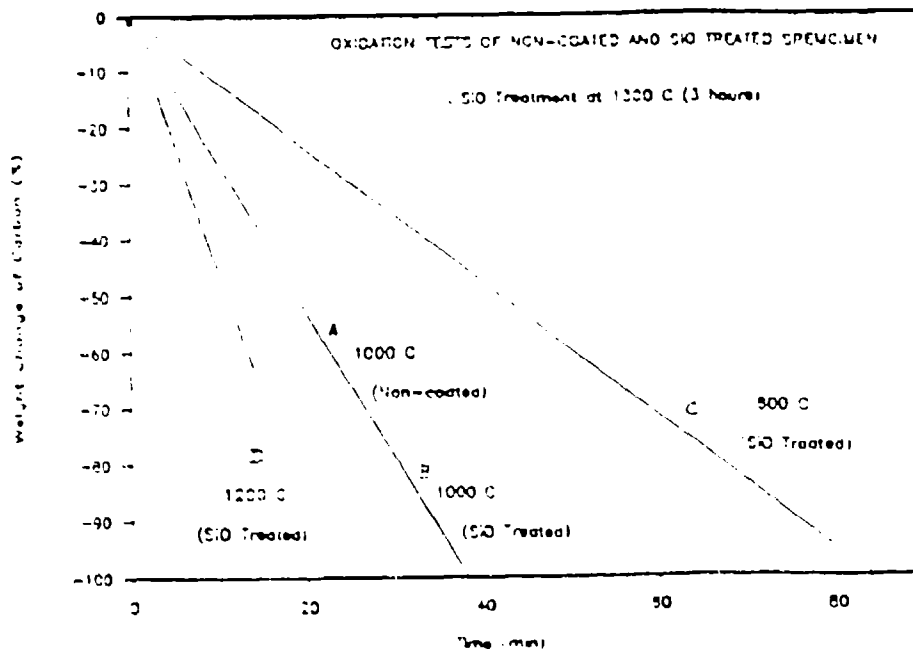
Figure 4-11. Results of oxidation tests performed on SiC vapor treated composite.

GAS FLOW RATES OF CVD SILICON CARBIDE
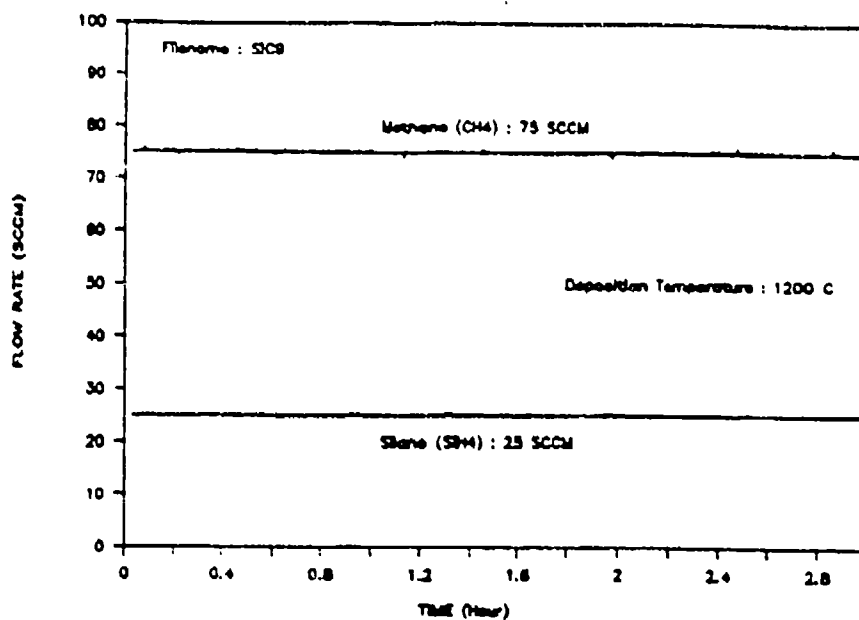
Figure 4-12. Real flow rate curves for obtaining CVD SiC coating.
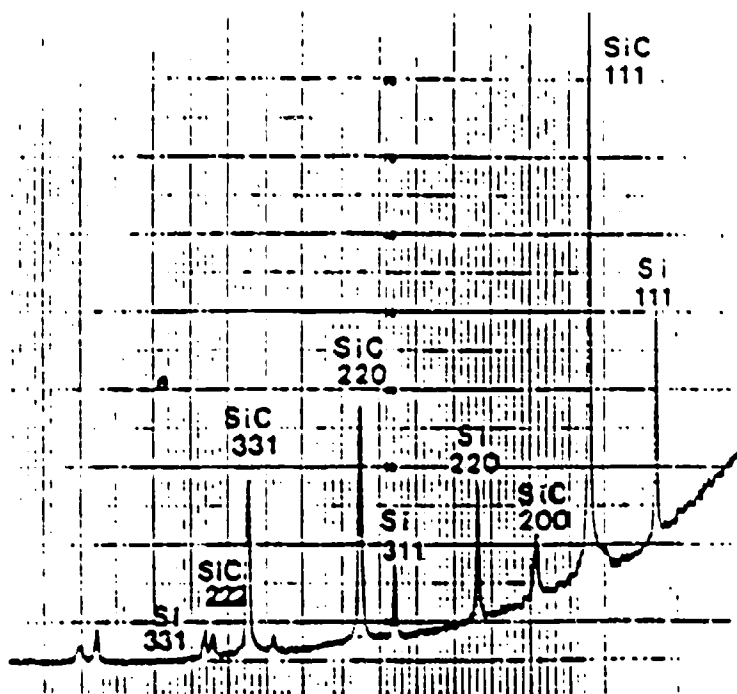
Figure 4-13. X-ray diffraction spectrum of a CVD SiC coated composite.

100 μm
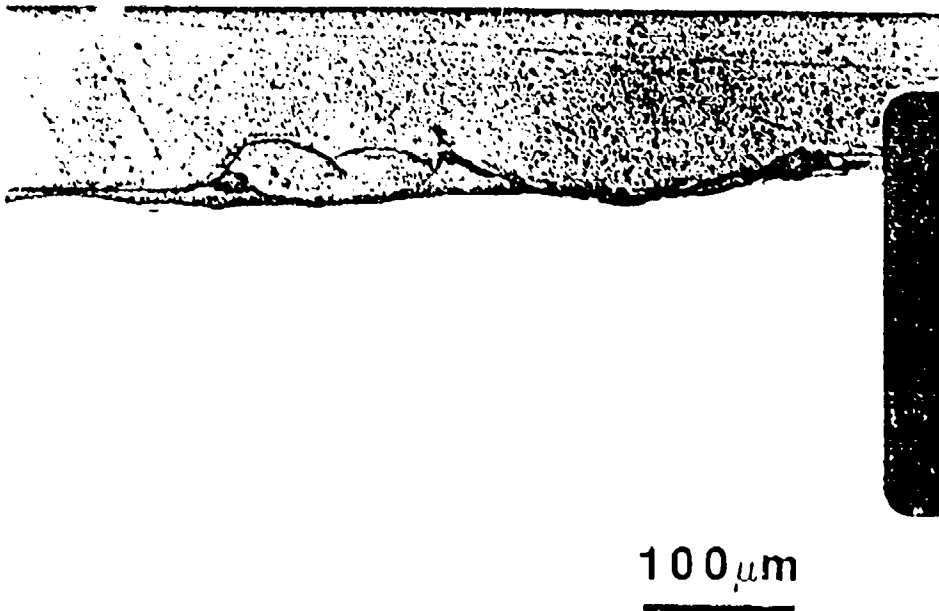
Figure 4-14a. Cross-section optical micrograph of a SiC-coated composite.

120 μm

Figure 4-14b. SEM micrograph showing the polycrystalline structure of SiC coating surface.
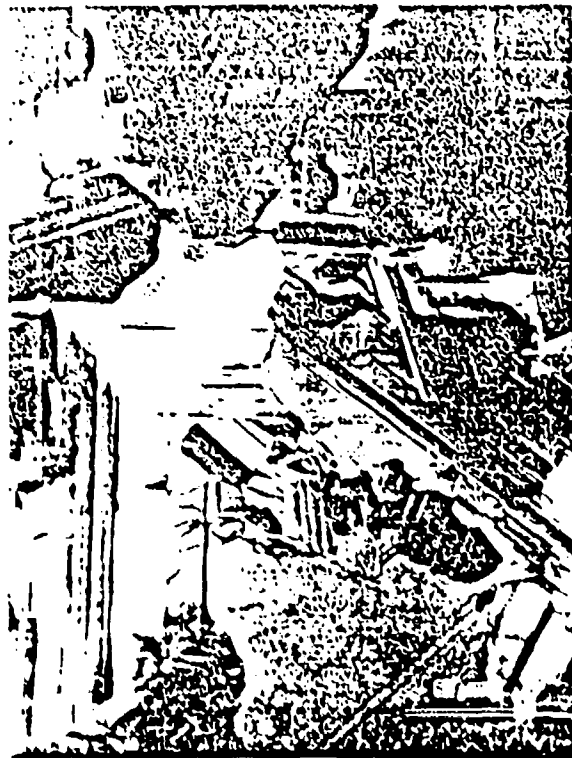
Figure 4-15a. TEM bright-field image of SiC coating. SiC crystals are heavily twined.

0.2 μm

Figure 4-15b. TEM bright-field image of the micro-twins in SiC coating.
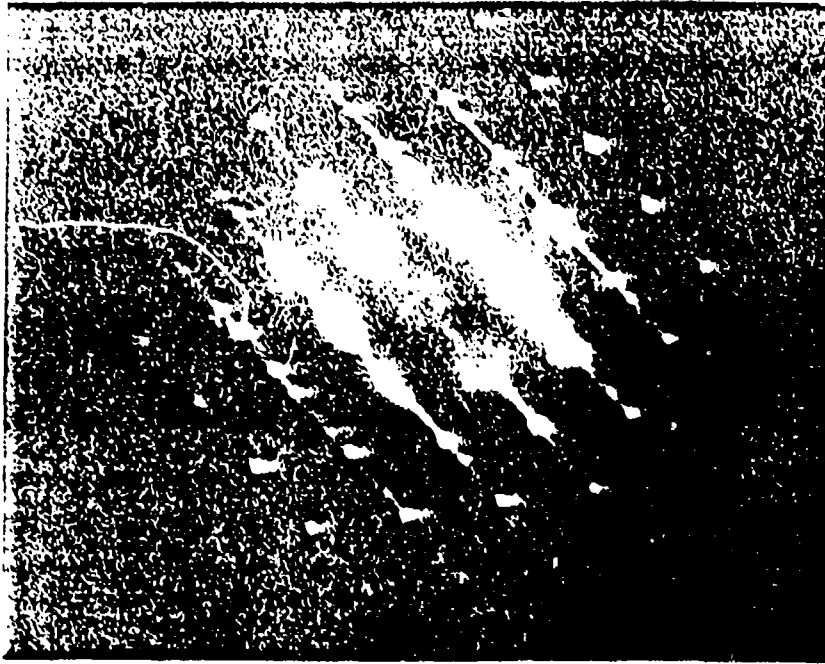
Figure 4-15c. TEM selecting area diffraction pattern taken
from the area shown in Figure 4-15b. Note that twin spots
and matrix spots are coincident in every 3 rows of
diffraction spots.

Isothermal Oxidation of SiC Coated C/C
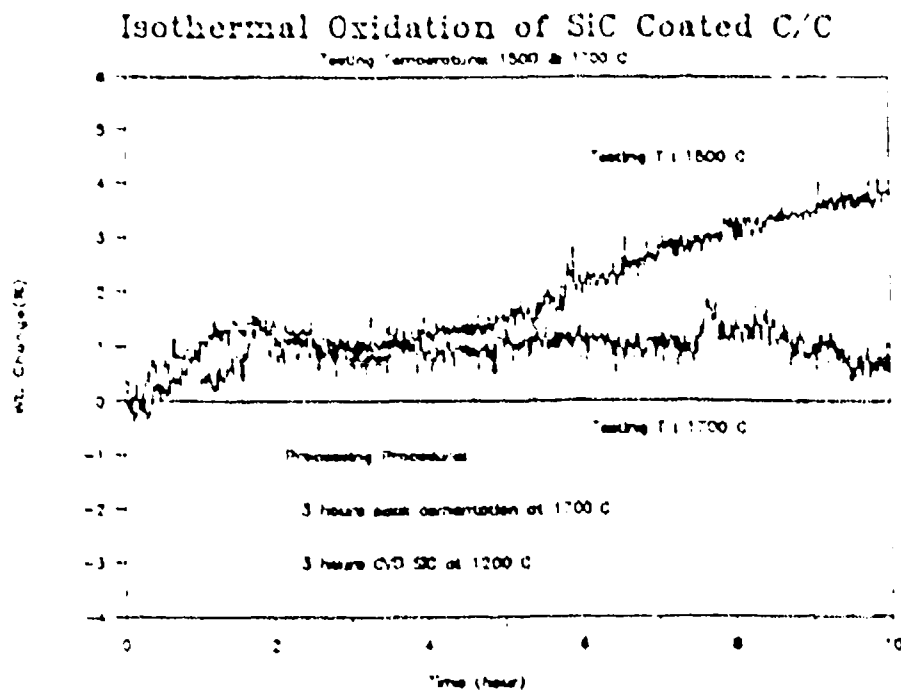
Figure 4-16. TGA results of SiC coated composites oxidized
at 1500°C and 1700°C isothermally.
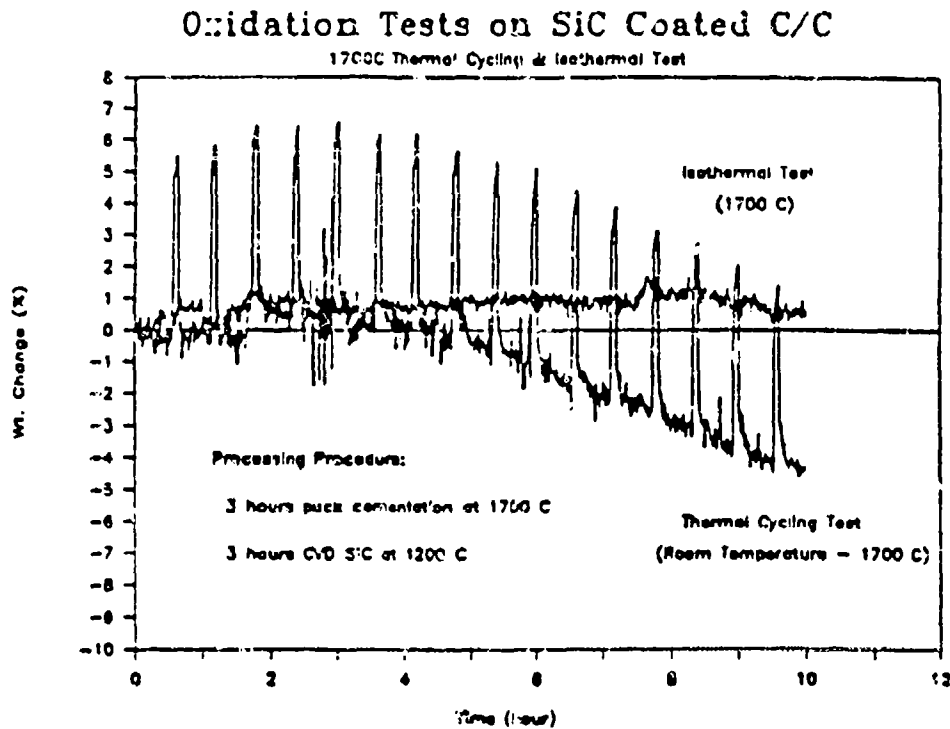
Figure 4-17. Comparison between isothermal and thermal
cycling tests at 1700°C for SiC-coated composite.

100μm
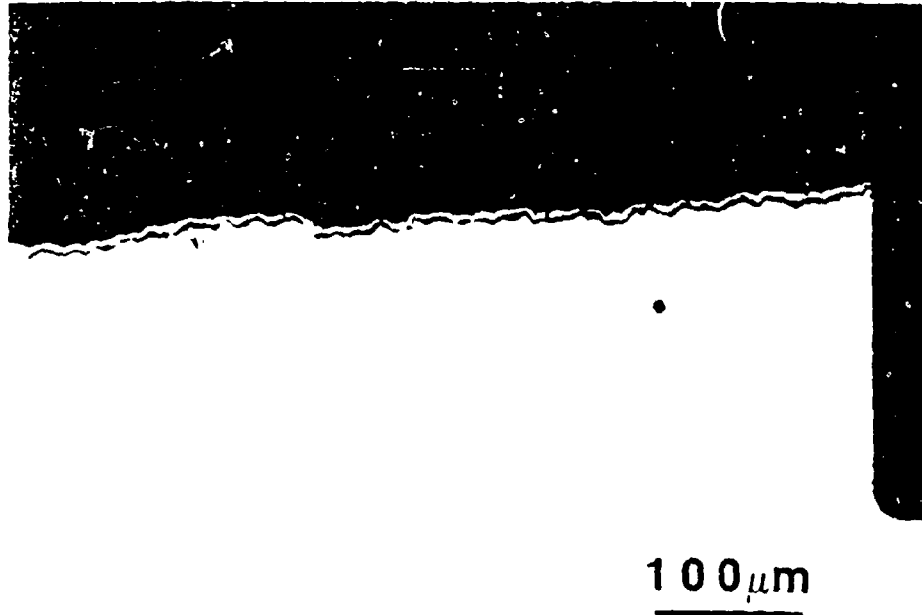
Figure 4-18. Cross-section optical micrograph of SiC-coated composite after isothermal oxidation test at 1700°C for 3 hours.
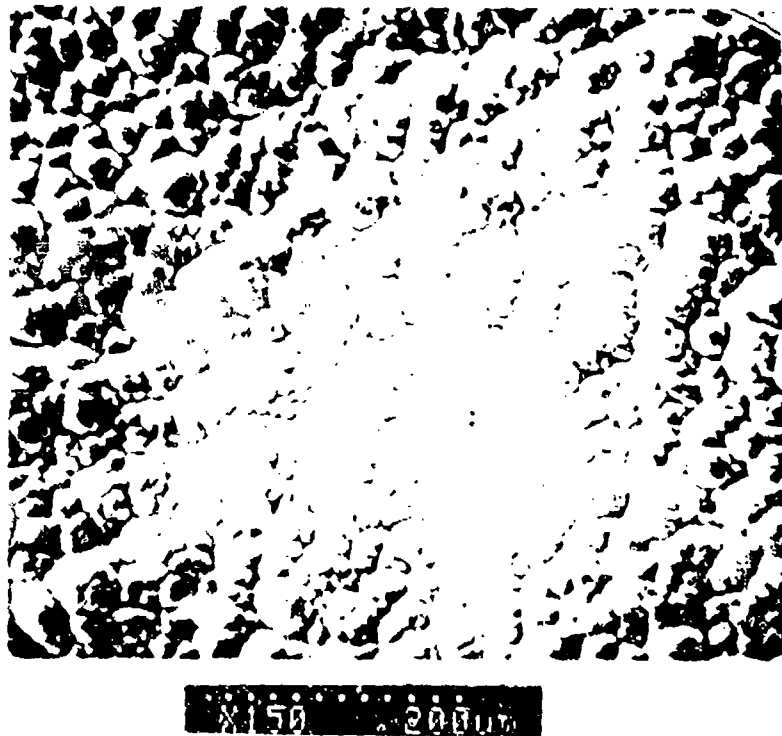
Figure 4-19. The micrograph of a SiC-coated composite after oxidation test at 1500°C, 10 hours.
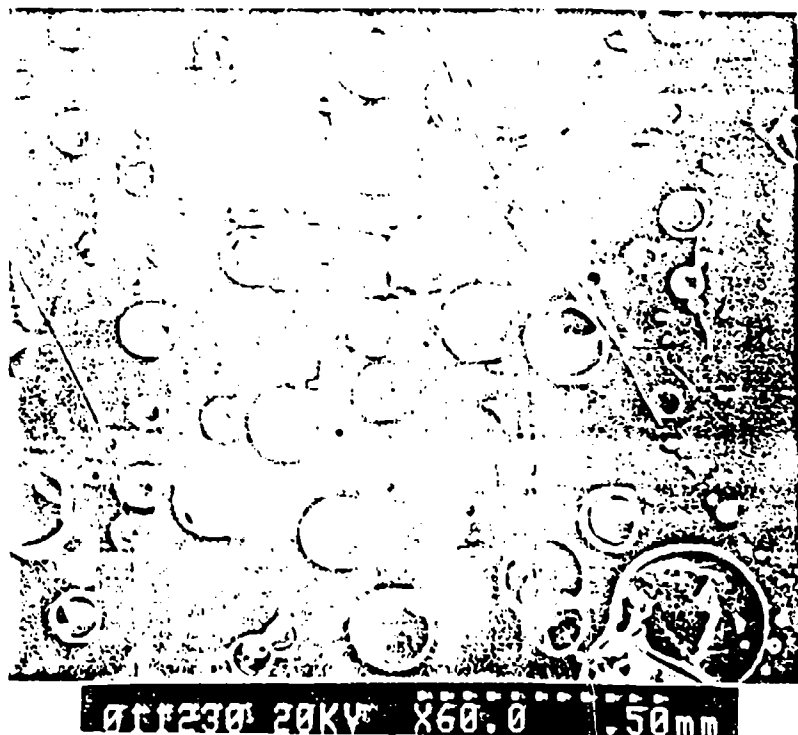
Figure 4-20. SEM micrograph of an oxidized SiC coating. The oxidation test was performed at 1700°C for 3 hours.

GAS FLOW RATES OF CVD ZrB2
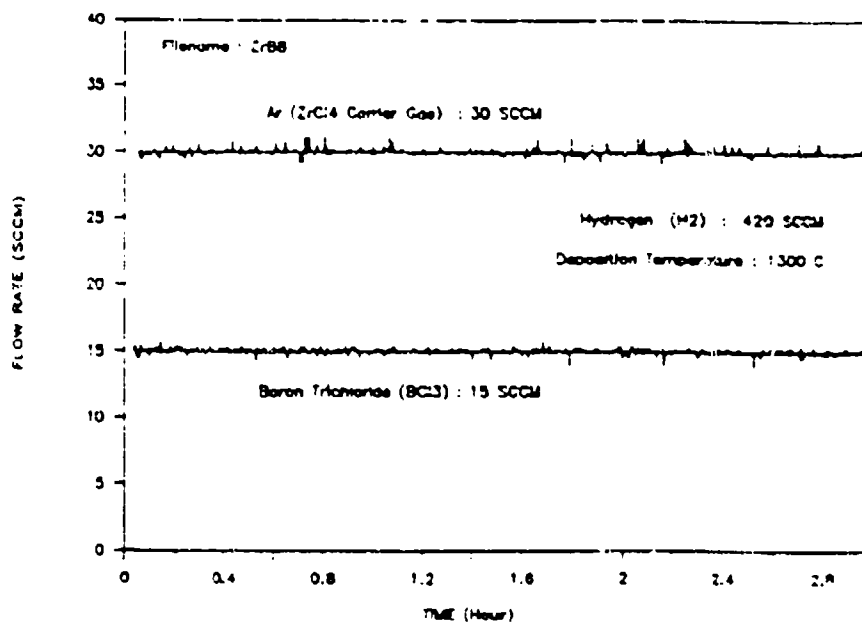
Figure 4-21a. Real flow rate curves for obtaining ZrB₂ coating.
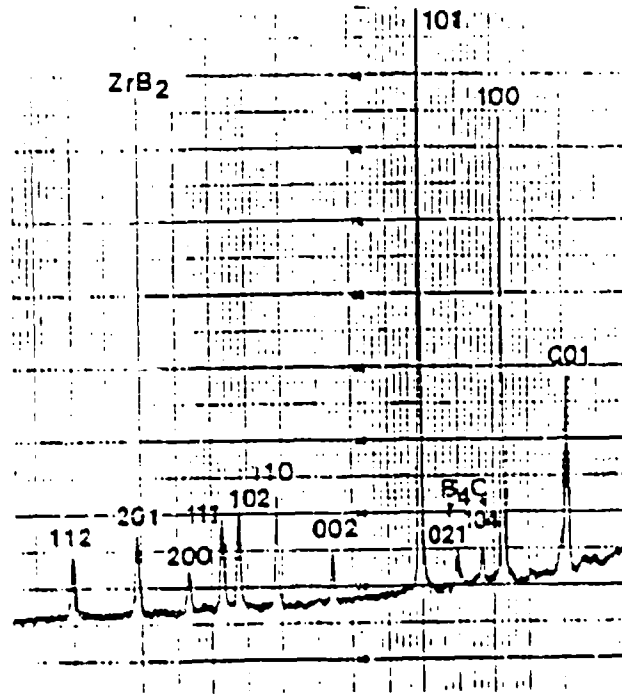
Figure 4-21b. X-ray diffraction spectrum of ZrB_2 coating. Small amount of B_4C was also detected.

Figure 4-22. Cross-section optical micrograph of ZrB_2 coating. The coating seemed to be prone to thermal cracking.
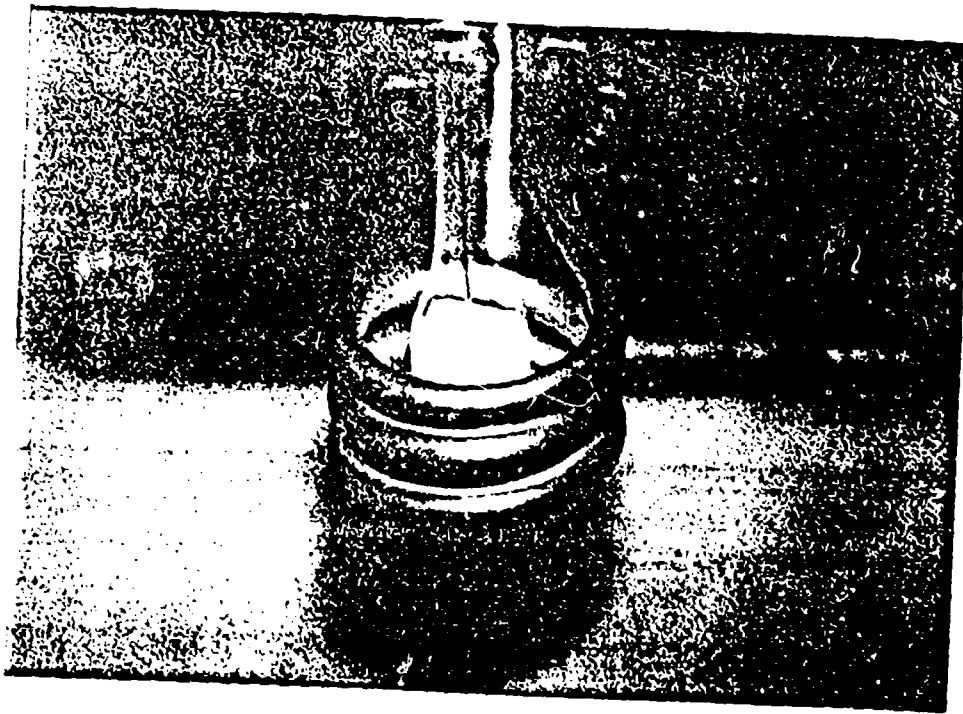
Figure 4-23. Picture showing the oxidation test of ZrB₂-coated composite. The specimen started to smoke at about 1000°C.
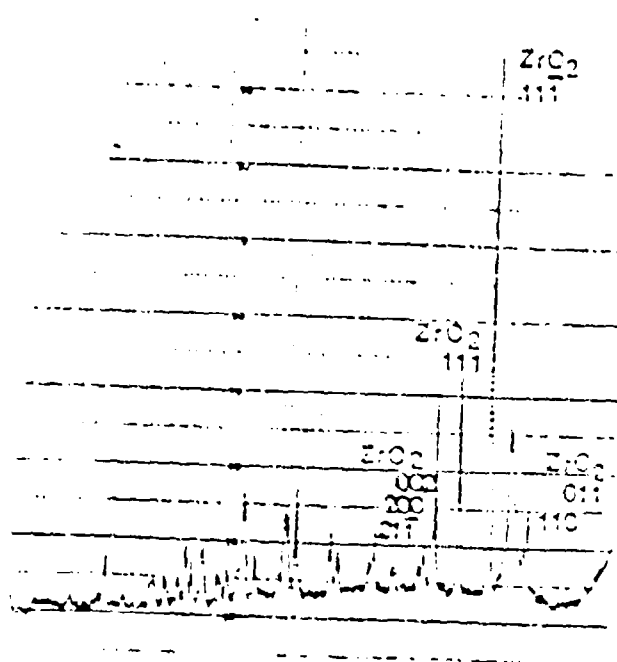
Figure 4-24. X-ray diffraction spectrum of oxidized ZrB₂ coating. After oxidation, the residue was predominately ZrO₂.
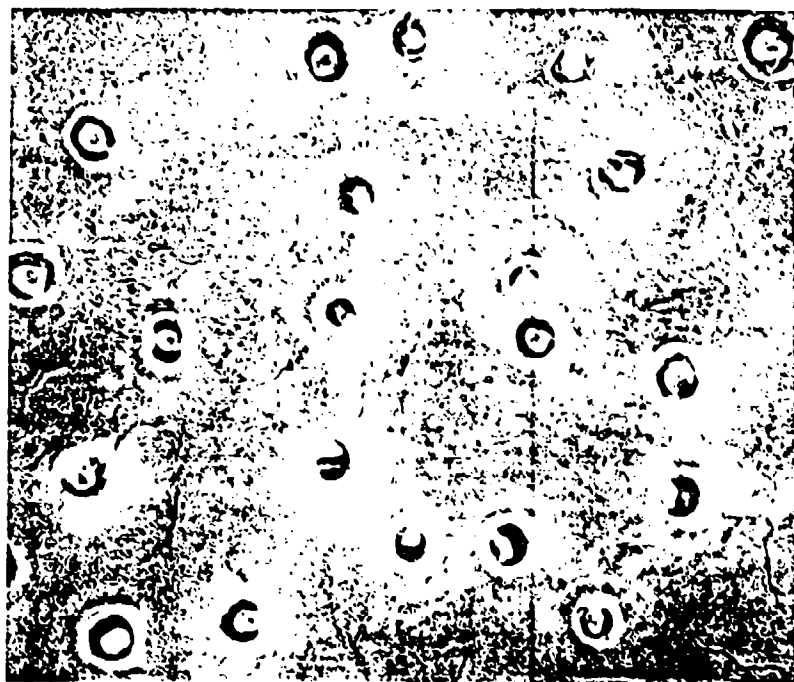
Figure 4-25a. SEM micrograph of oxidized ZrB_2 coating. Rupturing of B_2O_3 bubbles started to occur at about 1000°C, leaving particulate residue of ZrO_2 behind.
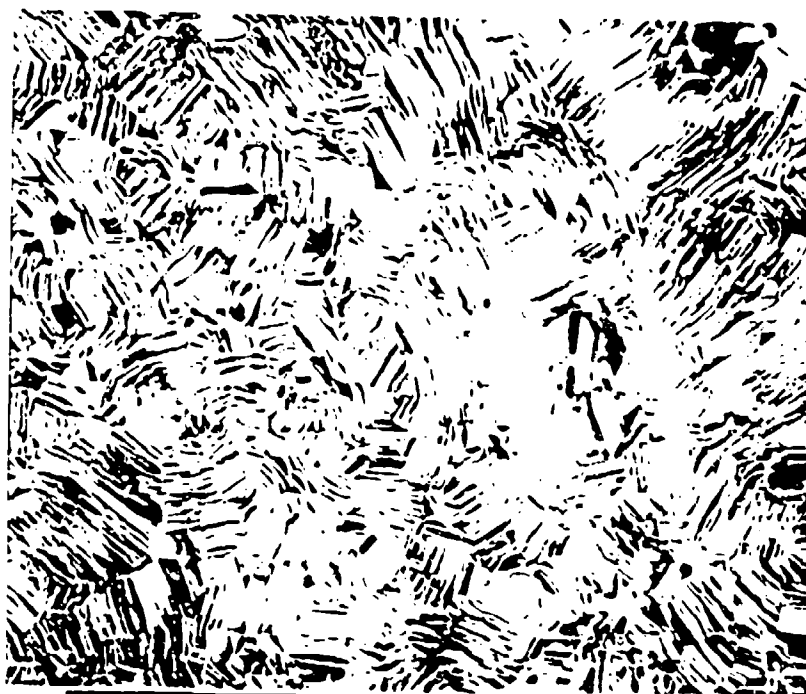
Figure 4-25b. SEM micrograph of a badly oxidized ZrB_2 coating. The laminar-shaped residue was proved by X-ray diffraction to be ZrO_2. The coating only last a few minutes at 1500°C.

Thermal Cycling Test of ZrB2+SIC
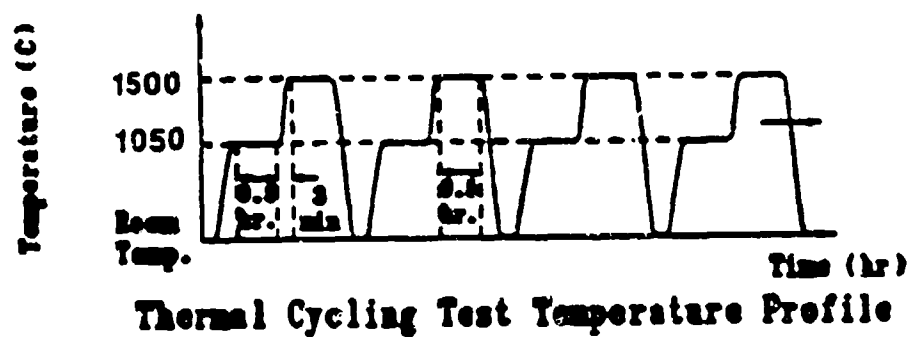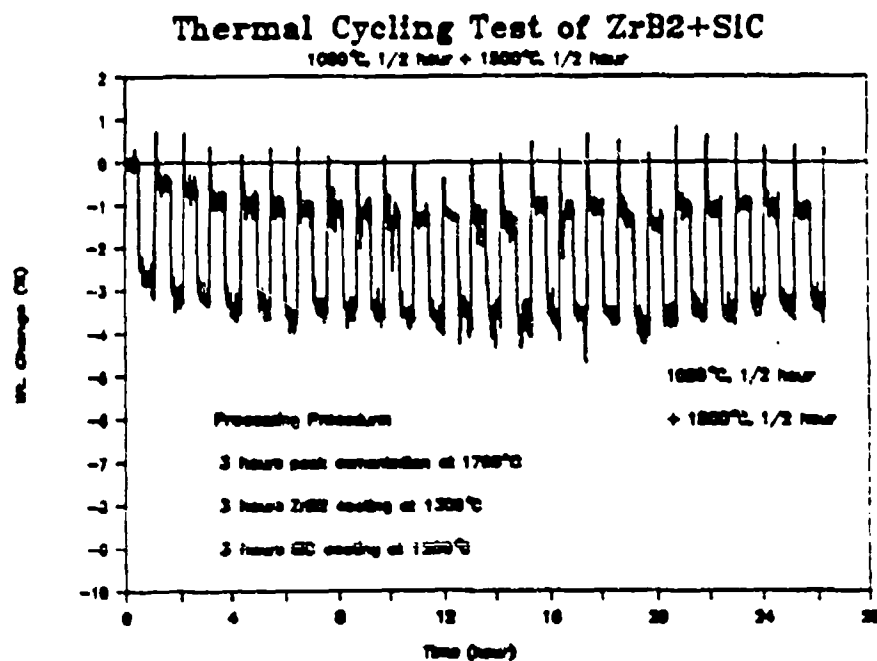
Figure 4-26. TGA result of a two-stage thermal cycling test performed on a ZrB$_2$ + SiC multilayer coating. After 25 hours of cycling, the specimen only lost 1% of its initial weight.
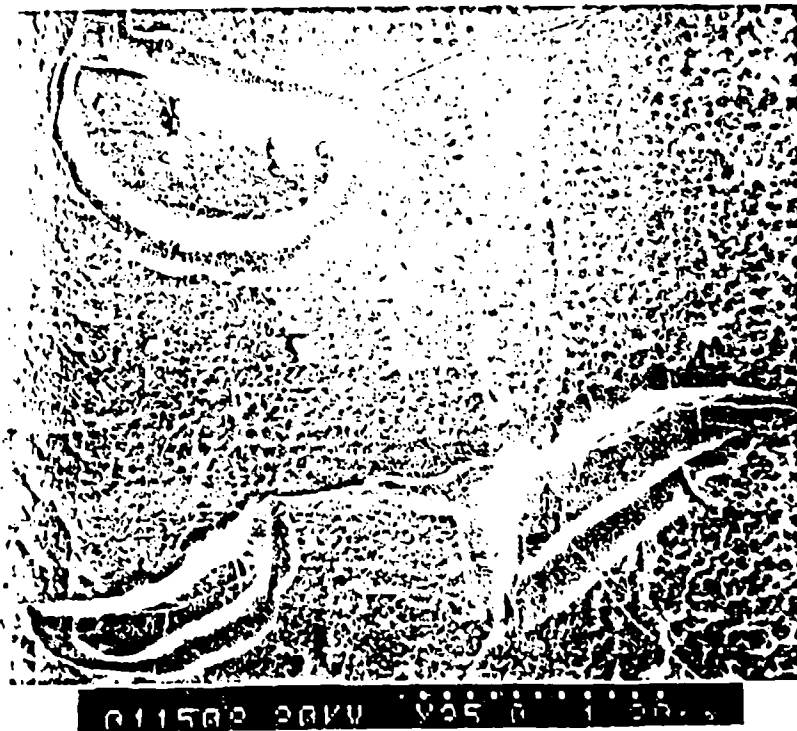
Figure 4-27. SEM micrograph of a ZrB_2 + SiC multilayer coating. Note that excellent sealing was achieved in 3 chipped areas. The TGA result of this specimen is shown in Figure 4-26.
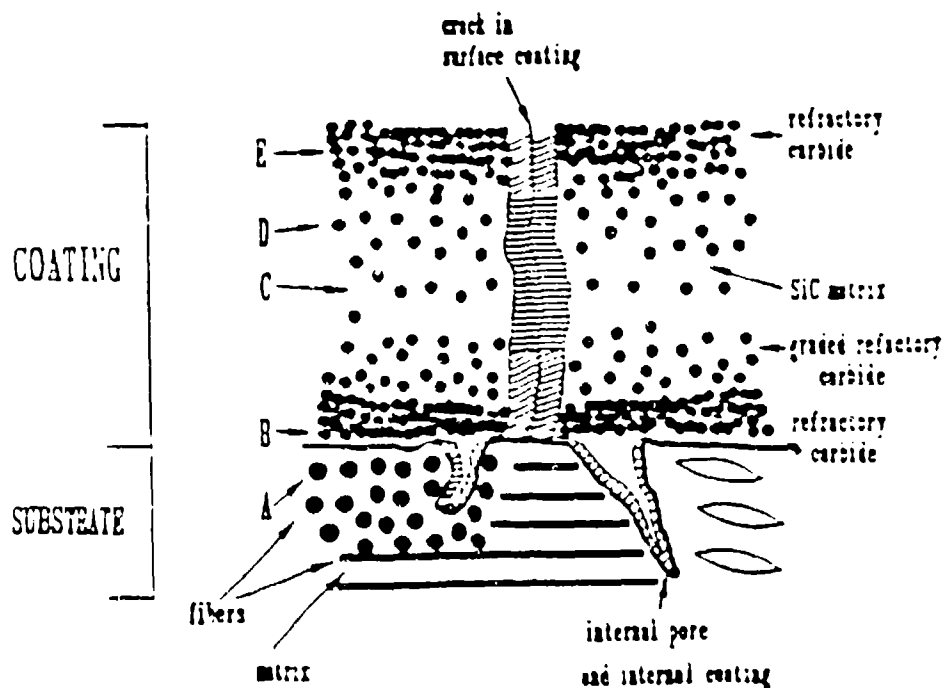
Figure 4-28. Schematic diagram showing the concept of the ZrC + SiC graded coating system.
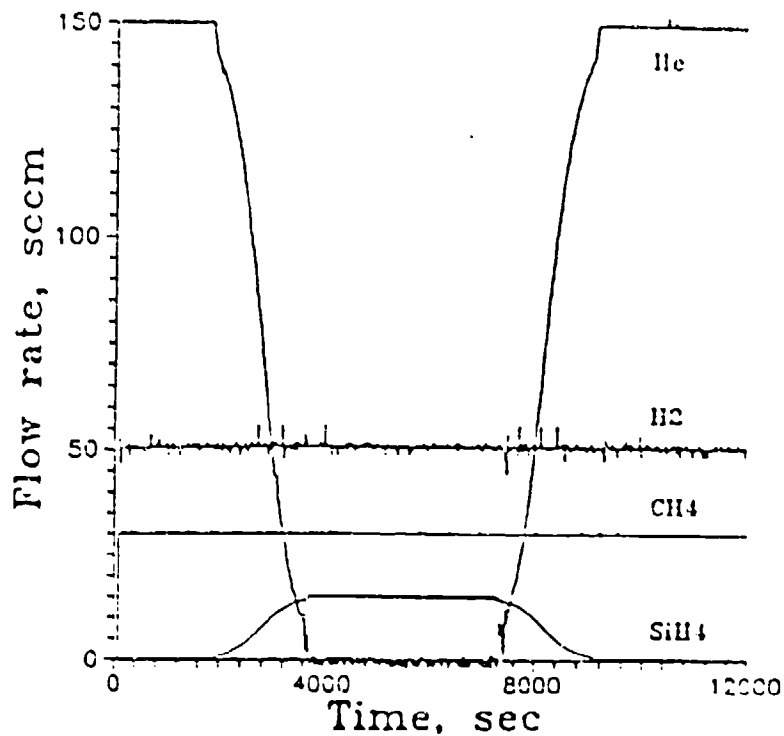
Figure 4-29a.   Curves of gas flow used in an attempt to
deposit ZrC + SiC graded coating.   Unfortunately, the
deposition was found predominately ZrC.

Figure 4-29b.   Cross-section optical micrograph of ZrC
coating obtained by using the gas control described in
Figure 4-29a.
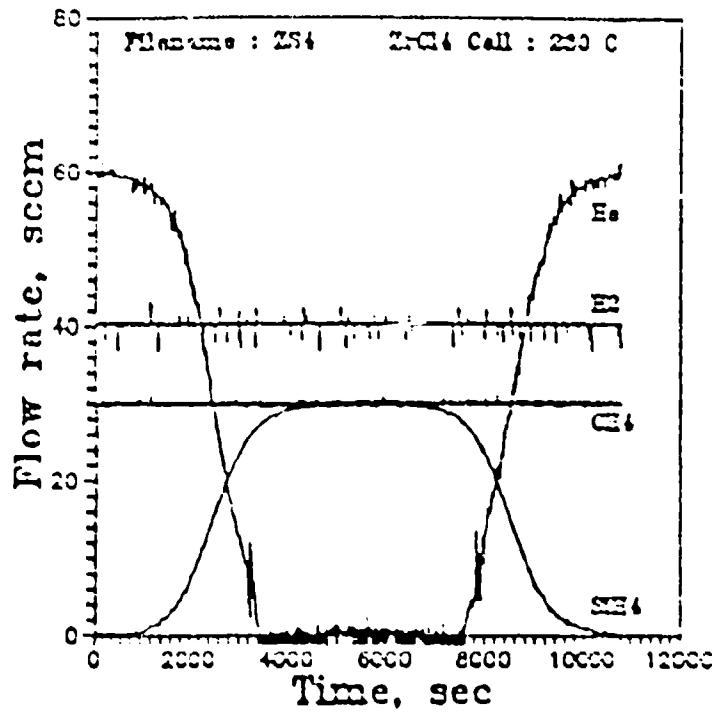
Figure 4-30a. Flow rate curves for ZrC + SiC codeposition where multilayered coating resulted.
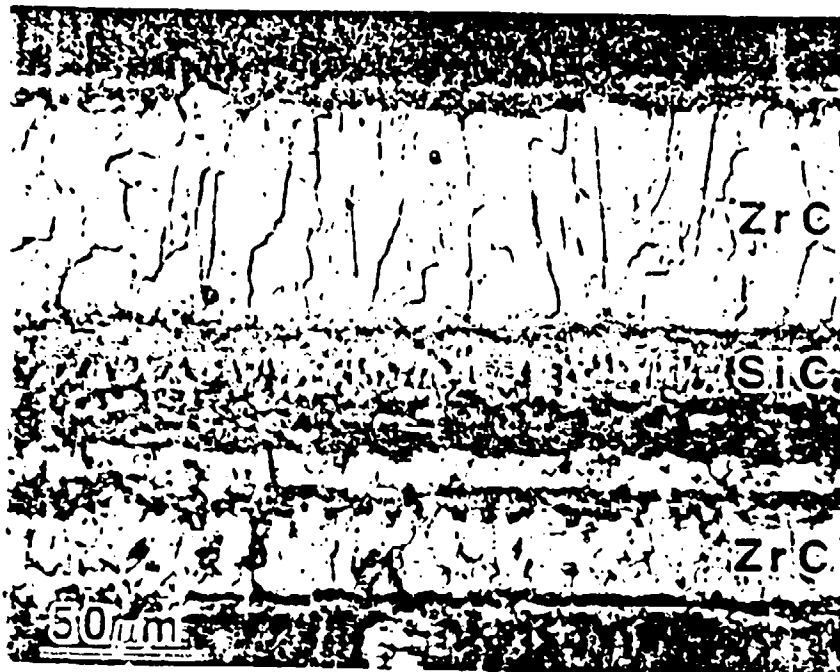
Figure 4-30b. Optical micrograph of the cross-section of a multilayered coating obtained using the gas flow rates shown in Figure 4-30a.

Figure 4-31. SEM micrograph of an oxidized specimen coated using flow condition shown in Figure 4-30a. The specimen was oxidized at 1500°C for 1 hour.
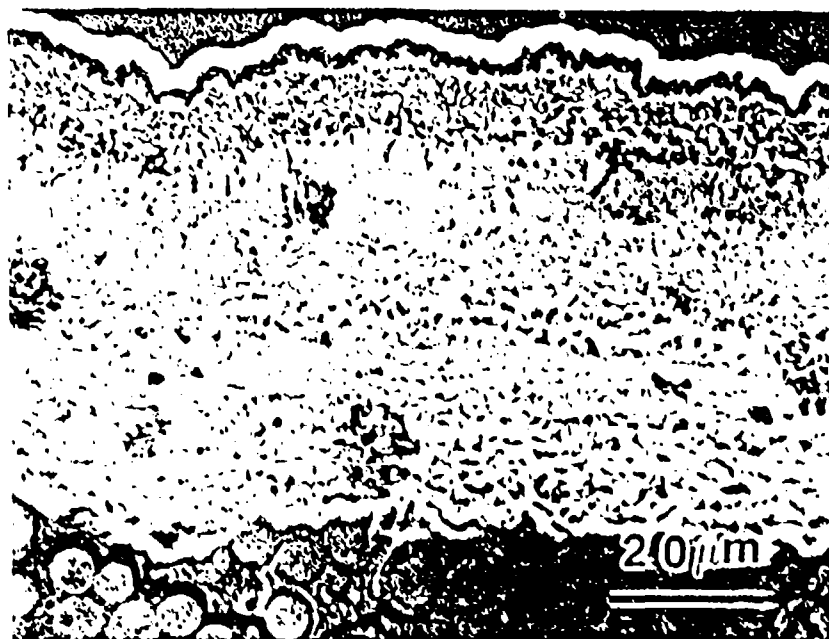
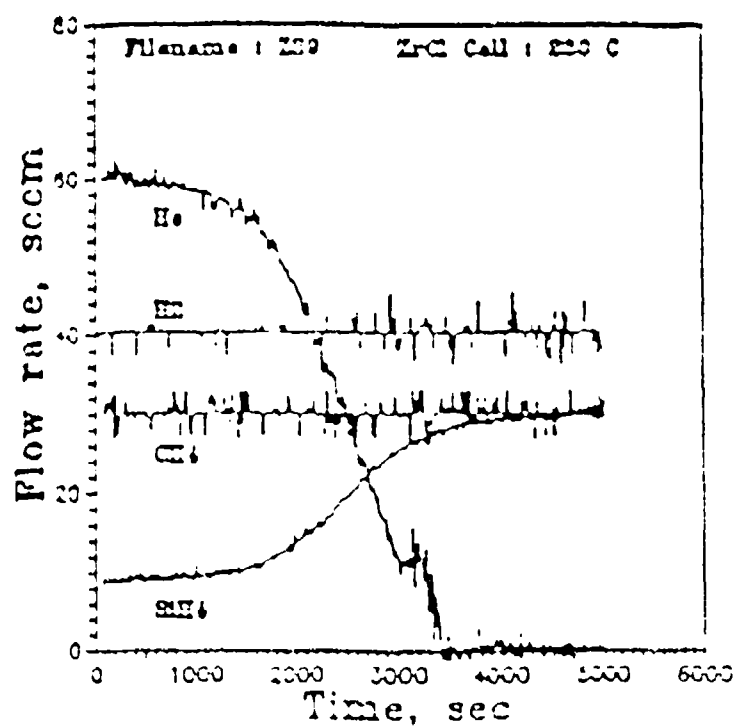Figure 4-32a. Optical micrograph of the cross section of a graded coating consisting of ZrC layer (light region) and SiC (dark phase).

Figure 4-32b. A diagram showing flow rate curves as a function of deposition time for the coating shown in Figure 4-32a.

Figure 4-33a. SEM micrograph of an oxidized specimen
coated using flow condition shown in Figure 4-32b. This
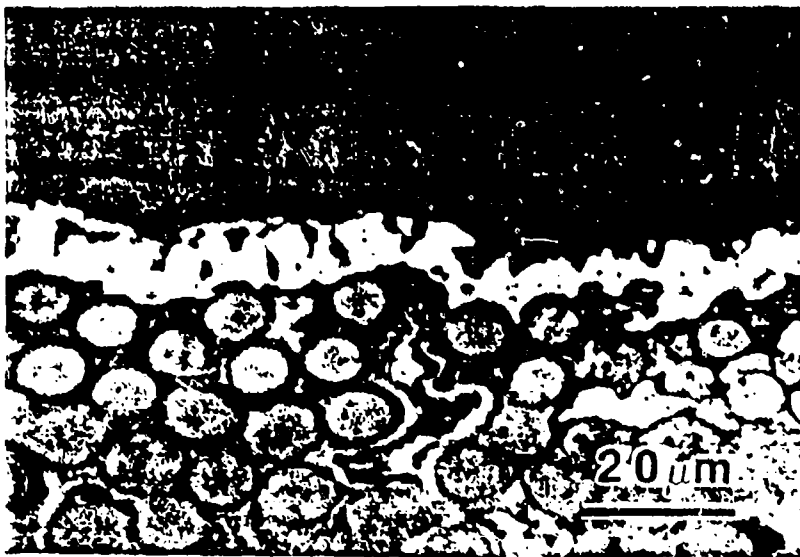specimen was oxidized at 1500°C for 10 hours.

Figure 4-33b. Cross-section optical micrograph of the
specimen shown in Figure 4-33a. A glass layer was formed
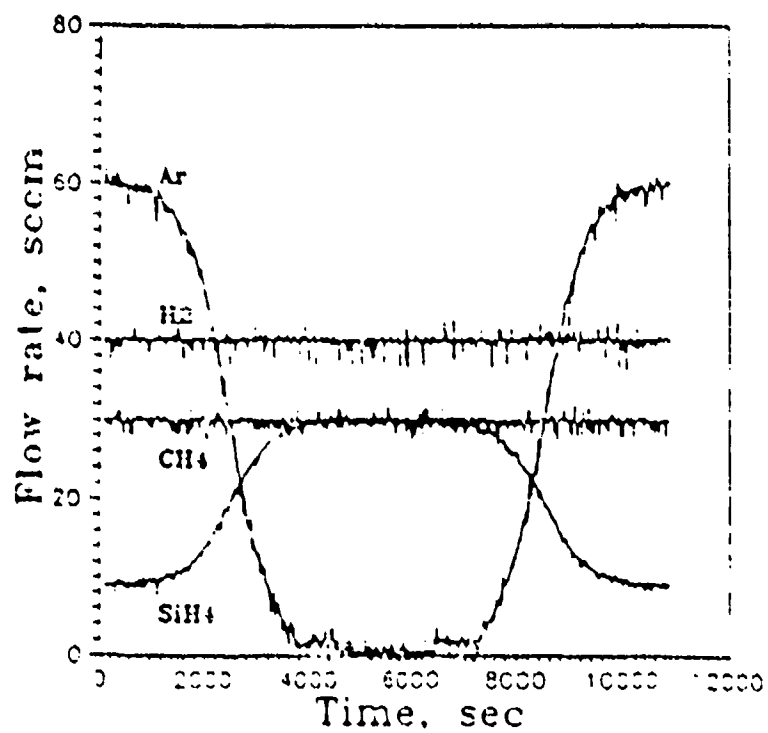during the oxidation test.

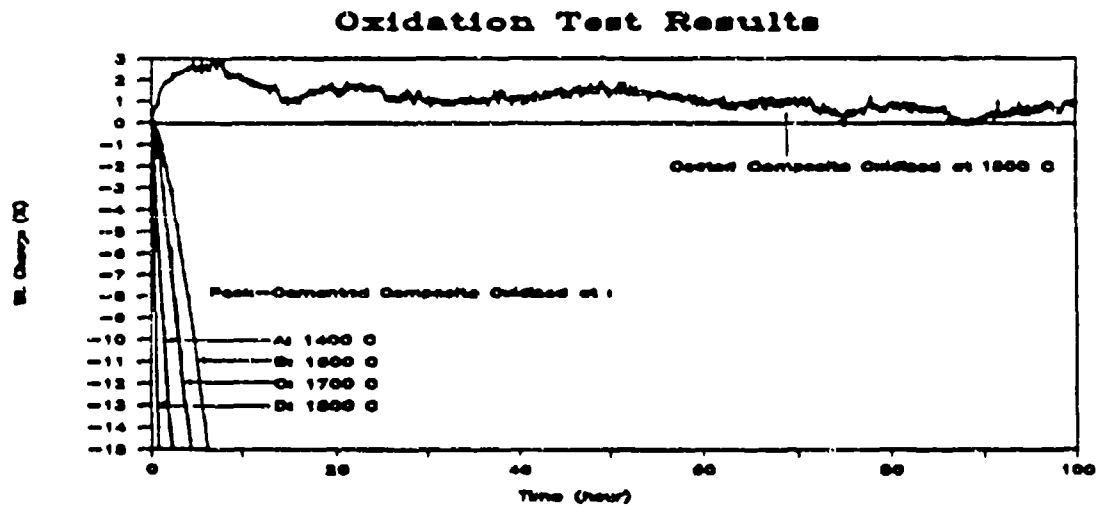Figure 4-34. Flow rate curves for obtaining optimum ZrC + SiC graded coating.

Figure 4-35. TGA result of a composite protected by a graded SiC + ZrC coating at 1500°C in air, as compared with test results of pack-cemented composite.

117

Figure 4-36. SEM micrograph of a coated composite oxidized at 1700°C, 10 hours in air.

Figure 4-37. SEM micrograph of the surface of an oxidized specimen (1700°C, 21 hours) Bubbles were formed during the oxidation.
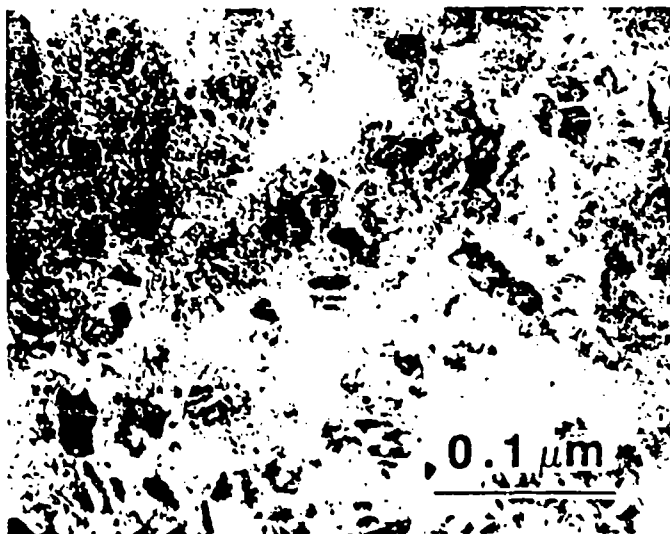
Figure 4-38a.   TEM micrograph of the glass layer formed on
an   oxidized specimen at 1700°C, 10 hours in air.

Figure 4-38b.   TEM selecting area diffraction pattern of
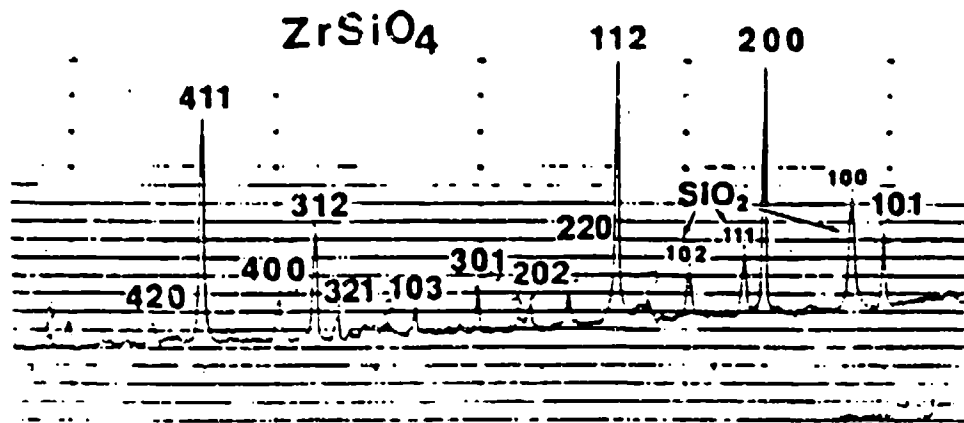the glass phase shown in Figure 4-36a.

Figure 4-39. X-ray diffraction spectrum of ZrC + SiC graded coating obtained using flow condition shown in Figure 4-34. The oxidized surface was identified as $ZrSiO_4$ with little amount of SiO_2.